Theoretical Studies of the Interaction between U(VI) and Mineral Surfaces

Pengyuan Gao

ÉCOLE DOCTORALE *Énergie - Matériaux - Sciences de la Terre et de l'Univers*

Institut des Sciences de la Terre d'Orléans

School of Nuclear Science and Technology / Lanzhou University

THÈSE EN COTUTELLE INTERNATIONALE présentée par :

Pengyuan GAO

soutenue le : 20 Novembre 2023

pour obtenir le grade de :

Docteur de Université d'Orléans

et de l'Université de Lanzhou

Discipline : Sciences de la Terre et de l'Univers

Theoretical Studies of the Interaction between U(VI) and Mineral Surfaces

THÈSE dirigée par :

TOURNASSAT Christophe	Professeur, Université d'Orléans
GUO Zhijun	Professeur, Lanzhou University

RAPPORTEURS :

QIN Zhi (Président du jury)	Chargé de recherche, Chinese Academy of Sciences
FAN Qiaohui	Chargé de recherche, Chinese Academy of Sciences

JURY :

QIN Zhi (Président du jury)	Chargé de recherche, Chinese Academy of Sciences
FAN Qiaohui	Chargé de recherche, Chinese Academy of Sciences
GUO Zhijun	Professeur, Lanzhou University
TOURNASSAT Christophe	Professeur, Université d'Orléans

Acknowledgments

At the moment of the completion of the dissertation, as far as the eye can see, all are memories, and as far as the heart is concerned, all are the past. In twenty years of study, there has been the delight of success and the frustration of failure. There are too many people and things worth remembering. I would like to express my gratitude through this article.

This work was completed at Lanzhou University and Institut des Sciences de la Terre d'Orléans (ISTO), Université d'Orléans. I would like to thank all those who participated in this work.

Thanks to my thesis supervisors, **Prof. Christophe Tournassat** and **Prof. Zhijun Guo**. They faithfully followed my work and I would like to thank them for their guidance and for trusting me. I appreciate their enthusiasm and daily availability.

Thanks to **Prof. Xiandong Liu** in Nanjing University and **Prof. Dongqi Wang** in Dalian University of Technology. They shared their professional knowledge and skills. Through their help, I have learned the knowledge of different fields.

Thanks to **Prof. Wangsuo Wu, Zongyuan Chen, and Qiang Jin** at Lanzhou University for their passionate guidance and assistance. Thanks to **Prof. Yan Chen** in ISTO for his help and kind attention, as well as for sharing his experience in research and life.

Thanks to my colleagues at ISTO, **Léo Chevrier, Humbrecht Amélie, Li Jia, Xinghua Ni, and Jiashuo Liu**, for their communication and help during the work. Thanks to my colleagues at Lanzhou University, **Junwei Yang, Mengtuan Ge, Zhen Zhang, Daming Zhang, and Haolong Wang** for their discussions and help.

I would like to thank ISTO staff **Marie-France Rouillier and Olivier Gaudefroy**, for helping me in various administrative processes.

I would also like to thank all the reviewers, **Researcher Zhi Qin and Researcher Qiaohui Fan**, for their scientific comments and suggestions, strengthening this work.

Thanks for the financial support from the China Scholarship Council (CSC), Lanzhou University, and Université d'Orléans. Thanks to the Supercomputing Center of Lanzhou University, the CaSciMoDoT – Leto Supercomputing facilities of Region Centre Val de Loire, High-Performance Computing Center (HPCC) of Nanjing University for providing me with valuable computational resources.

Finally, thanks to my family, for their support, love and everything they do for me.

Contents

Résumé étendu de la thèse en Français

L'étude des processus d'adsorption des radionucléides sur les surfaces minérales est fondamentale pour la conception et l'évaluation de la sûreté des futurs systèmes de stockage des déchets radioactif, ainsi que pour les diagnostics environnementaux des milieux pollués par des radionucléides. Parmi ces radionucléides, l'uranium a une abondance relativement élevée dans les systèmes naturels et a un rôle central dans le cycle du combustible nucléaire. L'uranium peut se trouver sous plusieurs états d'oxydation. L'U(VI) est l'état d'oxydation le plus pertinent dans la plupart des eaux de surface et des eaux souterraines oxygénées. L'adsorption de l'U(VI) sur les surfaces de divers minéraux a été largement étudiée par des expériences en batch complémenté par des techniques spectroscopiques. Des sites de complexation possibles et des espèces de surface ont été proposés, mais il est encore difficile d'obtenir des informations précises sur les mécanismes moléculaires responsables des processus d'adsorption. Ces informations sont essentielles pour comprendre les mécanismes physico-chimiques impliqués dans les expériences et pour développer des modèles prédictifs pour les environnements concernés. Les calculs théoriques à l'échelle moléculaire se sont avérés être un outil efficace pour étudier les processus d'adsorption des radionucléides à l'interface minéral-eau. Dans cette thèse, les caractéristiques structurales et les mécanismes d'adsorption des espèces d'U(VI) sur les surfaces des principaux minéraux constitutifs du granite (orthoclase et quartz) et des matériaux tampons/remblais (montmorillonite) des futurs systèmes de stockage en couche géologique profonde ont été obtenus à l'aide de calculs de dynamique moléculaire ab initio. Les mécanismes de polymérisation des espèces d'U(VI) en solution aqueuse et sur les surfaces minérales ont été étudiés. En outre, l'influence de la variabilité des sites d'adsorption des minéraux argileux de type montmorillonite sur les réaction d'adsorption a également été étudié de manière systématique. Les principales conclusions sont résumées ci-dessous:

1. La structure des complexes bidentates et monodontates de sphère interne, la structure du complexe de sphère externe, l'énergie de liaison correspondante et la structure électronique de l'uranyle à la surface de l'orthoclase (feldspath potassique) ont été étudiées en détail. En comparant les résultats avec ceux correspondants pour l'uranyle sur les surfaces de silice, nous fournissons une stratégie pour la construction de sites de surface afin de modéliser l'adsorption de l'U(VI) sur le granite, une roche composée principalement d'orthoclase et de quartz. La structure du complexe bidentate de sphère interne de l'uranyle est la plus stable, et la capacité de liaison diminue progressivement avec

la protonation de la surface. Par ailleurs, la force de liaison du complexe bidentate du site de déprotonation unique est similaire à celle de la structure de complexation monodentate du site de déprotonation. En outre, les liaisons hydrogène, les interactions électrostatiques et les liaisons chimiques jouent un rôle majeur dans l'adsorption de l'uranyle. Sur les sites présentant le même degré de déprotonation, la force de liaison de la surface du quartz est similaire à celle de la surface de l'orthoclase, ce qui suggère qu'il est raisonnable de modéliser à plus grande échelle l'adsorption de l'U(VI) sur le granite à l'aide de sites génériques non différenciés à l'aide de modèles de complexation de surface.

2. Les structures de complexation de trois espèces d'uranyle multinucléaires majeures en solution aqueuse ont été étudiées à la surface de la silice (001). Il a été constaté que $(UO_2)_2(OH)^{3+}$ préférait la structure « side-on », dans laquelle chaque groupe uranyle est lié au site de surface par un mode bidentate. $(UO_2)_2(OH)_2^{2+}$ et $(UO_2)_3(O)(OH)_3^{+}$ préféraient les structures « end-on », dans lesquelles un seul uranyle est coordonné au site de surface via un mode bidentate. L'analyse de la structure électronique a montré que les atomes d'uranyle de la structure « end-on » qui ne sont pas en contact avec la surface sont indirectement impliqués dans la liaison chimique, ce qui augmente la stabilité des complexes de surface. Les études EXAFS et les études de modélisation de la complexation de surface de la littérature ont postulé l'existence de complexes de surface multinucléaires d'U(VI), mais peu de recherches avaient été effectuées sur les structures des ces complexes. Cette partie du travail de thèse contribue à la compréhension des complexes multinucléaires d'uranyle sur les surfaces de silice.

3. En utilisant la dynamique moléculaire des premiers principes, les énergies libres des réactions de dissociation de trois espèces d'uranyle multinucléaires en solution aqueuse et sur des surfaces de silice ont été calculées. En outre, le mécanisme possible de génération de complexes de surface d'uranyle multinucléaire sur la surface de la silice (001) a été clarifié d'un point de vue thermodynamique. Il a été constaté que les espèces d'uranyle multinucléaires se formaient d'abord en solution aqueuse avant de s'adsorber sur les surfaces. Parallèlement, il a été constaté que le précipité des surface issu de l'hydrolyse de l'uranyle est composé de deux types d'unités structurelles formées par la combinaison d'espèces d'uranyle mononucléaires et multinucléaires. Ce travail fournit une base pour comprendre le mécanisme des complexes multinucléaires de l'uranium et le processus de précipitation en surface de l'U(VI).

4. Les varations des propriétés de surface de bord (edge surfaces) des montmorillonites en fonction du pH sont dues aux réactions acido-basiques de leurs groupes fonctionnels de surface. L'acidité des sites de surface (caractérisé par la constante d'équilibre de la réaction acido-basique intrinsèque, pKa) est une propriété chimique influencée par la structure cristalline. Bien que les montmorillonites aient très majoritairement une structure non centrosymétrique *cis*-vacante de leur feuillet octaédrique, les études de modélisation à l'échelle moléculaire des montmorillonites ont souvent fait l'hypothèse d'une structure *trans*-vacante à symétrie centrale, ce qui peut conduire à des prévisions incorrectes des propriétés de surface acido-basiques de la montmorillonite. Nous avons calculé les constantes d'acidité intrinsèque pour les sites sur les surfaces les plus abondantes, c'est-à-dire les surfaces (010), ($0\bar{1}0$), (110) et ($\overline{1}10$), d'une montmorillonite *cis*-vacantes en nous basant sur des calculs de dynamique moléculaire ab initio. Par ailleurs, les surfaces basales des minéraux argileux peuvent être chargées négativement comme dans le cas des montmorillonites. Ces charges sont causées par des substitutions isomorphiques hétérovalentes des ions présents dans la couche octaédrique et dans les couches tétraédriques des feuillets. Dans les minéraux argileux dioctaédriques, les substitutions les plus courantes sont la substitution de Si(IV) par Al(III) dans les feuillets tétraédriques et de Al(III) par Mg(II), Fe(II) ou Fe(III) dans les feuillets octaédriques. L'influence de ces substitutions sur l'acidité des sites de surface de bord nécessite d'être caractérisée pour avoir une compréhension détaillée des propriétés interfaciaux des minéraux argileux au cours des réactions environnementales. Nous avons étudié les constantes d'acidité intrinsèques des sites de surface des bords des montmorillonites cis-vacantes substituées par Mg(II), Fe(II)/Fe(III) et Al(III). Les résultats montrent que la substitution du Fe(II) conduit à une augmentation significative des valeurs pKa des sites locaux, tandis que la substitution du Fe(III) conduit à une diminution. En outre, la substitution du Fe(II) augmente simultanément les valeurs pKa des sites silanols adjacents, tandis que l'effet des substitutions au Fe(III) est faible. Nous avons également constaté que les sites silanol avaient des valeurs pKa élevées et que la substitution Al(III) dans les feuilles tétraédriques entraînait une augmentation significative des valeurs pKa des sites oxygène pontants sur les surfaces (010) et (110). Toutes les valeurs pKa disponibles pour la montmorillonite cis-vacante ont été utilisées pour construire un modèle de complexation de surface et les meilleures données expérimentales de titrage acide-base disponibles dans la littérature ont été reproduites avec succès en l'absence de paramètre totalement ajustable, ce qui constitue la base d'une modélisation quantitative des propriétés

d'adsorption des ions métalliques dans les minéraux argileux naturels.

5. Le mécanisme de complexation et la modélisation de la complexation de surface de l'uranyle sur la surface du bord de la montmorillonite cis-vacante ont été étudiés. Au moyen de la méthode d'intégration thermodynamique, nous avons exploré la structure de complexation de surface et les changements d'énergie libre de dissociation de l'uranyle sur différents sites de la surface du bord. Un modèle de complexation de surface à partir de la microstructure a été construit en combinant ces résultats avec la base de données des constantes d'acidité obtenues précédemment. Nous avons constaté que l'utilisation des paramètres acido-basiques intrinsèques de la montmorillonite cis-vacante permettait une meilleure reproduction de la courbe d'adsorption de l'uranyle à faible pH, tout en soulignant la contribution des espèces d'uranyle multinucléaires à la complexation de surface à pH élevé.

Mots clés : U(VI) ; Orthoclase ; Silice ; Montmorillonite ; FPMD ; Structure des complexes de surface ; Structures électroniques ; Energie libre ; Constante d'acidité ; Modélisation de la complexation de surface.

Chapter 1. Introduction

1.1 Nuclear Energy Development and Radioactive Waste Disposal

1.1.1 Nuclear Energy Development

Fossil fuel energy is a major contributor to greenhouse gas emissions that cause global warming and climate change. Nuclear energy is one option to transforming dependence on fossil fuels into clean, low-carbon, efficient, and sustainable energy. At the end of 2020, statistics from the International Atomic Energy Agency (IAEA) show that there are 442 nuclear power reactors in operation worldwide, with a net installed capacity of 392.6 GW(e) (IAEA, 2009). In addition, a total of 52 nuclear power units are also under construction with a total capacity of 57 GW(e) (Alam et al., 2019).

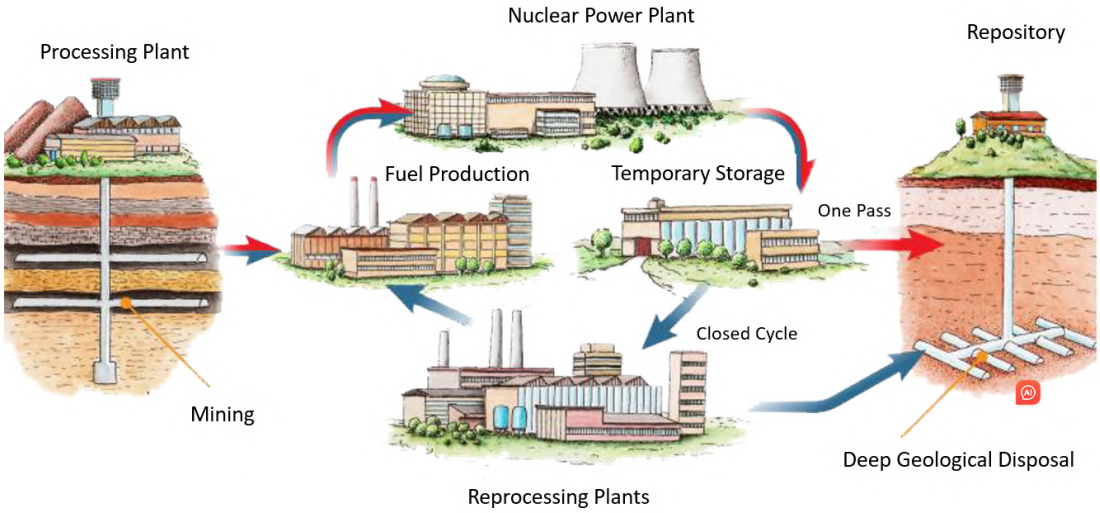

Figure 1.1 Nuclear Fuel Cycle Schematic

Activities involving the use of radionuclides and nuclear energy development, especially steps in the nuclear fuel cycle (Figure 1.1), generate large quantities of radioactive waste. Global spent fuel is increasing at a rate of 12,000 tons of heavy metals per year, and it is estimated that 400,000 tons of heavy metal spent fuel will be produced globally by 2030 (Zhou, 2011). Therefore, the demand for radioactive waste treatment is increasingly prominent and urgent. The simplest and most common form of spent fuel treatment is the one-pass method, that is, the spent fuel is disposed of directly without treatment. This recycling method is simple and direct and has high economic benefits. Another form of treatment is the closed nuclear fuel cycle, i.e., the uranium and plutonium in the

spent fuel are extracted through reprocessing and then reused as new fuel. All the remaining disposal is mainly liquid waste, which contains high-activity. The fission products also contain high concentrations and highly toxic minor actinides, which are called high-level waste liquid. According to the specific activity of radioactive waste, the IAEA divides radioactive waste into very short-lived radioactive waste (VSLW), very low-level radioactive waste (VLLW), low-level radioactive waste (LLW), intermediate-level radioactive waste (ILW) and high-level radioactive waste Waste (HLW). Regardless of whether it is a one-pass or closed-cycle method, the final object of spent fuel disposal is high-level radioactive waste (IAEA, 2009).

1.1.2 Deep geological disposal of high-level radioactive waste

There is a large amount of spent fuel worldwide awaiting final disposal, and repository facilities housing this radioactive waste must be able to ensure long-term isolation to protect the environment and ensure future safety. Deep geological disposal is currently generally considered to be the most feasible disposal option for high-level radioactive waste.

The design concept of deep geological repositories is based on the theory of multiple barrier systems, which usually include natural geological barriers and engineering barrier systems provided by the surrounding rock of the repository (Figure 1.2) (Wang, 2010). Some countries choose highly stable granite as the natural geological barrier of the repository. Granite is a mixed mineral that contains various types of mineral components, the main components of which are quartz and feldspar (Nebelung and Brendler, 2010). The engineering barrier system is composed of buffer backfill material, packaging container and vitrified body from outside to inside. The buffer and backfill material acts as a chemical adsorption barrier for radionuclides, and at the same time has both hydraulic and engineering structure barriers. Clay minerals are considered cushioning backfill materials worldwide due to their high adsorption, low permeability and cushioning properties.

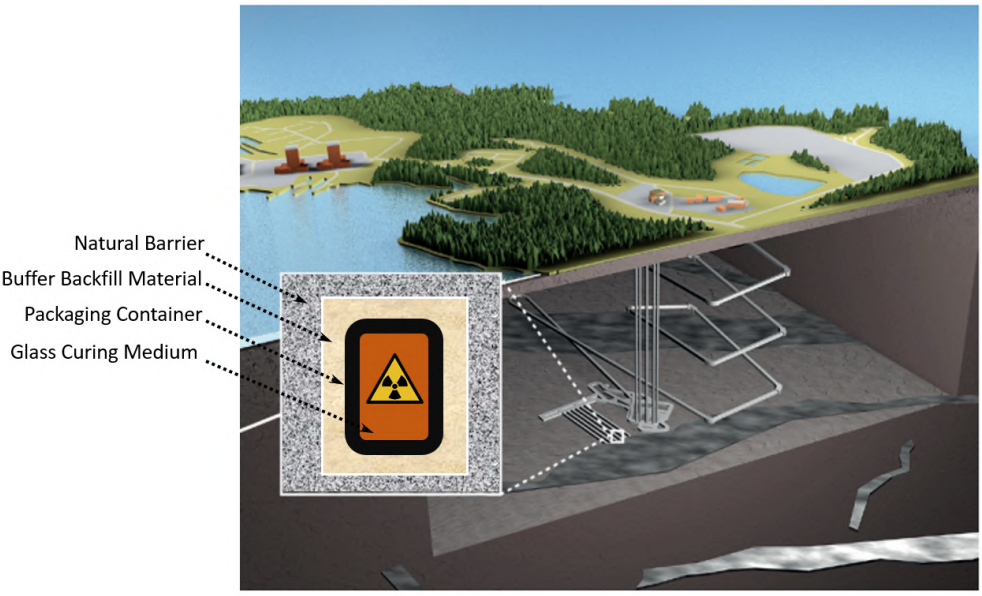

Figure 1.2 Schematic diagram of the multiple barrier system of the high-level radioactive waste geological repository

The performance and safety assessment of deep geological repositories for high-level radioactive waste has strict and special scientific requirements. The purpose of the assessment is mainly to determine the long-term safety-related characteristics, events and processes that affect the performance of the repository system, especially the behavior of radionuclides with long half-lives, high mobility and high radiotoxicity (Campbell and Cranwell, 1988). The main objective of the multiple barrier system is to prevent the radionuclides contained in high-level waste from reaching the human environment for as long as possible in order to reduce the radioactive impact of disposed waste to acceptable levels. Therefore, it is important to study the reactions between radionuclides dissolved or suspended in groundwater and the surrounding rock material in order to estimate the quantities of radionuclides that can migrate in the aqueous phase or be delayed by adsorption on mineral surfaces, as well as the basis for design and safety assessment of geological repositories for high-level radioactive waste.

1.2 Interaction of Radionuclides with Mineral Surfaces

The reaction of radionuclides at the mineral-water solution interface has been extensively studied, and the main purpose of the research is to provide basic data and theoretical foundation for performance evaluation modeling or remediation development of repository projects. In order to better understand the research content of this work, this section will introduce the current research status, the theoretical background of actinide aqueous solution chemistry and mineralogy.

1.2.1 Interactions

The mobility of radionuclides is strongly dependent on the adsorption and desorption processes that take place on mineral surfaces. The initial research on radionuclides in mineral systems was mainly carried out through batch adsorption experiments, so as to obtain the adsorption distribution coefficient K_d (the ratio of the amount of radionuclides adsorbed on the surface of a unit mass of minerals to the amount of radionuclides per unit volume of solution). The focus of these studies has mainly focused on the determination of adsorption boundaries (K_d as a function of pH) and adsorption isotherms (K_d as a function of initial radionuclide concentration), using empirical and semi-empirical equations (Freundlich, Langmuir, etc.) and surface complexation models (SCMs) to fit the relevant experimental data, and then describe the adsorption reaction of radionuclides on the solid-liquid interface (Bradbury and Baeyens, 2005, 2009, 2011). The above equilibrium models reveal the basic laws of radionuclides and mineral surfaces. However, developing appropriate geochemistry models to reliably describe and predict the environmental behavior of radionuclides requires a deep understanding of the adsorption reaction mechanism and the true surface species morphology (Geckeis et al., 2013). But, this cannot be obtained from wet chemical data. Figure 1.3 shows the general steps of developing the surface coordination model. It can be seen that the determination of the surface species reaction of the radionuclide is the last step in completing the SCM, and it is also a key step in model fitting. However, the accuracy of the SCM depends to a certain extent on the model parameters used. If the adsorption reaction mechanism is not clear, the selection of model parameters and surface reactions will be variable, and eventually become a "mechanical" fitting.

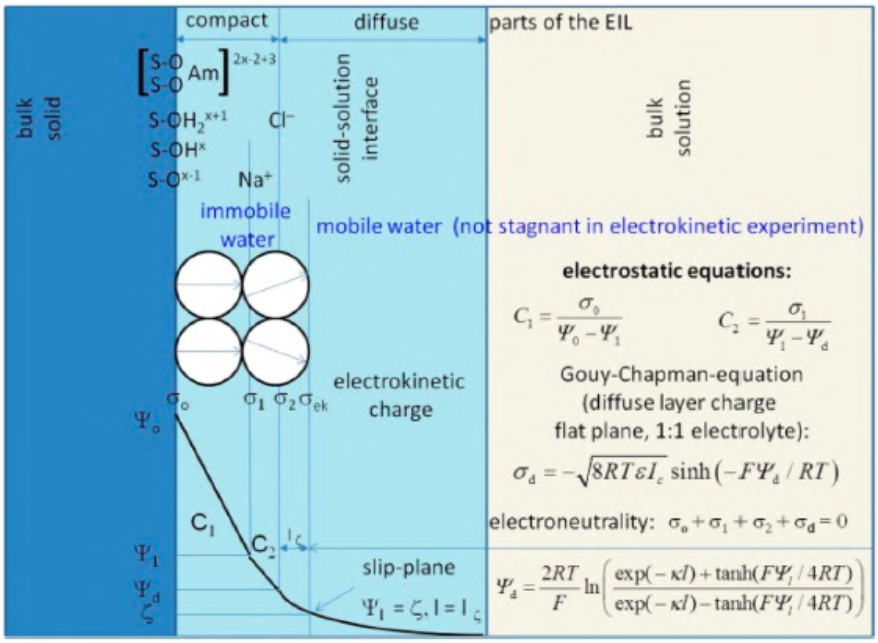

Figure 1.3 Schematic diagram of the mechanism of a surface complexation model (Geckeis et al., 2013)

The behavior of radionuclides on mineral surfaces is complex and diverse, including inner-/outer-sphere complexation adsorption processes, redox processes, nucleation processes, and surface precipitation processes, etc. (Figure 1.4). With the continuous development of spectroscopic techniques, the adsorption reaction mechanism and the surface morphology of radionuclides can be studied in detail, such as EXAFS (Extended X-ray Absorption Fine Structure Spectroscopy), TRLFS (Time-Resolved Laser Fluorescence Spectroscopy), Raman (Raman Spectroscopy) or IR (Infrared Spectroscopy), XPS (X-ray Photoelectron Spectroscopy), etc (Reich et al., 1998; Bargar et al., 2000; Kowal-Fouchard et al., 2004; Bradbury and Baeyens, 2005, 2009, 2011; Froideval et al., 2006; Marques Fernandes et al., 2012; Geckeis et al., 2013). These methods can be used to determine the species morphology and local atomic structure of radionuclides in aqueous/non-aqueous solutions, at mineral-water interfaces, or embedded in solid-phase minerals. For surface species information of radionuclides at the molecular scale, EXAFS is undoubtedly the most versatile spectroscopic technique. By utilizing EXAFS to determine the structural parameters of radionuclides adsorbed on the mineral surface at a molecular level, in conjunction with TRLFS for surface species identification, it becomes feasible to differentiate between the complexation structures of radionuclides within the surface (inner-sphere/outer-sphere), mononuclear and multinuclear surface complexes, as well as the formation of surface precipitates. The spectroscopic results of U(VI) obtained under different pH and

ionic strength on the surface of various minerals show that U(VI) outer-sphere complexation structures are formed at low pH and low ionic strength, while U(VI) inner-sphere complexation structures are formed under other conditions. However, due to the window limitation of spectroscopy experiments, the obtained information is an averaged result of various surface complexes, and the process of surface reactions cannot be studied. For example, for the inner-sphere complexation structures of U(VI) on montmorillonite at medium pH and high ionic strength, EXAFS shows indistinguishable U-Si shells in the second coordination layer, which suggests that EXAFS has considerable uncertainty in interpreting the structure of surface complexes involving second-layer neighbor atoms (Zhang et al., 2018).

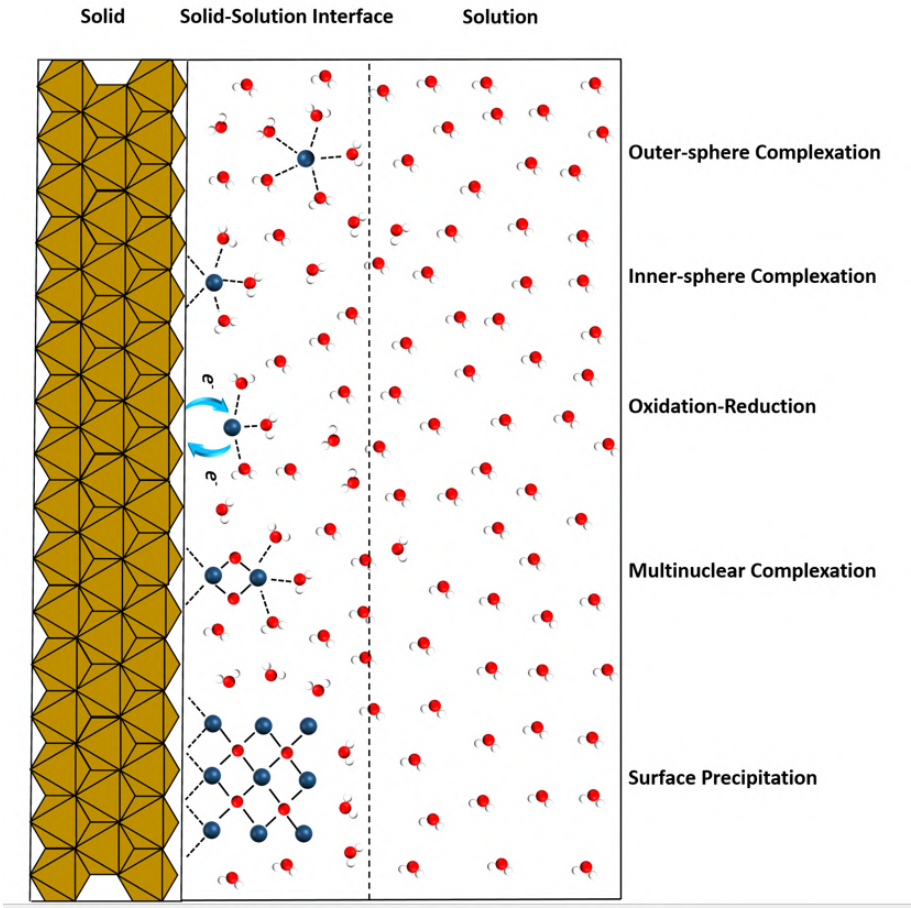

Figure 1.4 Schematic diagram of the chemical process of radionuclides at the mineral-water interface

Theoretical calculations complement the results of spectroscopy, especially in those cases where experimental insight cannot be fully realized. Figure 1.5 shows typical time and space scales for different levels of simulation in theoretical calculations. For simulations of radionuclide adsorption on mineral surfaces, quantum mechanical (QM) and molecular mechanical (MM) scale studies have

achieved remarkable success. Such theoretical calculations can obtain information on the structural and electronic properties and energetic relative stability of the adsorption sites of different surface complexes, which are directly related to the experimental results and allow for a better understanding of the adsorption process of radionuclides on mineral surfaces. In recent years, almost all theoretical calculation models have been applied to the chemical adsorption of uranyl. Kremleva et al. studied the coordination structure of uranyl on the surface of 1:1 and 2:1 type clays through the DFT static calculation and confirmed that the bidentate coordination structure on the surface of uranyl can be stable (Kremleva et al., 2010, 2011, 2013, 2015; Kremleva and Krüger, 2016). Similar results were also obtained on TiO_2, α-FeOOH, $Al(OH)_3$, SiO_2 and other surfaces (Hattori et al., 2009; Pan et al., 2012; Wang et al., 2015, 2017). Wheaton et al. reported optimized geometries of various uranyl silicate complexes to understand how uranyl ions bind to colloids (Wheaton et al., 2003). Molecular dynamics probed the formation of inner- and outer-sphere complexation structures of uranyl on the silica surface and found that this process depends on the protonation state of the surface (Wang et al. 2015). At the same time, the relevant theoretical calculation results can further constrain the parameters in the SCM to construct a more reasonable geochemical model. Zhang et al. explored the adsorption free energy of uranyl at different sites on the edge surfaces of montmorillonite by first-principle molecular dynamics and used the simulation results as the input parameters of the SCM to reproduce the experimental adsorption data (Zhang et al., 2018). Therefore, this thesis adopts the method of theoretical simulation to explore the mechanism of interaction between radionuclides and mineral surface at QM and MM levels.

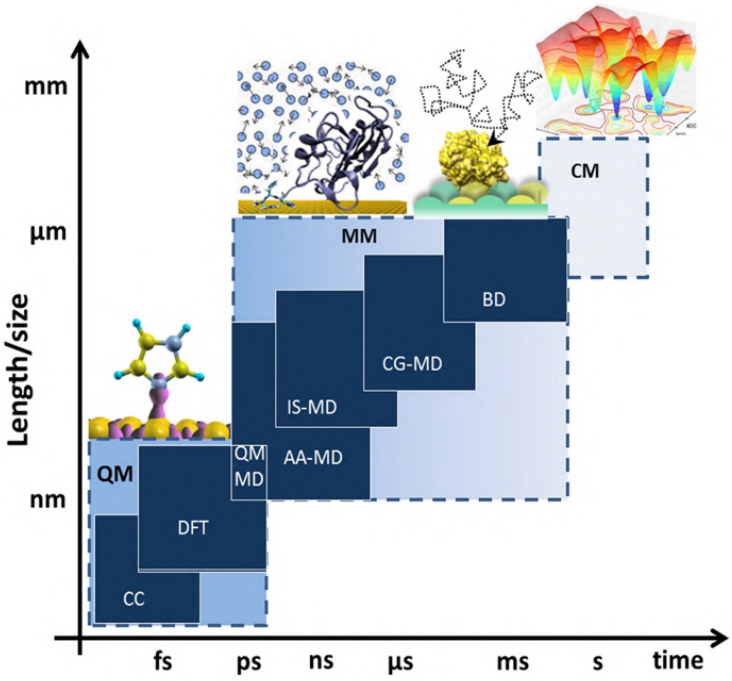

Figure 1.5 Typical time and space scales for different levels of simulation in theoretical calculations (Ozboyaci, M. et al.). : quantum mechanics (QM), including coupled cluster (CC) and DFT methods (inset adapted with permission from (Iori et al. 2008). Copyright (2008) American Chemical Society); molecular mechanics (MM) including all-atom molecular dynamics (AA-MD) simulations, implicit solvent and coarse grained MD (IS-MD and CG-MD), and the Brownian dynamics (BD) technique; and continuum mechanics (CM). The ranges of time and length scales are approximate.

1.2.2 U(VI) Aqueous Chemistry

Uranium is relatively abundant in nature and plays a central role in the nuclear fuel cycle, therefore, uranium is the most important radioactive element. The electronic configuration of uranium is [Rn]5f36d17s2, which can exhibit oxidation states from +3 to +6. Uranyl ($U(VI)O_2^{2+}$) is the main pollutant in groundwater systems due to its stability in oxidizing environments. Uranyl, which is geometrically linear and has rich coordination chemistry with many ligands (H_2O、OH^-、CO_3^{2-} etc.) (Tsushima and Suzuki, 2000). The only transport medium for radionuclides in the underground environment is the aqueous phase, and it is important to understand the relative stability of the compounds and complexes they may form under relevant conditions. Relevant thermodynamic information can be provided by calculations using thermodynamic data and the accuracy of which depends on the thermodynamic parameters. Commonly used databases include NEA (Nuclear Energy Agency) database and PSI database (Grenthe et al., 2014). Figure 1.6 shows the speciation of 1×10^{-4} M U(VI) at room temperature and 0.01M NaCl in the absence of CO_2. It can be found that under

acidic conditions, uranyl is dominant. As the pH value increases, hydrolysis and polymerization reactions will occur, and the polymerized uranyl hydroxyl species will gradually dominate. In the ambient pH range, the main U(VI) species in aqueous solution are: UO_2^{2+}、$(UO_2)_2(OH)^{3+}$、$(UO_2)_2(OH)_2^{2+}$ and $(UO_2)_3(OH)_5^{+}$.

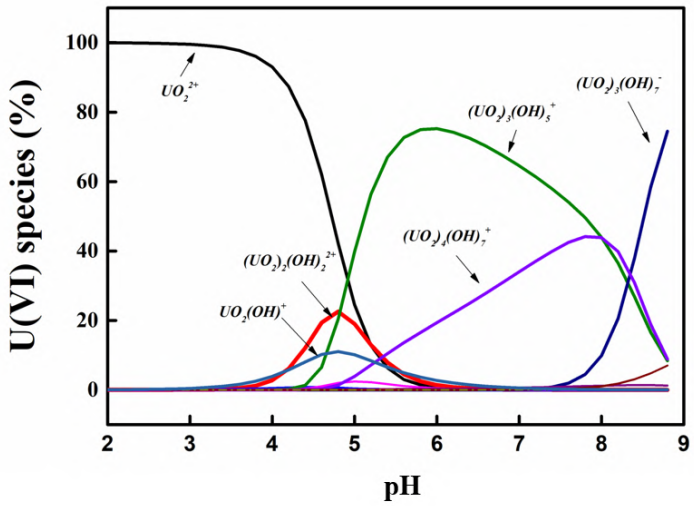

Figure 1.6 Species distribution of 1×10^{-4} M U(VI) at 25°C and 0.01M NaCl in the absence of CO_2

The U(VI) species information and reaction constants in the thermodynamic database are obtained through potential, spectrophotometry, chromatography, solvent extraction and other experimental methods under different pH, temperature and uranyl concentrations (Nguyen-Trung et al., 2000). That is to say, the structure of U(VI) species in the real water environment cannot be obtained through the above-wet chemical experiments. Under these conditions, there are many co-existing polymeric U(VI) hydroxyl species at low concentrations, leaving large uncertainties in the hydrolyzate and associated data. EXAFS can give some structural information of U(VI) hydroxyl complexes, and it found that the compound usually described as $(UO_2)_3(OH)_5^{+}$ is actually $(UO_2)_3(O)(OH)_3^{+}$. Also, similar to the structural studies of surface complexes, EXAFS is limited by limited distal resolution and a general lack of angular information, which can be resolved by combining theoretical calculations with EXAFS. Through theoretical calculations and EXAFS, Tsushima et al. identified $(UO_2)_2(OH)^{3+}$ bridged by single hydroxyl group, $(UO_2)_2(OH)_2^{2+}$ bridged by double hydroxyl group and $(UO_2)_2(OH)^{3+}$ bridged by oxygen center in water phase. The microscopic molecular structure of $(UO_2)_3(O)(OH)_3^{+}$ (Figure 1.7) (Tsushima et al., 2007). However, the formation

process and reaction mechanism of these U(VI) species remain unclear.

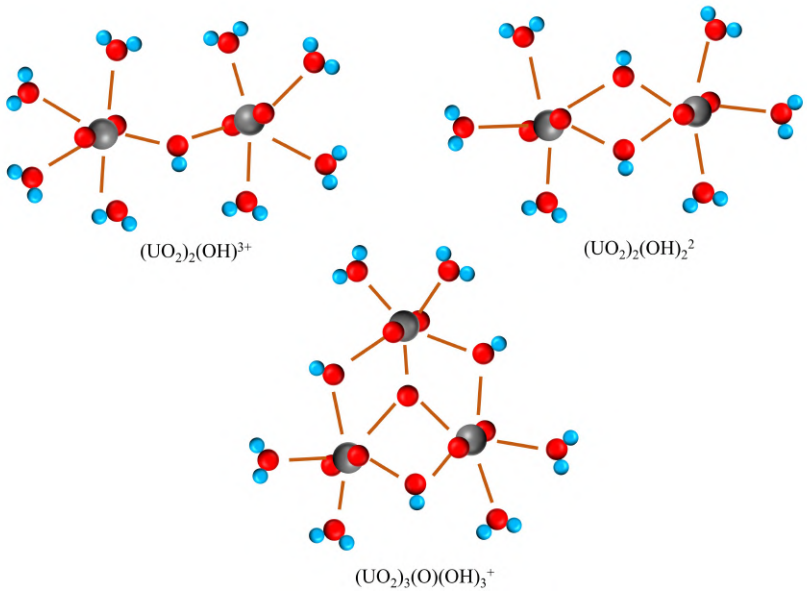

Figure 1.7 Structural diagram of three multinuclear uranyl hydroxyl species in solution

1.2.3 Mineral Structure and Surface Properties

The natural geological barrier of deep geological repository can be granite, which is an igneous rock mainly composed of quartz and feldspar. Quartz and feldspar are also the most widely distributed minerals in nature and play an important role in the interface process in nature (Schlegel et al., 2002). Therefore, quartz and feldspar were also chosen as the minerals of interest in this work. Quartz is a hard crystalline mineral consisting of silicon dioxide (SiO_2). Silica is made up of silicon-oxygen tetrahedra, with each oxygen shared between two tetrahedra. In the natural low-temperature environment, quartz exists in the α phase (α-SiO_2) (Figure 1.8a). Low Miller index α-SiO_2 surfaces, such as (001), (010), and (101), etc., are the main exposed surfaces in nature. These surfaces are prone to hydroxylation and are therefore the main contributors to the interaction with radionuclides. Feldspar amounts to 60 % of continental crust materials and is thus one of the most abundant mineral at Earth's surface. The major feldspar types include orthoclase (also known as potassium feldspar) ($KAlSi_3O_8$), albite ($NaAlSi_3O_8$) and anorthite ($CaAl_2Si_2O_8$). The structure of feldspar is based on silicon-oxygen tetrahedron. In the structure of these minerals, 1/4 or 1/2 of Si is replaced by Al, the distortion of the replacement tetrahedron changes the direction of other tetrahedrons, and the voids of the tetrahedrons are filled by K^+, Na^+ and Ca^{2+} (Figure 1.8b). X-ray reflectance data at the feldspar

interface indicate that (001) and (010) surfaces are the main exposed surfaces (Fenter et al., 2003).

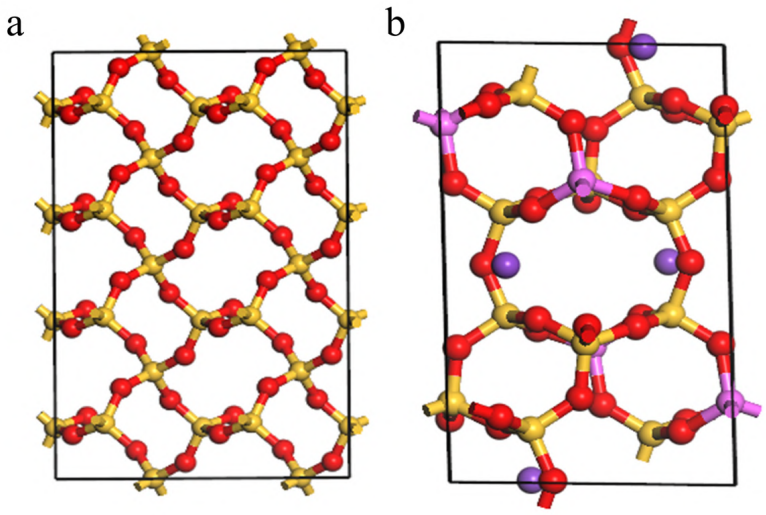

Figure 1.8 Schematic diagram of the crystal structure of (a) quartz and (b) feldspar

Clay materials such as bentonite are the important material foreseen to be used in the buffer and backfill materials in engineering barriers of deep geological repositories and natural barriers in some countries. Clay minerals are layered alumino silicates. Their basic structure is composed of one layer of edge-sharing octahedron (Octahedron) and one or two layers of corner-sharing tetrahedron (Tetrahedron) (Figure 1.9). Therefore, clay minerals can be divided into 1:1 type and 2:1 type. For 2:1 type clay minerals, when the octahedral sheets are replaced by Mg and Fe, it is a swelling clay mineral, such as montmorillonite. If the tetrahedral sheets are replaced by Al, it is a non-swelling clay mineral, such as illite. In the octahedral layer, each octahedral site is surrounded by two OH groups and four O atoms. The octahedral sites can differentiate geometric isomerisms according to the position of the OH groups. When the OH group is in the opposite position of the octahedron, it is a trans octahedron, and when the OH group is in the neighboring position of the octahedron, it is a cis octahedron. The cis and trans octahedral sites are distributed in a 2:1 ratio in the complete octahedral layer (Figure 1.9). Therefore, the clay mineral structure is divided into cis-vacant clays and trans-vacant clay minerals according to the vacancy situation of cis- and trans-octahedrons in the octahedral layer (Tsipursky and Drits, 1984; Brigatti et al., 2011). Montmorillonite is a typical clay mineral with both cis-vacant and trans-vacant structures. Most montmorillonite samples have a cis-vacant structure.

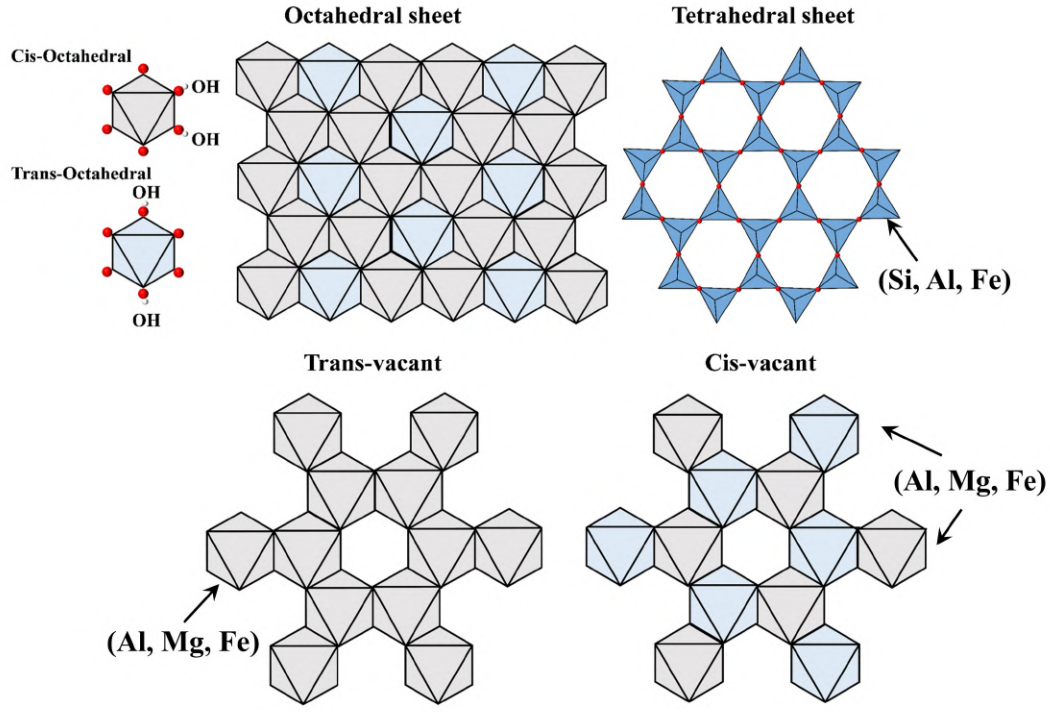

Figure 1.9 Octahedral layer structure (trans-vacant and cis-vacant) and tetrahedral layer structure of clay minerals

Most macroscopic properties of mineral are related to the physical and chemical processes taking place at the mineral surface. The interfacial properties of minerals have a strong dependence on the environmental pH, which is mainly derived from the surface protons generated by the hydroxylation of the mineral surface (Tournassat et al., 2015). The key to understanding the geochemistry of mineral interfaces is surface acid-base reactivity, which is strongly influenced by proton surface chemistry. For simple oxides, such as quartz, the intrinsic acidity constants of surface functional groups have been predicted over the past decades by combining experiments (especially acid-base titrations and electrophoretic mobility measurements), surface complexation models (SCM), and valence-bond theory (Tournassat et al., 2016). For clay minerals, the solid-phase structure often has permanent structural charges due to the isomorphic substitution of cations, and there are two surfaces with completely different properties, the basal surfaces and the edge surfaces, which have brought great difficulties to the study of clay mineral surface properties. The basal surfaces have no surface protons and mainly undergoes ion exchange reactions, while the edge surfaces have complex hydroxyl sites, showing a significant pH effect (Liu et al., 2022). For the study of the acidity constant of the surface protons on the edge surface, in recent decades, the theoretical estimation of the intrinsic pKa value of the edge surface protons is based on the bond valence theory. However, the obtained pKa values

cannot accurately predict experimental titration data and are sensitive to hypothetical models (Tournassat et al. 2016). In recent years, first-principles molecular dynamics (FPMD) combined with vertical gap method simulations have proven to be a powerful tool to accurately calculate the intrinsic pKa values of clay edge surfaces. Liu et al. published a series of works on the intrinsic pKa values of trans-vacant clay structures on (010) and (110) surfaces, which were perfectly applied in SCM (Figure 1.10) (Liu et al., 2013, 2014, 2015, 2016, Tournassat et al. 2016). Therefore, this work adopts this method in the calculation of the acidity constant value of protons on the edge surface of clay minerals.

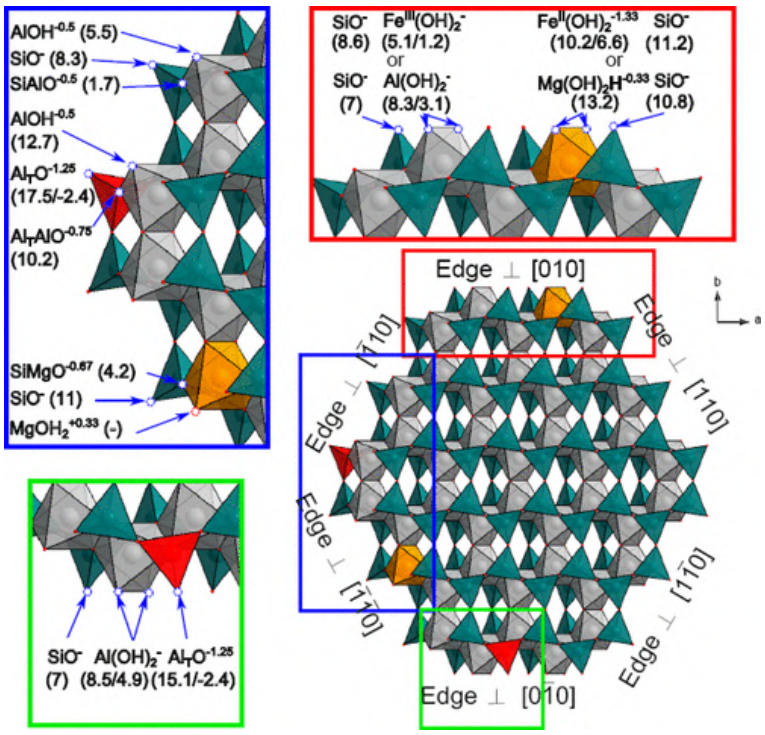

Figure 1.10 Intrinsic pKa values of surface sites at the edge of trans-vacant clay structures

1.3 The Research Significance and Research Contents of the Thesis

1.3.1 Research Significance

Because of the development of nuclear energy, the safe storage of radioactive waste in repositories is an important task to protect humans and the environment from radioactive and chemical toxicity. In order to predict the behavior of potential environmental pollutants (mainly radionuclides) for long-term safety assessment, it is necessary to understand the transport behavior of radionuclides in the environment. This mainly depends on the speciation of the radionuclide in aqueous solution, the interfacial chemistry of the relevant environmental minerals and the retardation caused by the sorption of the radionuclide by the mineral. A lot of research has been done on related

topics, and a deep understanding has been obtained. Batch experiments, surface complexation models, spectroscopy and theoretical calculations have made significant progress in the basic understanding of radionuclide adsorption mechanisms, radionuclide and mineral surface morphology, such as inner-/outer-sphere surface complexes, identification of surface-induced redox reactions and lattice intercalation, etc (Tan et al., 2010).

It is worth noting that (1) because of the late development of theoretical simulation calculations and the fact that surface complexes cannot be regarded as species with an apparently uniform structure, there are only few studies on the molecular level mechanistic information on the interaction of radionuclides with mineral surfaces and on the modeling of the data by applying them to different systems. (2) The structure information of some surface complex species is vague, especially the surface multinuclear polymer species, which have a great influence on the construction of microscopic geochemical adsorption models to describe and predict the environmental behavior of radionuclides. (3) For the limited molecular-level studies of radionuclides in aqueous solutions and on mineral surfaces, the vast majority of work is still focused on static studies, i.e., to obtain final species structure information. However, understanding the physical and chemical process of the reaction has important implications for understanding the characteristics and nature of the environmental behavior of radionuclides. (4) At present, almost all the microscopic theoretical calculations on the edge surface of montmorillonite have been built based on the model structure of pyrophyllite, which has a trans-vacant structure. However, the existing experimental data show that most of the montmorillonites have a cis-vacant structure. Therefore, clarifying the difference between the two structures in terms of physical and chemical properties is of great significance for understanding the physical and chemical behavior of montmorillonite.

1.3.2 Research Contents

In this thesis, the adsorption mechanism of U(VI) on the surface of potassium feldspar, silica, and cis-vacant montmorillonite, uranyl polymerization/precipitation mechanism, and the acidity on the edge surface of cis-vacant montmorillonite were studied by theoretical simulation calculation method. The specific content of the thesis includes the following aspects:

Chapter 1 is the introduction, which introduces the current utilization and development of nuclear energy, the disposal methods of radioactive waste, the research status and progress of the interaction between radionuclides and mineral surfaces, and the research significance and content of

this paper.

Chapter 2 is the theoretical basis and calculation method, which introduces the basic knowledge of the research method used in this thesis. Including wave function method, density functional theory, electronic structure analysis method, first principle molecular dynamics, free energy and acidity constant calculation method, surface complexation model and related software.

Chapter 3 studies the adsorption and complexation mechanism of mononuclear uranyl on the surface of potassium feldspar (001), which is the main component of granite. The U(VI) surface complexation structure was optimized, the electronic structure of the related stable structure was explored, and the main mode of surface interaction was clarified. By comparing with the theoretical calculation results of uranyl on the surface of silica (001), molecular level information is provided for multi-component mineral adsorption modeling.

Chapter 4 investigates the adsorption and complexation mechanism of multinuclear uranyl on the silica (001) surface, characterizes the complexation structures of three representative multinuclear uranyl species on the silica surface, and explores the adsorption process of multinuclear uranyl. The electronic structure and interaction mechanism provide compelling evidence for incorporating multinuclear uranyl species into the surface complexation model, which is in excellent agreement with spectroscopic measurements conducted at relevant high pH levels.

In Chapter 5, based on the research conducted in the previous chapter, we investigated the polymerization reaction mechanism of three types of multinuclear uranyl in aqueous solution and on the silica surface. Additionally, we confirmed the formation reaction process of surface multinuclear uranyl complexation structure. Building upon this foundation, we explored the reaction mechanism of uranyl nucleation and precipitation on the surface and proposed the concept of precipitation through combination of basic structural units.

Chapter 6 explores the acid-base properties of the cis-vacant montmorillonite edge surface, calculates the acidity constants of aluminol and silanol groups on the cis-vacant edge surface, constructs a surface complexation model, and compares the SCM with the titration model of the trans-vacant montmorillonite as well as the real titration experimental data, pointing out the differences in surface reactivity between the cis-vacant montmorillonite and the trans-vacant montmorillonite. Furthermore, the effect of the acidity constant caused by Mg(II), Fe(II)/Fe(III) and Al(III) isomorphic substitution on the edge surface of cis-vacant montmorillonite were also revealed. A fully constrained

acid-base titration model was constructed, and the acid-base titration curves of clay minerals in different regions were predicted.

Chapter 7 studies the coordination mechanism and surface complexation model of uranyl on the edge surface of cis-vacant montmorillonite. Using the method of thermodynamic integration, the surface complexation structures and free energy change of uranyl at different sites on the edge surfaces are explored. Combined with the dataset of the acidity constant, a state-of-the-art surface complexation model based on the atomic information is constructed. These results provide important inspiration and new ideas for future adsorption research.

Chapter 8 is the summary and perspective of this thesis, encompassing the main results and conclusions. Meanwhile, the future research directions are further discussed.

Chapter 2. Theoretical Basis and Calculation Methods

2.1 Introduction

In recent years, theoretical computational chemistry has developed into a very powerful tool, which contributes to a better understanding of physical/chemical systems. The synergies gained from theoretical/experimental studies are enormous, often providing deeper insight into the system. Over the past three decades, the advent of supercomputers and enormous advances in theoretical methods have allowed increasingly complex systems to be simulated at remarkable speed (Geckeis et al., 2013).

For the study of aqueous solution chemistry of actinides, mineral interfacial chemistry, and interactions between actinides and mineral surfaces, traditional wet chemistry experiments and spectroscopy techniques are unable to obtain mechanistic insights at the molecular level. However, molecular-level knowledge is critical for understanding the physicochemical mechanisms in experiments and for developing predictive models of these systems. Theoretical calculations have been successfully applied to study related topics to obtain information at the molecular level. Therefore, this thesis adopts the relevant theoretical calculation methods for research.

Classical simulation is based on a set of force field that describe the empirical parameters of atomic interactions to calculate energy and force (Cygan et al., 2021), Classical molecular dynamics uses the force calculated by the force field to generate dynamic trajectories, and the time scale of the simulation can reach the second level. However, although the calculation speed of this method is fast, and the simulated system can contain tens of thousands of atoms, the simulation results are too dependent on the empirical parameters of the force field, which is not suitable for the calculation of the breaking and formation of chemical bonds, the structure optimization of complexes, and the electronic structure. Therefore, all calculation methods in this thesis adopt the electronic structure calculation method based on the principle of quantum mechanics. This method does not have any empirical parameters, and can explain the mechanism of the research system from the molecular/atomic/electronic level. Next, I will introduce the theories, principles, methods and software used in the calculations in this thesis.

2.2 Schrödinger Equation

Classical mechanics only applies to macroscopic particles. For microscopic particles, we need a new form of mechanics called quantum mechanics. Heisenberg uncertainty principle states that we cannot simultaneously determine the precise position and velocity of microscopic particles, and

therefore cannot gain the knowledge that classical mechanics requires to predict the future motion of a system. Therefore, the way to study quantum mechanics is to assume fundamental principles. In order to describe the state of the system, we assume that there is a function Ψ that can describe the state of the particle, this function is called the wave function. At the same time, the state of the system also changes with time, which shows that Ψ is a function of coordinates and time Ψ (**r**, t). To describe the motion of microscopic particles from a quantum mechanical system, we need an equation for the wave function as a function of time. For a microscopic particle of mass m moving in the V (**r**,t) potential field, this equation is defined as:

$$\left[-\frac{\hbar^2}{2m}\nabla^2+V(\mathbf{r},t)\right]\Psi(\mathbf{r},t)=i\hbar\frac{\partial\Psi(\mathbf{r},t)}{\partial t}$$

This equation is called the time-dependent Schrödinger equation, where **r** is the coordinate of the electron, ħ is the reduced Planck constant, and i is a complex number. Many applications of quantum mechanics to physical chemistry do not use this equation, and the simpler time-independent Schrödinger equation is used. Among them, the potential function V will no longer be a function of time, but only related to the electron coordinates, and the time-dependent Schrödinger equation will be transformed into a stationary Schrödinger equation:

$$\left[-\frac{\hbar^2}{2m}\nabla^2+V(\boldsymbol{r})\right]\Psi(\boldsymbol{r})=E\Psi(\boldsymbol{r})$$

or

$$\hat{H}\Psi(\boldsymbol{r})=E\Psi(\boldsymbol{r})$$

where $\hat{H}$ is the Hamiltonian, and E represents the energy of the system. When the system is a multi-particle system, the stationary Schrödinger equation is:

$$\hat{H}\Psi(\boldsymbol{r},\boldsymbol{R})=E\Psi(\boldsymbol{r},\boldsymbol{R})$$

The stationary wave function Ψ(**r, R**) contains both the coordinates of the nucleus and the coordinates of the electrons. This also means that the Hamiltonian of the system is huge, and it becomes very difficult to solve the Schrödinger equation. Fortunately, we can solve on an approximate basis. Since the mass of the nucleus is much larger than that of the electron, the movement of the electron is much faster than that of the nucleus. As far as electrons are concerned, it can be approximated that the nucleus is fixed. We call this approximation the Born-Oppenheimer Approximation. Therefore, during the solution process, the movement of electrons has nothing to do

with the movement of atomic nuclei, and the variables of the stationary wave function Ψ(**r, R**) can be separated. Therefore, the stationary Schrödinger equation for many-particle systems becomes the stationary Schrödinger equation for electrons:

$$\hat{\mathrm{H}}_{el}\Psi_{el}(\boldsymbol{r}) = E_{el}\Psi_{el}(\boldsymbol{r})$$

This approximation greatly simplifies the difficulty of solving. Under different nuclear coordinates, there is a set of electronic eigenequations. The solution of the many-electron stationary Schrödinger equation requires the one-electron approximation to transform the many-electron problem into a one-electron problem. The single-electron approximation, also known as the Hatree-Fock approximation, regards each electron as moving under the nuclear coulomb field and the average potential field of other electrons. Therefore, the multi-electron coupled wave function can be written in the form of the product of single-electron wave functions:

$$\Psi_{el}(r_1, r_2, r_3 \ldots r_N) = \varphi_1(r_1)\varphi_2(r_2) \ldots \varphi_N(r_N)$$

However, this form does not conform to the exchange-antisymmetric nature of the wave function, and the wave function of the system needs to be expanded into the form of the slater determinant:

$$\psi(r_1, r_2, r_3 \ldots r_N) = \frac{1}{\sqrt{N!}}\begin{pmatrix} \varphi_1(x_1) & \varphi_2(x_1) & \cdots & \varphi_N(x_1) \\ \varphi_1(x_2) & \varphi_2(x_2) & \cdots & \varphi_N(x_2) \\ \vdots & \vdots & \ddots & \vdots \\ \varphi_1(x_N) & \varphi_2(x_N) & \cdots & \varphi_N(x_N) \end{pmatrix}$$

The stationary Schrödinger equation of the electron is further transformed into the form of the Fock operator, that is, the Hartree-Fock equation:

$$\hat{F}_i\varphi_a(\boldsymbol{r}_i) = \varepsilon_a\varphi_a(\boldsymbol{r}_i)$$

In the actual solution process of the Hartree-Fock equation, it is solved by the variational method in matrix form, that is, the Hartree-Fock-Roothaan (HFR) equation:

$$\mathbf{FC} = \boldsymbol{\varepsilon}\mathbf{SC}$$

Among them, **F** is the Fock matrix, **S** is the overlapping matrix, **C** is the coefficient matrix, and **ε** is the energy matrix. Afterward, the wave function can be further solved by self-consistent field iteration (SCF).

2.3 Density Functional Theory

2.3.1 The Hohenberg-Kohn Theorems

From the Hartree-Fock equation, it can be seen that the energy of any quantum state is a function of the entire wave function Ψ(**r_1, r_2 … r_N**), which contains 3N variables. The first Hohenberg-Kohn

theorem points out that the energy of the ground state of the system depends only on the electron density $\rho(\mathbf{r})$, which is only a function of three variables. Therefore, the 3N-dimensional solution problem becomes a 3-dimensional solution problem, which also explains why this theory is also called Density Functional Theory (DFT), namely:

$$\rho(\mathbf{r}) = 2\sum_i \psi_i^*(\mathbf{r})\psi_i(\mathbf{r})$$

$$E_0 = E_0[\rho_0(\boldsymbol{r})]$$

The ground state electron density $\rho_0(\mathbf{r})$ is in principle sufficient to obtain all properties of interest. However, how we determine that a certain electron density is the ground state density is a problem. The second Hohenberg-Kohn theorem gives the solution. Simply put, this theorem shows that for any electron density $\tilde{\rho}(\mathbf{r})$, under the exact energy functional, the energy must be higher than the corresponding real ground state energy E_{real} of the real ground state electron density $\rho_{real}(\mathbf{r})$. The second Hohenberg-Kohn theorem is also called the variational theorem, that is, if the exact energy functional is known, and the system is minimized by continuously adjusting $\tilde{\rho}(\mathbf{r})$, the system will finally obtain accurate ground state energy, electron density and wave function, etc., which can be expressed as:

$$\langle\widetilde{\Psi}|\widehat{\mathrm{H}}|\widetilde{\Psi}\rangle = \mathrm{T}[\tilde{\rho}] + \mathrm{V_{ee}}[\tilde{\rho}] + \int \tilde{\rho}(\vec{\mathrm{r}})\mathrm{V_{ext}}\mathrm{d}\vec{\mathrm{r}} = \mathrm{E}[\tilde{\rho}] \geq \mathrm{E}_0[\rho_0] = \langle\Psi_0|\widehat{\mathrm{H}}|\Psi_0\rangle$$

2.3.2 Kohn-Sham Equation

The complete electron density-based energy function can be written as:

$$\mathrm{E}[\rho(\mathbf{r})] = \mathrm{T}[\rho(\mathbf{r})] + \mathrm{V_{ee}}[\rho(\mathbf{r})] + \int \mathrm{V_{ext}}(\mathbf{r})\rho(\mathbf{r})\mathrm{dr} + \mathrm{V_{nn}}[\rho(\mathbf{r})] + \mathrm{E_{XC}}[\rho(\mathbf{r})]$$

The first item on the right side of the above formula is the electron kinetic energy item, the second item is the coulomb interaction item between the electrons, the third item is the attraction item between the electron and the nucleus, the fourth item is the nuclear-nuclear interaction item, and the fifth item is the electron exchange associated items. The electron exchange correlation term refers to the exchange interaction between spin-parallel electrons and the correlation between spin-antiparallel electrons. The energy functional $\mathrm{E}[\rho(\mathbf{r})]$ is subjected to variational processing on the single-electron wave function $\varphi(\mathbf{r})$ to obtain the Kohn-Sham equation:

$$\left[-\frac{\hbar^2}{2m}\nabla^2 + V(\boldsymbol{r}) + V_H(\boldsymbol{r}) + V_{XC}(\boldsymbol{r})\right]\varphi(\boldsymbol{r}) = \varepsilon\varphi(\boldsymbol{r})$$

Among them, the first three terms are the single-electron kinetic energy term, the external

potential term and the hartree term, which can be solved exactly. While the last exchange-correlation term can only be approximated by the approximate exchange-correlation functional to approximate the exact solution.

The Local Density Approximation (LDA) sets the exchange-correlation potential at each location to that of the homogeneous electron gas observed at that location. This approximation only uses the local electron density to define an approximate exchange-correlation function, which underestimates the exchange energy and overestimates the correlation energy. As a result, it usually overestimates the binding energy, underestimates the bond length and lattice constant, and underestimates the reaction barrier. Generalized Gradient Approximation (GGA) increases the gradient information of electron density on the basis of local density approximation, which can further describe the chemical reaction process while taking into account the calculation speed and calculation accuracy, so it becomes the most common functional in the first principle calculation. There are many types of GGA functionals that have been developed, for example, PBE, BLYP, and PW91 functionals. Among them, the most commonly used function in the condensed phase system is the PBE functional proposed by Perdew, Burke and Ernzerhof, and all calculations in this thesis use the PBE functional (Perdew et al., 1997).

2.3.3 Basis Sets and Pseudopotentials

When solving the Hartree Fock equation, the specific form of the Fock orbit $\varphi(\boldsymbol{r})$ is not known, and it needs to be written in the form of linear combination of atomic orbitals (LCAO), namely:

$$\varphi(\mathbf{r}) = \sum c_i \chi_i(\mathbf{r})$$

Where {χi} represents a set of basis functions, called the Basis Set. The Gaussian function is most commonly used in quantitative calculations, while the plane wave basis set is used for solid and surface systems that extend infinitely in space. The latest mixed Gaussian and Plane Wave basis group also has good applications (Lippert et al., 1997).

When atoms come together to form a solid, the core electrons (usually those in the inner shell) stick tightly to the nucleus in the deep potential well, and in most cases remain unchanged, that is, the core electrons remain stable state, rarely participates in any physicochemical properties of the system. On the contrary, the valence electrons are far away from the nucleus, the energy is much higher than the potential well, relatively independent and highly active, and can participate in bonding, ionization, conduction in metals, and formation of energy bands and other activities. From a

computational point of view, we can remove the nucleus and core electrons and only deal with active valence electrons, which is called the frozen core approximation (Frozen-core Approximation). At the same time, when the wave function of valence layer electrons passes through the highly localized core region, its oscillation becomes very severe. This multi-node wave function greatly increases the amount of calculation, especially for heavy elements, the amount of calculation is unbearable of. If the wave function in the core region is adjusted to a properly featureless curve, it will make the calculation very suitable, and this process is called pseudofake. The potential jointly produced by the core electrons replacing the nucleus and the nucleus is called a pseudopotential. For solid-phase systems, commonly used pseudopotentials are Projector Augmented Wave and GTH pseudopotentials (Blöchl, 1994; Goedecker et al., 1996; Kresse and Joubert, 1999).

2.3.4 Periodic Boundary Condition

1 mole of solid phase requires approximately 10^{23} atoms, which is impossible to include in any simulation framework. The so-called periodic boundary conditions are about to set infinite mirror images in the box that simulates finite atoms. This means that the electrons in the bulk move in a periodic equivalent potential field, and the potential acting on the electrons is periodic and invariant under translation with respect to the lattice vector **R**:

$$U(\boldsymbol{r}) = U(\boldsymbol{r} + \boldsymbol{R})$$

Bloch's theorem states that when the wave function of solid-phase electrons remains in the form of a plane wave, a new phase factor can be used to redefine the electron wave function:

$$\psi(\boldsymbol{r} + \boldsymbol{R}) = e^{i\boldsymbol{k}\cdot\boldsymbol{R}}\psi(\boldsymbol{r})$$

$\boldsymbol{k}$ is a reduced wave vector in reciprocal space, which means that when the lattice vector is translated, the wave function only increases by a phase factor $e^{i\boldsymbol{k}\cdot\boldsymbol{R}}$. Any periodic function can be expanded by Fourier series and transformed into e-exponent form through Euler's formula, so that our calculation can be performed in the reciprocal space, namely:

$$n(x) = \sum n_p \exp\,(i2\pi px/a)$$

The basis vector relationship between reciprocal space and real space is:

$$\boldsymbol{a}_i \cdot \boldsymbol{b}_j = 2\pi\delta_{ij}$$

Therefore, each solid-phase lattice has two crystal structures of reciprocal space lattice and real space lattice. Among them, the Wigner-Seitz cell of the reciprocal space is called the Brillouin zone. The first Brillouin zone is the original unit cell of the reciprocal lattice, which contains all the

properties of the system. Any point in the first Brillouin zone represents a simple wave vector $\boldsymbol{k}$, so there are infinite discrete $\boldsymbol{k}$ that can quantify the wave function well. The wave function is smooth, so the KS equation of a limited number of k points can be solved independently, and then the weighted average can be performed to obtain the electron energy and other properties. The denser the selected k-points, the more accurate the result.

2.4 Electronic Structure Analysis Methods

When the solution of the Schrödinger equation is completed, in addition to the energy, we also obtain the wave function of the system. The wave function reflects all the properties of the electrons in the system. Therefore, the analysis of the wave function can give us an in-depth understanding of the physical and chemical properties of the system from the electronic level. There are many kinds of electronic structure analysis methods. Next, I will briefly introduce the methods used in this thesis.

2.4.1 Electronic Density of States

The energy levels of molecular systems are separated. For the solid phase, it can be regarded as a huge molecular structure, so the number of its energy levels is huge. For a discrete molecule, we can select HOMO/LUMO orbitals and valence orbitals to analyze the reactivity of the system, but it is impossible to select one or more orbitals for analysis in the large number of discrete crystal orbitals in the solid phase. However, we can define all energy levels in the energy interval to analyze the energy level changes of the system. Therefore, the number of electronic states per unit energy is called the density of states (DOS):

$$D(E) = \frac{1}{N_k} \sum_{i,\mathbf{k}} \delta\left(\varepsilon_{i,\mathbf{k}} - E\right)$$

If the density of state is decomposed into each atom and the spdf orbital of the atom, we call it the local density of state (LDOS); if the density of state is further decomposed into orbitals such as px, py and pz, we call it is the projected density of states (PDOS). The application of density of states in first-principle calculations is more important, especially for the analysis of the energy level change relationship of the interaction between molecules and surfaces. For example, the number of electrons can be obtained by integrating the density of states; the more energy levels per unit energy, the higher the density of state peak and the smaller the broadening, so as to judge the strength of the interaction between orbitals; the shift of the density of state peak position can also affect interactions between systems (Camellone and Fabris, 2009; Lu et al., 2018; Tsuji and Yoshizawa, 2018).

2.4.2 Bader Charge

Bader charges are also known as QTAIM (Quantum Theory Atom in Molecule) charges (Tang et al., 2009; Bader and Matta, 2013). In this method, the zero-flux surface of electron density (the two-dimensional surface with the smallest charge density perpendicular to the surface) is used as the interface to divide the atomic space. Thus, the total electronic charge belonging to a particular atom can be defined by integrating the charge density over the entire atomic space, after which the atomic charge of this atom is equal to the difference between the nuclear charge and the total electronic charge. The atomic charge is obviously affected by the division method, so for the atomic charge, the horizontal comparison is particularly important. The Bader charge of the atom can reflect the electrostatic interaction in the system. The larger the Bader charge, the stronger the electrostatic interaction. At the same time, multipole moments of atomic or molecular interactions can also be determined.

2.4.3 Charge Density Difference

When a system undergoes a physicochemical reaction, the difference in charge density can describe the electronic rearrangement between two fragments. Charge Density Difference is defined as the charge density of the system minus the density of the individual fragments that make it up:

$$\Delta\rho = \rho_{AB} - \rho_A - \rho_B$$

Through the charge density difference, we can intuitively see the direction of electron transfer during the reaction. We clearly obtained the properties such as the bonding polarization direction in the process of electronic coupling, and explored the nature of chemical bonds (Tozini et al., 2015).

2.4.4 Electron Localization Function

The Electron Localization Function (ELF) is a three-dimensional real-space function that represents the degree of localization of electrons at different spatial positions (Becke and Edgecombe, 1990; Silvi and Savin, 1994). It is defined as:

$$\mathrm{ELF}(\mathbf{r}) = \frac{1}{1 + [\mathrm{D}(\mathbf{r}) / D_0(\mathbf{r})]^2}$$

Among them, D(r) represents the excess kinetic energy density due to Pauli mutual repulsion, also called Pauli kinetic energy density. ELF reflects the degree of localization of electrons in space, and its value range is [0,1]. The larger the value, the higher the degree of localization of electrons. 0 means that the electrons are in a uniform electron gas at this time, and 1 means that the electrons are

completely localized. Generally, if ELF>0.5, it means that the electrons are in the region where covalent bonds, lone pair electrons, inner shell electrons, multi-center bonds, etc. And when ELF<0.5, at this time we think that the electrons are in the region of higher ionic bond composition.

2.5 First Principles Molecular Dynamics

Atoms of matter in the real environment are always moving all the time, and understanding how atoms in matter move with time is a prerequisite for describing some properties with practical significance. For example, the coordination reaction process and interface reaction process in a real solution. Molecular Dynamics (MD) is a tool for tracking the trajectory of atoms. The simulated trajectory obtained through statistical analysis can often obtain information that cannot be obtained in static calculations. First Principle Molecular Dynamics (FPMD) means that in the process of computational simulation, the force on atoms comes from DFT to solve the Schrödinger equation, while the force on atoms in classical simulation comes from force fields or empirical potentials. All FPMD simulations in the thesis adopt the Born–Oppenheimer Molecular Dynamics (BOMD) method. BOMD refers to directly solving the static electronic structure at each step when a set of fixed atomic nucleus positions is given in the molecular dynamics simulation. Thus, the electronic structure part is reduced to solving a time-independent quantum problem while the nucleus evolves via classical mechanics.

The movement of atomic nuclei in all FPMD simulations in this thesis adopts the Verlet algorithm based on Newton's equation of motion in classical mechanics. The position and velocity at time t+δt can be written as:

$$R(t+\delta t) = R(t) + \delta \mathrm{t} \mathrm{V}(t) + \frac{\delta \mathrm{t}^2}{2m} \mathrm{F}(\mathrm{t})$$

$$V(t+\delta \mathrm{t}) = V(t) + \frac{\delta \mathrm{t}}{2m} [\mathrm{F}(\mathrm{t}) + \mathrm{F}(\mathrm{t}+\delta \mathrm{t})]$$

where F is the atomic force and m is the atomic mass. At this moment, the property A at any time in the system is a function of the momentum and coordinates of the particles in the system. The molecular dynamics simulation is carried out in a large number of independent systems (ensembles) with the same macroscopic properties but different microscopic states, and the property A takes an ensemble average:

$$\langle A \rangle = \iint d\mathbf{p}^N d\mathbf{r}^N \mathrm{A}(\mathbf{p}^N, \mathbf{r}^N) \rho(\mathbf{p}^N, \mathbf{r}^N)$$

Common ensembles include canonical ensemble (NVT), microcanonical ensemble (NVE),

isothermal and isobaric ensemble (NPT), giant canonical ensemble (μVE). Due to the limited number of atoms simulated by FPMD, it will lead to very severe pressure fluctuations. Therefore, the NVT ensemble is used in this theis, that is, the number of particles N, volume V and temperature T are kept constant during the simulation process. The temperature control of the NVT ensemble mainly uses a thermal. There are many types of thermals, such as Berendsen thermostat, Anderson thermal, and Nosé-Hoover thermal. Among them, the Nosé-Hoover thermal regards the thermal as a part of the system, and interacts with the system through coupling parameters, so that the particles of the system satisfy the Maxwell-Boltzmann distribution and evolve together with the system (Martyna et al., 1992). Therefore, this thesis uses Nosé-Hoover thermal as a means of temperature control.

When analyzing the local coordination structure between atoms in the system through simulated trajectories, the results of Radial Distribution Function (RDF) can be compared with the structure predicted by spectroscopy, so as to serve as a standard for testing a specific structure. RDF is defined as the ratio between the particle number density at a distance r from any reference atom and the average particle number density ρ:

$$g(r) = \frac{n(r)}{\rho 4\pi r^2 \Delta r}$$

It can be seen from the formula that when r tends to infinity, g(r) = 1. Any g(r) peaks reflect interparticle correlations due to interactions, which, when integrated over the peak areas, yield a coordination number for the reference atom (Kirkwood and Boggs, 1942).

2.6 Free Energy Calculation Method

To fully understand most chemical processes, it is often necessary to examine their underlying free energy behavior. Perturbation theory (PT) and thermodynamic integration (TI) have become standard methods for evaluating free energy differences (Kirkwood, 1935; Zwanzig, 1954). The main core idea of both methods is to accurately determine the configurations of the target system and the reference system, and then sufficiently sample the relevant low-energy states of the two systems to obtain the free energy difference. In comparison, the TI method is more rigorous in principle, and its calculation results are more accurate. Therefore, all the methods in this paper to explore the change of reaction free energy use the TI method.

FPMD obtains the potential energy surface of the internal energy of the system. The potential energy surface is converted into a Boltzmann distribution through the Boltzmann distribution law, and then transformed into a free energy potential energy surface through a partition function. For the

canonical ensemble, its characteristic function is Helmholtz free energy, so the free energy discussed in this thesis is Helmholtz free energy (A). The basic principle of TI is easy to understand. For a reaction process, the free energy change can be written as the following integral:

$$A(\xi_1) - A(\xi_0) = \int_{\xi_0}^{\xi_1} \mathrm{d}A/\mathrm{d}\xi \mathrm{d}\xi$$

where ξ represents the degree of freedom of the reaction process, which can also be called the reaction coordinate. ξ_0 and ξ_1 correspond to the coordinates of the initial and final states of the reaction, respectively. In this thesis, the sampling simulation of the control reaction coordinates is realized by constrained first-principles molecular dynamics, where dA/dξ represents the constraint mean force potential (Constraint Potential of Mean Force). The selection of reaction coordinates is diverse, and is different in different reaction paths, such as interatomic distance, angle, dihedral angle, coordination number, etc., of course, can also be customized. The reaction coordinates used in this paper are mainly interatomic distance and coordination number (Coordination Number, CN) (Sprik, 1998; Sprik and Ciccotti, 1998). The definition of the coordination number is as follows:

$$\mathrm{CN} = \sum_i \frac{1 - (r_i/r_c)^{12}}{1 - (r_i/r_c)^{24}}$$

where r_i is the distance of related atoms; r_c is the cutoff value.

2.7 Calculation Method of Acidity Constant

The microscopic mechanism of proton dissociation applies only to self-ionization in aqueous solution, and determining the reaction pathway for proton dissociation from weak acids and subsequent diffusion in solution is an important challenge because of the long time involved in the reaction and, more importantly, Protons have complex solvent recombination and protons in aqueous solution are indistinguishable in theoretical simulations. Here, we investigated the pKa values of acidic functional groups of our interest (e.g., protons on mineral surfaces and protons in aqueous solution complexes) by the FPMD-based vertical energy gap method (Cheng et al., 2009, 2014; Costanzo et al., 2011).

In this method, the half-reaction scheme was applied. The proton of an acid (denoted as AH) is gradually transformed into a ghost atom that can be considered a classical particle without any charge. The free energy of the transformation is computed as

$$\Delta A = \int_0^1 \langle \Delta E \rangle_\eta \, d\eta$$

Here the ΔE is the vertical energy gap which is defined as the difference between the potential energies of the reactant and the product states. The subscript η is a coupling parameter that increases from 0 (the protonated state) to 1 (the deprotonated state). The mean value of ΔE is derived with the restrained mapping Hamiltonian:

$$H_\eta = (1-\eta)H_R + \eta H_P + V_r$$

H_R and H_P refer to the reactant and product states, respectively. The restrained harmonic potential V_r is used to ensure that the ghost atom stays at the same position as that in the simulation of the reactant state. The restraining potential is of the form familiar from classical force field models:

$$V_r = \sum_{i=1}^{n_d} \frac{1}{2} k_d (d-d_0)^2 + \sum_{i=1}^{n_\alpha} \frac{1}{2} k_\alpha (\alpha-\alpha_0)^2$$

The leading term is a sum of harmonic potentials of bond distance and bond angles with the respective equilibrium values of d_0 and α_0, which were derived from the prior simulations of their reactant states without constraint.

In actual calculations, the ΔA is estimated by the three-point Simpson's rule which requires running the simulations of η = 0.0, 0.5, and 1.0, respectively. Then the deprotonation-free energy can be expressed as:

$$\Delta A = \frac{1}{6}\left(\langle \Delta E \rangle_0 + \langle \Delta E \rangle_1\right) + \frac{2}{3}\langle \Delta E \rangle_{0.5}$$

With the same method, one proton of an H_3O^+ in the solution area of the same system gradually switched off to become a dummy, the free energy of which is denoted as $\int_0^1 d\eta \langle \Delta E_{H_3O^+} \rangle_\eta$.

Combining the results for the two steps provides the result for the pK_a:

$$2.30 k_B T \mathrm{p}K_a = \int_0^1 d\eta \langle \Delta E \rangle_\eta - \int_0^1 d\eta \langle \Delta E_{H_3O^+} \rangle_\eta + k_B T \ln\left[c^0 \Lambda_{H^+}^3\right]$$

Here, c^0 is the unit molar concentration whose value is 1.0 mol/L. Λ_{H^+} is the thermal wavelength of the proton. The third term $k_B T \ln\left[c^0 \Lambda_{H^+}^3\right]$ represents the translational entropy caused by proton dissociation, approximated by the chemical potential of a free proton at the standard concentration (-0.19 eV or 3.2 pK_a units).

2.8 Surface Complexation Models

Surface Complexation Models (SCMs) use the concepts of mass balance, surface charge balance, and thermodynamic chemical equilibrium to quantitatively predict the partitioning of chemical species between aqueous solutions and mineral surfaces (Wen et al., 1998; Zhang et al., 2017). At the same time, SCMs can be coupled with large-scale fluid transport models to build reliable predictions in environmental science. In recent decades, model parameters have been obtained by fitting macroscopic adsorption experimental data, and spectroscopy has further constrained the observed main reaction mechanisms. The construction of the SCMs needs to follow the principle of simplicity, that is, to build the model with the fewest adjustable parameters to avoid the correlation between fitting parameters. The goal of the modeling work proposed in this thesis is to construct a model with as few empirical parameters as possible compared to the traditional fitting data model. The progress of molecular level simulation provides a new possibility to reduce the number of empirical fitting parameters in the surface coordination model.

The SCMs constructed in this thesis are all based on the edge surface of 2:1 clay minerals. When constructing the model on the edge surface, the surface potential Ψ_{edge} needs to explicitly consider the spillover effect of the basal surface potential to the edge surface potential. Bourg et al. solved the PBE 2D form of Ψ_{edge} for an isolated montmorillonite layer edge surface (Bourg et al., 2007):

$$\frac{F\psi_{\text{edge}}}{RT} = A_1 \text{asinh}\left[A_2\left(Q_{\text{edge}} + A_3\right)\right]$$

where Q_{edge} ($C \cdot m^{-2}$) is the edge charge, A_1 (unitless), A_2 (m^{-2} C) and A_3 (C m^{-2}) are obtained by fitting the Ψ_{edge} value from the two-dimensional full-resolution PB equation parameters. For montmorillonite at 25 °C, Tournassat et al. refined the values of these parameters to A_1 = 1.4-1.2 log I, A_2 = 11 + log I, A_3 = -0.02 (-log I)$^{1.60}$ (Tournassat et al., 2016).

Edge surfaces with different crystal orientations exhibit different properties and different site densities. Surface site types and densities will therefore be derived from constructed mineral crystallographic microstructures and experimental observations. Reaction equilibrium constants, including surface protonation/deprotonation constants and adsorption equilibrium constants, are derived from computational predictions with first-principles molecular dynamics.

2.9 Softwares

All the first-principle static calculations in this thesis are realized by the VASP (Vienna Ab initio Simulation Package) software package for solving the KS equation based on periodic density

functional theory (Kresse and Hafner, 1993; Kresse and Furthmüller, 1996a, b). VASP has its own independent set of reliable PAW pseudopotential databases, including all key elements in the periodic table. VASP runs fast and has high parallel efficiency, and supports GPU acceleration, especially in structural optimization. VASP input files are concise, and because VASP is widely used, the programs and visualization software supporting its pre- and post-processing are very complete, for example, VASPKIT, p4VASP, qVASP and VESTA, etc (Momma and Izumi, 2008; Yi et al., 2020; Wang et al., 2021).

All the first-principles molecular dynamics simulations in this thesis are implemented by the Quickstep module of CP2K software (Kühne et al., 2020). CP2K uses the latest GTH mode conservation pseudopotential to describe the state of electrons in the atomic nucleus, and uses the mixed Gaussian plane wave (GPW) method to calculate the KS equation through DFT. Therefore, for the optimization of electronic steps, CP2K can use more cutting-edge algorithms, especially OT (Orbital Transformation) algorithms. The OT algorithm finds the ground state density (wave function) by directly minimizing the KS energy (expressed in Gaussian basis) with the wave function coefficient as a function, which means that there is no need to do expensive diagonal calculations, and the electronic step convergence speed is very fast. Thousands of atoms of FPMD can be performed. At present, CP2K has been widely used in solid phase, liquid phase, molecular and biological systems. The trajectory analysis and visualization of molecular dynamics use VMD software.

In this thesis, the SCMs was constructed using the thermodynamic software PHREEQC (Parkhurst and Appelo, 2013). PHREEQC is widely used to simulate the chemical reaction and transport process of aqueous solution in natural environment or laboratory. The procedure is based on the equilibrium chemistry of aqueous solutions with surface interactions such as exchange and adsorption of minerals, gases, and solid solutions. The thermodynamic database of chemical components in aqueous solution uses THERMOCHIMIE v.11a (Giffaut et al., 2014).

Chapter 3. Mechanism of Uranyl Adsorption on the Orthoclase (001) Surface

3.1 Introduction

In the context of geological disposal based on the multi-barrier concept, the migration of radionuclides in natural aqueous systems is an ongoing concern in environmental research and for the long-term performance of nuclear waste repositories. Granite is considered as host rock formation in many countries due to its high compressive strength, low total porosity, good thermal conductivity and thermal stability for future disposal sites of high-level radioactive wastes (Jin et al., 2014, 2016). The retardation and transport of radionuclides in geological environments are primarily affected by their sorption/desorption reactions at solid/solution interfaces, which could be predicted by surface complexation models (SCMs). Granite is a multi-component igneous rock composed mainly of quartz and alkali feldspar (orthoclase and microcline). For the modeling of radionuclides on multi-component minerals, the main methods are component additivity (CA) and generalized composite (GC) methods (Davis et al., 1998, 2004). The CA method needs to consider the relevant information of each component of the mineral. In contrast, the GC method homogenizes all the component minerals, but with the assumption that each component of the mineral should not be strong site-specific.

Uranium is a commonly studied radionuclide based on its relatively high abundance in the environment, which exists as the most stable form of uranyl (UO_2^{2+}). Both CA and GC models have been successfully applied to the adsorption model of uranyl on granite. Therefore, it is of profound significance to clarify the uranyl adsorption specificity properties of the main component mineral of granite for the accuracy and reliability of the models. At present, the adsorption properties of U(VI) on quartz have been characterized on multi-scales, but the mechanism of the corresponding site-specific complexation of U(VI) on feldspar is not well understood. Only a few data and rare spectroscopic evidence for the U(VI) sorption onto feldspar. Richter performed batch experiments combined with time-resolved laser-induced fluorescence spectroscopy (TRLFS) and in situ attenuated total reflection Fourier transform infrared (ATR FT-IR) spectroscopy to confirm the presence of mononuclear uranyl species on the surface of orthoclase (K-feldspar) (Richter et al., 2016). Kerisit and Liu simulated U(VI) adsorption on nano-sized fractures of orthoclase and concluded that UO_2^{2+} directly bonded to surface hydroxyl oxygen (Kerisit and Liu, 2012). For albite (Na-feldspar), Walter et al. observed an inner-sphere, mononuclear, bidentate uranyl surface

complexes using Extended X-ray Absorption Fine Structure (EXAFS) spectroscopy at pH 5.8 and 5 × 10^{-6} mol/L U(VI) concentration (Walter et al., 2005). However, such information on U(VI) feldspar surface species does not provide particular complexation sites on the surfaces, which makes it unclear about the adsorption specificity on the surface. A proper characterization of the U(VI) interaction with feldspar is still missing.

The density functional theory (DFT) method has proven to be a powerful tool and is successfully applied in the study of actinide adsorption on mineral surfaces. Kremleva et al. have performed a series DFT studies of the atomic structure of uranyl adsorption on edge surfaces of kaolinite as well as montmorillonite and proposed possible binding surface sites and major surface species of uranyl. Furthermore, the adsorption of U(VI) on silica also has been extensively studied using DFT calculations. Wang et al. identified the ≡SiO(H)SiO(H) site on silica (001) surface is the most stable site for binding uranyl and the binding strength becomes weaker as the site protonated (Wang et al. 2015). In addition, the basic electronic properties of uranyl on silica surface have been further studied. These studies suggested possible complexing sites for U(VI) on silica as well as the interactions of major surface species. Thus, information at the atomic and electronic scales can be used for detailed properties investigations of mineral adsorption mechanisms. However, the characterization of the interaction of U(VI) with feldspar surface sites at such level remains unexplored.

In this study, DFT calculations and periodic slab models were utilized to investigate the adsorption of uranyl on the orthoclase (001) surface. Structures of the inner- and outer-sphere as well as bidentate and monodentate complexes types of surface complexation were examined and the formation and binding energies were also estimated. Bader charge analysis and electron density difference were carried out to understand the charge transfer during the adsorption process and local density of states (LDOS) were also analyzed comprehensively to explore the bonding mechanism. By comparing the calculated results with uranyl at the silica surface sites, a generalized site ≡SOH_2^0 which originated at the atomic level was used to construct an SCM of uranyl on granite.

3.2 Calculation Details and Models

3.2.1 Calculation Details

All the calculations were performed using the Vienna Ab initio Simulation Package (VASP) which based on first principles density functional theory. We applied the generalized gradient approximation (GGA) in the form of Perdew–Burke–Ernzerhof (PBE) exchange correlation potential,

and the effect of core electrons was described by the full-potential projector augmented (PAW) method as implemented in VASP. Scalar relativistic effects were incorporated into effective core potential via explicit mass-velocity and Darwin corrections. Integrations in the Brillouin zone were performed using a (2 × 2 × 1) k-point grid generated with the Monkhorst-Pack grid centered at the *Γ*-point and carried out to the orthoclase bulk and surface models. An energy cutoff of 500 eV was adopted for surface models and the orthoclase bulk (to reduce the effect of Pulay forces when the unit cell is optimized). A generalized Gaussian smearing method was applied with the smearing width 0.2 eV. In geometry optimizations, the total energy was converged to 10^{-5} eV, and forces acting on all unconstrained atoms were required to be less than 0.02 eV/Å. The energy was taken from one additional static run. In order to evaluate the effects of van der Waals interaction, the empirical dispersion corrections have been computed by using the DFT-D3 (BJ) method in several configurations (Grimme et al., 2010, 2011).

3.2.2 Models

Orthoclase ($KAlSi_3O_8$) is a feldspar with a silicate framework corner-sharing AlO_4 and SiO_4 tetrahedral form a three-dimensional lattice within which potassium ions fills a cavity to provide charge compensation for the substitution of Al for Si. The optimized primitive unit cell parameters of orthoclase are a = 8.72 Å, b = 13.11 Å, c =7.33 Å and α =90.95°, β = 116.03°, γ = 88.03°, in accordance with that from experiment.

The hydroxylated orthoclase (001) surface modeled by a periodic slab were done according to Kerisit et al (Kerisit et al., 2008). Terminal of surfaces were tetrahedral by distinct Si/Al sites. As a result, both the top and bottom faces of the mineral slab consisted of a full layer of non-bridging oxygens (both faces are therefore identical), which leads to relatively good sorption abilities (Figure 3.1). The initial configuration of the complete hydroxylated surface was obtained by saturating the terminal O atoms on the top and bottom surfaces with hydrogen atoms. The slab was repeated periodically in the z-direction with a vacuum region of 15 Å. A (2 × 1) supercell with a dimension of (17.43 Å × 13.11 Å × 22.77 Å) was used to study the uranyl adsorption. All atoms above the first layer K were allowed to fully relax while the bottom layer was fixed during optimization. There are four types surface groups $\equiv Si_1^{U}O(H)$, $\equiv Si_2^{U}O(H)$, $\equiv Si^{L}O(H)$ and $\equiv AlO(H)$. The $\equiv Si_1^{U}O(H)$ and $\equiv Si_2^{U}O(H)$ sites were in the upper position, whereas $\equiv Si^{L}O(H)$ and $\equiv AlO(H)$ were situated in a lower position relatively (Figure 3.1b). $\equiv Si_1^{U}O(H)$ connected $\equiv Si^{L}O(H)$ site via bridge oxygen atom,

whereas ≡$Si_2^UO(H)$ connected to ≡AlO(H). Furthermore, the surface sites may be deprotonated (≡SiO/AlO) or remain protonated (≡SiOH/AlOH) at different pH conditions.

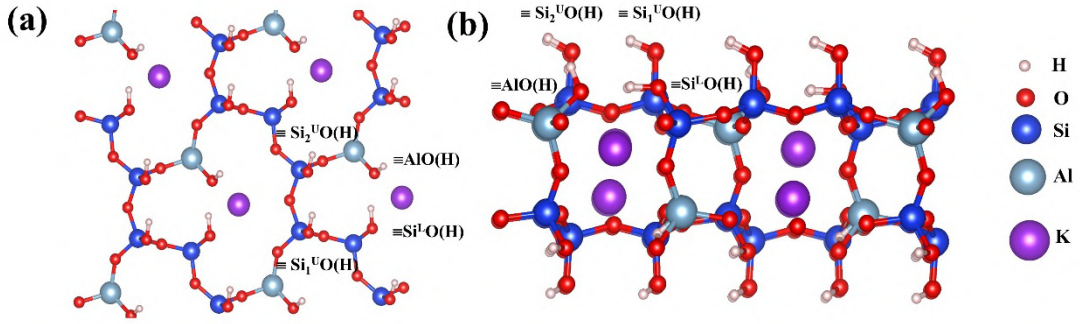

Figure 3.1 Top view of (a) the hydroxylated orthoclase (001) surface and (b) side view of hydroxylated orthoclase (001) surface.

The calculation of binding energy (ΔE_{bind}) and the derivation of formation energy (ΔE_{form}) were done according to Pan et al. and Kremleva et al., respectively (Kremleva et al., 2011, 2015; Pan et al., 2012). The changes of zero point energy (ZPE) for the whole system during the adsorption process would be rather small since there just forms one or two chemical bonds of U and surface O, accordingly, the correction of zero point energy (ZPE) was not considered here. The program VASP provides accurate compensating corrections for charged unit cells of cubic lattices only. Therefore, we optimized the structures of the molecular species $[UO_2(H_2O)_5]^{2+}$, H_2O, and H_3O^+ in simple cubic unit cells of 15 × 15 × 15 $Å^3$. For the slab model, a neutral unit cell was constructed by deprotonating one or two OH surface groups in the bottom surface.

3.3 Results and discussion

3.3.1 Inner-sphere Complexation Structures

The optimized configurations of inner-sphere bidentate and monodentate surface complexes were shown in Figure 3.2 and the key geometrical parameters, formation energies and binding energies were collected in Table 3.1.

For the most stable doubly deprotonated ≡$AlOSi^LO$ complex, as shown in Figure 2a, the two U-O_s distances are calculated to be 2.01 for aluminol O_s and 2.31 Å for silanol O_s atom, which indicated that aluminol had a stronger bond ability. Due to ≡$AlOSi^LO$ in a lower vacancy site, UO_2^{2+} group could adapt itself to interact with the closest hydroxyl group via a hydrogen bond with an O_t-H_s distance of 1.89Å. Hydrogen bonds were also formed between two H_2O molecules close to the surface.

The surface oxygen (O_s) with the H_w-O_s distance of 1.63 and 1.86 Å respectively, and the surface hydrogen (H_s) with the H_s-O_w distance of 1.88 Å. In contrast, for the $\equiv Si_1^UOSi_2^UO$ complex, the complex exhibited U-O_s bonds of 2.16 and 2.25 Å with an average bond length of 2.20 Å. The similarity in the average U-O_s bond of the $\equiv AlOSi^LO$ site complex (2.16 Å) suggested that both sites have analogous ability to bind uranyl. Notably, the uranyl bidentate surface complex with U-O_s of 2.13 and 2.15 Å were also calculated at ≡SiOSiO site on the silica (001) surface. In regards to the energetics, the uranyl binding energies were calculated to be -7.64, -7.08 and -8.69 eV at $\equiv AlOSi^LO$ and $\equiv Si_1^UOSi_2^UO$ sites on orthoclase and ≡SiOSiO site on silica, and the formation energies were endothermic by 4.80, 5.18 and 4.63 eV, respectively. The atomic structures and energetic indicated that the silica surfaces were similar to orthoclase surfaces for binding uranyl.

The adsorption configurations on partially and complete protonated sites were also simulated. Compared to $\equiv AlOSi^LO$ site, the complexes at $\equiv AlOHSi^LO$ site had longer U-O_s distances of 2.39 and 2.43 Å and much longer distances of 2.60 and 2.62 Å at $\equiv AlOHSi^LOH$ site, indicating a weaker bond of uranyl and orthoclase surface as the increase of surface site protonation. The binding energies were calculated to be -4.26 and -1.52 eV at $\equiv AlOHSi^LO$ and $\equiv AlOHSi^LOH$ sites, whereas the formation energies were -1.91 and -6.17 eV. Energetics suggested that protonation of surface sites weakens the binding, however, the protonated sites were thermodynamically more favorable because the surface deprotonation was much endothermic. Simultaneously, the consistent trend was also followed for the $\equiv Si_1^UO(H)Si_2^UO(H)$ sites on orthoclase (001) surface and ≡SiO(H)SiO(H)/≡SiO(H)O(H) sites on silica (001) surface. Variations in surface protonation might affect the surface complexation configuration. For $\equiv Si_1^UOHSi_2^UO$ site, the uranyl moiety exhibited one contact to the $\equiv Si_2^UO$ site and coordinated three aqua ligands in the first solvation shell, thus exhibiting the uranyl coordination number (CN) of 4. The H_w-O_s hydrogen bonds with distances of 1.62 Å and 1.72 Å played a key role for the structural adaptation, which do not exist at the $\equiv Si_1^UOSi_2^UO$, $\equiv Si_1^UOSi_2^UOH$ and $\equiv Si_1^UOHSi_2^UOH$ sites.

Inner-sphere monodentate complexes at $\equiv Si_1^UO(H)$, $\equiv Si_2^UO(H)$, $\equiv Si^LO(H)$ and ≡AlOH sites were also investigated, including protonated and deprotonated site configurations. The four H_2O molecules are still in the first coordination shell with the U-O_w distances around 2.60 Å. The U-O_s distances at $\equiv Si_1^UO$, $\equiv Si_2^UO$ and $\equiv Si^LO$ sites were 2.17, 2.23 and 2.23 Å, respectively, and the binding energies were -3.28, -3.87 and -4.01 eV. For the uranyl monodentate complexes at ≡SiO site on silica

(001) surface, the U-O_s distance was 2.25 Å and the binding energy was -6.10 eV. The U-O_s bond suggested that uranyl monodentate complexes on orthoclase were structurally similar to the silica surface, whereas the binding energies suggested that monodentate complexes on the silica surfaces were slightly stable compared to the orthoclase surfaces. In addition, the binding ability of uranyl bidentate complexes at partially deprotonated sites and monodentate complexes at deprotonated sites was similar for both orthoclase and quartz surfaces, which indicated that one type of site could be used to represent the two complexes in SCMs. In contrast, the monodentate surface complexes at the protonated ≡Si_1^UOH, ≡Si_2^UOH, ≡Si^LOH and ≡AlOH sites were the most unstable in the inner-sphere complexation mode, which was also found in the uranyl monodentate complexes at ≡SiOH site on silica (001) surface (Wang et al., 2015).

Table 3.1 The structural parameters (in Å for bond length and degree for bond angle), binging and formation energies (in eV) of bidentate complex for the adsorption of uranyl on the orthoclase (001) surface.

Sites	U-O_s	U-O_t	∠O_tUO_t	O_t-H_s	H_w-O_s	O_w-H_s	ΔE_{bind}	ΔE_{form}
≡$AlOSi^LO$	2.01,2.31	1.83,1.84	167.5	1.89	1.63,1.86	1.88	-7.64	4.80
≡$AlOHSi^LO$	2.39,2.43	1.83,1.81	171.9	1.94	1.61,1.81	1.99	-4.26	-1.91
≡$AlOHSi^LOH$	2.62,2.60	1.83,1.83	175.2	1.98	1.84,1.88		-1.52	-6.17
≡$Si_1^UOSi_2^UO$	2.16,2.25	1.82,1.82	168.1		1.72		-7.08	5.18
≡$Si_1^UOSi_2^UOH$	2.18,2.57	1.82,1.82	168.0			2.30	-4.20	0.92
≡$Si_1^UOHSi_2^UO$	2.14	1.81,1.82	169.2		1.62,1.72		-4.42	0.92
≡$Si_1^UOHSi_2^UOH$	2.48,2.57	1.82,1.82	175.3			1.79	-1.03	-3.34
≡AlOH	2.66	1.82,1.83	176.3	1.90	1.57,1.48		-0.93	-5.87
≡Si^LO	2.23	1.82,1.84	170.9	1.93	1.75,1.80		-4.01	-1.61
≡Si^LOH	2.69	1.81,1.83	176.1		1.69,1.47	2.19	-0.33	-5.87
≡Si_1^UO	2.17	1.82,1.83	170.2		1.55		-3.28	1.22
≡Si_1^UOH	2.69	1.82,1.83	177.5		1.58,2.06	2.47	-0.65	-3.04
≡Si_2^UO	2.23	1.82,1.81	172.8		1.72,1.69		-3.87	1.22
≡Si_2^UOH	2.63	1.82,1.83	175.2		1.73,1.74		-0.62	-3.04

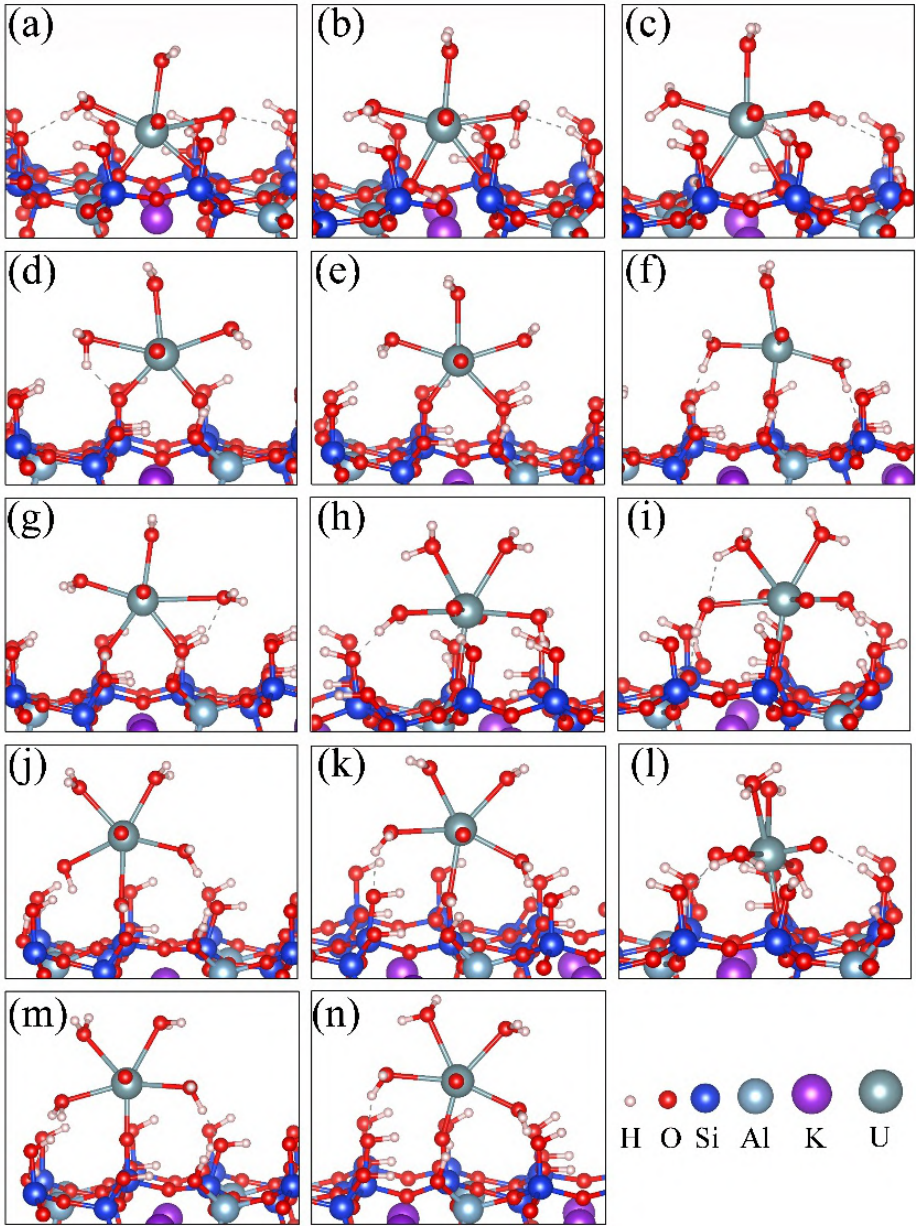

Figure 3.2 Optimized adsorption configurations of uranyl adsorbed on the hydroxylated orthoclase (001) surface. Inner-sphere bidentate and monodentate complexes (a) ≡AlOSi^{L}O, (b) ≡AlOHSi^{L}O, (c) ≡AlOHSi^{L}OH, (d) ≡Si$_1^{U}$OSi$_2^{U}$O, (e) ≡Si$_1^{U}$OSi$_2^{U}$OH, (f) ≡Si$_1^{U}$OHSi$_2^{U}$O, (g) ≡Si$_1^{U}$OHSi$_2^{U}$OH. (h) ≡AlOH, (i) ≡Si^{L}O, (j) ≡Si^{L}OH, (k) ≡Si$_1^{U}$O, (l) ≡Si$_1^{U}$OH, (m) ≡Si$_2^{U}$OH, (n) ≡Si$_2^{U}$OH.

3.3.2 Outer-sphere Complexation Structures

The key geometrical parameters, formation energies and binding energies of outer-sphere adsorption complexes were collected in Table 3.2 and the equilibrium configurations of outer-sphere complexes located on the ≡AlOHSi^{L}OH and ≡Si$_1^{U}$OHSi$_2^{U}$OH sites were shown in Figure 3.3, respectively. The hydrogen bonds were formed between the two H_2O ligands near the surface and the surface O atoms with the H_w-O_s distances of 1.64 and 1.73 Å for ≡AlOHSi^{L}OH site and 1.74 and 1.83

Å for ≡$Si_1^UOHSi_2^LOH$ sites. The U–O_t bonds are 1.82 and 1.83 Å for ≡$AlOHSi^LOH$ and ≡$Si_1^UOHSi_2^LOH$ sites respectively. The binding energy was considerably smaller because only hydrogen bonding interaction was built in the outer-sphere complex by -0.11 and 0.04 eV respectively, indicating the interaction between uranyl and the surface was considerably weaker. Moreover, the formation energy was -5.57 and -2.75 eV on ≡$AlOHSi^LOH$ and ≡$Si_1^UOHSi_2^UOH$ sites, which suggested the outer-sphere complexes is also thermodynamically feasible. In addition, the empirical dispersion corrections of DFT-D3 (BJ) method showed that the dispersion correction had a significant influence on the bonding energy (-0.95 and -0.61 eV) which made the bond more stable and a slight effect in the adsorption structures.

Table 3.2 The structural parameters (in Å for bond length and degree for bond angle), binging and formation energies (in eV) of outer-sphere complex for the adsorption of uranyl on the orthoclase (001) surface.

Model	U-O_t	∠O_tUO_t	H_w-O_s	ΔE_{bind}	ΔE_{form}
≡$AlOHSi^LOH$	1.82,1.82	173.2	1.64,1.73	-0.11	-5.57
	1.82,1.83	*170.2*	*1.64,1.66*	*-0.95*	
≡$Si_1^UOHSi_2^UOH$	1.83,1.83	174.5	1.74,1.83	0.04	-2.75
	1.83,1.83	*173.5*	*1.74,1.85*	*-0.61*	

[a] The values in italic are obtained with the DFT-D3(BJ) method

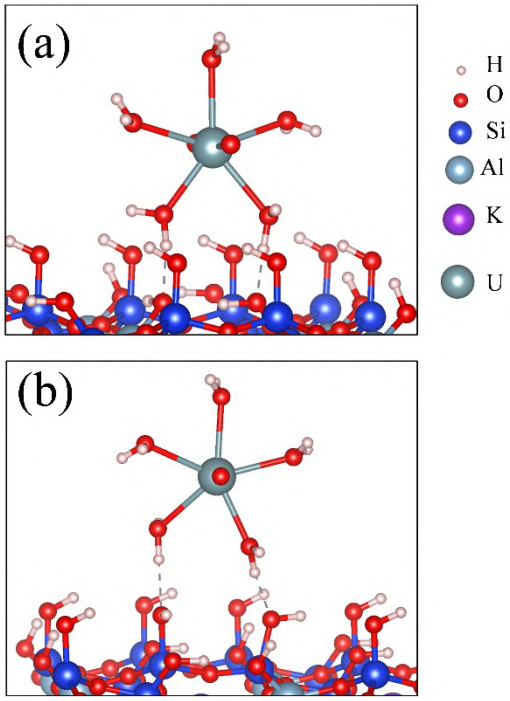

Figure 3.3 Optimized adsorption configurations of uranyl adsorbed on the hydroxylated orthoclase (001) surface. Outer-sphere complexes (a) ≡AlOHSi^{L}OH, (b) ≡Si$_1$^{U}OHSi$_2$^{U}OH.

3.3.3 Electronic Structural Properties

Charge density difference was able to describe the electron rearrangement between two atoms when a molecule was adsorbed on a surface. The difference charge density is defined as:

$$\Delta\rho = \rho_{\text{uranyl/surface}} - \rho_{\text{uranyl}} - \rho_{\text{surface}}$$

in which $\rho_{\text{uranyl/surface}}$, ρ_{uranyl} and ρ_{surface} were the electron densities of the adsorption complex, solvated uranyl and slab surface before adsorption, respectively.

The plot of the typical sites ≡AlO(H)Si^{L}O(H) of the charge density difference for the uranyl adsorption is shown in Figure 3.4a-3.4c. In the plot of electron density difference, the yellow regions represented the accumulation of electrons and the blue regions represented the depletion of electrons respectively. The color distribution showed that there was significant electron depletion around U atom and accumulation around the surface oxygen O_w atom, indicating that the electron density mainly transfers from U to O_s, and form chemical bond between U and O_s. It is noted that there is also a small amount of electron transfer of H_w, O_w, H_s and O_s, corresponding to the hydrogen bond which mentioned in the interaction between water and montmorillonite (Peng et al., 2016).

Based on Bader's theory of atoms in molecules (AIM), we have also calculated the Bader atomic charge of each atom quantitatively and clearly to understand the flux of electrostatic interaction during the adsorption process. The corresponding results for these adsorption complexes are listed in Table 3.3. Atoms of surface oxygen O_s denoted some electrons during their complexation with uranyl and the surface was negatively charged after adsorption with a value varied from -1.27 to -0.90 |e|. The value gets smaller compared to the intact surface, indicating that the charge transfer in the adsorption process weakens the electrostatic interaction between uranyl and the surface. In the inner-sphere adsorption complexes, the surface charge value becomes smaller as the increase of surface H atoms at the adsorption sites, indicating that the charge-charge interaction becomes weaker which was entirely consistent with previous section from bonding energy standpoint. In the outer-sphere adsorption complex, the Bader charge is similar to the inner-sphere complexes, indicating that the outer-sphere complex also has electrostatic interaction in addition to hydrogen bonding interaction. However, more remarkable, chemical bonding is the most important interaction in the inner-sphere

complexes.

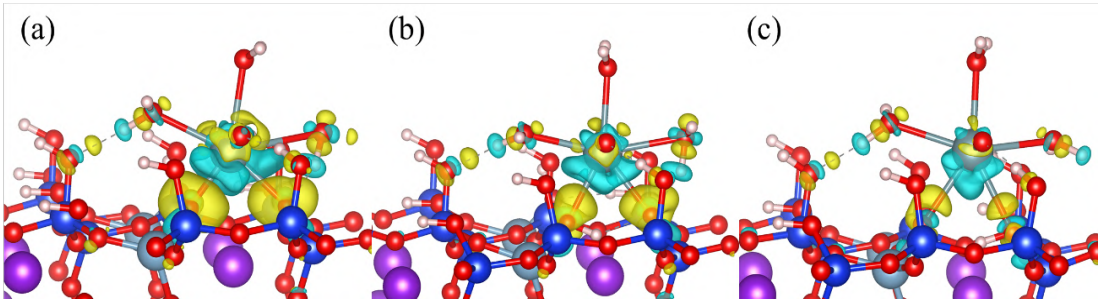

Figure 3.4 The charge density difference for uranyl adsorption at (a) ≡AlOSi^{L}O, (b) ≡AlOHSi^{L}O, (c) ≡AlOHSi^{L}OH. Isosurfaces of charge density were 0.005 e/Å^3.

Table 3.3 The Bader charge (Q_s in |e|) of surface in the Inner-sphere bidentate, monodentate complexes and outer-sphere complexes.

Bidentate	Q_s	Monodentate	Q_s	Outer-sphere	Q_s
≡AlOSi^{L}O	-1.16	≡AlOH	-0.90	≡AlOHSi^{L}OH	-0.97
≡AlOHSi^{L}O	-1.15	≡Si^{L}OH	-0.92	≡Si$_1^{U}$OHSi$_2^{U}$OH	-0.96
≡AlOHSi^{L}OH	-0.92	≡Si$_1^{U}$OH	-0.95		
≡Si$_1^{U}$OSi$_2^{U}$O	-1.27	≡Si$_2^{U}$OH	-0.95		
≡Si$_1^{U}$OSi$_2^{U}$OH	-1.16	≡Si^{L}O	-1.13		
≡Si$_1^{U}$OHSi$_2^{U}$O	-1.15	≡Si$_1^{U}$O	-1.16		
≡Si$_1^{U}$OHSi$_2^{U}$OH	-0.93	≡Si$_2^{U}$O	-1.18		

Further analysis by projected density of states confirms the bonding nature among atoms. The PDOS of aluminum oxygen atom, silicate oxygen atom and uranium atom in the four types of adsorption configurations were shown in Figure 3.5. The orbital overlapping part was below and nearest the Fermi level. Both the U f orbital and the U 6d orbital hybridized with the O p orbital, in addition, the U f orbital hybridizes with O p orbital to a much higher degree and within a higher energy range than the U 6d orbital. It is found that the U f and d orbital show strong hybridization with the O p at both ≡AlOSi^{L}O and ≡Si$_1^{U}$OSi$_2^{U}$O sites in the range of -5 to 0 eV, indicating strong chemical bonds are formed.

At ≡AlOSi^{L}O site, the U f and d orbital hybridize with the O p in the range of -6 to -2 eV, and the silica oxygen p orbital shows a stronger hybridization than alumina oxygen p orbital. While the hybridization is not obvious at ≡AlOHSi^{L}OH site, mainly involved in hybridization is the U d orbital. The oxygen O p orbital at protonated site were much localized, indicating the bonding between the two atoms is weak. Similarly, compared with previous result, strong U-Os bonds ranging from 2.01 to 2.39 Å and weak U-Os bonds ranging from 2.43 to 2.69 Å.

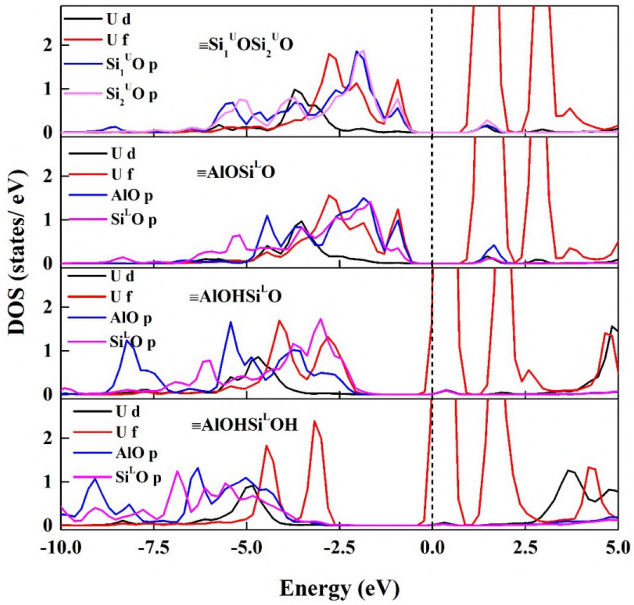

Figure 3.5 Local density of states (LDOS) for uranyl adsorption at ≡Si$_1$^{U}OSi$_2$^{U}O, ≡AlOSi^{L}O, ≡AlOHSi^{L}O and ≡AlOHSi^{L}OH sites. The Fermi levels are set to be zero.

3.4 Summary

Table 3.4 Generalized summary of silica and feldspar surface sites in SCMs

DFT		SCM
Silica (001)	Orthoclase (001)	
≡SiOO, ≡SiOSiO	≡AlOSi^{L}O, ≡Si$_1$^{U}OSi$_2$^{U}O	≡SO^{2-}
≡SiOSiOH, ≡SiO	≡AlOHSi^{L}O, ≡Si$_1$^{U}OHSi$_2$^{U}O, ≡Si$_1$^{U}OSi$_2$^{U}OH, ≡Si$_1$^{U}O, ≡Si$_2$^{U}O	≡SOH^{-}
≡SiOHOH, ≡SiOHSiOH, ≡SiOH	≡Si$_1$^{U}OHSi$_2$^{U}OH, ≡AlOHSi^{L}OH, ≡Si$_1$^{U}OH, ≡Si$_2$^{U}OH, ≡AlOH	≡SOH$_2$^{0}

From our calculations of uranyl adsorption on orthoclase and previous work on silica, a categorization of surface adsorption sites seems to be possible. Table 3.4 presents a typology of all

adsorption sites according to the complexation structures, energetics and electronic properties of uranyl on orthoclase (001) and silica (001) surfaces. This typology provided a well-defined guideline for a two-proton surface site as a homogenization site for multi-component granite.

Chapter 4. Structures of Multinuclear U(VI) Species on Hydroxylated α-SiO_2 (001) Surface: Density Functional Theory Study

4.1 Introduction

Because of the wide distribution of uranium in the environment and the growing public concern about radioactive pollution, many efforts have been devoted to understanding U(VI) adsorption on minerals. Similar to other heavy metals, a quantitative description of U(VI) adsorption on minerals has been carried out with surface complexation models (SCMs), in which surface functional groups are defined as surface ligands that interact with adsorbate to form surface complexes, including surface reactions of uranyl (UO_2^{2+}) and its mononuclear hydrolysis species (Clark et al., 1995; Zielinski et al., 1997; Burns and Finch, 1999; Tan et al., 2010; Geckeis et al., 2013; Liu et al., 2022). To improve confidence in the safety assessment of radioactive waste disposals and the predictions of uranium mobility in contaminated areas, it is necessary to check the validity of SCM predictions with adsorption data measured under a wide range of conditions, but also to verify the nature of surface species using spectroscopic characterization. Mononuclear U(VI) surface complexes have been extensively characterized by using e.g. Extended X-ray Absorption Fine Structure (EXAFS) spectroscopy, Time-Resolved Laser-induced Fluorescence Spectroscopy (TRLFS) and Attenuated Total Reflectance – Fourier Transform InfraRed (ATR-FTIR)spectroscopy. For instance, Sylwester et al. investigated U(VI) adsorption on silica, alumina, and montmorillonite surfaces at pH 3.1–6.5 using EXAFS spectroscopy, and found that uranyl forms mono/bidentate inner-sphere surface complexes besides outer-sphere species (Sylwester et al., 2000). Gabriel et al. identified two fluorescent surface complexes, i.e., $\equiv SiO_2UO_2^0$ (at pH 5.5) and $\equiv SiO_2UO_2OH^-$ (at 7.7), and a third nonfluorescent $\equiv SiO_2UO_2OHCO_3^{3-}$ surface species for U(VI) adsorption on silica under atmospheric according to TRLFS (Gabriel et al., 2001). In addition, simulation methods based on density functional theory (DFT) and molecular dynamics (MD) have also been applied to reveal the structures of mononuclear U(VI) surface complexes, which reported the preference of uranyl and its mononuclear hydrolysis species to form inner-sphere bidentate surface complexes by coordinating with neighboring hydroxyl sites on the surface (Wang et al., 2015, 2017). The structures of mononuclear U(VI) surface complexes on silica surfaces have been revealed using DFT and first principle molecular dynamic (FPMD) simulations. Good agreement between DFT/MD simulations and spectroscopic

investigations regarding structural information benefits the proposition of reliable SCM for engineering applications.

SCMs based on mononuclear U(VI) surface complexes are usually successful in fitting the adsorption data collected at low U(VI) concentrations. However, SCMs that consider only mononuclear U(VI) surface complexes can hardly fit U(VI) adsorption data obtained at high U(VI) concentrations, especially under conditions where multinuclear aqueous U(VI) species dominate (Wolthers et al., 2006; Marques Fernandes et al., 2012; Zhang et al., 2018; Tournassat et al., 2018). In contrast, if multinuclear U(VI) surface species are included, SCMs show better fitting performance to the experimental data. The formation of multinuclear U(VI) surface species at high U(VI) concentrations and near-neutral pH values are supported by many spectroscopic investigations. For instance, Kowal-Fouchard et al. ascribed the species with a fluorescence lifetime of 400 μs to a multinuclear U(VI) surface species $\equiv SiO(UO_2)_3(OH)_5$ on smectite under pH 5.0 in an air atmosphere (uranium concentration of 1×10^{-4} mol/L) (Kowal-Fouchard et al., 2004). Similarly, Baumann et al. attributed a longer fluorescence lifetime of U(VI) surface species on gibbsite at pH 8.5 (uranium concentration of 1×10^{-5} mol/L) to multinuclear U(VI) surface species in the air atmosphere (Baumann et al., 2005). The EXAFS spectroscopy results from Hattori et al. evidenced a U–U distance of 4.30 Å (pH 5.6) and 3.92 Å (pH 9.7) for gibbsite under N_2 atmosphere ([U(VI)] = 1×10^{-5} mol/L), which is close to the theoretical distance of binuclear U(VI) species in aqueous solutions. Sylwester et al. found similar U-U distances for systems of U(VI) adsorption on silica (3.97 Å) and alumina (4.01 Å) in an air atmosphere ([U(VI)] = 4×10^{-5} mol/L, pH ~ 6.5) (Sylwester et al., 2000).

Multinuclear U(VI) surface species are important for comprehensively understanding U(VI) adsorption on mineral surfaces, while their structures have been rarely investigated. The possible surface configurations of multinuclear species include both end-on and side-on modes (Figure 4.1). Up to date, only two examples of binuclear U(VI) surface species at aluminol sites have been reported. Hattori et al. investigated the surface structures of a di-hydroxyl bridging binuclear U(VI) species on an Al (hydr)oxide hexamer cluster, and their DFT simulation results suggested that binuclear U(VI) surface complexes in corner-sharing and/or edge-sharing binding modes coexist on gibbsite surfaces (Hattori et al., 2009). By using FPMD, Zhang et al. investigated the adsorption mechanism of U(VI) on the (010) surface edge of montmorillonite and identified a di-hydroxyl bridging binuclear U(VI)

surface complex. The surface complex can be regarded as the adsorption of $(UO_2)_2(\mu\text{-}OH)_2(H_2O)_6^{2+}$ in an end-on mode, in which μ represents the bridge hydroxyl group. Besides U(VI), multinuclear surface species have also been studied as an important topic for the distribution of other actinides in the environment (Zhang et al., 2018).

Knowledge of the adsorption of U(VI) on silica is of great significance to the geological disposal of nuclear waste in granite formations. To understand the adsorption of multinuclear U(VI) surface complexes on α-SiO_2 (001) surface, which is a key component to constitute an extensive understanding of the behavior of uranyl on the silica surface. Here we reported DFT simulations to reveal the configurations of surface complexes of binuclear and trinuclear U(VI) species at different surface sites. Both end-on and side-on binding modes were considered, and preferential adsorption modes were identified based on calculated binding energies. Charge transfer during the adsorption was interpreted by Bader charge and charge density difference analysis. Valence electron localization function (ELF) and projected density of states (PDOS) of the surface silanol oxygen atom and the binding uranium atom in the surface structures were calculated to reveal the change in the chemical environment upon adsorption. The results provide insights into a molecular level of understanding of the U(VI) adsorption mechanism under conditions where multinuclear U(VI) species are important in the aqueous phase.

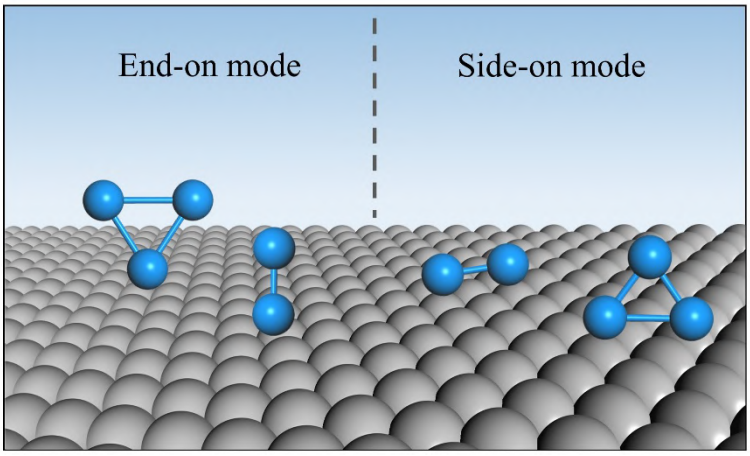

Figure 4.1 Schematic of end-on and side-on modes for bi-nuclear and tri-nuclear structures

4.2 Theoretical Methods and Models

4.2.1 Computational Details

All the calculations were performed using the Vienna Ab initio Simulation Package (VASP) which is based on periodic density functional theory. The generalized gradient approximation (GGA) in the form of Perdew–Burke–Ernzerhof (PBE) exchange-correlation potential was applied, and the effect of core electrons was described by the full-potential projector augmented (PAW) method as implemented in VASP.[42,43] Scalar relativistic effects were incorporated into effective core potential via explicit mass velocity and Darwin corrections. Integrations in the Brillouin zone were performed using a (2 × 2 × 1) k-point grid generated with the Monkhorst–Pack grid centered at the *Γ*-point. The electron localization function (ELF) and the electronic density of state (DOS) were calculated using a denser (3 × 3 × 2) k-point grid. A cutoff energy of 500 eV was adopted for surface models and the bulk to reduce the effect of Pulay forces when the unit cell was optimized. A generalized Gaussian smearing method was applied with a smearing width of 0.2 eV. In geometry optimizations, the total energy was converged to 10^{-5} eV, and forces acting on all unconstrained atoms were required to be less than 0.02 eV/Å. All the energy was taken from one additional static run. The calculation of binding energy (ΔE_{bind}) was done according to Pan's work, (Pan et al., 2012)

$$\Delta E_{bind} = E_{sc} - E_{sc}'$$

where E_{sc} referred to the energy of the optimized surface complex and E_{sc}' the energy of the system in which the free multinuclear species and the surface were kept apart at 8.00 Å. At a span of 8.00 Å, the interaction between the adsorbate and the surface was weak enough to mimic the non-interacting scenario to obtain a semi-quantitative value of ΔE_{bind}. The changes in zero-point energy (ZPE) for the whole system during the adsorption process would be rather small and accordingly the correction of zero-point energy (ZPE) was not considered.

4.2.2 Models

The experimental values of the primitive unit cell parameters of α-SiO_2 were adopted, i.e. a = 4.99 Å, b = 4.99 Å, c =5.50 Å, α =90.3°, β = 89.9° and γ = 120.2°. The hydroxylated α-SiO_2 (001) periodic slab with three O-Si-O layers was established by saturating the terminal O atoms on both top and bottom surfaces with hydrogen atoms (Figure 4.2). The pK_a values corresponding to the deprotonation reaction of those surface functional groups have been predicted to be 5.6-11.2,

suggesting that the silanols could dissociate in the common pH range in the solution. A neutral unit cell was constructed by deprotonating hydroxyl groups on the bottom surface. The slab was repeated periodically in the z-direction with a vacuum region of 20 Å. A $(\sqrt{2}\times\sqrt{2})$ orthorhombic surface was created by redefining the lattice, and then a (2×1) supercell with a dimension of 17.21 × 14.90 × 26.01 $Å^3$ was used to study the adsorption of multinuclear U(VI) species on the top surface. The two upper layers were allowed to fully relax while the bottom layer was fixed during optimization. The initial structures of the multinuclear U(VI) adsorbates in an aqueous solution, i.e., $(UO_2)_2OH^{3+}$, $(UO_2)_2(OH)_2^{2+}$, and $(UO_2)_3(O)(OH)_3^{+}$ (see Figure 4.3), were taken from the work of Tsushima et al., which were obtained based on both DFT calculation and spectroscopic (EXAFS, FTIR, UV-vis) investigation (Tsushima et al., 2007).

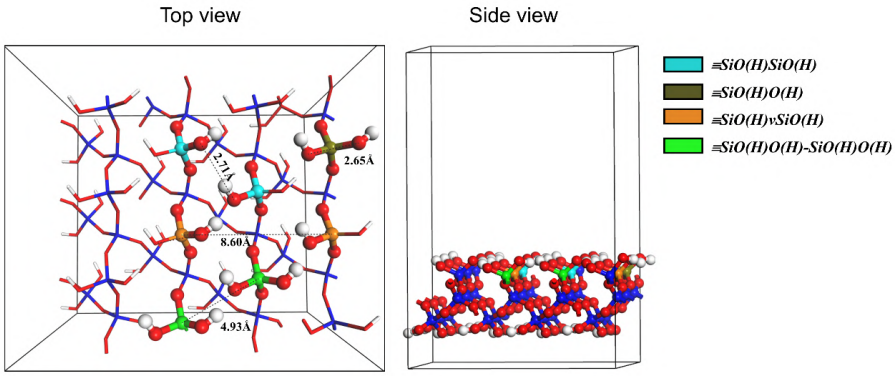

Figure 4.2 Elucidation of possible species on the hydroxylated α-SiO_2 (001) surface. O-O distance: 2.65 Å for ≡SiO(H)O(H), 2.71 Å for ≡SiO(H)SiO(H); Si-Si distance: 4.93 Å for ≡SiO(H)O(H)-SiO(H)O(H), 8.60 Å for ≡SiO(H)*v*SiO(H).

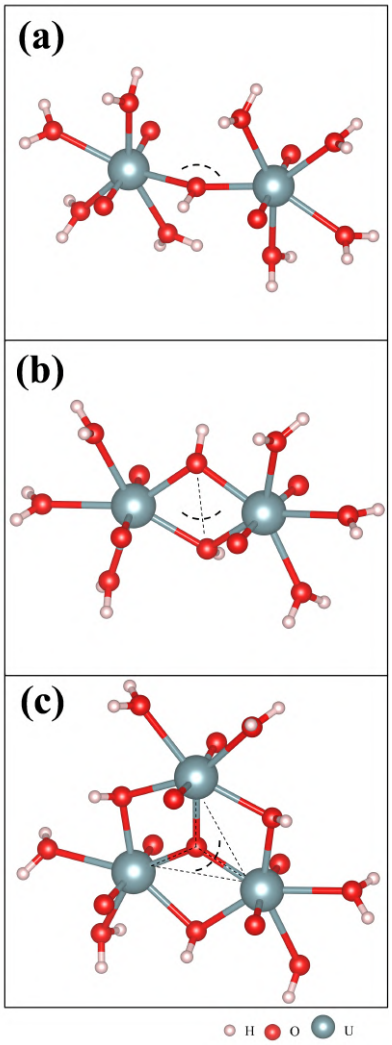

Figure 4.3 Geometries of bi- and tri-nuclear uranyl complexes in aqueous phase: (a) $(UO_2)_2(\mu\text{-}OH)(H_2O)_8^{3+}$, (b) $(UO_2)_2(\mu\text{-}OH)_2(H_2O)_6^{2+}$ and (c) $(UO_2)_3(\mu\text{-}O)(\mu\text{-}OH)_3(H_2O)_6^{+}$.

4.3 Results and Discussion

4.3.1 Adsorption Configuration

4.3.1.1 Adsorbates and Adsorption Sites

Depending on U(VI) total concentration, multinuclear U(VI) species occur around neutral pH values (Figure 4.4). In this study, three typical multinuclear U(VI) species in an aqueous solution are considered adsorbates (see Figure 4.3). Since silanols on the surface can exist in either their neutral or negatively charged (deprotonated) form under weak alkaline conditions, when more than one silanol is involved in surface complexation, different hydrolysis states of silanols (neutral or in deprotonated forms) are considered in this study except for the adsorption of $(UO_2)_3(O)(OH)_3^{+}$. Compared to $(UO_2)_2(OH)^{3+}$and $(UO_2)_2(OH)_2^{2+}$, $(UO_2)_3(O)(OH)_3^{+}$ are considered only for

deprotonated silanol sites. Because of the differences in the adsorbate configuration and the binding mode, a variety of sites on the α-SiO_2 (001) surface are involved in the adsorption of multinuclear U(VI) species, which are listed in Table 4.1 and schematically shown in Figure 4.2.

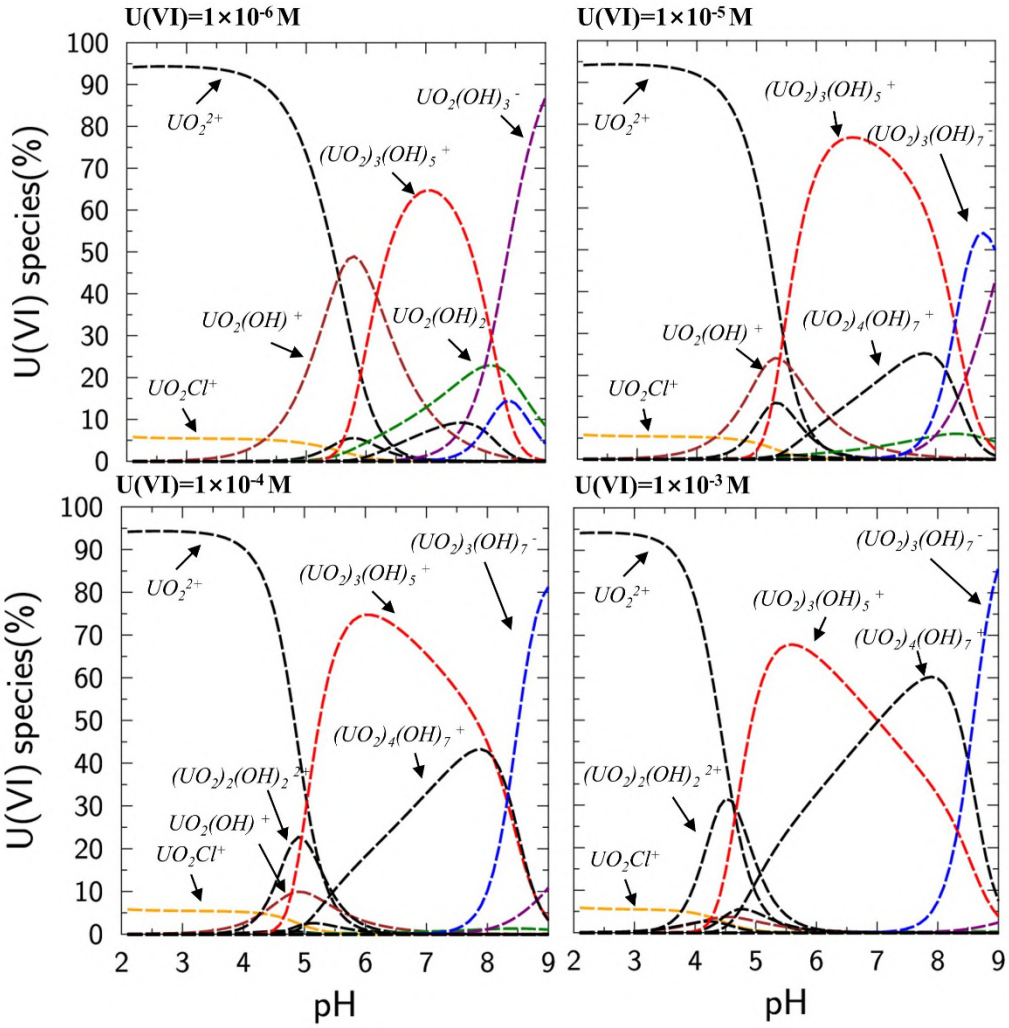

Figure 4.4 U(VI) speciation at concentrations of 10^{-6}-10^{-3} M in 0.1mol/L NaCl solution at 25°C. The PHREEQC code with THERMOCHIMIE v.11a thermodynamic database was used in speciation calculations.

Table 4.1 Typical α-SiO_2 (001) surface sites involved in the adsorption of binuclear and trinuclear U(VI) species. For each adsorbate, the end-on and the side-on binding modes require different sites. All sites are schematically shown in Figure 4.2.

Adsorbate	Binding mode	Sites		
$(UO_2)_2(OH)^{3+}$	End-on	≡SiOO	≡SiOHO	≡SiOHOH
		≡SiOSiO	≡SiOHSiO	≡SiOHSiOH
	Side-on	≡SiOO-SiOO	≡SiOHO-SiOHO	≡SiOHOH-SiOHOH

$(UO_2)_2(OH)_2^{2+}$	End-on	≡SiOO	≡SiOHO	≡SiOHOH
		≡SiOSiO	≡SiOHSiO	≡SiOHSiOH
	Side-on	≡SiO*v*SiO	≡SiOH*v*SiO	≡SiOH*v*SiOH
$(UO_2)_3(O)(OH)_3^+$	End-on	≡SiOO		
		≡SiOSiO		
	Side-on	≡SiO*v*SiO		

For each adsorbate of multinuclear U(VI) species, there are two possible binding modes in terms of the approaching orientation to α-SiO_2 (001) surface. In the first mode (see Figures 4.5a-4.5f and Figure 4.6), only one uranium atom chemically bonds to surface silanols, which results in an end-on binding/adsorption structure. The adsorption may happen at sites ≡SiO(H)O(H) and ≡SiO(H)SiO(H), respectively.

In the second mode (Figures 4.5g-4.5i and Figure 4.7), two uranium atoms of the same adsorbate coordinate simultaneously with two properly oriented silanols, which leads to the formation of a side-on binding/adsorption structure. The silanols of the site match the adsorbate configuration and enable two chemical bonds to be simultaneously formed with two uranyl moieties of the adsorbate. As shown in Figures 4.5g-4.5i and Figure 4.7, ≡SiO(H)O(H)-SiO(H)O(H) and ≡SiO(H)*v*SiO(H) (*v* represents a cavity between two silanols), with adjacent Si-Si distances of 4.93 and 8.60 Å, respectively, are two possible sites for the side-on adsorption mode.

For the adsorption of tri-nuclear uranyl complexes $(UO_2)_3(\mu\text{-}O)(\mu\text{-}OH)_3(H_2O)_6^+$, the simultaneous participation of all three uranyl moieties requires a corner topology to accommodate the complex, and is not considered here. We focus on the adsorption of the complex on a flat surface for a fair comparison with the adsorption of di-nuclear uranyl complexes. In the DFT calculations, the surface complexes in both modes are initially prepared in a way that the penta-coordinated uranyl moieties of the adsorbate lose one or two of the aqua ligands to coordinate with the silanols of the above-mentioned surface sites.

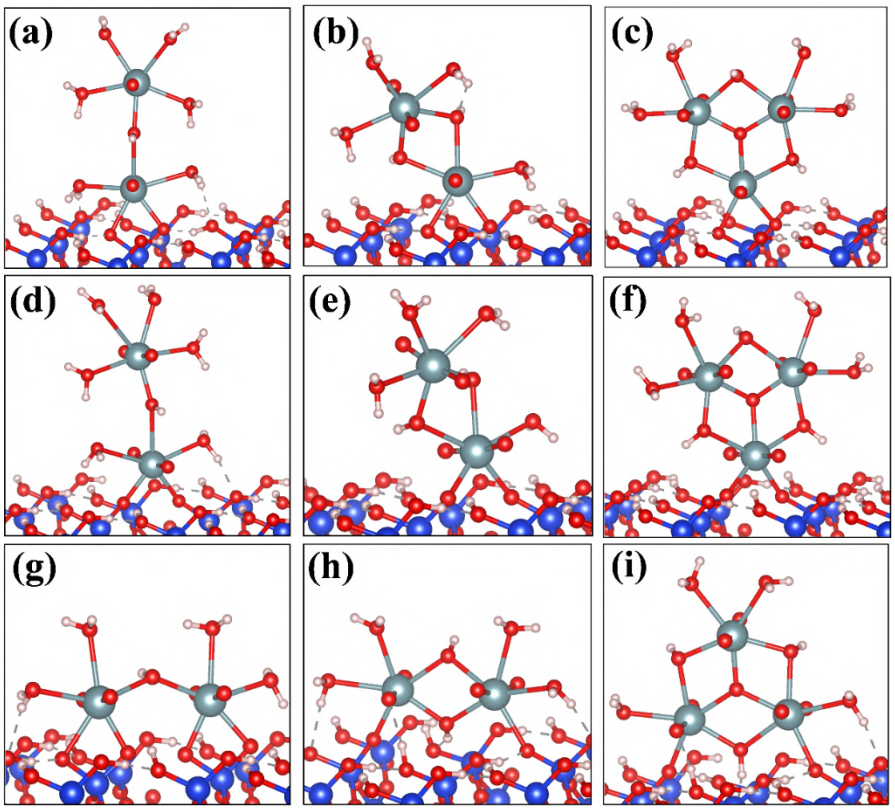

Figure 4.5 Configurations of the surface complexes in end-on (a-f) and side-on (g-i) binding modes for $(UO_2)_2(\mu\text{-}OH)(H_2O)_8^{3+}$, $(UO_2)_2(\mu\text{-}OH)_2(H_2O)_6^{2+}$ and $(UO_2)_3(\mu\text{-}O)(\mu\text{-}OH)_3(H_2O)_6^{+}$ on hydroxylated α-SiO_2(001) surface. (a)-(c) the adsorption at ≡SiOO site; (d)-(f) the adsorption at ≡SiOSiO site; (g) the adsorption at ≡SiOO-SiOO site; (h)-(i) the adsorption at ≡SiO*v*SiO site.

4.3.1.2 Structures and Binding Energy

The optimized configurations of the surface complexes in both modes are shown in Figure 4.5, and the key geometric parameters and the corresponding binding energy are collected in Table 4.2.

When multinuclear U(VI) adsorbates approach a hydroxylated α-SiO_2 (001) surface in the perpendicular orientation, one of its uranyl moieties interacts with surface silanols to form a surface complex in the end-on mode. Two coordinating water molecules in the equatorial plane of the uranyl are replaced when binding at ≡SiOO or ≡SiOSiO sites (see Figures 4.5a-4.5f). In the bidentate surface complexes, the two bond lengths of U-O_{surf} are in the range of 2.00-2.40 Å, which are shorter than that of U-O_{water} (around 2.60 Å), implying enthalpic gain upon the formation of the coordination bond between uranyl and the deprotonated surface silanol sites. For all adsorption species of $(UO_2)_2(OH)^{3+}$and $(UO_2)_2(OH)_2^{2+}$, hydrogen bonds are formed between the coordinating H_2O on the uranyl moiety and the accessible silanol O_{surf}. The H_{water}-O_{surf} distances in the bidentate structures are

in the range of 1.88-2.14 Å (see Table 4.2).

When $(UO_2)_2(\mu\text{-}OH)(H_2O)_8^{3+}$ approaches the hydroxylated α-SiO_2 (001) surface in a parallel orientation, it can adopt a side-on binding mode to interact with the ≡SiOO-SiOO site to form a "quadridentate" surface complex. Both uranyl moieties of the binuclear adsorbate participate in the surface coordination, which results in the bidentate coordination of each uranyl moiety with the surface (Figure 4.5g). In the case of $(UO_2)_2(\mu\text{-}OH)_2(H_2O)_6^{2+}$ and $(UO_2)_3(\mu\text{-}O)(\mu\text{-}OH)_3(H_2O)_6^{+}$, side-on mode are adopted similarly at the site ≡SiO*v*SiO (Figures 4.5h-4.5i) but with only one coordination bond between each uranyl moiety and the silanol group it binds.

The relative stability of the multinuclear surface complexes could be compared in terms of their overall binding energies on the surface, which vary significantly with the charge of the adsorbate, the steric hindrance of the site, and the binding mode of the surface complex. For surface complexes adopting end-on mode at the same site (≡SiOSiO or ≡SiOO), the binding energies (ΔE_{bind}) increase with the charge of the adsorbate in the order of $(UO_2)_3(\mu\text{-}O)(\mu\text{-}OH)_3(H_2O)_6^{+}$ < $(UO_2)_2(\mu\text{-}OH)_2(H_2O)_6^{2+}$ < $(UO_2)_2(\mu\text{-}OH)(H_2O)_8^{3+}$ (see Table 4.2), indicating that electrostatic interaction plays an important role in the adsorption of the multinuclear U(VI) species. The stronger attraction between the negatively charged surface site and the oppositely charged multinuclear U(VI) adsorbate promotes the adsorption and results in a higher ΔE_{bind}. The stronger interaction is in line with the shorter U–O_s distance of the formed surface complexes (see Table 4.2).

Table 4.2 Structural parameters (in Å), binging energies (in eV), and bond/dihedral angles (in degree) of $(UO_2)_2(OH)^{3+}$, $(UO_2)_2(OH)_2^{2+}$ and $(UO_2)_3(O)(OH)_3^{+}$ surface complexes at ≡SiOO-SiOO, ≡SiOO and ≡SiOSiO sites.

Binding mode	Adsorbate	Surface site	U-O_s	U-U	U-Si	H_w-O_s	H_s-O_{yl}	H_b-O_s	∠UO(U/O)U	ΔE_{bind}
End-on	$(UO_2)_2(OH)^{3+}$	≡SiOO	2.00, 2.32	4.76	2.98	2.01, 2.00	-	-	170.49 (158.20)	-6.46
	$(UO_2)_2(OH)_2^{2+}$	≡SiOO	2.23, 2.35	3.75	2.92	2.11	-	-	154..05 (164.46)	-5.16
	$(UO_2)_3(O)(OH)_3^{+}$	≡SiOO	2.31, 2.40	3.78, 3.82, 3.84	2.99	-	-	-	170.25 (174.24)	-2.66
	$(UO_2)_2(OH)^{3+}$	≡SiOSiO	2.16, 2.20	4.91	3.65, 3.71	1.88	-	-	159.86 (158.20)	-7.22
	$(UO_2)_2(OH)_2^{2+}$	≡SiOSiO	2.19, 2.23	3.82	3.52, 3.71	2.14	-	-	154.86 (164.46)	-6.30
	$(UO_2)_3(O)(OH)_3^{+}$	≡SiOSiO	2.20, 2.20	3.78, 3.83, 3.88	3.60, 3.70	-	-	-	179.81 (174.24)	-4.06
Side-on	$(UO_2)_2(OH)^{3+}$	≡SiOO-SiOO	2.16, 2.21 2.28, 2.51	4.42	3.01, 2.95	2.01, 2.27	-	-	134.71 (158.20)	-9.90
	$(UO_2)_2(OH)_2^{2+}$	≡SiOvSiO	2.20, 2.50	3.92	3.79, 3.96	1.82, 2.08	1.90	1.96	170.78 (164.46)	-5.48
	$(UO_2)_3(O)(OH)_3^{+}$	≡SiOvSiO	2.33, 2.45	3.79, 3.81, 4.00	3.88, 3.88	1.79	1.72	1.95	177.78 (174.24)	-3.07

[a] The values in brackets are the angles of the corresponding molecules

Table 4.3 Structural parameters (in Å), binging energies (in eV), and bond/dihedral angles of surface complexes of $(UO_2)_2(OH)^{3+}$ and $(UO_2)_2(OH)_2^{2+}$ at ≡SiOHO(H)-SiOHO(H), ≡SiOHO(H) and ≡SiOHSiO(H) sites.

Bind mode	Adsorbate	Surface site	U-O_s	U-U	U-Si	H_w-O_s	H_s-O_{yl}	H_b-O_s	∠UO(O)U	ΔE_{bind}
End-on	$(UO_2)_2(OH)^{3+}$	≡SiOHO	2.20, 2.84	4.69	3.22	2.07, 2.22	-	-	165.57 (158.20)	-3.61
	$(UO_2)_2(OH)_2^{2+}$	≡SiOHO	2.22, 2.63	3.68	3.10	-	-	-	154..25 (164.46)	-2.75
	$(UO_2)_2(OH)^{3+}$	≡SiOHOH	2.60, 2.69	4.61	3.42	1.65	-	-	153.66 (158.20)	-1.50
	$(UO_2)_2(OH)_2^{2+}$	≡SiOHOH	2.56, 2.70	3.70	3.38	-	-	-	155.02 (164.46)	-1.26
	$(UO_2)_2(OH)^{3+}$	≡SiOHSiO	2.16, 2.58	4.67	3.58, 4.00	2.05	-	-	166.35 (158.20)	-4.21
	$(UO_2)_2(OH)_2^{2+}$	≡SiOHSiO	2.11, 2.49	3.76	3.60, 3.93	1.82	-	-	158.78 (164.46)	-3.48

	$(UO_2)_2(OH)^{3+}$	≡SiOHSiOH	2.51, 2.69	4.74	3.94, 4.02	1.88, 2.26	-	-	166.31 (158.20)	-1.56
	$(UO_2)_2(OH)_2^{2+}$	≡SiOHSiOH	2.52, 2.54	3.71	3.91, 4.08	1.65	-		158.41 (164.46)	-1.50
Side-on	$(UO_2)_2(OH)^{3+}$	≡SiOHO-SiOHO	2.43, 2.43, 2.53, 2.77	4.43	3.34, 3.22	1.97	-	-	142.28 (158.20)	-5.66
	$(UO_2)_2(OH)^{3+}$	≡SiOHOH-SiOHOH	2.54, 2.60, 2.75, 2.79	4.58	3.45, 3.46	2.01	-	-	154.21 (158.20)	-2.73
	$(UO_2)_2(OH)_2^{2+}$	≡SiOHvSiO	2.22, 3.05	3.92	3.83, 4.48	1.70	1.63	2.01	164.10 (164.46)	-2.62
	$(UO_2)_2(OH)_2^{2+}$	≡SiOHvSiOH	2.59, 3.10	3.85	4.17, 4.53	1.80, 1.94	1.68	1.75	157.91 (164.46)	-1.33

[a] The values in brackets are the angles of the corresponding molecules

Table 4.4 U-U distances measured by EXAFS for different U(VI) adsorption systems

System	U(VI) initial concentration (μM)	pH	U-U distance(Å)
U(VI)-Silica	41.5	6.46	3.97
U(VI)-Alumina	41.8/1000	6.50/9.00	4.01/3.91
U(VI)-Gibbsite	10	5.60/9.70	4.30/3.92
U(VI)- Hematite	12-133	6.39-8.49	3.85-3.92
U(VI)-Al hydroxide	1.26-960	3.00-6.90	3.91-3.93

Besides the charge of the adsorbate, the steric hindrance also affects ΔE_{bind}. For instance, the overall binding energy of the same multinuclear U(VI) adsorbate at ≡SiOSiO is always about 1 eV higher than that at ≡SiOO, which corresponds to shorter U–O_s distances in the surface complex at ≡SiOSiO sites. Because the site ≡SiOSiO has a longer O(Si)-O(Si) distance than the ≡SiOO site, it shows the less steric effect and accommodates better the multinuclear U(VI) adsorbates. In addition, compared to the terminal hydroxyls on the same silicon atom, the hydroxyls on two neighboring silicon atoms have a more significant inductive effect, which also enhances the binding affinity of the site ≡SiOSiO. The stronger interaction at ≡SiOSiO than that at ≡SiOO was also observed for uranyl adsorption on the α-SiO_2 (001) surface.

The binding mode of the surface complex also influences its binding strength ΔE_{bind}. In comparison, the stabilities of the surface complexes in the side-on mode are relatively weaker than those in the end-on mode given the relatively lower binding energy of the same adsorbate in the former case. The relatively weak stabilities can be interpreted by the increasing tension of the surface complexes. Compared to the adsorption in the end-on mode, the adsorbates undergo more significant configurational rearrangement to attain suitable geometries for surface complexation in the side-on mode. For instance, the U-O-U bond angle of free $(UO_2)_2(\mu\text{-}OH)(H_2O)_8^{3+}$ is 158.20° , which changes to 159.86° and 171.49° when binding in an end-on manner at the ≡SiOSiO and ≡SiOO sites, respectively, whereas in the side-on surface complex, the corresponding angle is 134.71° . The dramatic decrease of the U-O-U bond angle results in a higher bond tension within the adsorbed species, which rationalizes the relatively weaker stability and smaller ΔE_{bind} of the side-on surface

complex as compared to those in the end-on mode. There seems a discrepancy in the case of $(UO_2)_2(\mu\text{-}OH)(H_2O)_8^{3+}$ adsorption in the side-on mode, where the overall binding energy is -9.9 eV. However, the coordinate bonds are weaker than those in the end-on surface complexes because the specific binding energy per bond is still smaller in the former case. In addition, the adsorption in the side-on mode with the same adsorbate loading leads to a higher surface coverage which shows a disadvantage to the adsorption because of a stronger repulsion between adsorbents. Moreover, hydrogen bonds form between the surface silanols and the equatorial water ligands in $(UO_2)_2(\mu\text{-}OH)_2(H_2O)_6^{2+}$ and $(UO_2)_2(\mu\text{-}OH)(H_2O)_8^{3+}$ (see Figure 4.5). The contribution of hydrogen bonds to the overall binding energy is relatively small because the formation energy of each hydrogen bond is around 0.13 eV (Kumar et al., 2007).

The adsorption configurations on partially deprotonated and neutral sites were also simulated (Figures 4.6-4.7 and Table 4.3). Protons are released during the adsorption at sites with neutral hydroxyl groups to form inner-sphere surface complexes. For a given adsorbate at a specific site taking the same adsorption mode, the extent of deprotonation of the surface sites shows nearly no noticeable influence on the configurations of the surface complexes. All ΔE_{bind} of the surface complexes at partially deprotonated sites and completely protonated sites have lower values compared to that at the deprotonated site, indicating relatively weaker interaction on the surface.

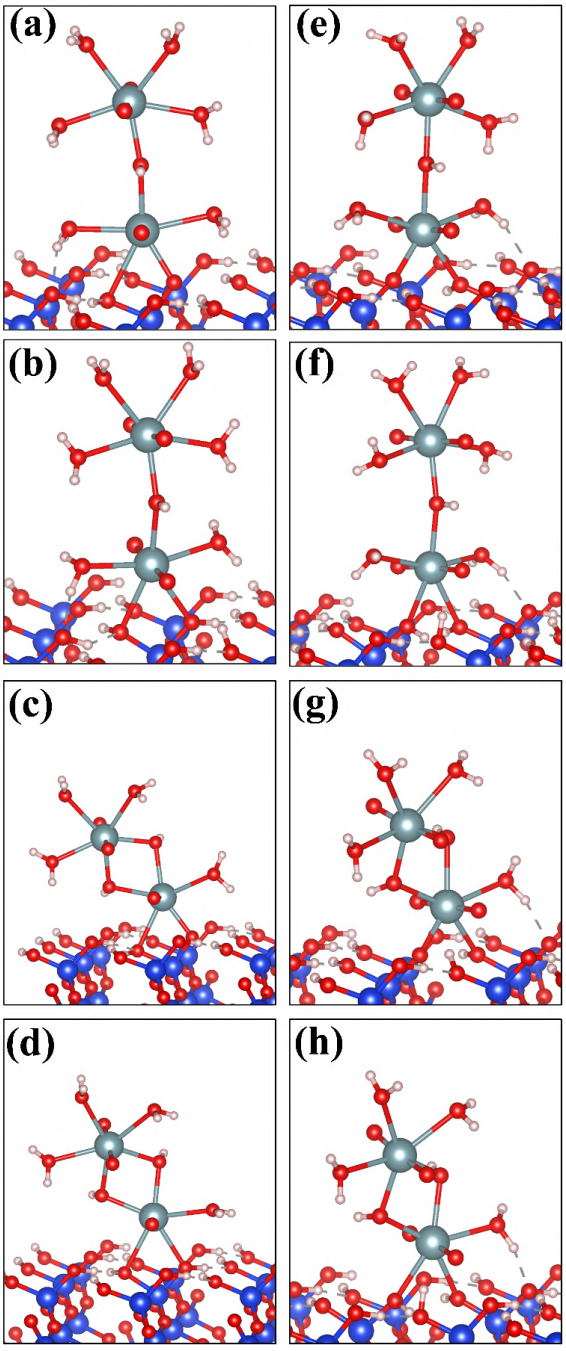

Figure 4.6 Configurations of the end-on surface complexes of $(UO_2)_2(\mu\text{-}OH)(H_2O)_8^{3+}$ and $(UO_2)_2(\mu\text{-}OH)_2(H_2O)_6^{2+}$ at (a)-(d) ≡SiOHO(H) and (e)-(h) ≡SiOHSiO(H).

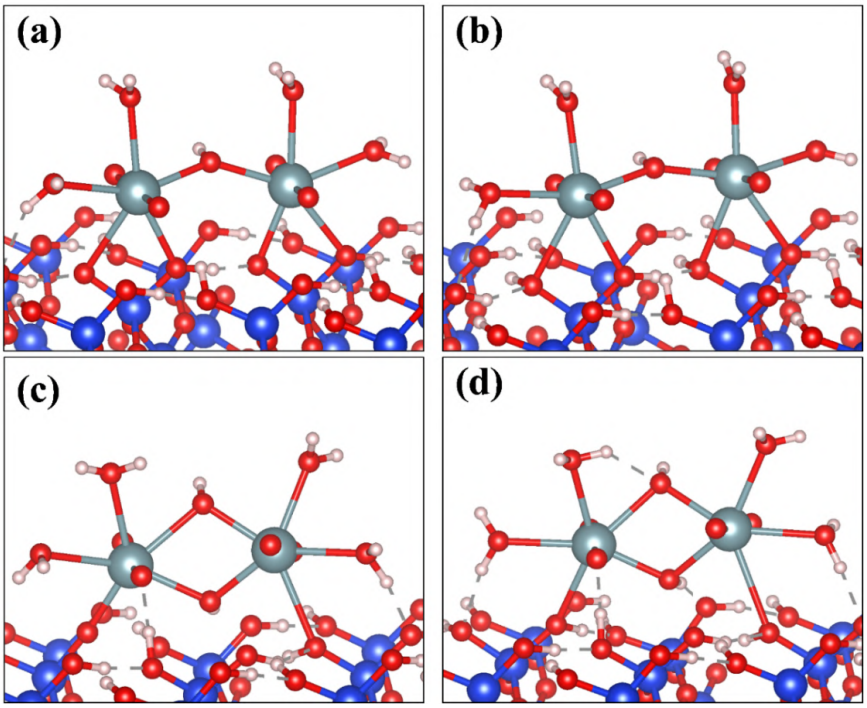

Figure 4.7 Configurations of the side-on surface complexes of (a)-(b) $(UO_2)_2(\mu\text{-}OH)(H_2O)_8^{3+}$ at ≡SiOHO(H)-SiOHO(H) and those of (c)-(d) $(UO_2)_2(\mu\text{-}OH)_2(H_2O)_6^{2+}$ at ≡SiOH*v*SiO(H).

Since the U-U distances of the multinuclear U(VI) species just slightly change after adsorption, the U-U distance obtained from spectroscopic measurements may be an indicator for the formation of multinuclear U(VI) surface species. For the single hydroxyl bridged species, $(UO_2)_2(OH)^{3+}$, the change in U-U distance in the adsorption process is within 0.3 Å, whereas for the double hydroxyl bridged species, $(UO_2)_2(OH)_2^{2+}$ and $(UO_2)_3(O)(OH)_3^{+}$, the U-U distance changes within 0.1 Å before and after adsorption. The U-U distances around 3.90 Å and 4.30 Å have been observed in many U(VI) adsorption systems at relatively high pH and high U(VI) concentrations (Table 4.4). The U-U distances of 3.92 Å and 4.30 Å are in good agreement with those (3.70~4.00 Å) for the end-on adsorption structures of $(UO_2)_2(OH)_2^{2+}$ and $(UO_2)_3(O)(OH)_3^{+}$, and that (4.42 Å) for the side-on adsorption species of $(UO_2)_2(OH)^{3+}$ in this study, respectively (Bargar et al., 2000; Froideval et al., 2006; Tang and Reeder, 2009; Hattori et al., 2009). According to the results listed in Table 2 and Table S1, however, multinuclear U(VI) surface complexes could not be distinguished based on only U-U or U-Si distance, and knowledge of both U-U and U-Si distances is necessary to identify multinuclear U(VI) surface complexes.

4.3.2 Electronic Properties

The electronic properties of the multinuclear uranyl surface complexes have been characterized by Bader charge analysis, the projected density of states, charge density difference, and valence ELF. Based on Bader's theory of atoms in molecules (AIM), the Bader atomic charge of each atom has been calculated to understand the fluctuation of electrostatic interaction during the adsorption process.

The initial hydroxylated α-SiO_2 (001) surface is negatively charged, i.e., -3, -2, and -1|e| for the adsorption of $(UO_2)_2(OH)^{3+}$, $(UO_2)_2(OH)_2^{2+}$ and $(UO_2)_3(OH)_5^{+}$, respectively. After adsorption, the surface remains negatively charged, but the amount of surface charge decreases to some extent (Table 4.5). The amount of the charge transfer reflects the contribution of chemical interactions via coordination. In general, the strength of electrostatic and chemical bonding interactions shows a positive correlation with the charge transfer between the surface site and the adsorbate. For example, at ≡SiOSiO sites, the surface charges after the adsorption of $(UO_2)_2(OH)^{3+}$, $(UO_2)_2(OH)_2^{2+,}$ and $(UO_2)_3(O)(OH)_3^{+}$ are -1.81 |e|, -1.33 |e| and –0.99 |e|, indicating that the corresponding charge transfer is 1.19 |e|, 0.67 |e| and 0.01 |e|, respectively, in agreement with decreasing bonding energy for the adsorption of $(UO_2)_2(OH)^{3+}$, $(UO_2)_2(OH)_2^{2+}$ and $(UO_2)_3(O)(OH)_3^{+}$ at ≡SiOSiO site, i.e., -7.22 eV, -6.30 eV, and -4.06 eV, respectively.

In addition, the protonation state of a surface site significantly influences the electrostatic interaction. For each multinuclear U(VI) adsorbate at the same surface site (see Tables 4.2 and 4.3), the increase of pH, which causes the deprotonation of the surface silanol groups, results in higher binding energy (ΔE_{bind}). This is in accord with the enhanced U(VI) adsorption at higher pH. The trend of increasing electrostatic interaction between the surface and the multinuclear U(VI) adsorbates is the same as that for mononuclear uranyl on the α-SiO_2 (001) surface (Wang et al., 2015).

Table 4.5 Bader charge (Q_s in |e|) of the surface after adsorption.

Binding mode	$(UO_2)_2(OH)^{3+}$	Q_s	$(UO_2)_2(OH)_2^{2+}$	Q_s	$(UO_2)_3(O)(OH)_3^{+}$	Q_s
End-on	≡SiOO	-1.83	≡SiOO	-1.33	≡SiOO	-0.95
	≡SiOHO	-1.66	≡SiOHO	-1.21		
	≡SiOHOH	-1.46	≡SiOHOH	-1.04		
	≡SiOSiO	-1.81	≡SiOSiO	-1.33	≡SiOSiO	-0.99

	≡SiOHSiO	-1.66	≡SiOHSiO	-1.17		
	≡SiOHSiOH	-1.45	≡SiOHSiOH	-1.00		
	≡SiOO-SiOO	-1.90	≡SiOvSiO	-1.38	≡SiOvSiO	-1.05
Side-on	≡SiOHO-SiOHO	-1.63	≡SiOHvSiO	-1.20		
	≡SiOHOH-SiOHOH	-1.43	≡SiOHvSiOH	-1.04		

Besides electrostatic interaction, chemical bonding also plays an important role in the adsorption process. The broadening and shifting of the density of states (DOS) can be used to evaluate the interactions in the system. According to the analysis of the projected density of states (PDOS), the orbital overlapping part below and nearest Fermi level of surface silicate oxygen atoms and the surface binding uranium atom in the adsorption configurations are illustrated (Figures 4.8-4.10). Comparing the PDOS of U and O atoms before adsorption, the U-f and U-d orbitals after adsorption show strong hybridization with the O-p in the range of -5 to 0 eV, indicating strong chemical bonds formed between the atoms (Figure 4.8). In particular, the peaks of U-f and U-d orbitals shift from −5.0 ∼ −2.5 eV to −2.5 ∼ 0 eV under the condition of uniform fermi energy level, which means that U atoms lose electrons in the adsorption process. This is consistent with the charge transfer obtained from Bader charge analysis. Interestingly, the stability of the multinuclear U(VI) surface complexes in the end-on binding mode is also influenced by the far side U atom. The f orbital of the far-side U atom after adsorption shows obvious hybridization due to the delocalization of the f electrons, providing additional stability to the surface complex (Figure 4.9, compare PDOS diagram of the U atom before and after adsorption). Moreover, for the adsorption at partial and fully protonated sites, the PDOS diagrams (Figure 4.10) show that the orbitals are localized below the Fermi level, indicating a relatively weak bonding in these cases. Particularly, the hybridization is apparent for the p orbital of the protonated O and the U-f orbital in the energy range of -5 to -2.5 eV. This is consistent with the fact that the U-O_{OH} bonds have a partial π character which weakens the axial uranyl bond (Zhang et al., 2017).

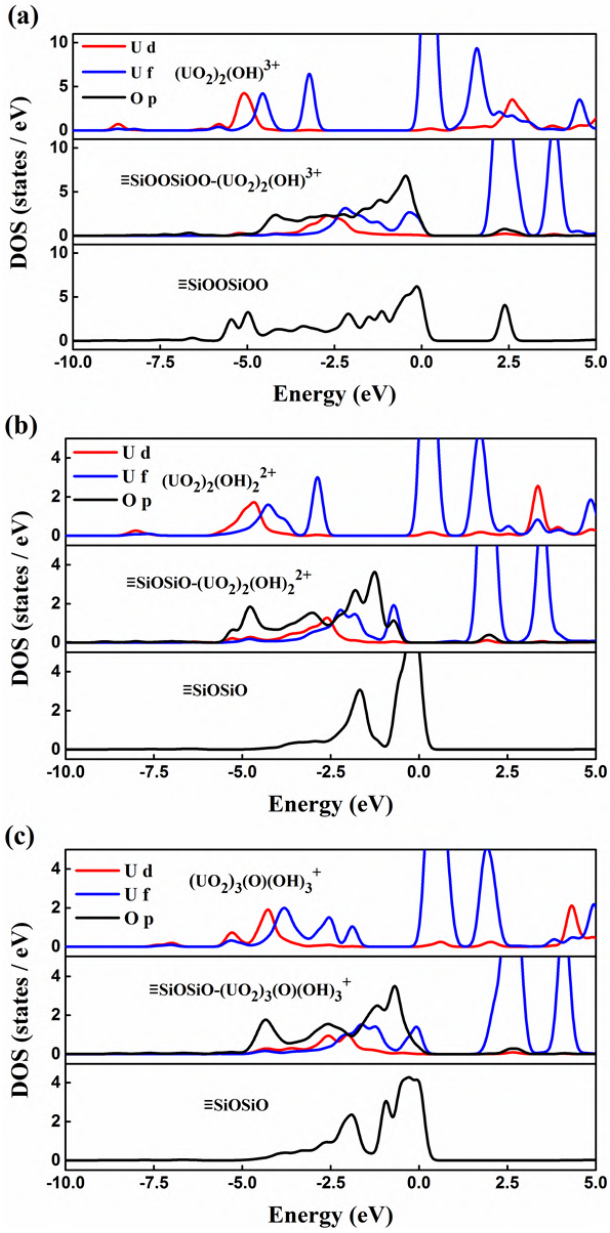

Figure 4.8 Projected density of states (PDOS) of surface silanol oxygen atom and the binding uranium atom before and after adsorption of (a) $(UO_2)_2(OH)^{3+}$ at ≡SiOO-SiOO site, (b) $(UO_2)_2(OH)_2^{2+}$ at ≡SiOSiO site, and (c) $(UO_2)_3(O)(OH)_3^{+}$ at ≡SiOSiO site. The Fermi levels are set to zero.

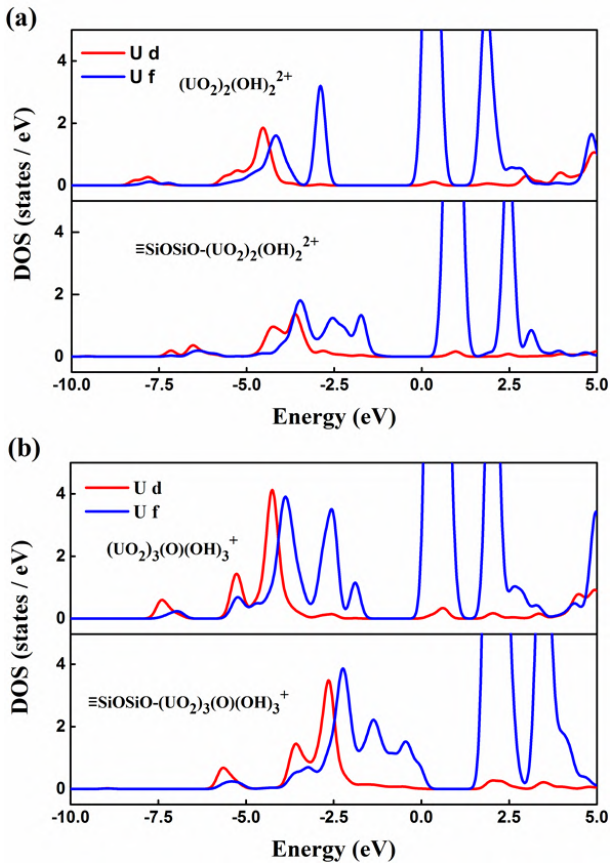

Figure 4.9 Projected density of states (PDOS) for the far side U atom before and after adsorption of (a) $(UO_2)_2(OH)_2^{2+}$ at ≡SiOSiO site and (b) $(UO_2)_3(O)(OH)_3^{+}$ at ≡SiOSiO site. The Fermi levels are set to zero.

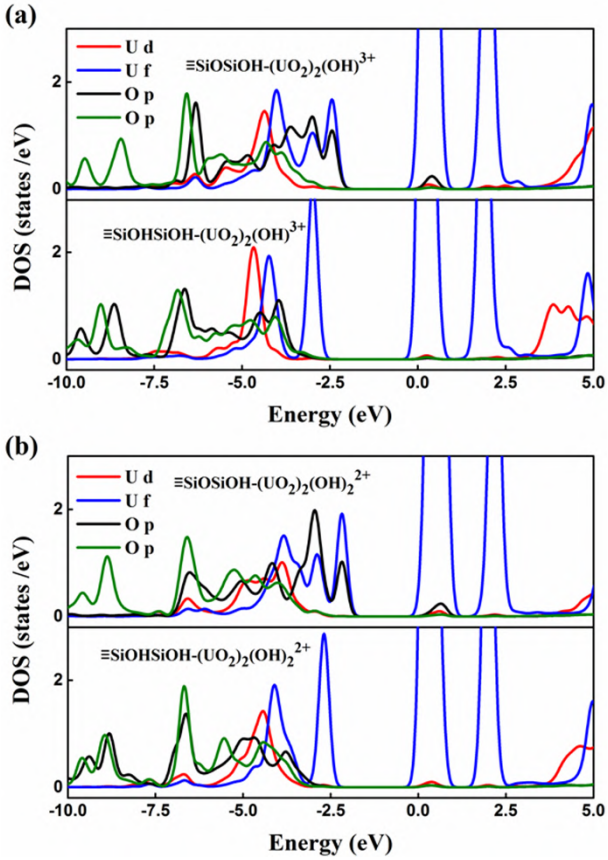

Figure 4.10 Projected density of states (PDOS) of surface silanol oxygen atom and the binding uranium atom in the surface structures of (a) $(UO_2)_2(OH)^{3+}$ and (b) $(UO_2)_2(OH)_2^{2+}$ at partial and fully protonated sites. The Fermi levels are set to zero.

To understand straightforwardly the electronic structures in the multinuclear U(VI) adsorption configurations, the charge density difference and valence ELF (Figure 4.11) is calculated according to:

$$\Delta\rho = \rho_{\text{multinuclear uranyl/surface}} - \rho_{\text{multinuclear uranyl}} - \rho_{\text{surface}},$$

where $\rho_{\text{multinuclear uranyl/surface}}$, $\rho_{\text{uranyl,}}$ and ρ_{surface} are the electron densities of the surface multinuclear U(VI) complex, multinuclear U(VI) molecular species, and slab surface before adsorption, respectively. The yellow regions represent the accumulation of electrons and the blue regions represent the depletion of electrons, respectively (Figures 8a-8c). The color distribution shows significant electron depletion around the surface binding U atom and an accumulation around the surface oxygen O_s atom of the binding site, indicating that the electron density transfers mainly from U to O_s, which is in accord with the Bader charge as well as the PDOS results. Similar results are also

found in the mononuclear uranyl adsorption system. In addition, charge transfer also occurs along the hydrogen bonds between the O_s atom and H atoms of neighboring coordination waters. A similar phenomenon was found at the water-montmorillonite interface.[60] Moreover, the far side U atoms in the end-on mode also lose electrons after adsorption, indicating an indirect participation in the surface complexation, which confirms the previous PDOS results (Figures 4.11a-4.11b). The results of valence ELF (Figures 4.11d-4.11f) suggest that partially covalent chemical bonds are stably formed between the U atom and surface O atoms, which is similar to most mononuclear uranyl adsorption systems (Zhang et al., 2016; Pan et al., 2022).

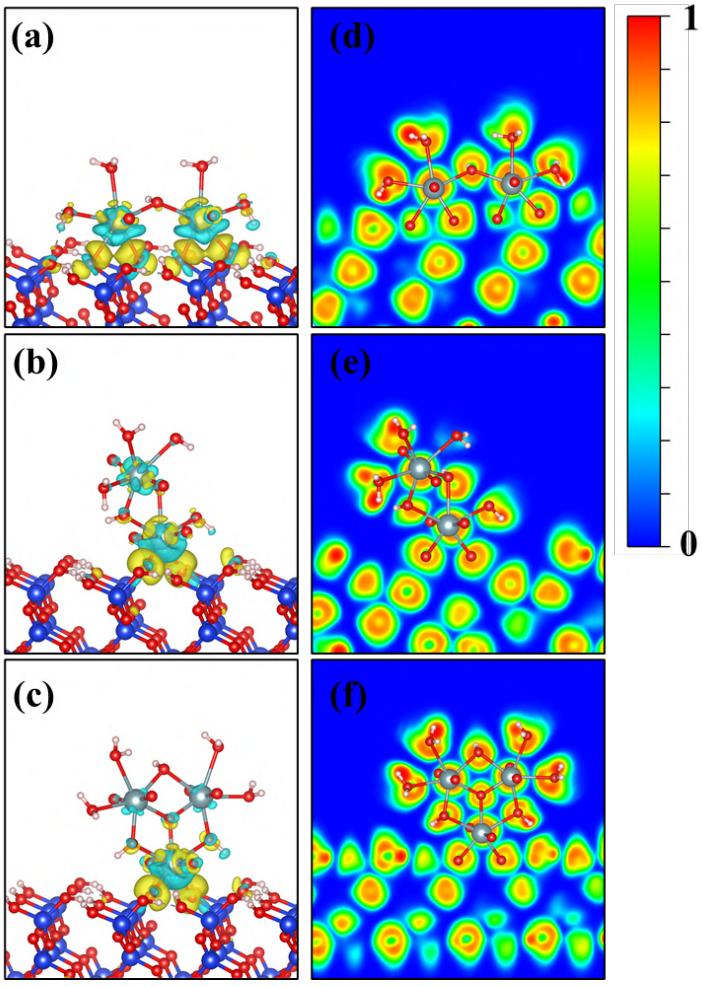

Figure 4.11 The charge density difference (a-c) and valence ELF (d-f) of $(UO_2)_2(OH)^{3+}$ at ≡SiOO-SiOO site (a and d), $(UO_2)_2(OH)_2^{2+}$ at ≡SiOSiO site (b and e) and $(UO_2)_3(O)(OH)_3^{+}$ at ≡SiOSiO site (c and f).

4.4 Conclusions

In this study, the structures of multi-dentate inner-sphere surface complexes of three multinuclear U(VI) adsorbates, i.e., $(UO_2)_2(OH)^{3+}$, $(UO_2)_2(OH)_2^{2+}$ and $(UO_2)_3(O)(OH)_3^{+}$, on α-SiO_2 (001) surface have been investigated using DFT calculations. $(UO_2)_2(OH)^{3+}$ prefers a side-on binding mode in which both uranyl moieties of the binuclear U(VI) species interact with two deprotonated surface sites, whereas $(UO_2)_2(OH)_2^{2+}$ and $(UO_2)_3(O)(OH)_3^{+}$ favor end-on structures where only one uranyl moiety coordinates with the surface sites via a bidentate model as well. The bidentate surface structures form at ≡SiO(H)O(H) or ≡SiO(H)SiO(H). In comparison, surface complexes at ≡SiO(H)SiO(H) have shorter U-O_s bonds, and higher binding energy but a longer U-Si distance. Both electrostatic interaction and chemical bonds (partially covalent) are responsible for the surface complexation of the multinuclear U(VI) species. The O_s-p orbital hybridizes strongly with U-f and U-d orbitals, meanwhile, the transfer of electron density from U to O_s occurs. The sequence of binding energy at the same site follows $(UO_2)_2(OH)^{3+}$ > $(UO_2)_2(OH)_2^{2+}$ > $(UO_2)_3(O)(OH)_3^{+}$, whereas the binding energy of the same multinuclear adsorbate at the same site increases with the increasing deprotonation extent. In addition, hydrogen bonds between surface hydroxyls and the coordination waters and acyl oxygen of uranyl moieties contribute slightly to the overall binding energy of the surface complexes. Moreover, the end-on surface complexes of $(UO_2)_2(OH)_2^{2+}$ and $(UO_2)_3(O)(OH)_3^{+}$ also benefit from the U-f electron delocalization of far-side U atoms. This study improves our understanding of the adsorption of U(VI) on silica and provides new insights into the structures of multinuclear U(VI) surface complexes.

Chapter 5. Polymerization Reaction Mechanism of Multinuclear Uranyl in Aqueous Solution and on Silica Surfaces

5.1 Introduction

Uranium in the biogeosphere is manifold and the solution chemistry of U(VI) system is important for understanding reactions of water with nuclear waste under geological disposal conditions. The uranyl (UO_2^{2+}) widely exists in aqueous solutions due to its high solubility and mobility. There are a number of coexisting polymeric hydroxo species with medium pH and U(VI) concentrations, leaving substantial uncertainties on the hydrolysis products.(Nguyen-Trung et al., 2000) Hence, hydrolysis reactions have been the subject of many experimental studies in the past. Peer-reviewed thermodynamic data of various U(VI) polymeric species are available in the OECD/NEA database. Exploring the thermodynamics properties of uranyl hydroxyl complexes is of great importance for understanding the chemical evolution of uranyl in nature. However, the formation process of multinuclear uranyl and the effect of multinuclear uranyl on the nucleation mechanism of uranyl hydroxyl oxide are not clear. This is a gap in actinide process chemistry.

Under aqueous aerobic environments, the composition and stability constants of the various hydroxo uranyl complexes have been investigated under various conditions of pH, temperature, and uranyl concentration by such techniques as potentiometry, spectrophotometry, chromatography, solvent extraction, and solubility. Results obtained from these studies indicated conclusively that three species: UO_2^{2+}, $(UO_2)_2(OH)_2^{2+}$, and $(UO_2)_3(OH)_5^{+}$ are progressively present from pH increased at modest concentrations of uranium. One minor species, $(UO_2)_2(OH)^{3+}$, was also found under higher uranium concentration. $(UO_2)_3(OH)_5^{+}$ is often described as $(UO_2)_3(O)(OH)_3^{+}$ as its stoichiometric equivalent. However, they are indistinguishable by potentiometric titration because both result in a loss of five protons. From the observed Raman frequencies, Nguyen Trung et al. proposed the structures of four uranyl trimeric complexes based on the assigned symmetrical stretching frequencies of the UO_2 group, all of which are oxo bridging among uranyl moieties (Nguyen-Trung et al., 2000). UV-vis and FTIR are also in line with the results. Reich et al. made the first EXAFS (extended X-ray absorption fine structure) measurements of the uranyl hydroxo trimer $(UO_2)_3(OH)_5^{+}$ and observed a U-U distance of 3.80 Å (Reich et al., 1998). EXAFS is still unable to confirm structures due to limited distal resolution and a general lack of angular information. DFT can serve

as a tool to correlate thermodynamic speciation and the species obtained by EXAFS. Tsushima et al. further identified the structure of $(UO_2)_2(OH)^+$, $(UO_2)_2(OH)_2^{2+}$ and $(UO_2)_3(O)(OH)_5^+$ by combining spectroscopic (EXAFS, FTIR, UV-vis) and DFT calculations (Tsushima et al., 2007). Nevertheless, the process of condensation of hydroxyuranyl to form multinuclear uranyl is unclear as yet.

The adsorption of radionuclides on mineral surfaces is a key process affecting their migration in the environment. Extensive experimental studies have been carried out using batch adsorption experiments, EXAFS, TRLFS (time-resolved laser-induced fluorescence spectroscopy) and XPS techniques to study the surface complexation of uranyl on minerals. It is concluded that under near neutral conditions, uranyl groups form multinuclear uranyl surface complexes, for instance on silica, alumina, hematite, gibbsite and kaolinite. For another, surface complexation model has been constructed based on the batch experimental results and the spectroscopic experimental data of uranyl surface complexes. It was found that the introduction of multinuclear complexes in the surface complexation model could significantly improve the fitting to the experimental data at high pH values. Theoretical simulation also has been proved to be an effective tool for identifying the structure of mineral surface complexes. At pH 9.7 and the initial uranium concentration of 1×10^{-5} mol/L, Hattori et al. reported the structures of $(UO_2)_2(OH)_2^{2+}$ surface complexes on gibbsite by DFT calculations in parallel with EXAFS spectroscopy (Hattori et al., 2009). The same structure was also found on the edge of montmorillonite by first principle molecular dynamics (FPMD) simulation. Gao et al. studied the surface complexation structures of $(UO_2)_2(OH)^+$, $(UO_2)_2(OH)_2^{2+}$ and $(UO_2)_3(O)(OH)_3^+$ on silica surface through periodic DFT simulation, which was consistent with the spectral results. Although multinuclear uranyl species have been identified in aqueous solution and solid surface, what remains to be understood is which environment will be inclined to form multinuclear uranyl, i.e. aqueous solution or surface.

Heterogeneous nucleation and precipitation of uranyl can occur during mineral surface adsorption, which will provide long-term stabilization of actinide pollutants. It has been proposed that heterogeneous nucleation is the most important mechanism for the formation of minerals. The process is dependent on uranium concentration and pH, and generally occurs in oxidizing environments where stable uranyl-hydroxides such as schoepite may form. In the presence of silicates or aluminates, coprecipitation of compounds containing Si or Al is also possible (i.e.,

soddyite, weeksite). The structural information of uranyl hydroxyl oxide precipitation has been studied by advanced experimental characterizations, such as time-resolved X-ray diffraction, neutron powder diffraction, X-ray absorption, mass spectroscopy, EXAFS and high-resolution transmission electron microscopy for several decades. The U atomic distance is summarized as the characteristic. For example, Uranyl hydroxides such as β-hydroxide (4.22Å), γ-hydroxide (4.23Å), the peroxide mineral studtite (4.21 Å) and amorphous hydrous oxide precipitate (3.90Å). However, most of previous works only focused on the description of their morphology and crystal structures. As far as we know, the mechanism of U(VI) nucleation and precipitation on mineral surface, including reaction pathways and thermodynamics, are not clear. Generally speaking, the bonding interaction and electronic structure in the structure unit determine the intrinsic physical and chemical properties of crystals, similar to the key role of genes in life. The process of early nucleation and precipitation can be better understood by searching the minimum structural unit from crystal structure and quantitatively exploring the thermodynamic properties of structural unit interaction. Nevertheless, even with state-of-the-art experimental tools it is still difficult to reveal the structure unit interaction relies mainly on theoretical simulations, such as DFT calculations, classical and first-principles molecular dynamics simulations (Zhang et al., 2019).

In this study, we perform first principle molecular dynamics (FPMD) simulations to systematically investigate the dissociation properties of $(UO_2)_2(OH)^+$, $(UO_2)_2(OH)_2^{2+}$ and $(UO_2)_3(O)(OH)_3^+$ in aqueous solution and on silica surface. It discovered that multinuclear uranyl tends to form in aqueous solution. We further combined the FPMD-based vertical energy gap method to construct multinuclear uranyl condensation reaction in aqueous solution and obtained the stability constant to compare with the experimental data. It revealed that the difference between $(UO_2)_3(OH)_5^+$ and $(UO_2)_3(O)(OH)_3^+$. By observing the crystal structure of schoepite, we obtain the repeated structures of penta- and hexa-nuclear clusters with uranyl species as structural units. Free energy simulations of structural unit reactions revealed the chemical mechanisms of the early nucleation stage of uranyl hydroxyl oxide (i.e. schoepite) on silica surface. Our work provides an atomistic-level understanding of the chemical behavioral processes of multinuclear species.

5.2 Simulation Details and Models

5.2.1 First Principles Molecular Dynamics

All simulations were performed with the CP2K/QUICKSTEP package. Density Functional Theory (DFT)-based electronic structure calculations are implemented using a hybrid Gaussian Plane Wave (GPW) method. the PBE generalization is applied to the exchange-correlation generalization, and Goedecker-Teter-Hutter (GTH) pseudopotentials are used to avoid core electrons. The cutoff energy for the electron density is 400 Ry. The DZVP basis set is applied to H, O, U, and Si. The Grimme-D3 method is used for dispersion correction in all calculations. the Born-Oppenheimer Molecular Dynamics (BOMD) simulations are performed with a wavefunction convergence of 10-6 . Regular system synthesis (NVT) conditions were imposed by a Nóse-Hoover thermostat with a target temperature of 300 K and a molecular dynamics time step of 0.5 fs. For each system, we performed an initial equilibrium simulation of 3.0 ps (6000 steps), followed by equilibrium sampling calculations of 5.0-10.0 ps.

5.2.2 Free Energy Calculations

We have considered the dissociation free energies of the three polynuclear uranyl species both in aqueous solution and on the surface of silica (001). For the dissociation reaction of binuclear uranyl, the U-U distance was chosen as the reaction coordinate to control the dissociation process, while for trinuclear uranyl, the distance between the U atom and the central O atom was chosen as the reaction coordinate. For the dissociation of pentanuclear clusters on the surface of uranyl hydroxyl oxide precipitates, the U coordination number to two O atoms was chosen as the reaction coordinate. The dissociation is into two mononuclear uranyl as well as one trinuclear uranyl. For the dissociation of the tetranuclear clusters, the dissociation reaction was divided into two stages for the dissociation process of two groups of U atoms.

5.2.3 Models

Figures 5.1 and 5.2 show the computational models of the three polynuclear uranyl in aqueous solution and on the surface of silica (001). For the computational model of aqueous solution, the system size is a cubic cell of 16.49 Å × 16.49 Å × 16.49 Å containing 142 solvent water molecules. For the structure of the surface complexes, the adsorption site was selected as the adsorption site based on the results of previous studies with the fully deprotonated ≡SiOSiO site. For the surface

complex calculation system, the box is an orthogonal box of size 17.21 Å × 14.90 Å × 28.79 Å and contains 163 solvent water molecules. The density of the aqueous solvent was approximately equal to 1 g/cm^3. In the simulation, a uniform background charge was applied to neutralize the net charge of the system. For the computational model of the multinuclear systems, the pentanuclear cluster model consisted of two mononuclear uranyl and one trinuclear uranyl adsorbed on the surface of silica (001), and the tetranuclear cluster model consisted of one monohydroxyl-bridged binuclear uranyl adsorbed on the surface and one bis(hydroxyl)-bridged binuclear uranyl (Figure 5.3).

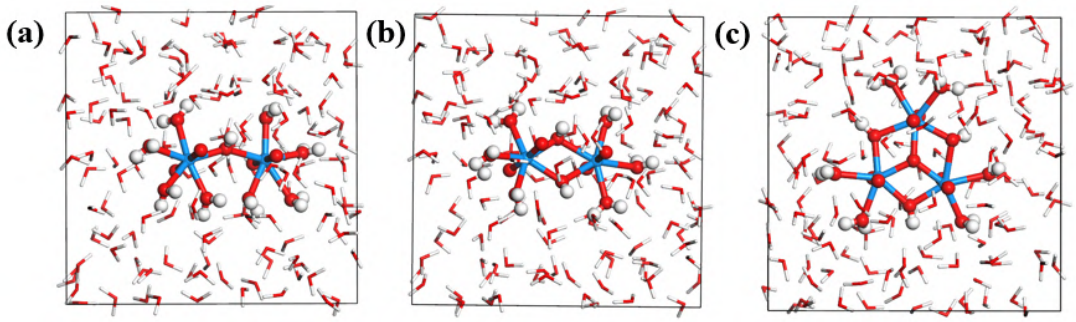

Figure 5.1 Computational models for multinuclear uranyl hydration systems. (a) $(UO_2)_2(\mu\text{-}OH)(H_2O)_8^{3+}$, (b) $(UO_2)_2(\mu\text{-}OH)_2(H_2O)_6^{2+}$ and (c) $(UO_2)_3(\mu\text{-}O)(\mu\text{-}OH)_3(H_2O)_6^{+}$

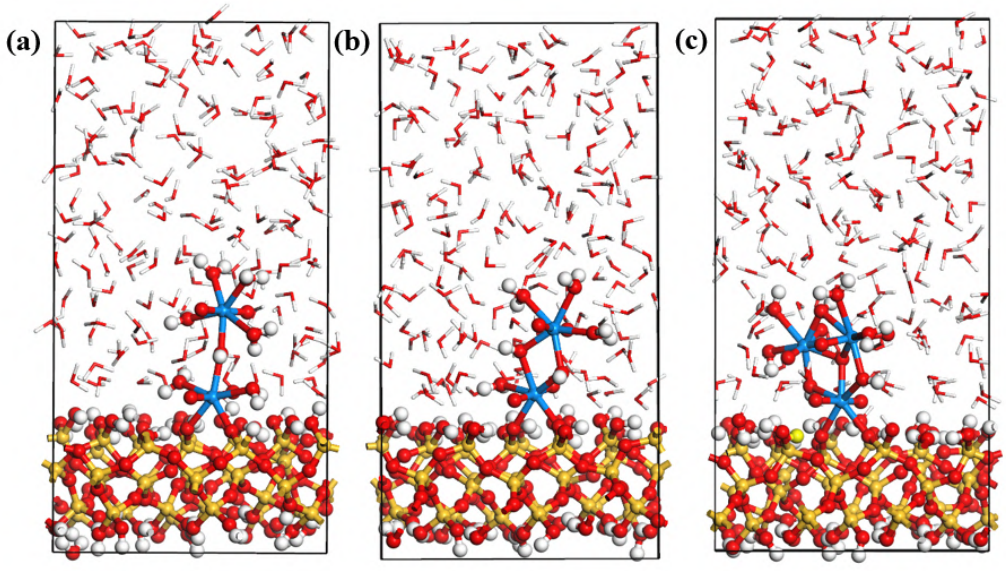

Figure 5.2 Computational models of end-on mode hydration systems for multinuclear uranyl on ≡SiOSiO surface coordination sites. (a) $(UO_2)_2(\mu\text{-}OH)(H_2O)_8^{3+}$, (b) $(UO_2)_2(\mu\text{-}OH)_2(H_2O)_6^{2+}$ 和 (c) $(UO_2)_3(\mu\text{-}O)(\mu\text{-}OH)_3(H_2O)_6^{+}$.

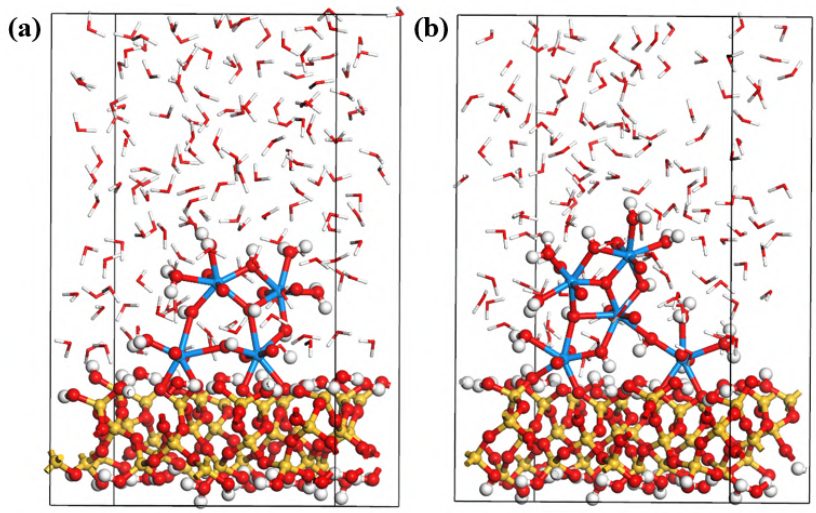

Figure 5.3 Models of (a) tetranuclear clusters and (b) pentanuclear clusters of uranyl hydroxyl oxides on the surface of α-SiO_2 (001)

5.3 Results and Discussion

5.3.1 Dissociation Processes of Multinuclear Uranyl in Aqueous Solution and on Silica Surfaces

We first investigated the dissociation of three polynuclear uranyl $(UO_2)_2(OH)^{3+}$, $(UO_2)_2(OH)_2^{2+}$ and $(UO_2)_3(O)(OH)_3^+$ in an aqueous solution and on a silica (001) surface. During the molecular dynamics equilibrium phase, each of the three polynuclear uranyl species maintains a stable five-coordination structure in aqueous solution and on the surface, which is consistent with previous DFT calculations. Figure 5.4 shows the radial distribution functions (RDFs) and integral coordination numbers (CN) of $(UO_2)_2(OH)^{3+}$, $(UO_2)_2(OH)_2^{2+}$ and $(UO_2)_3(O)(OH)_3^+$, which indicate that the average bond length in aqueous solution is 2.36 Å for U-OH, 2.58 Å for U-OH_2, and, in $(UO_2)_3(O)(OH)_3^+$, the average bond lengths between U and the bond length between the bridging O is 2.20 Å. Surface adsorption does not cause large structural changes, but does cause changes in the U-O RDF. At 2.20 Å, a U-Os bond occurs, while adsorption reduces the average bond length between U-OH and U-OH_2. The U-U distance is considered to be characteristic of multinuclear uranyl. By analyzing the kinetic trajectories, Figure 5.5 shows the time evolution of the U-U distances between $(UO_2)_2(OH)^{3+}$, $(UO_2)_2(OH)_2^{2+}$ and $(UO_2)_3(O)(OH)_3^+$ in aqueous solution and at the surface over the simulation time. It can be seen that in aqueous solution, the values of the U-U distances are 4.50 Å for $(UO_2)_2(OH)^{3+}$, 3.90 Å for $(UO_2)_2(OH)_2^{2+}$, and 3.82 Å for $(UO_2)_3(O)(OH)_3^+$, respectively. The distances change slightly when multinuclear uranyl adsorbed on surface, suggesting that the

adsorption process does not affect the U-U distances. This is consistent with our previous results obtained using the DFT method.

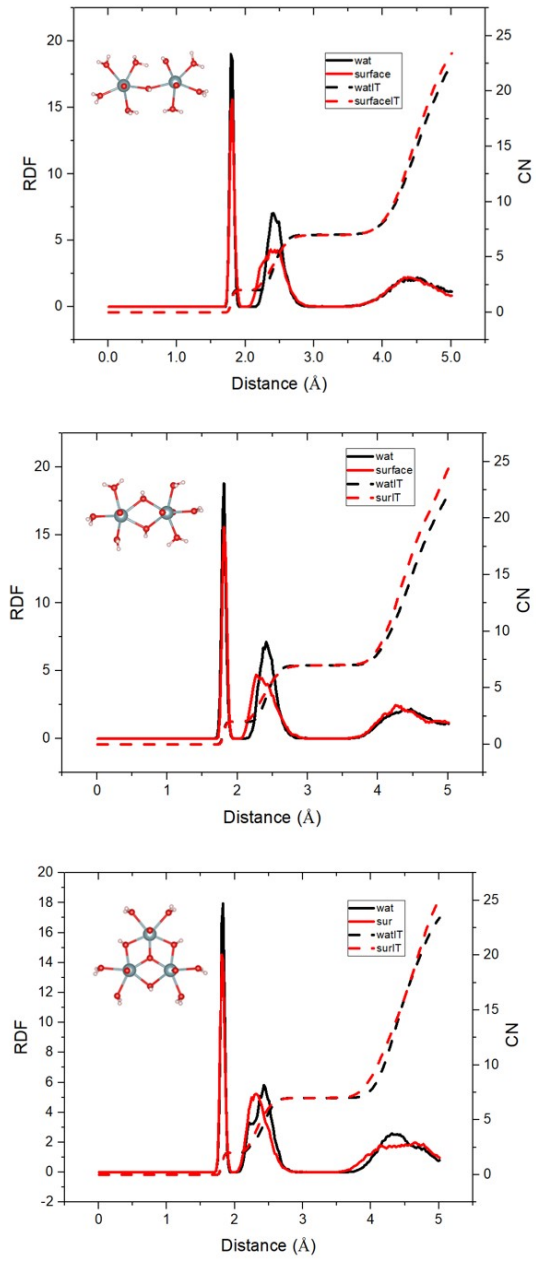

Figure 5.4 Radial distribution function (RDF) and coordination number (CN) of aqueous phase and surface polynuclear uranyl U around O.

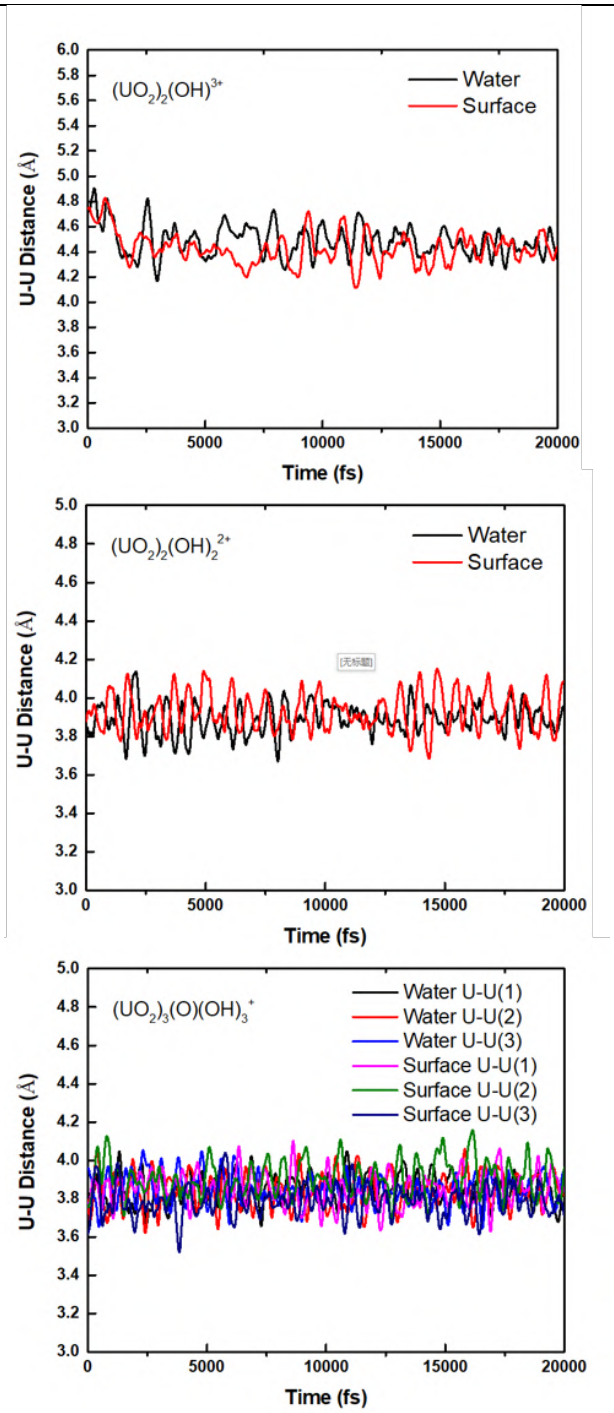

Figure 5.5 Evolution of U-U distances over simulation time for $(UO_2)_2(OH)^+$, $(UO_2)_2(OH)_2^{2+}$and $(UO_2)_3(O)(OH)_3^+$ in aqueous solution and surface systems

In order to reveal the stability of the $(UO_2)_2(OH)^{3+}$, $(UO_2)_2(OH)_2^{2+}$ and $(UO_2)_3(O)(OH)_3^+$ complexes, we calculated their free energies for the dissociation process in aqueous solution and on the silica surface, resulting in the free energy curves shown in Figure 5.6. In each curve, the free energy value of the first minimum (i.e., the equilibrium structure) is taken as the starting point, and

the minimum corresponding to the geometrical configuration of the outer ligand is taken as the end of the dissociation process. It is noteworthy that the three types of multinuclear uranyl have a continuous dissociation nature. For $(UO_2)_3(O)(OH)_3^+$, when a uranyl dissociates completely, a double bridged linkage structure similar to that of $(UO_2)_2(OH)_2^{2+}$ is formed. For the dissociation process of the $(UO_2)_2(OH)_2^{2+}$ complex, we find that the upward trend of the dissociation curve slows down significantly when the U-U distance is near 4.7 Å, corresponding to the same conformation as the monodentate $(UO_2)_3(O)(OH)_3^+$ complex. Therefore, we consider the dissociation of only one uranyl to assess stability.

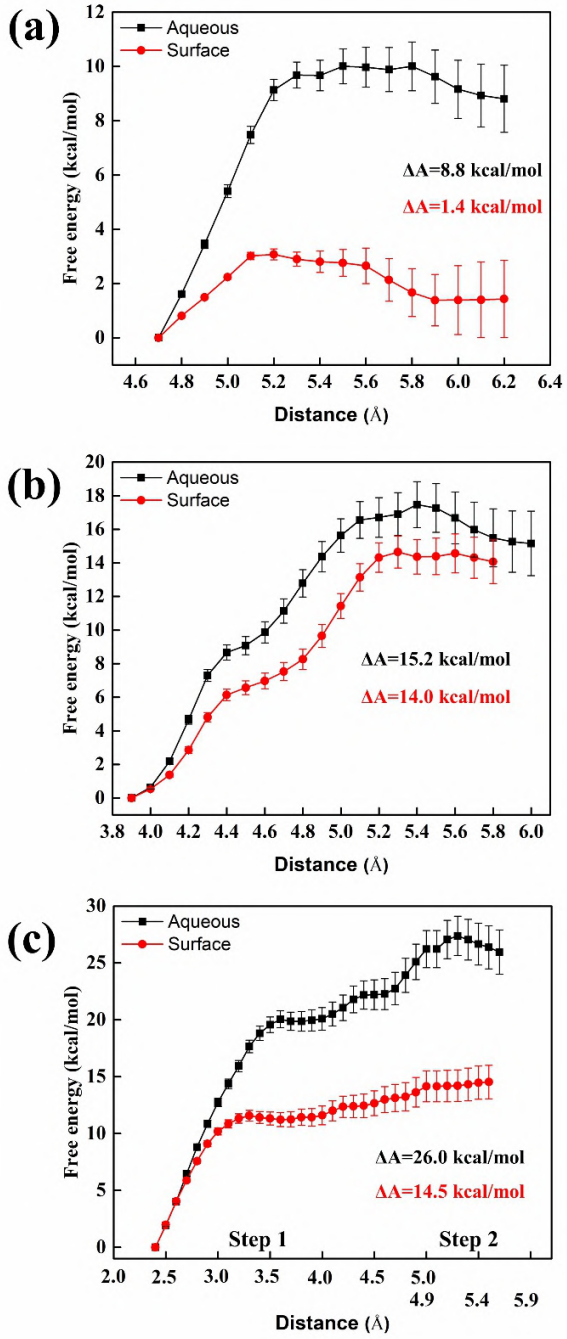

Figure 5.6 Dissociation free energy curves for (a) $(UO_2)_2(OH)^{3+}$, (b) $(UO_2)_2(OH)_2^{2+}$ and (c) $(UO_2)_3(O)(OH)_3^{+}$.

The free energy curves show that the formation of the three polynuclear uranyl complexes on both types of environments (i.e., aqueous solution and surface) is energetically exothermic and therefore spontaneous. More importantly, it can be seen that the free energies of dissociation of the three polynuclear uranyl complexes in aqueous solution are greater than those on the silica surface (8.8 kcal/mol vs. 1.4 kcal/mol for $(UO_2)_2(OH)^{3+}$, 15.2 kcal/mol vs. 14.0 kcal/mol for $(UO_2)_2(OH)_2^{2+}$ and 26.0 kcal/mol vs 14.5 kcal/mol for $(UO_2)_3(O)(OH)_3^{+}$), which implies that the formation of

polynuclear uranyl in aqueous solution is most feasible. Our simulations yielded trends in the formation of three typical polynuclear uranyl species in aqueous solution and on surfaces. This provides strong evidence for considering polynuclear uranyl species in aqueous solution as surface-coordinated species when constructing macroscopic surface coordination models.

5.3.2 Equilibrium Constants for Reactions of multinuclear Uranyl in Aqueous Solution

In order to reveal the thermodynamic stability of polynuclear uranyl complexes in aqueous solution, we have calculated the free energy of the total reaction according to Hess law, which states that the free energy change in a chemical reaction is pathway independent.

$$UO_2(H_2O)_5{}^{2+} = UO_2(OH)(H_2O)_4{}^{+} + H^+ \qquad \Delta G_1 = 16.01 \text{ eV (1)}$$

$$UO_2(H_2O)_5{}^{2+} + UO_2(OH)(H_2O)_4{}^{+} = (UO_2)_2(OH)(H_2O)_8{}^{3+} + H_2O$$

$$\Delta G_2 = -0.38\text{eV (2)}$$

$$2UO_2(OH)(H_2O)_4{}^{+} = (UO_2)_2(OH)_2(H_2O)_6{}^{2+} + 2H_2O \qquad \Delta G_3 = -0.68 \text{ eV (3)}$$

$$UO_2(OH)(H_2O)_4^{+} = UO_2(OH)_2(H_2O)_3 + H^+ \qquad \Delta G_4 = 16.09 \text{ eV (4)}$$

$$(UO_2)_2(OH)_2(H_2O)_6{}^{2+} = (UO_2)_2(O)(OH)(H_2O)_6{}^{+} + H^+ \qquad \Delta G_5 = 16.52 \text{ eV (5)}$$

$$UO_2(OH)_2(H_2O)_3 + (UO_2)_2(O)(OH)(H_2O)_6 = (UO_2)_3(O)(OH)_3(H_2O)_6{}^{+} + 3H_2O \qquad \Delta G_6 = -1.08 \text{ eV (6)}$$

$$H^+ + H_2O = H_3O^+(UO_2^{2+} \text{ system}) \qquad \Delta G_7 = -15.48 \text{ eV (7)}$$

$$H^+ + H_2O = H_3O^+((UO_2)_2(OH)_2^{2+} \text{ system}) \qquad \Delta G_8 = -15.53 \text{ eV (8)}$$

For $(UO_2)_2(OH)^{3+}$, equation (1) + (2)+ (7) to equation (9):

$$2UO_2(H_2O)_5^{2+} = (UO_2)_2(OH)(H_2O)_8^{3+} + H_3O^+ \qquad \Delta G_9 = 0.15 \text{ eV (9)}$$

For $(UO_2)_2(OH)_2{}^{2+}$, equation 2×(1)+ (3)+ (7)+ (8) to equation（10）:

$$2UO_2(H_2O)_5{}^{2+} = (UO_2)_2(OH)_2(H_2O)_6{}^{2+} + 2H_3O^+ \qquad \Delta G_{10} = 0.33 \text{ eV (10)}$$

For $(UO_2)_3(O)(OH)_3{}^{+}$, equation (1)+ (4)+ (5)+ (6)+ (10)+2×(7)+1×(8) to equation（11）:

$$3UO_2(H_2O)_5{}^{2+} = (UO_2)_3(O)(OH)_3(H_2O)_6{}^{+} + 5H_3O^+ \qquad \Delta G_{11} = 1.37 \text{ eV (11)}$$

Where ΔG_1,ΔG_4 and ΔG_5 can be derived from the pKa values of the corresponding complexes on the basis of $\Delta G = pK_a k_B T \ln 10$. ΔG_7 and ΔG_8 can be calculated using the proton dissociation energies on the basis of the vertical energy gap method. ΔG_2, ΔG_3, and ΔG_6 denote the free energy variations of the dissociation processes for the three types of polynuclear uranyl.

Using the Gibbs free energies of ΔG_9, ΔG_{10} and ΔG_{11}, the equilibrium constants of the reaction

can be obtained through the van't Hoff equation, and it can be found that for $(UO_2)_2(OH)^{3+}$, the calculated and experimental equilibrium constants of the reaction are -2.29 and -2.70, respectively, which are in agreement within the margin of error. For $(UO_2)_2(OH)_2^{2+}$, the calculated and experimental values are also in agreement with each other, which are -5.22 and 5.62, respectively, but for $(UO_2)_3(O)(OH)_3^{+}$, the difference between the experimental and calculated values is larger, which are -15.55 and -20.92, respectively, which is mainly due to the fact that there are many reaction steps to construct the cumulative reaction of $(UO_2)_3(O)(OH)_3^{+}$, and the error of each step is also is continuously transmitted, thus leading to a higher difference in the results. Therefore, it is difficult to obtain more accurate equilibrium constants by theoretical calculations for reactions with many steps in the unit reaction.

5.3.3 Mechanism of Early Nucleation and Precipitation of Uranyl Hydroxide

Schoephite is a typical solid-phase structure of uranyl hydroxide, and its molecular formula is $(UO_2)_8O_2(OH)_{12}\cdot 12H_2O$. The solid-phase structure is shown in Figure 5.7, which is a layered structure. In the single-layer structure, We found two smallest repeating units, namely a pentanuclear cluster structure composed of trinuclear uranyl and two mononuclear uranyl, and a tetranuclear structure composed of single hydroxyl bridged dinuclear uranyl and double hydroxyl bridged dinuclear uranyl cluster structure. Surface adsorption precipitation is considered to be an important mechanism for mineral formation in soil systems. When the solution is saturated with solutes, the surface acts as a nucleation site, and metal ions aggregate through water to form precipitates. Therefore, we explored the early precipitation mechanism of uranyl hydroxide on the surface of silica (001), and calculated the free energies of precipitation reactions of the two smallest repeating units.

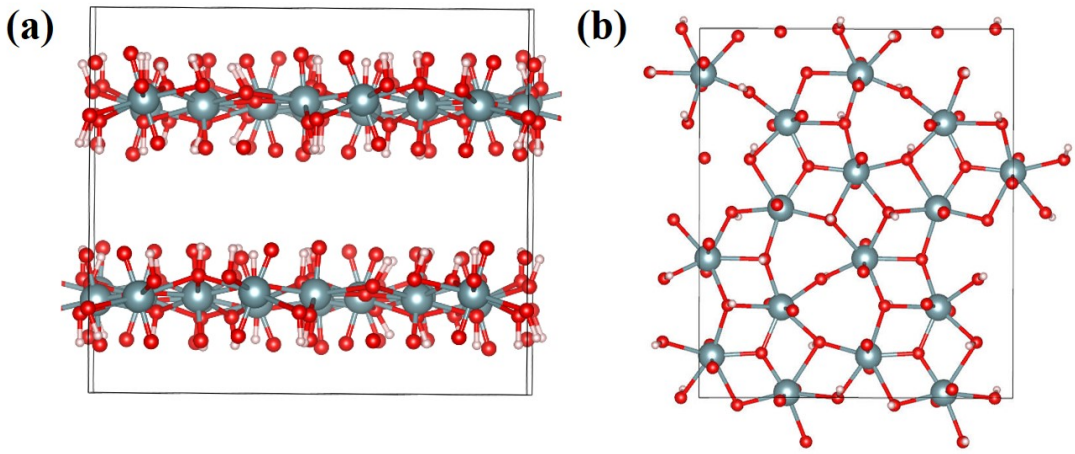

Figure 5.7 Crystallographic structure of schoephite (a) side view, (b) top view

Figure 5.8 shows the dissociation reaction of a pentanuclear cluster. The coordination numbers of one uranium atom of trinuclear uranyl and two proton dissociation oxygen atoms of mononuclear uranyl range from 2.0 to 0.1, respectively, and the dissociation free energy It is 26.4Kcal/mol. Figure 5.9 shows the dissociation reaction of a tetranuclear cluster with a dissociation free energy of 15.6 Kcal/mol. It can be seen that the free energy convergence of the two reaction pathways is better. On the dissociation curve of the pentanuclear cluster, it can be found that the free energy first increases then decreases, and then increases after CN=1.0. For tetranuclear clusters, the dissociation free energy continues to rise. Both precipitation mechanisms are energetically feasible, and pentanuclear clusters are more dominant than tetranuclear cluster reaction mechanisms.

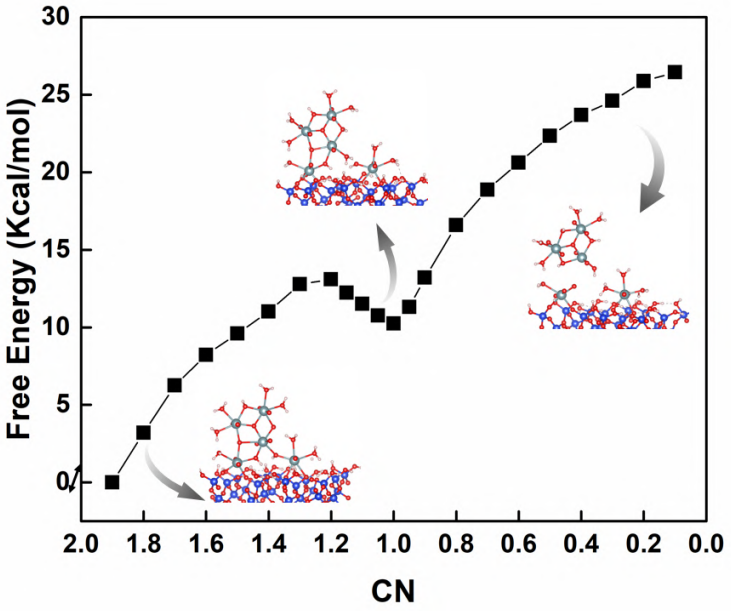

Figure 5.8 Dissociation free energy curves of uranyl oxyhydroxide pentanuclear cluster system.

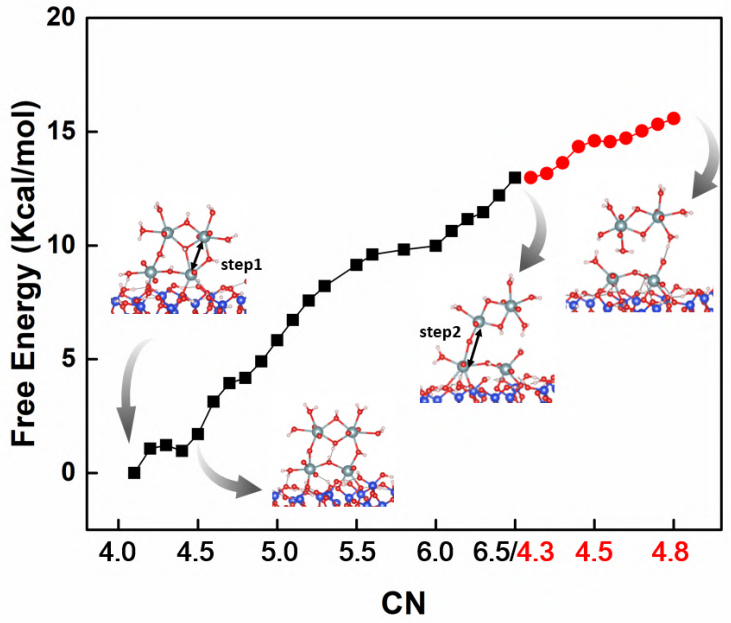

Figure 5.9 Dissociation free energy curves of uranyl oxyhydroxide tetranuclear cluster system.

Chapter 6. Acid−Base Properties of Cis-Vacant Montmorillonite Edge Surfaces: A Combined First-Principles Molecular Dynamics and Surface Complexation Modeling Approach

6.1 Introduction

High adsorption capacity of clay minerals plays a key role in nutrient cycling in soils and in retardation of heavy metals, oxyanions and organic pollutants migration in natural and engineered environments (Kome et al., 2019). In particular, clay materials are an essential part of most multi-barrier systems envisioned for nuclear waste storage under consideration worldwide. An accurate prediction of metal ion mobility in clay-rich environments is dependent upon the development of adsorption models. Surface complexation model (SCM) links surface speciation to adsorption process and has been applied to describe the adsorption behaviors of a wide range of metal ions (Bergaya et al., 2006; Sposito, 2008).

The representative structure of clay minerals consists of an edge-sharing octahedral sheet, connected to two corner-sharing tetrahedral sheets to form the 2:1 (i.e. TOT, Tetrahedron-Octahedral-Tetrahedral) layer type (Tournassat et al., 2015). Because of their layered structure, clay minerals exhibit two kinds of surfaces, basal and edge surfaces (Figure 6.1), with much contrasted adsorption properties: while basal surfaces interact with adsorbates mostly through electrostatic interaction, edge surfaces have amphoteric properties and can bind adsorbates through surface complexation (Liu et al., 2022). Ideally, the reactivity description of SCM adsorption sites should be rooted in the actual structural properties of surface sites.

A key for understanding interfacial properties of clay minerals edge surfaces is their acid-base reactivity. The acid-base chemistry of edge surfaces is complicated because of the very heterogeneous nature of surface sites in terms of chemistry and structural position. Potentiometric titration has been extensively carried out to study the acid-base reactivity of clay mineral (Tournassat et al., 2016). Among others, Baeyens and Bradbury and Duc et al. (Baeyens and Bradbury, 1997; Duc et al., 2005) established acid-base titration data sets of montmorillonite, and SCMs based on thermodynamic equilibrium equations were developed to simulate titration data, using fitted pKa for protons on edge surfaces. More recently, pKa values derived from ab initio calculations were made available and

Tournassat et al. pooled these newly available pKa values in a SCM to yield reasonable prediction of the titration data of montmorillonite edge surfaces (Tournassat et al., 2016). The representativeness of these pKa values is, however, questionable because of an additional structural peculiarity of clay mineral layers.

In a TOT layer, each octahedral site is surrounded by two OH groups and four O atoms, but not all octahedral sites have the same geometry regarding the positions of OH groups. Trans-octahedra have OH groups on opposite corners, while cis-octahedra have OH groups on adjacent corners. Consequently, a TOT layers may be either trans-vacant with pure trans-octahedra in the octahedral sheet or cis-vacant with half cis-octahedra and half trans-octahedra (Figure 6.1). Montmorillonite is a typical dioctahedral smectite that exhibits either cis- or trans-vacant structures, but cis-vacant structures are the most common in natural samples widely used in research studies, such as Wyoming montmorillonites available at the Source Clays Repository or Kunipia montmorillonite (Subramanian et al., 2020; Orucoglu et al., 2022). The cis-vacant structure of crystallographic planes was observed for Kunipia montmorillonite by using scanning transmission electron microscopy (STEM). Tournassat et al. pointed out that the theoretical estimates of intrinsic pKa values were carried out on the basis of a trans-vacant model, whereas experimental titration and adsorption data were obtained on montmorillonite samples with a cis-vacant structure (Tournassat et al., 2016). Because the structure of a clay mineral determines its intrinsic physical and chemical properties, the differences between cis- and trans-vacant configurations inevitably lead to different surface properties. Cis-vacant structures are not centrosymmetric (Figure 6.1), which indicates that the edges perpendicular to [010] and [$0\bar{1}0$], [110] and [$\bar{1}\bar{1}0$] crystallographic directions are different. In addition, different positions of structural OH groups and isomorphic substitutions lead to more complex edge surface groups. Whether these differences in structure cause different surface charging behaviors of montmorillonite had not been determined yet.

Heterovalent structural isomorphic substitutions of cations in cis-vacant TOT layers create a permanent negative layer charge (Stucki, 2013) (Figure 6.2). Iron occurs in clay minerals in both Fe(II) and Fe(III) oxidation states and it can participate in redox reactions and influence the surface properties of clay minerals as well as the adsorption process. Fe(II) and Fe(III) mainly exist in the octahedral sheet while minor quantities of Fe(III) can substitute for Si(IV) in the tetrahedral sheet.

Kéri et al. proposed that there is no preferential occupation of cis- or trans-octahedra by Fe(III) and Fe(III) in low Fe-bearing bulk montmorillonite, consistent with that of Mg(II) substitution in the octahedral sheet (Tsipursky and Drits, 1984; Drits et al., 2006; Kéri et al., 2017). Moreover, the common isomorphic substitutions in the tetrahedral sheet are Al(III) for Si(IV) tetrahedral. The influence of isomorphic substitutions on smectite properties has received extensive attention because it affects many physical-chemical properties, such as its ability to adsorb and exchange other ions (Liu et al., 2022). The substitution effect can also influence the clay density, porosity, and surface area, as well as its reactivity and stability (Bergaya et al., 2006). Therefore, a thorough understanding of the substitution effects involved is essential for elucidating the natural properties of clays.

Theoretical estimates of the intrinsic pKa values of edge surface sites have been based on bond-valence theories. However, the obtained pKa values were sensitive to model assumptions and did not reproduce the experimental titration data. First principles calculation provides a new research method for pKa estimation. In recent years, the first-principles molecular dynamics (FPMD) based vertical energy gap method has been proved a powerful tool to accurately calculate the intrinsic pKa values of mineral surfaces. Liu et al. have published a series of works about intrinsic pKa values of surfaces perpendicular to [010] and [110] for a trans-vacant TOT layer (Liu et al., 2013, 2014). The method has also been successfully applied to mineral surface OH groups including rutile, quartz, gibbsite and kaolinite (Sulpizi and Sprik, 2008; Tazi et al., 2012; Liu et al., 2014). However, to the best of our knowledge, the cis-vacant clay edge surface properties of montmorillonite have not been reported.

In this work, we calculated the pKa values of 2:1-type cis-vacant clay edge surfaces perpendicular to [010], [$0\bar{1}0$], [110] and [$\bar{1}\bar{1}0$] directions. The influence of Mg(II), Fe(II)/Fe(III) and Al(III) substituted substitution on acid-base properties was also investigated. The atomic-level acidity constants were then applied to construct a SCM for edge surfaces of a cis-vacant layer. By comparing our results with the previous pKa values and SCM models of trans-vacant layer edge surfaces, we elucidated the difference between cis- and trans-vacant clay edge surfaces acid-base properties. This study provides fundamental information for further multi-scale study of the interfacial processes of 2:1 type clay minerals, e.g., the adsorption of contaminants on clay minerals.

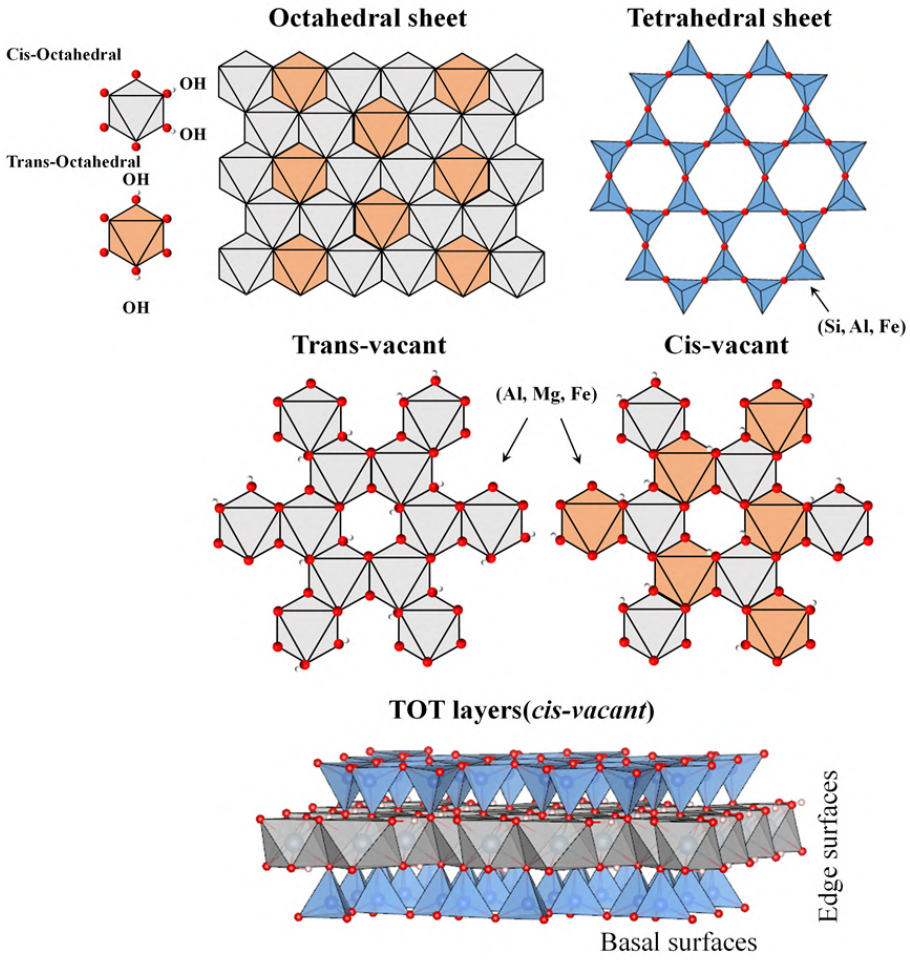

Figure 6.1 From top to bottom: Octahedral and tetrahedral sheets, Octahedral sheet with trans-vacant and cis-vacant configurations, TOT layers.

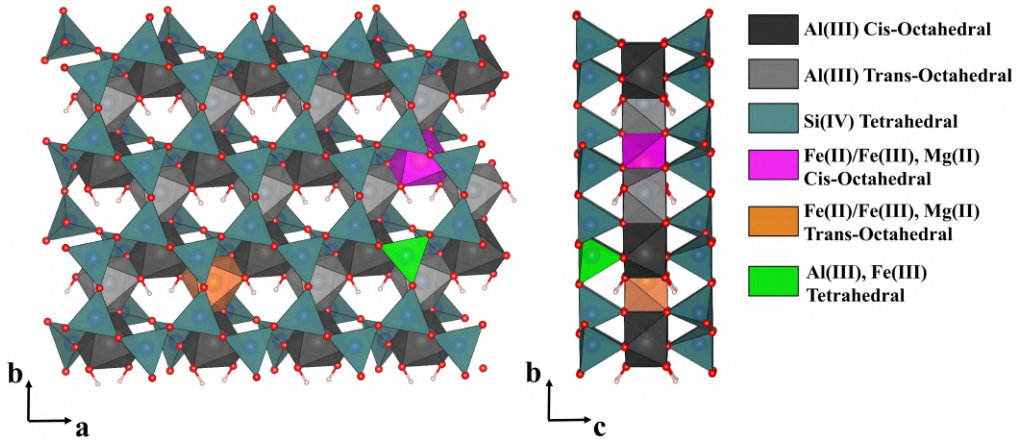

Figure 6.2 Views of the modeled cis-vacant TOT clay layer with substituted ions in the cis- and trans-sites of the octahedral sheet and in the tetrahedral sheet.

6.2 Methodology

6.2.1 Models

The optimized primitive unit cell parameters of cis-vacant 2:1 dioctahedral phyllosilicates are a = 5.22 Å, b = 9.04 Å, c =10.09 Å and α =89.82°, β = 99.55°, γ = 90.02°. The hydrated edge surface models including two unit cells were placed in 3D periodically repeated orthorhombic boxes (12.45 Å × 10.44 Å × 33.56Å) with a solution region of 20 Å. Edge surfaces perpendicular to [010], [0$\bar{1}$0], [110] and [$\bar{1}\bar{1}$0] crystallographic directions were modeled. The solution region contained 130 water molecules, approximately corresponding to the density of bulk water at ambient conditions.(Figure 6.3) Ten water molecules were inserted into the interlayer to create a monolayer hydrate (Figure 6.3 as an example). In the initial configuration, all surface O atoms were saturated with H atoms, and Al atoms were 6-fold coordinated (Figure 6.2).

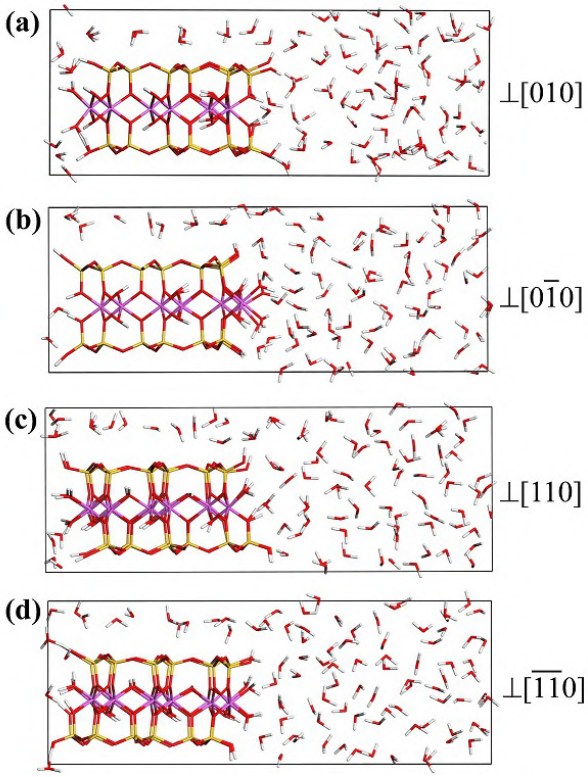

Figure 6.3 The edge surface model of non-substituted (No-sub) cis-vacant structure. (a) ⊥[010], (b) ⊥[0$\bar{1}$0], (c) ⊥[110], and (d) ⊥[$\bar{1}\bar{1}$0]. Color scheme: Si (yellow), Al (pink), O (red), H (white).

Octahedral Mg(II) substitution (Mg-sub), Octahedral Fe(II) substitution (Fe_{II}-sub), octahedral Fe(III) substitution (Fe_{III}-sub), and tetrahedral Al(III) substitution (Al-sub) on four edge surface

directions were all investigated (Figures 6.4-6.5). Surfaces perpendicular to [110] and [$\overline{1}\overline{1}0$] are beveled surfaces with different silanol groups, *i.e.* silanol on the upper tetrahedral sheet and the lower tetrahedral sheet. Also, we only considered the cases where Al(III) substitution occurs in the upper tetrahedral sheet on surfaces perpendicular to [110] and [$\overline{1}\overline{1}0$] directions (Figures 6.5g and 6.5h).

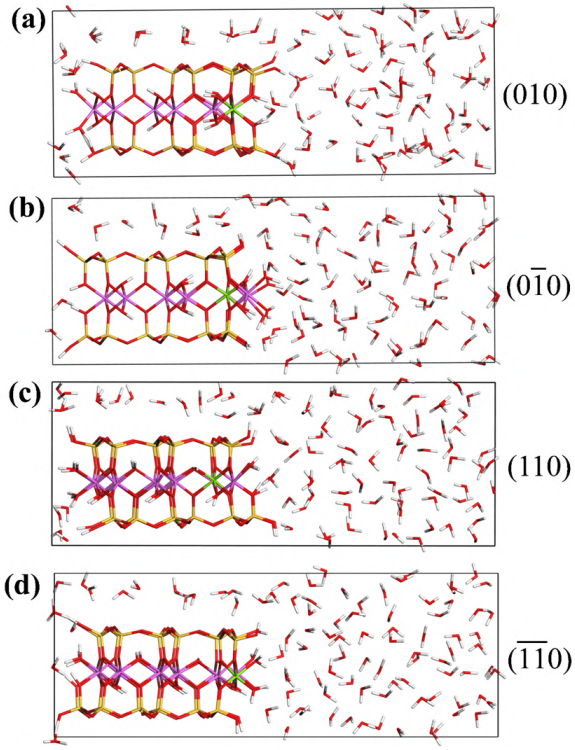

Figure 6.4 The edge surface model of Mg(II)-substituted (Mg-sub) cis-vacant structure. (a) ⊥[010], (b) ⊥[0$\overline{1}$0], (c) ⊥[110], and (d) ⊥[$\overline{1}\overline{1}$0]. Color scheme: Si (yellow), Al (pink), Mg (green), O (red), H (white).

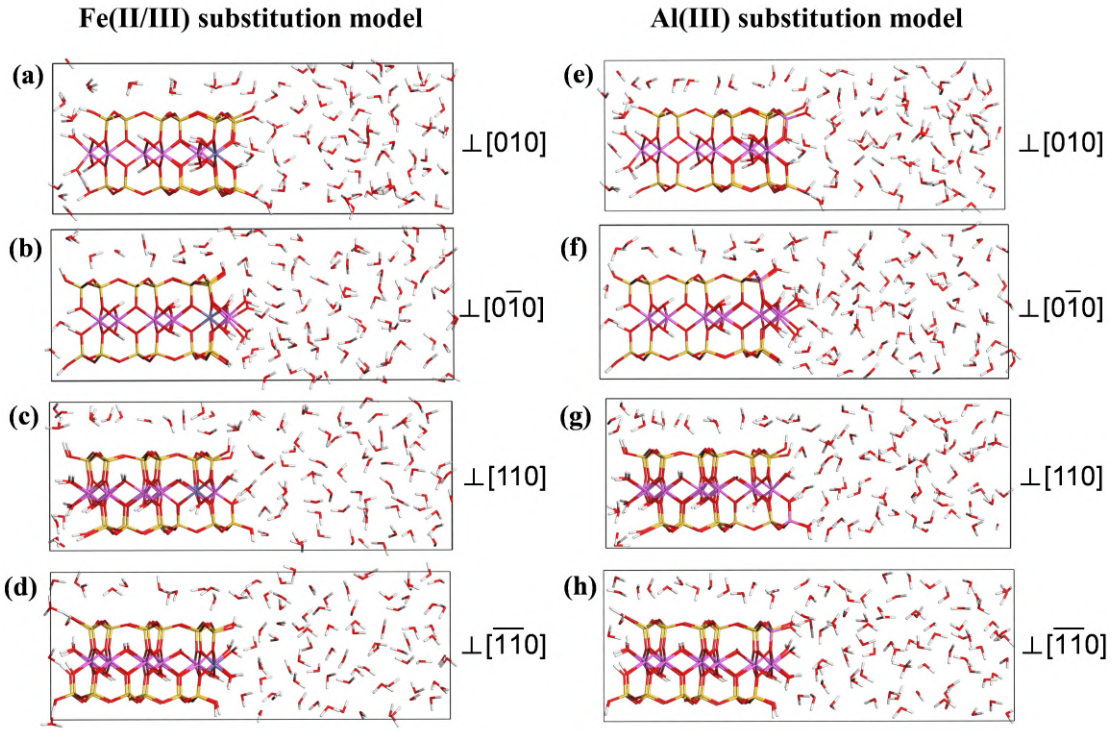

Figure 6.5 Edge surface models of Fe(II)/(III)-substituted ($Fe_{II/III}$-sub) and Al(III)-substituted (Al-sub) cis-vacant structure. (a) and (e) ⊥[010], (b) and (f) ⊥[0$\bar{1}$0], (c) and (g) ⊥[110], (d) and (h) ⊥[$\bar{1}\bar{1}$0]. Color scheme: Si (yellow), Al (pink), Fe (cyan), O (red), H (white).

6.2.2 First-Principles Molecular Dynamics

CP2K/Quickstep package based on mixed Gaussian Plane Wave (GPW) scheme was used to carry out all simulations. Perdew-Burke-Ernzerhof (PBE) functional was applied for exchange correlation effects and Goedecker-Teter-Hutter (GTH) pseudopotentials were used to represent the core electron state. The dispersion correction was applied in all calculations with the Grimme-D3 method. A double-ζ valence augmented with polarization (DZVP) basis set was employed for H, O, Fe, Mg, Al, Si, and the plane wave cutoff was set to be 400 Ry. Conventional DFT is known to underestimate the coulomb repulsion between the localized 3d-electrons of Fe. DFT+U method was applied to improve the description of these delocalized states within the DFT formalism. The simulations were performed with a multiplicity $(2S + 1)_{Fe(II)} = 5$ for systems with a ferrous iron and $(2S + 1)_{Fe(III)} = 6$ for systems with a ferric iron, respectively.

Born−Oppenheimer molecular dynamics (BOMD) simulations were carried out with a wave function optimization tolerance of 10^{-6}. Canonical ensemble (NVT) conditions were imposed using a Nóse-Hoover chain thermostat with a target temperature of 300 K. The MD time step was set to be

0.5 fs. For each system, we conducted an initial equilibration simulation of 3.0 ps, followed by a production period of 5.0~10.0 ps.

6.2.3 Acidity Constant Calculations

The intrinsic pK_a values of the edge surface sites were evaluated with the half-reaction scheme of the vertical energy gap method. In this method, the dissociating surface proton is gradually transformed into a dummy atom and the free energy is calculated using the thermodynamic integration relation.

Edge surface sites investigated were ≡Al/Mg$(OH_2)_2$, ≡Al/Mg(OH_2)OH, ≡Si(OH), ≡Al(OH_2), ≡Si$(OH)_2$Al/Mg, ≡SiO(OH)Al/Mg, and ≡Al/Si/Mg(OH)Al for surfaces perpendicular to [010], [$0\bar{1}0$], [110] and [$\bar{1}\bar{1}0$]. The slashes represent the different octahedral or tetrahedral connection sites. Dangling O atoms at the surface sites usually require two H atoms to saturate. The surface amphoteric sites of the Mg/Fe_{II}/Fe_{III}-sub model include ≡Si(OH), ≡Al(OH_2), ≡Al$(OH_2)_2$, ≡Al(OH)(OH_2), ≡Mg$(OH_2)_2$, ≡Mg(OH_2)OH, ≡Si$(OH)_2$Mg, ≡SiO(OH)Mg ≡Mg(OH)Al, ≡$Fe_{II/III}(OH_2)_2$, ≡$Fe_{II/III}$(OH)(OH_2), ≡Si$(OH)_2Fe_{II/III}$, ≡Si(O)(OH)$Fe_{II/III}$ and ≡Si/$Fe_{II/III}$(OH)Al sites, while Al-sub model include ≡Si(OH), ≡$Al^T(OH_2)$, ≡Al^T(OH), ≡$Al^T(OH)_2$Al, ≡Al^T(O)(OH)Al, ≡Al$(OH_2)_2$, ≡Al(OH)(OH_2), ≡Al(OH_2) and ≡Al^T(OH)Al sites.Doubly protonated silanol sites ≡Si(OH_2) do not exist in the normal pH range and do not contribute to the acid-base chemistry, and thus was not considered. For some sites, e.g., ≡Si$(OH)_2$Al on surface perpendicular to [010], one proton dissociated spontaneously within a few picoseconds in free simulations. Therefore, the O-H bonds were restrained in pKa calculations of these sites (Tables 6.1 -6.5). For some sites, e.g. ≡ Al/Mg(OH)Al and ≡Mg$(OH_2)_2$, the deprotonated forms would capture one proton from water molecule. For the calculations of these sites, all OH bonds of water molecules were restrained at 1.89 Bohr to prevent this from happening in the simulation.

Table 6.1 The parameters used in harmonic potentials restraining the dummy protons of the No-sub model. H_d means the dummy proton. Equilibrium bond lengths (d_0) are in bohr and equilibrium angles (α_0) are in radians. All the coupling constants are in a.u.

Models	Sites	n_d	d_0	k_d	n_α	α_0	k_α

⊥[010]	≡SiOH	1	1.89	0.1	1	2.02 (Si-O-Hd)	0.1
	≡$Si(OH)_2Al$	2	1.89 1.89	0.1	2	1.93 (Si-O-Hd) 2.03 (Al-O-Hd)	0.1
	≡Si(O)(OH)Al	1	1.89	0.1	2	1.93 (Si-O-Hd) 2.03 (Al-O-Hd)	0.1
⊥[0$\bar{1}$0]	≡SiOH	1	1.90	0.1	1	2.01 (Si-O-Hd)	0.1
	≡$Al(OH_2)_2$	1	1.89	0.1	2	1.86 (H-O-Hd) 2.12 (Al-O-Hd)	0.1
	≡$Al(OH)(OH_2)$	1	1.89	0.1	2	1.86 (H-O-Hd) 2.16 (Al-O-Hd)	0.1
	≡Al(OH)Al	1	1.92	0.1	2	2.23 (Al-O-Hd) 2.11 (Al-O-Hd)	0.1
⊥[110]	≡$SiOH^U$	1	1.89	0.1	1	2.01 (Si-O-Hd)	0.1
	≡$SiOH^L$	1	1.89	0.1	1	2.01 (Si-O-Hd)	0.1
	≡Si(OH)Al	1	1.89	0.1	2	2.20 (Si-O-Hd) 2.10 (Al-O-Hd)	0.1
	≡$Al(OH_2)$	1	1.93	0.1	2	1.83 (H-O-Hd) 2.15 (Al-O-Hd)	0.1
⊥[$\bar{1}\bar{1}$0]	≡$SiOH^U$	1	1.89	0.1	1	1.99 (Si-O-Hd)	0.1
	≡$SiOH^L$	1	1.86	0.1	1	1.98 (Si-O-Hd)	0.1
	≡$Al(OH_2)_2$	1	1.89	0.1	2	1.83 (H-O-Hd) 2.10 (Al-O-Hd)	0.1
	≡Al(OH)Al	1	1.89	0.1	2	2.20 (Al-O-Hd) 2.10 (Al-O-Hd)	0.1
	H_3O^+	3	1.89	1.0	3	1.94 (H-O-Hd) 1.94 (H-O-Hd) 1.94 (H-O-H)	0.1

Table 6.2 The parameters used in harmonic potentials restraining the dummy protons of the Mg-sub model. H_d means the dummy proton. Equilibrium bond lengths (d_0) are in bohr and equilibrium angles (α_0) are in radians. All the coupling constants are in a.u.

Models	Sites	n_d	d_0	k_d	n_α	α_0	k_α

⊥[010]	≡SiOH	1	1.91	0.1	1	1.92 (Si-O-Hd)	0.1
	≡$Si(OH)_2Mg$	2	1.92 1.92	0.1	2	1.99 (Si-O-Hd) 2.27 (Mg-O-Hd)	0.1
	≡Si(O)(OH)Mg	1	1.89	0.1	2	1.93 (Si-O-Hd) 2.03 (Mg-O-Hd)	0.1
⊥[0$\bar{1}$0]	≡SiOH	1	1.89	0.1	1	2.02 (Si-O-Hd)	0.1
	≡$Al(OH_2)_2$	1	1.89	0.1	2	1.86 (H-O-Hd) 2.12 (Al-O-Hd)	0.1
	≡Al(OH)(OH_2)	1	1.89	0.1	2	1.83 (H-O-Hd) 2.18 (Al-O-Hd)	0.1
	≡Mg(OH)Al	1	1.92	0.1	2	2.25 (Al-O-Hd) 2.07 (Mg-O-Hd)	0.1
⊥[110]	≡$SiOH^U$	1	1.89	0.1	1	2.01 (Si-O-Hd)	0.1
	≡$SiOH^L$	1	1.89	0.1	1	2.01 (Si-O-Hd)	0.1
	≡Si(OH)Al	1	1.89	0.1	2	2.20 (Si-O-Hd) 2.10 (Al-O-Hd)	0.1
	≡$Al(OH_2)$	1	1.93	0.1	2	1.83 (H-O-Hd) 2.15 (Al-O-Hd)	0.1
⊥[$\bar{1}\bar{1}$0]	≡$SiOH^U$	1	1.89	0.1	1	1.99 (Si-O-Hd)	0.1
	≡$SiOH^L$	1	1.98	0.1	1	2.12 (Si-O-Hd)	0.1
	≡$Mg(OH_2)_2$	1	1.89	0.1	2	1.80 (H-O-Hd) 2.10 (Mg-O-Hd)	0.1
	≡Mg(OH)Al	1	1.87	0.1	2	2.20 (Al-O-Hd) 2.10 (Mg-O-Hd)	0.1
	H_3O^+	3	1.89	1.0	3	1.94 (H-O-Hd) 1.94 (H-O-Hd) 1.94 (H-O-H)	0.1

Table 6.3 The parameters used in harmonic potentials restraining the dummy protons of the Fe_{II}-sub model. H_d means the dummy proton. Equilibrium bond lengths (d_0) are in bohr and equilibrium angles (α_0) are in radians. All the coupling constants are in a.u.

Surface	Acids	n_d	d_0	k_d	n_α	α_0	k_α

⊥[010]	≡SiOH	1	1.89	0.1	1	1.94 (Si-O-Hd)	0.1
	≡$Si(OH)_2Fe$	1	1.92	0.1	2	1.88 (Si-O-Hd) 1.93 (Fe-O-Hd)	0.1
	≡Si(O)(OH)Fe	1	1.93	0.1	2	1.88 (Si-O-Hd) 1.93 (Fe-O-Hd)	0.1
⊥[0$\bar{1}$0]	≡SiOH	1	1.89	0.1	1	2.02 (Si-O-Hd)	0.1
	≡$Al(OH_2)_2$	1	1.90	0.1	2	2.02 (H-O-Hd) 2.06 (Al-O-Hd)	0.1
	≡Fe(OH)Al	1	1.93	0.1	2	2.20 (Al-O-Hd) 1.98 (Fe-O-Hd)	0.1
⊥[110]	≡$SiOH^U$	1	1.89	0.1	1	1.96 (Si-O-Hd)	0.1
	≡$SiOH^L$	1	1.89	0.1	1	2.01 (Si-O-Hd)	0.1
	≡Si(OH)Al	1	1.89	0.1	2	2.20 (Si-O-Hd) 2.10 (Al-O-Hd)	0.1
	≡$Al(OH_2)$	1	1.83	0.1	2	1.89 (H-O-Hd) 2.02 (Al-O-Hd)	0.1
⊥[$\bar{1}\bar{1}$0]	≡$SiOH^U$	1	1.89	0.1	1	2.04 (Si-O-Hd)	0.1
	≡$SiOH^L$	1	1.92	0.1	1	2.09 (Si-O-Hd)	0.1
	≡$Fe(OH_2)_2$	1	1.89	0.1	2	1.89 (H-O-Hd) 2.13 (Fe-O-Hd)	0.1
	≡Fe(OH)Al	1	1.87	0.1	2	2.25 (Al-O-Hd) 1.94 (Fe-O-Hd)	0.1
	H_3O^+	3	1.89	1.0	3	1.94 (H-O-Hd) 1.94 (H-O-Hd) 1.94 (H-O-H)	0.1

Table 6.4 The parameters used in harmonic potentials restraining the dummy protons of the Fe_{III}-sub model. H_d means the dummy proton. Equilibrium bond lengths (d_0) are in bohr and equilibrium angles (α_0) are in radians. All the coupling constants are in a.u.

Surface	Acids	n_d	d_0	k_d	n_α	α_0	k_α
⊥[010]	≡SiOH	1	1.89	0.1	1	1.94 (Si-O-Hd)	0.1

	≡$Si(OH)_2Fe$	2	1.92 1.92	0.1	2	1.88 (Si-O-Hd) 1.93 (Fe-O-Hd)	0.1
	≡Si(O)(OH)Fe	1	1.92	0.1	2	1.88 (Si-O-Hd) 1.93 (Fe-O-Hd)	0.1
⊥[$0\bar{1}0$]	≡SiOH	1	1.89	0.1	1	2.02 (Si-O-Hd)	0.1
	≡$Al(OH_2)_2$	2	1.88 1.88	0.1	2	1.88 (H-O-Hd) 2.05 (Al-O-Hd)	0.1
	≡$Al(OH)(OH_2)$	1	1.88	0.1	2	1.95 (H-O-Hd) 2.16 (Al-O-Hd)	0.1
	≡Fe(OH)Al	1	1.93	0.1	2	2.20 (Al-O-Hd) 1.98 (Fe-O-Hd)	0.1
⊥[110]	≡$SiOH^U$	1	1.89	0.1	1	1.96 (Si-O-Hd)	0.1
	≡$SiOH^L$	1	1.89	0.1	1	2.01 (Si-O-Hd)	0.1
	≡Si(OH)Al	1	1.89	0.1	2	2.20 (Si-O-Hd) 2.10 (Al-O-Hd)	0.1
	≡$Al(OH_2)$	1	1.83	0.1	2	1.89 (H-O-Hd) 2.05 (Al-O-Hd)	0.1
⊥[$\overline{1}\overline{1}0$]	≡$SiOH^U$	1	1.89	0.1	1	2.04 (Si-O-Hd)	0.1
	≡$SiOH^L$	1	1.92	0.1	1	2.09 (Si-O-Hd)	0.1
	≡$Fe(OH_2)_2$	1	1.89	0.1	2	1.89 (H-O-Hd) 2.10 (Fe-O-Hd)	0.1
	≡$Fe(OH)(OH_2)$	1	1.89	0.1	2	1.89 (H-O-Hd) 2.13 (Fe-O-Hd)	0.1
	≡Fe(OH)Al	1	1.87	0.1	2	2.28 (Al-O-Hd) 1.94 (Fe-O-Hd)	0.1
	H_3O^+	3	1.89	1.0	3	1.94 (H-O-Hd) 1.94 (H-O-Hd) 1.94 (H-O-H)	0.1

Table 6.5 The parameters used in harmonic potentials restraining the dummy protons of the Al-sub model. H_d means the dummy proton. Equilibrium bond lengths (d_0) are in bohr and equilibrium angles (α_0) are in radians. All the coupling constants are in a.u.

Surface	Acids	n_d	d_0	k_d	n_α	α_0	k_α

⊥[010]	≡$Al^{T}(OH_2)$	1	1.88	0.1	2	1.91 (H-O-Hd) 2.11 (Al^{T}-O-Hd)	0.1
	≡$Al^{T}(OH)$	1	1.88	0.1	1	2.03 (Al^{T}-O-Hd)	0.1
	≡$Al^{T}(OH)_2Al$	1	1.82	0.1	2	1.80 (Al^{T}-O-Hd) 2.07 (Al-O-Hd)	0.1
	≡$Al^{T}(O)(OH)Al$	1	1.82	0.1	2	1.80 (Al^{T}-O-Hd) 2.07 (Al-O-Hd)	0.1
⊥[0$\bar{1}$0]	≡$Al^{T}(OH_2)_2$	1	1.89	0.1	2	1.88 (H-O-Hd) 2.13 (Al^{T}-O-Hd)	0.1
	≡$Al^{T}(OH)$	1	1.89	0.1	1	2.02 (Al^{T}-O-Hd)	0.1
	≡$Al(OH_2)_2$	1	1.89	0.1	2	2.01 (H-O-Hd) 2.21 (Al-O-Hd)	0.1
	≡$Al(OH)(OH_2)$	1	1.89	0.1	2	1.95 (H-O-Hd) 2.01 (Al-O-Hd)	0.1
⊥[110]	≡$Al^{T}(OH_2)_2$	1	1.86	0.1	2	1.86 (H-O-Hd) 2.12 (Al^{T}-O-Hd)	0.1
	≡$Al^{T}(OH)$	1	1.86	0.1	1	2.02 (Al^{T}-O-Hd)	0.1
	≡$Al^{T}(OH)Al$	1	1.88	0.1	2	2.01 (Al^{T}-O-Hd) 1.92 (Al-O-Hd)	0.1
	≡$Al(OH_2)$	1	1.87	0.1	2	1.82 (H-O-Hd) 2.12 (Al-O-Hd)	0.1
⊥[$\bar{1}\bar{1}$0]	≡$Al^{T}(OH_2)_2$	1	1.89	0.1	2	1.81 (H-O-Hd) 2.03 (Al^{T}-O-Hd)	0.1
	≡$Al^{T}(OH)$	1	1.89	0.1	1	2.01 (Al^{T}-O-Hd)	0.1
	≡$Al(OH_2)_2$	1	1.92	0.1	2	1.91 (H-O-Hd) 2.19 (Al-O-Hd)	0.1
	≡$Al(OH)(OH_2)$	1	1.92	0.1	2	1.91 (H-O-Hd) 2.19 (Al-O-Hd)	0.1
	H_3O^+	3	1.89	1.0	3	1.94 (H-O-Hd) 1.94 (H-O-Hd) 1.94 (H-O-H)	0.1

6.2.4 Surface Complexation Modeling

An in-house version of PHREEQC which considers the spillover of electrostatic potential from basal surfaces was used to calculate the protonation state of clay layer edge surfaces.

6.3 Results and Discussion

6.3.1 FPMD Simulations

6.3.1.1 Surface Structures of Cis-Vacant Model

Compared with the trans-vacant model, the surface perpendicular to [010] of cis-vacant model has a special structure with symmetrical vacancy surrounded by ≡$Si(OH)_2Al/Mg$ and ≡Si(OH) (Figure 6.3a). Vacancy usually serves as adsorption site for heavy metals. Similar to trans-vacant edge perpendicular to [010] direction, [$0\bar{1}0$] direction has ≡$Al(OH_2)_2$ and ≡Si(OH) (Figure 6.3b). Both surfaces perpendicular to [110] and [$\overline{1}\overline{1}0$] on cis-vacant model are inclined edges which are the similar as trans-vacant edge perpendicular to [110]. Such beveled surfaces have different silanol groups, i.e., ≡$Si(OH)^U$ (silanol on upper T-sheet) and ≡$Si(OH)^L$ (silanol on lower T-sheet). For edge perpendicular to [$\overline{1}\overline{1}0$], there are ≡$Al(OH_2)_2$ and ≡Al(OH)Al sites (Figure 6.3c). In addition, edge perpendicular to [110] has the same type of surface sites (i.e. ≡$Al(OH_2)$ and ≡ Si(OH)Al) (Figure 6.3d) as the trans-vacant edge perpendicular to [110]. In the case of Mg^{2+} substitution, ≡$Si(OH)_2Mg$ and ≡$Mg(OH_2)_2$ appeared on surfaces perpendicular to [010] and [$\overline{1}\overline{1}\,0$], while the surface sites on surfaces perpendicular to [$0\bar{1}0$] and [110] are the same to No-sub model because the cis-octahedron substituted by Mg^{2+} is inside the bulk phase (Figure 6.4).

The energy gaps and deprotonation-free energies were listed in Tables 6.6-6.10. The calculated vertical energy gaps were well converged within 0.08 eV and the statistical errors for pKa were smaller than 1.6 pKa units for all surface groups. The uncertainties of the pKa value were evaluated with the semi-difference method. Similar to the Mg(II)-substituted model in our previous report, the surface sites of the Fe_{II}/Fe_{III}-sub model on surfaces perpendicular to [$0\bar{1}0$] and [110] are identical to the non-substituted model because the substituted cis-octahedron is inside the bulk phase,(Figures 6.5b and 6.5c) while the surface sites on surfaces perpendicular to [010] and [$\overline{1}\overline{1}0$] are altered (e.g., ≡$Fe_{II/III}(OH_2)_2$ and ≡$Si(OH)_2Fe_{II/III}$ sites).(Figures 6.5a and 6.5d) In the Al-sub model, there is an additional specific site of ≡$Al^T(OH_2)$ compared to the non-substituted model. Because the influence of isomorphic substitution on surface pKa values is usually limited in one unit cell, the properties of the opposite ≡Si(OH) group were not calculated in the Al-sub model.

Table 6.6 Free energies (in eV) and pKa values of surface groups of the No-sub model.

Models	Sites	η = 1.0	η = 0.5	η = 0.0	Δ_{dp}A/eV	pKas
⊥[010]	≡SiOH	13.62 ± 0.03	17.21 ± 0.05	20.47 ± 0.06	17.16 ± 0.05	6.8 ± 1.4
	≡Si(OH)$_2$Al	14.56 ± 0.08	16.65 ± 0.06	19.05 ± 0.05	16.70 ± 0.06	-0.8 ± 1.6
	≡Si(O)(OH)Al	13.92 ± 0.06	17.26 ± 0.05	19.65 ± 0.01	17.10 ± 0.05	5.9 ± 1.3
	H_3O^+	12.82 ± 0.02	16.76 ± 0.04	19.51 ± 0.02	16.56 ± 0.03	—
⊥[0$\bar{1}$0]	≡SiOH	14.49 ± 0.05	17.59 ± 0.04	20.51 ± 0.04	17.56 ± 0.04	8.1 ± 1.2
	≡Al(OH$_2$)$_2$	12.50 ± 0.08	17.95 ± 0.05	20.21 ± 0.06	17.42 ± 0.06	5.7 ± 1.4
	≡Al(OH)(OH$_2$)	13.65 ± 0.03	18.01 ± 0.05	20.27 ± 0.04	17.66 ± 0.05	9.8 ± 1.2
	≡Al(OH)Al	12.67 ± 0.04	18.48 ± 0.06	20.61 ± 0.04	17.87 ± 0.05	13.2 ± 1.4
	H_3O^+	12.64 ± 0.02	17.26 ± 0.03	19.67 ± 0.03	16.89 ± 0.03	—
⊥[110]	≡SiOH^U	14.13 ± 0.03	17.78 ± 0.07	20.30 ± 0.05	17.59 ± 0.06	6.3 ± 1.5
	≡SiOH^L	14.28 ± 0.03	17.81 ± 0.05	20.22 ± 0.02	17.62 ± 0.04	6.8 ± 1.2
	≡Si(OH)Al	13.15 ± 0.04	16.59 ± 0.04	19.64 ± 0.03	16.53 ± 0.04	-11.7 ± 1.1
	≡Al(OH$_2$)	13.63 ± 0.06	17.98 ± 0.06	19.78 ± 0.04	17.56 ± 0.09	5.6 ± 1.4
	H_3O^+	13.10 ± 0.03	17.29 ± 0.03	19.91 ± 0.02	17.03 ± 0.03	—
⊥[$\bar{1}\bar{1}$0]	≡SiOH^U	13.95 ± 0.04	17.49 ± 0.06	19.64 ± 0.03	17.26 ± 0.05	7.4 ± 1.4
	≡SiOH^L	13.55 ± 0.03	17.51 ± 0.05	20.21 ± 0.02	17.30 ± 0.04	8.1 ± 1.2
	≡Al(OH$_2$)$_2$	13.06 ± 0.04	17.58 ± 0.08	20.03 ± 0.02	17.24 ± 0.06	7.0 ± 1.6
	≡Al(OH)Al	12.64 ± 0.07	18.52 ± 0.04	20.49 ± 0.03	17.87 ± 0.04	17.6 ± 1.3
	H_3O^+	12.28 ± 0.04	16.97 ± 0.03	19.60 ± 0.03	16.63 ± 0.03	—

Table 6.7 Free energies (in eV) and pKa values of surface groups of the Mg-sub model.

Models	Sites	η = 1.0	η = 0.5	η = 0.0	Δ_{dp}A/eV	pKas
⊥[010]	≡SiOH	13.99 ± 0.05	18.23 ± 0.03	19.15 ± 0.03	17.68 ± 0.03	9.0 ± 1.0
	≡Si(OH)$_2$Mg	13.57 ± 0.04	18.03 ± 0.06	19.03 ± 0.04	17.45 ± 0.05	5.3 ± 1.3
	≡Si(O)(OH)Mg	13.48 ± 0.02	18.37 ± 0.04	19.02 ± 0.05	17.66 ± 0.04	8.8 ± 1.0

	H_3O^+	13.34 ± 0.03	17.12 ± 0.02	19.87 ± 0.02	16.95 ± 0.02	—
$\perp[0\bar{1}0]$	≡SiOH	13.89 ± 0.04	17.81 ± 0.05	20.24 ± 0.05	17.56 ± 0.05	11.0 ± 1.2
	≡Al(OH$_2$)$_2$	12.51 ± 0.03	17.69 ± 0.02	20.31 ± 0.04	17.26 ± 0.03	5.9 ± 0.9
	≡Al(OH)(OH$_2$)	12.48 ± 0.02	18.03 ± 0.03	20.47 ± 0.02	17.51 ± 0.03	10.1 ± 0.8
	≡Mg(OH)Al	12.89 ± 0.06	18.19 ± 0.03	21.73 ± 0.03	17.90 ± 0.04	16.6 ± 1.0
	H_3O^+	12.83 ± 0.03	16.99 ± 0.02	19.52 ± 0.03	16.72 ± 0.02	—
$\perp[110]$	≡SiOH^U	12.94 ± 0.07	17.79 ± 0.04	20.36 ± 0.02	17.41 ± 0.04	9.1 ± 1.1
	≡SiOH^L	13.21 ± 0.04	17.82 ± 0.05	20.44 ± 0.03	17.49 ± 0.05	10.4 ± 1.2
	≡Si(OH)Al	12.87 ± 0.03	16.58 ± 0.02	19.49 ± 0.03	16.45 ± 0.02	-7.1 ± 0.8
	≡Al(OH$_2$)	13.57 ± 0.03	17.62 ± 0.01	20.19 ± 0.02	17.37 ± 0.02	8.5 ± 0.7
	H_3O^+	13.21 ± 0.01	16.87 ± 0.03	19.41 ± 0.02	16.68 ± 0.03	—
$\perp[\bar{1}\bar{1}0]$	≡SiOH^U	12.82 ± 0.05	17.93 ± 0.06	20.08 ± 0.04	17.44 ± 0.06	8.9 ± 1.4
	≡SiOH^L	12.87 ± 0.04	17.88 ± 0.04	20.35 ± 0.03	17.46 ± 0.04	9.2 ± 1.1
	≡Mg(OH$_2$)$_2$	12.81 ± 0.04	18.31 ± 0.03	20.81 ± 0.04	17.81 ± 0.03	15.1 ± 1.0
	≡Mg(OH)Al	13.22 ± 0.02	18.56 ± 0.03	20.66 ± 0.03	18.02 ± 0.03	18.7 ± 0.9
	H_3O^+	13.52 ± 0.02	16.85 ± 0.03	19.42 ± 0.02	16.72 ± 0.03	—

Table 6.8 Free energies (in eV) and pKa values of surface groups of the Fe_{II}-sub model.

Models	Sites	η = 1.0	η = 0.5	η = 0.0	Δ_{dp}A/eV	pKas
$\perp[010]$	≡SiOH	12.86 ± 0.03	18.31 ± 0.03	20.25 ± 0.05	17.73 ± 0.03	12.2 ± 1.0
	≡Si(OH)$_2$Fe	14.31 ± 0.05	17.96 ± 0.04	20.57 ± 0.03	17.79 ± 0.04	13.2 ± 1.1
	≡Si(O)(OH)Fe	13.69 ± 0.03	18.52 ± 0.02	20.38 ± 0.03	18.03 ± 0.02	17.2 ± 0.8
	H_3O^+	13.04 ± 0.03	17.18 ± 0.02	19.08 ± 0.04	16.81 ± 0.03	—
$\perp[0\bar{1}0]$	≡SiOH	14.42 ± 0.05	17.95 ± 0.04	20.00 ± 0.04	17.70 ± 0.04	13.5 ± 1.1
	≡Al(OH$_2$)$_2$	13.46 ± 0.08	17.91 ± 0.05	19.93 ± 0.05	17.51 ± 0.03	10.2 ± 0.9
	≡Fe(OH)Al	14.14 ± 0.04	18.39 ± 0.06	20.88 ± 0.03	18.10 ± 0.03	20.1 ± 1.2
	H_3O^+	13.45 ± 0.03	16.83 ± 0.02	19.50 ± 0.02	16.71 ± 0.02	—
$\perp[110]$	≡SiOH^U	13.94 ± 0.04	18.25 ± 0.03	20.06 ± 0.02	17.83 ± 0.03	13.8 ± 0.9

	≡SiOH^{L}	13.65 ± 0.06	18.23 ± 0.04	20.03 ± 0.05	17.77 ± 0.05	12.7 ± 1.2
	≡Si(OH)Al	13.38 ± 0.03	16.78 ± 0.05	18.83 ± 0.02	16.56 ± 0.04	-7.7 ± 1.1
	≡Al(OH_2)	14.40 ± 0.02	17.88 ± 0.01	19.94 ± 0.02	17.64 ± 0.01	10.7 ± 0.6
	H_3O^+	12.34 ± 0.04	17.21 ± 0.02	19.76 ± 0.02	16.82 ± 0.02	—
	≡SiOH^{U}	14.26 ± 0.04	18.25 ± 0.03	20.10 ± 0.03	17.89 ± 0.03	12.3 ± 1.0
	≡SiOH^{L}	13.75 ± 0.03	18.32 ± 0.08	20.00 ± 0.02	17.84 ± 0.06	11.4 ± 1.5
$\perp[\overline{1}10]$	≡Fe(OH_2)$_2$	13.48 ± 0.03	18.25 ± 0.06	20.36 ± 0.02	17.81 ± 0.05	10.9 ± 1.3
	≡Fe(OH)Al	15.61 ± 0.05	18.36 ± 0.02	20.98 ± 0.01	18.34 ± 0.02	19.8 ± 0.9
	H_3O^+	12.55 ± 0.02	17.46 ± 0.03	19.40 ± 0.03	16.97 ± 0.03	—

Table 6.9 Free energies (in eV) and pKa values of surface groups of the Fe_{III}-sub model.

Models	Sites	η = 1.0	η = 0.5	η = 0.0	Δ_{dp}A/eV	pKas
	≡SiOH	14.23 ± 0.01	17.97 ± 0.03	19.50 ± 0.01	17.60 ± 0.02	8.8 ± 0.6
	≡Si(OH)$_2$Fe	14.15 ± 0.03	17.28 ± 0.03	19.05 ± 0.02	17.05 ± 0.03	-0.4 ± 0.7
$\perp[010]$	≡Si(O)(OH)Fe	14.95 ± 0.02	17.48 ± 0.01	19.63 ± 0.03	17.42 ± 0.02	5.7 ± 0.5
	H_3O^+	12.81 ± 0.02	17.42 ± 0.01	18.84 ± 0.02	16.89 ± 0.02	—
	≡SiOH	14.12 ± 0.02	17.79 ± 0.02	19.64 ± 0.04	17.49 ± 0.02	9.0 ± 0.7
	≡Al(OH_2)$_2$	13.05 ± 0.01	17.29 ± 0.03	19.45 ± 0.03	16.94 ± 0.03	-0.1 ± 0.8
$\perp[0\overline{1}0]$	≡Al(OH)(OH_2)	13.06 ± 0.03	17.78 ± 0.01	19.71 ± 0.02	17.32 ± 0.02	6.1 ± 0.6
	≡Fe(OH)Al	13.71 ± 0.01	17.90 ± 0.03	19.55 ± 0.04	17.48 ± 0.03	8.9 ± 0.8
	H_3O^+	12.27 ± 0.02	17.32 ± 0.02	18.99 ± 0.01	16.76 ± 0.02	—
	≡SiOH^{U}	14.22 ± 0.01	18.31 ± 0.02	19.77 ± 0.03	17.87 ± 0.02	8.4 ± 0.7
	≡SiOH^{L}	14.17 ± 0.03	18.29 ± 0.04	19.42 ± 0.05	17.79 ± 0.04	7.1 ± 1.0
$\perp[110]$	≡Si(OH)Al	13.35 ± 0.02	16.80 ± 0.07	18.47 ± 0.02	16.50 ± 0.05	-14.6 ± 1.2
	≡Al(OH_2)	14.83 ± 0.04	17.81 ± 0.02	19.12 ± 0.02	17.53 ± 0.02	2.7 ± 0.7
	H_3O^+	13.26 ± 0.01	17.69 ± 0.02	19.04 ± 0.03	17.18 ± 0.02	—
	≡SiOH^{U}	14.31 ± 0.02	17.95 ± 0.06	20.08 ± 0.03	17.70 ± 0.05	7.9 ± 1.3
$\perp[\overline{1}10]$	≡SiOH^{L}	13.85 ± 0.03	18.08 ± 0.03	20.09 ± 0.01	17.71 ± 0.03	8.1 ± 0.9

	≡Fe(OH$_2$)$_2$	14.61 ± 0.07	16.82 ± 0.01	18.76 ± 0.06	16.78 ± 0.03	-7.7 ± 0.9
	≡Fe(OH)(OH$_2$)	13.53 ± 0.03	17.51 ± 0.08	20.30 ± 0.04	17.37 ± 0.07	2.3 ± 1.5
	≡Fe(OH)Al	13.69 ± 0.01	18.20 ± 0.01	19.74 ± 0.03	17.71 ± 0.01	8.0 ± 0.7
	H_3O^+	12.80 ± 0.03	17.66 ± 0.03	18.77 ± 0.01	17.04 ± 0.03	—

Table 6.10 Free energies (in eV) and pKa values of surface groups of the Al-sub model.

Models	Sites	η = 1.0	η = 0.5	η = 0.0	Δ_{dp}A/eV	pKas
	≡Al^T(OH$_2$)	13.88 ± 0.08	17.68 ± 0.03	20.13 ± 0.04	17.46 ± 0.04	3.1 ± 1.3
	≡Al^T(OH)	13.57 ± 0.03	18.48 ± 0.04	21.11 ± 0.03	18.10 ± 0.04	14.0 ± 1.3
⊥[010]	≡Al^T(OH)$_2$Al	14.34 ± 0.03	17.91 ± 0.05	20.17 ± 0.05	17.69 ± 0.05	7.1 ± 1.4
	≡Al^T(OH)(O)Al	13.27 ± 0.01	18.88 ± 0.03	20.58 ± 0.02	18.23 ± 0.03	16.1 ± 1.0
	H_3O^+	12.76 ± 0.02	17.43 ± 0.04	19.99 ± 0.04	17.08 ± 0.04	—
	≡Al^T(OH$_2$)$_2$	13.48 ± 0.03	17.21 ± 0.01	20.64 ± 0.03	17.16 ± 0.02	2.9 ± 0.7
	≡Al^T(OH)	14.67 ± 0.05	17.81 ± 0.03	20.84 ± 0.04	17.79 ± 0.04	14.2 ± 1.0
⊥[0$\bar{1}$0]	≡Al(OH$_2$)$_2$	12.90 ± 0.05	17.85 ± 0.04	20.44 ± 0.03	17.46 ± 0.04	7.8 ± 1.2
	≡Al(OH)(OH$_2$)	12.49 ± 0.04	18.31 ± 0.03	20.14 ± 0.04	17.65 ± 0.03	11.0 ± 1.0
	H_3O^+	12.55 ± 0.02	17.05 ± 0.03	19.82 ± 0.02	16.76 ± 0.03	—
	≡Al^T(OH$_2$)$_2$	14.16 ± 0.06	17.96 ± 0.04	20.08 ± 0.02	17.68 ± 0.04	3.0 ± 1.1
	≡Al^T(OH)	14.19 ± 0.03	18.75 ± 0.03	21.00 ± 0.05	18.37 ± 0.03	14.5 ± 1.2
⊥[110]	≡Al^T(OH)Al	14.23 ± 0.03	18.18 ± 0.02	20.51 ± 0.01	17.91 ± 0.02	6.9 ± 0.9
	≡Al(OH$_2$)	15.24 ± 0.05	18.23 ± 0.02	20.54 ± 0.02	18.12 ± 0.03	10.4 ± 1.0
	H_3O^+	13.08 ± 0.04	17.72 ± 0.03	19.91 ± 0.03	17.31 ± 0.03	—
	≡Al^T(OH$_2$)$_2$	13.84 ± 0.02	17.48 ± 0.03	20.74 ± 0.06	17.42 ± 0.03	1.5 ± 1.0
	≡Al^T(OH)	14.91 ± 0.03	18.34 ± 0.06	20.86 ± 0.03	18.07 ± 0.05	14.4 ± 1.3
⊥[$\bar{1}\bar{1}$0]	≡Al(OH$_2$)$_2$	14.38 ± 0.07	17.87 ± 0.02	20.03 ± 0.04	17.69 ± 0.03	6.0 ± 1.0
	≡Al(OH)(OH$_2$)	14.32 ± 0.03	18.16 ± 0.05	20.49 ± 0.03	17.91 ± 0.04	9.7 ± 1.2
	H_3O^+	13.37 ± 0.03	17.44 ± 0.03	19.60 ± 0.02	17.14 ± 0.03	—

6.3.1.2 Acidity Constant of Cis-Vacant Model

The pKa values of all edge surfaces sites for the No-sub, Mg-sub, Fe(II)/Fe(III)-sub and Al-sub models were computed with statistical uncertainties within 1.6 pKa units (Tables 6.6-6.10). The uncertainties of pKa value were evaluated as the semi-difference between the value using the first half of the trajectory only and the second half of the trajectory only. Figure 6.6 shows the accumulating averages of vertical energy gaps of ≡Al(OH$_2$)$_2$ on edge perpendicular to [$\bar{1}$10] and ≡Si(OH) on edge perpendicular to [0$\bar{1}$0], which indicated that the results coverged within the simulation period and the effect of possible dipole was negligible.

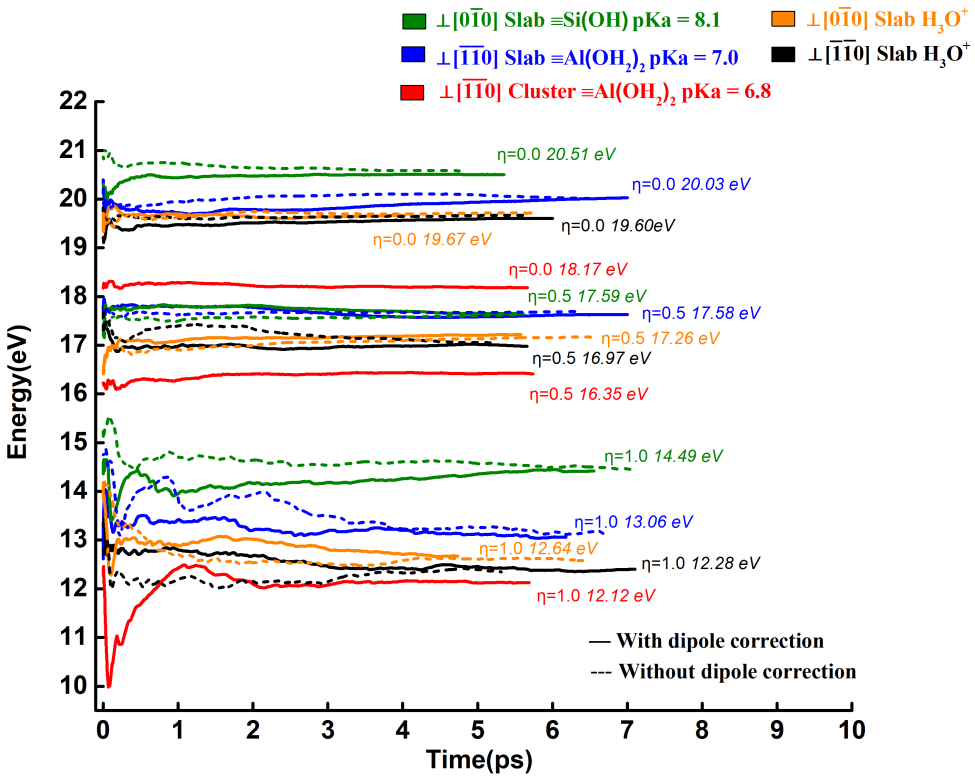

Figure 6.6 Evolution of the time-averaged energy gaps for ≡Al(OH$_2$)$_2$ on surface perpendicular to [$\bar{1}$10] (cluster and slab systems) and ≡Si(OH) on surface perpendicular to [0$\bar{1}$0] (slab system). The origin of the time axis is set at the start of the averaging.

On surface perpendicular to [010], ≡Si(OH)$_2$Al site had the lowest pKa (-0.8), indicating that the site mostly deprotonated at a common pH value. Proton dissociation at ≡Si(OH)$_2$Al site increased the pKa of ≡SiO(OH)Al to 5.9, suggesting that ≡SiO(OH)Al and ≡SiO(O)Al are dominant surface

species under environmentally relevant conditions. The ≡Si(OH) site had a pKa of 6.8, which was similar to the pKa of 7.0 of the silanol on trans-vacant model (Figure 6.7). Furthermore, the pKa values of ≡Si(OH) site on edge perpendicular to [0 $\bar{1}$ 0] and the bound water at ≡Al$(OH_2)_2$/≡Al(OH)(OH_2) sites were 8.1 and 5.7/9.8, respectively. These results were also consistent with the similar sites (≡Si(OH), ≡Al$(OH_2)_2$ and ≡Al(OH)(OH_2)) on trans-vacant edge perpendicular to [010] considering the model calculation error margin. The ≡Al(OH)Al site on edge perpendicular to [0$\bar{1}$0] had a pKa value of 13.2, indicating that it remained protonated even at high pH values.

On surface perpendicular to [110], the pKa values of ≡Si$(OH)^U$ and ≡Si$(OH)^L$ were 6.3 and 6.8, close to the values obtained for the silanols on edge perpendicular to [$\overline{11}$0](i.e., 7.4 and 8.1, respectively) (Figure 6.7b). A similar result has been described for silanol sites on trans-vacant surface (i.e. 8.0 vs 8.3 for ≡Si$(OH)^U$ and ≡Si$(OH)^L$ sites). Similar to the trans-vacant model, ≡ Si(OH)Al on edge perpendicular to [110] had a pKa of -11.7, implying that it was unstable in the presence of water. ≡Al(OH_2) site on edge perpendicular to [110] and ≡Al$(OH_2)_2$ on edge perpendicular to [$\overline{11}$0] of cis-vacant model had pKa values of 5.6 and 7.0, respectively, which were close to the ≡Al(OH_2) site on trans-vacant edge perpendicular to [110] (i.e. pKa of 5.5). For ≡Al(OH)Al site on edge perpendicular to [$\overline{11}$0] (i.e. the structural OH), the pKa value was 17.6, indicating that it should not contribute to edge surface acid-base properties.

Previous studies show that the influence of isomorphic substitution on surface pKa values is usually limited in one unit cell. In our cis-vacant model, Mg^{2+} substitution took place in the first octahedral layer on the surface perpendicular to [010] (Figure 6.4a). The pKa of the ≡Si(OH) site connected with Mg via bridging oxygen was 9.0, while the pKa values of ≡Si$(OH)_2$Mg and ≡SiO(OH)Mg sites were 5.3 and 8.8, respectively (Figure 6.7b). Therefore ≡ Si$(OH)_2$Mg can contribute to the titration data, which is in contrast to the ≡ Si$(OH)_2$Al site on the No-sub model described previously. All of the pKa values were higher than their counterparts on the No-sub model, similar to the finding for trans-vacant surfaces. On surface perpendicular to [0$\bar{1}$0], the edge surface sites have the same nomenclature as on No-sub surface except that they connect with Mg via bridge oxygen. The ≡Si(OH) site had a pKa of 11.0, which was consistent with the Mg-sub trans-vacant edge

perpendicular to [010] (10.8). However, the pKa values of ≡Al$(OH_2)_2$ and ≡Al(OH_2)(OH) site were 5.9 and 10.1, respectively, which were close to the values of the counterparts on the No-sub model (i.e. 5.7 and 9.8), suggested that the effect of Mg^{2+} substitution on Al sites was weak. ≡Mg(OH)Al site had a very high pKa of 16.6, and therefore should be kept protonated in water.

Similar effect of Mg-sub has been found for the other surfaces. ≡Si$(OH)^U$ and ≡Si$(OH)^L$ sites on Mg-sub cis-vacant edge perpendicular to [110] had pKa values of 9.1 and 10.4, respectively, which were higher than their counterparts on the No-sub model (Figure 6.4b). The ≡Al(OH_2) site mostly kept protonated under a neutral pH (pKa of 8.5), while ≡Si(OH)Al site was deprotonated (pKa of -7.1). On surface perpendicular to [$\overline{1}10$] of Mg-sub model, the pKa values of ≡Si$(OH)^U$ and ≡Si$(OH)^L$ sites increased slightly to 8.9 and 9.2 compared to No-sub model (i.e., 7.4 and 8.1), respectively. ≡Mg$(OH_2)_2$ and the structural OH site (i.e., ≡Mg(OH)Al) were inert because of their high pKas (15.1 and 18.7 respectively).

For the reduced Fe_{II}-sub model, the ≡Si(OH) sites on surfaces perpendicular to [010] and [0$\overline{1}$0] had high pKa values of 12.2 and 13.5, which was similar to the silanol on Fe(II) substituted trans-vacant model (i.e. pKa of 11.2). On surfaces perpendicular to [110] and [$\overline{1}\overline{1}$0], ≡Si$(OH)^U$ and ≡Si$(OH)^L$ also had high pKa values while being similar within 1.1 pKa unit (i,e., pKa of 13.8 vs 12.7 and 12.3 vs 11.4, respectively). The results suggested that the substitution of Fe(II) led to an increase in the pKa value of the adjacent ≡Si(OH) site to the extent that it would remain protonated in water.

On the surface perpendicular to [010], the vacancy sites ≡Si$(OH)_2Fe_{II}$ and ≡Si(O)(OH)Fe_{II} had higher pKa values of 13.2 and 17.2, respectively, and therefore did not dissociate under ambient pH conditions. Furthermore, the pKa values of ≡Al$(OH_2)_2$ site on edge perpendicular to [0$\overline{1}$0] and the structural OH group of the ≡Fe_{II}(OH)Al site were 10.2 and 20.1 respectively, both of which had higher pKa values compared to the non-substituted model (pKa of 5.7 and 13.2). On the surface perpendicular to [110], the pKa value of the ≡Si(OH)Al site was -7.7, indicating that it was unstable in water and this site remained dissociated, which was consistent with the non-substituted model (pKa of -11.7). The pKa value of the ≡Al$(OH_2)_2$ site on the surface perpendicular to [110] was similar to that of the surface perpendicular to [0$\overline{1}$0] (10.7 vs 10.2). In the meantime, the pKa value of ≡$Fe_{II}(OH_2)_2$ site on surface perpendicular to [$\overline{1}\overline{1}$0] was similar to ≡Al$(OH_2)_2$ on the surface

perpendicular to [110] with 10.9, while the results were also consistent with the $\equiv Fe_{II}(OH_2)_2$ site on the trans-vacant model (i.e. pKa of 10.2). Structural $\equiv Fe_{II}(OH)Al$ site on the surface perpendicular to [$\overline{1}10$] remained nonreactive because of a high pKa value of 19.8.

In the Fe_{III}-sub model, $\equiv Si(OH)_2Fe_{III}$ and $\equiv Si(O)(OH)Fe_{III}$ on edge perpendicular to [010] had pKa values of -0.4 and 5.7 (Table 6.9), which were close to the $\equiv Si(OH)_2Al$ and $\equiv Si(O)(OH)Al$ sites of the non-substituted model (pKa of -0.8 and 5.9). However, on the surface perpendicular to [0$\overline{1}$0], the $\equiv Al(OH_2)_2$ site had a much lower pKa value than in the non-substituted model (-0.1 and 5.7 respectively), while the pKa values of $\equiv Al(OH)(OH_2)$ and $\equiv Fe_{III}(OH)Al$ were also decreased to 6.1 and 8.9, respectively. On the surface perpendicular to [110], $\equiv Si(OH)Al$ and $\equiv Al(OH_2)$ had pKa values of -14.6 and 2.7, which suggested that the protonated forms were not stable at environmentally relevant pH values. The pKa values of $\equiv Fe_{III}(OH_2)_2$ and $\equiv Fe_{III}(OH)(OH_2)$ on surface perpendicular to [$\overline{1}10$] were -7.7 and 2.3, respectively. Moreover, the pKa value of the $\equiv Fe_{III}(OH)Al$ site on the surface perpendicular to [$\overline{1}10$] closely resembled the same site on the surface perpendicular to [0$\overline{1}$0] with a pKa value of 8.7 (vs 8.9).

The pKa values of the ≡Si(OH) site on surfaces perpendicular to [010], [0$\overline{1}$0], [110] and [$\overline{1}10$] of the $\equiv Fe_{III}$-sub model were all increased by 0.0~2.0 pKa units compared to the non-substituted model. For example, the ≡Si(OH) site on surfaces perpendicular to [010] and [0$\overline{1}$0] had pKa values of 8.8 and 9.0, which was slightly higher than that of the non-substituted model (i.e. pKas of 6.8 and 8.1). $\equiv Si(OH)^U$ and $\equiv Si(OH)^L$ had pKa values of 8.4 and 7.1 on the surface perpendicular to [110], while it was 6.3 and 6.8 for the non-substituted model. Meanwhile, $\equiv Si(OH)^U$ and $\equiv Si(OH)^L$ had pKa values of 8.1 and 7.9 on the surface perpendicular to [$\overline{1}10$], both of which were close to the non-substituted model, i.e. 8.1 and 7.4. Considering the computational error, it is difficult to state unequivocally that Fe(III)-substitution affects the neighboring silanol site. But from another perspective, compared to the acidity constants obtained with the Fe_{II}-sub model, Fe oxidation (Fe_{III}-sub) decreased the pKa values of the counterpart sites, which was consistent with results obtained previously with a trans-vacant model.

The calculated pKa values of tetrahedral $\equiv Al^T(OH_2)$ and $\equiv Al^T(OH)$ sites on the edge

perpendicular to [010] were 3.1 and 14.0, respectively. The lower pKa value of the $\equiv Al^{T}(OH_2)$ site indicated that it rarely occurred in the normal pH range. In addition, the pKa values of $\equiv Al^{T}(OH_2)/\equiv Al^{T}(OH)$ were 2.9/14.2, 3.0/14.5, and 1.5/14.4 on surfaces perpendicular to $[0\bar{1}0]$, [110] and $[\bar{1}\bar{1}0]$, while on the trans-vacant surfaces perpendicular to [010] and [110] the pKa values were -2.4/15.1 and -2.4/17.5, respectively. Hence, similar results were obtained for all $\equiv Al^{T}(OH_2)/\equiv Al^{T}(OH)$ sites. On the surface perpendicular to [010], $\equiv Al^{T}(OH)_2Al$ and $\equiv Al^{T}(O)(OH)Al$ site had pKa values of 7.1 and 16.1, suggesting that $\equiv Al^{T}(O)(OH)Al$ was the dominant surface species under environmentally relevant conditions. As shown in Figure 6.8, octahedral $\equiv Al(OH_2)_2$ and $\equiv Al(OH)(OH_2)$ site on surfaces perpendicular to $[0\bar{1}0]$ and $[\bar{1}\bar{1}0]$ were 7.8/11.0 and 6.0/9.7, respectively, which were similar to the pKa values of the counterpart site on the surface perpendicular to $[0\bar{1}0]$ of the non-substituted model (5.7/9.8), indicating a weak influence of Al(III) substitution. Bridging sites $\equiv Al^{T}(OH)Al$ on the surface perpendicular to [110] exhibited a pKa value of 6.9, which was different from other substitution cases of the ≡Si(OH)Al site having a very low pKa value (-7.7 for the Fe_{II}-sub model, -14.6 for the Fe_{III}-sub model, -7.1 for the Mg-sub model and -11.7 for the No-sub model). On the other hand, the $\equiv Al^{T}(OH)Al$ site could participate in acid-base reactions in the common pH range and was similar to the sites on the surface perpendicular to [110] in an Al(III)-substituted trans-vacant model. Furthermore, the pKa value of the $\equiv Al(OH_2)$ site on the surface perpendicular to [110] was also increased to 10.4 compared to 5.6 of the non-substituted model.

From the above analysis, the Fe(III) substitution decreased the pKa values at the local sites while iron reduction (Fe(II) substitution) increased significantly the pKa values at the local and adjacent sites. Such influence of Fe(II) substitution was similar to that of Mg-substitution in trans- and cis-vacant structures. Al(III) substitution generated a reactive site $\equiv Al^{T}(OH_2)$ in the ambient pH condition. In addition, the effect of the Al(III) substitution on neighboring sites was weak, however, the effect on the acidity of the bridging site ($\equiv Al^{T}(OH)Al$, $\equiv Al^{T}(OH)_2Al$ and $\equiv Al^{T}(O)(OH)Al$ sites) was particularly significant. This phenomenon was similar to that found in the trans-vacant model.

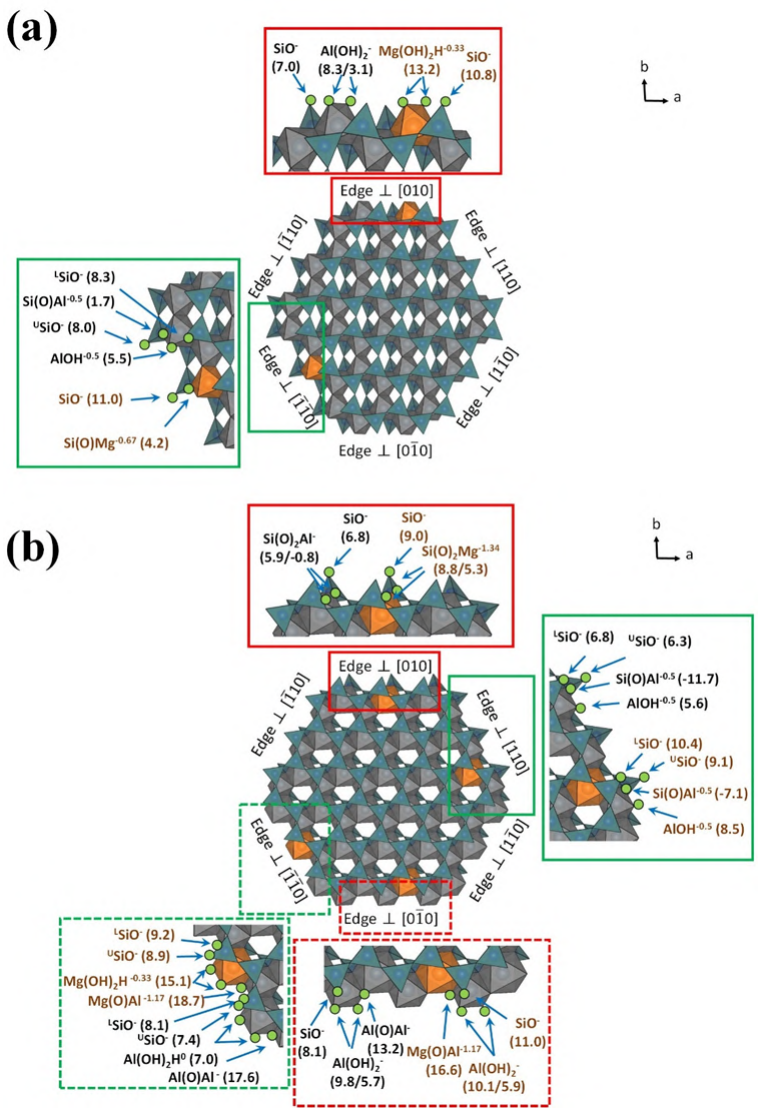

Figure 6.7 Edge surface sites and pKa values of trans-(a) and cis-(b) vacant clay models.

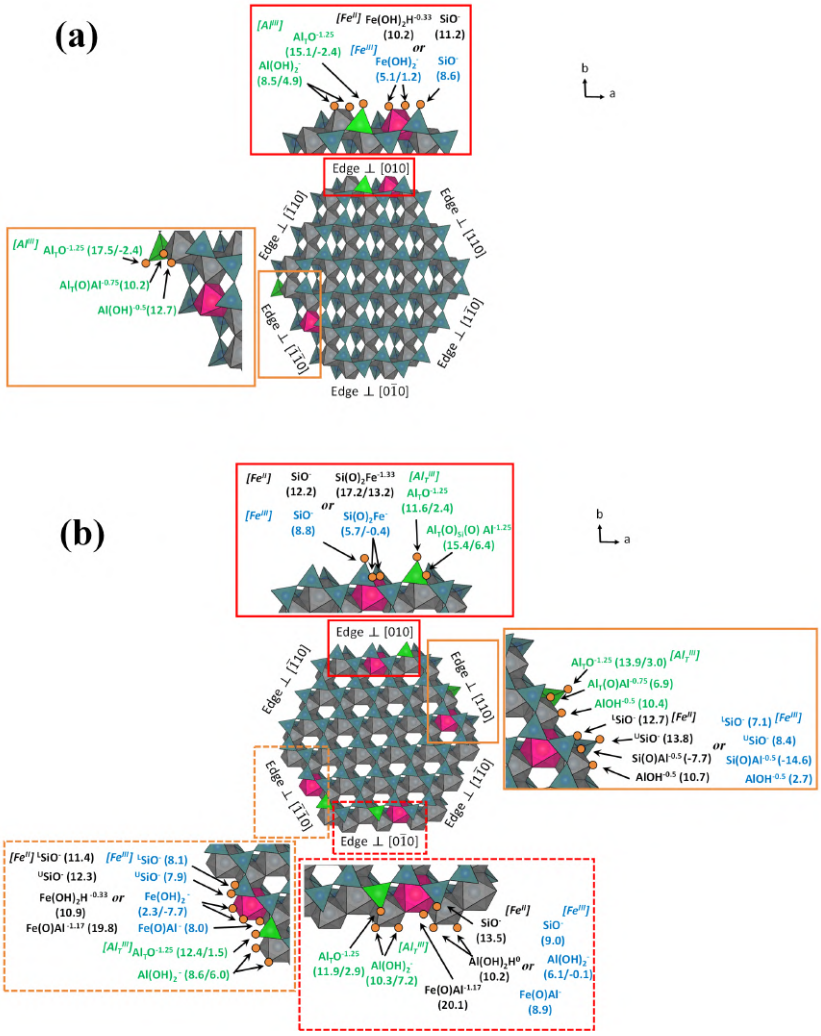

Figure 6.8 Edge surface sites and pKa values of Fe(II)/(III)- and Al(III)-substituted clay models. (a) trans-vacant model and (b) cis-vacant model.

Table 6.11 summarized the pKa values calculated in this study as well as the results obtained previously for non- and Mg-substituted cis-vacant TOT layer and trans-vacant TOT layer. This database can be used for further modeling studies of natural montmorillonites which contain various substitutions. A cis-vacant model has more diverse sites than a trans-vacant model. For example, ≡Si(OH)$_2$Al was the unique site on edge surfaces on cis-vacant model, and it was the major reactive site under ambient pH. Moreover, the structural OH sites (≡Al(OH)Al) on surfaces perpendicular to [0$\bar{1}$0] and [$\bar{1}\bar{1}$0] had extremely high pKa values, which do not show reactivity at a common pH. Overall, these acidity results imply that, ≡Si(OH), ≡Al(OH$_2$)$_2$/≡Al(OH)(OH$_2$),≡Si(O)(OH)Al and ≡Al(OH$_2$) sites on edge surfaces of non-substituted cis-vacant layer are the major reactive sites, whereas the reactivity of trans-vacant layers mainly depends on ≡Si(OH), ≡Al(OH$_2$)$_2$/≡Al(OH)(OH$_2$)

and ≡Al(OH_2) sites. The distributions of dominant surface sites on No-sub cis-vacant edge surfaces were shown in Figure 6.9. Mg^{2+} substitution increased the pKa values of neighboring sites, which can alter the acid chemistry of some sites (e.g., ≡Si$(OH)_2$Mg and ≡Mg$(OH_2)_2$).

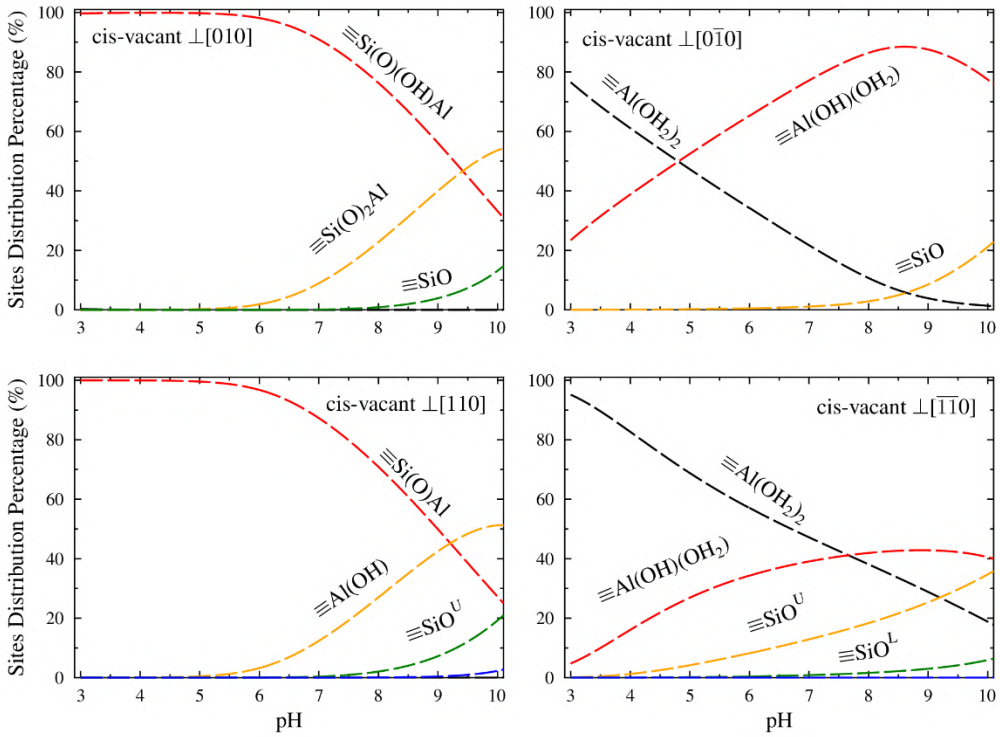

Figure 6.9 Distributions of dominant surface sites on cis-vacant structure as a function of pH.

The Fe(III) substitution decreased the pKa values at the local sites. Iron reduction (Fe(II) substitution) caused the pKa values at the local and adjacent sites significantly increased, which was similar to the case of Mg-substituted in montmorillonite (including trans- and cis-vacant structures). Al(III) substitution generated a reactive site ≡$Al^T(OH_2)$ in the ambient pH condition. In addition, the effect of the Al(III) substitution on neighboring sites was weak, however, the effect on the acidity of the bridge site (≡Al^T(OH)Al, ≡$Al^T(OH)_2$Al and ≡Al^T(O)(OH)Al sites) was particularly significant. This phenomenon was also found in the trans-vacant model. With these pristine acidity constants, we established the complete edge surfaces acidity dataset for the TOT clay layer. The database can be used for further modeling studies of real montmorillonites which contain various substitution cases.

Table 6.11 Summary of Complete pKa Values of Edge Sites on Individual Surfaces of Trans/Cis-Vacant Models (tv and cv, Respectively)

	Sites	*cv* ⊥ [010]	*cv* ⊥ [0$\bar{1}$0]	*cv* ⊥ [110]	*cv* ⊥ [$\bar{1}\bar{1}$0]	*tv* ⊥ [010]	*tv* ⊥ [110]
No-sub	≡Si(OH)	6.8	8.1	$6.3^{U}/6.8^{L}$	$7.4^{U}/8.1^{L}$	7.0	$8.0^{U}/8.3^{L}$
	≡Al(OH$_2$)$_2$/ ≡Al(OH)(OH$_2$)	—	5.7/9.8	—	7.0/—	3.1/8.3	—
	≡Al(OH$_2$)	—	—	5.6	—	—	5.5
	≡Si(OH)Al	—	—	-11.7	—	—	1.7
	≡Si(OH)$_2$Al/ ≡Si(O)(OH)Al	-0.8/5.9	—	—	—	—	—
	≡Al(OH)Al	—	13.2	—	17.6	—	—
Mg-sub	≡Si(OH)	9.0	11.0	$9.1^{U}/10.4^{L}$	$8.9^{U}/9.2^{L}$	10.8	11.0
	≡Mg(OH$_2$)$_2$	—	—	—	15.1	13.2	—
	≡Si(OH)Mg	—	—	—	—	—	4.2
	≡Al(OH$_2$)$_2$/ ≡Al(OH)(OH$_2$)	—	5.9/10.1	—	—	—	—
	≡Al(OH$_2$)	—	—	8.5	—	—	—
	≡Si(OH)Al	—	—	-7.1	—	—	—
	≡Si(OH)$_2$Mg/ ≡Si(O)(OH)Mg	5.3/8.8	—	—	—	—	—
	≡Mg(OH)Al	—	16.6	—	18.7	—	—
Fe_{II}-sub	≡Si(OH)	12.2	13.5	$13.8^{U}/12.7^{L}$	$12.3^{U}/11.4^{L}$	11.2	—
	≡Fe(OH$_2$)$_2$	—	—	—	10.9	10.2	—
	≡Al(OH$_2$)$_2$	—	10.2	—	—	—	—
	≡Al(OH$_2$)	—	—	10.7	—	—	—
	≡Si(OH)Al	—	—	-7.7	—	—	—
	≡Si(OH)$_2$Fe/ ≡Si(O)(OH)Fe	13.2/17.2	—	—	—	—	—
	≡Fe(OH)Al	—	20.1	—	19.8	—	—

Fe_{III}-sub	≡Si(OH)	8.8	9.0	$8.4^{U}/7.1^{L}$	$7.9^{U}/8.1^{L}$	8.6	—
	≡$Fe(OH_2)_2$/ ≡Fe(OH)(OH_2)	—	—	—	-7.7/2.3	1.2/5.1	—
	≡$Al(OH_2)_2$/ ≡Al(OH)(OH_2)	—	-0.1/6.1	—	—	—	—
	≡$Al(OH_2)$	—	—	2.7	—	—	—
	≡Si(OH)Al	—	—	-14.6	—	—	—
	≡$Si(OH)_2$Fe/ ≡Si(O)(OH)Fe	-0.4/5.7	—	—	—	—	—
	≡Fe(OH)Al	—	8.9	—	8.0	—	—
Al-sub	≡$Al^{T}(OH_2)$/ ≡Al^{T}(OH)	2.4/11.6	2.9/11.9	3.0/13.9	1.5/12.4	-2.4/15.1	-2.4/17.5
	≡$Al(OH_2)_2$/ ≡Al(OH)(OH_2)	—	7.2/10.3	—	6.0/8.6	4.9/8.5	—
	≡$Al(OH_2)$	—	—	10.4	—	—	12.7
	≡Al^{T}(OH)Al	—	—	6.9	—	—	10.2
	≡$Al^{T}(OH)_2$Al/ ≡Al^{T}(O)(OH)Al	6.4/15.4	—	—	—	—	—

[a]The pKa values of the trans-vacant model were taken from Liu et al. (Liu et al. 2014, 2015)

[b]The pKa values of the No-sub and Mg-sub cis-vacant model were taken from Gao et al. (Gao et al. 2023)

6.3.2 Predicted SCM for Cis-Vacant Clay Minerals

Previous studies have established prediction models of the acid-base titration data, in which the acidity constants were based on trans-vacant model, and the results indicated that the surfaces perpendicular to the different crystallographic directions have different surface charge. For comparison, we employed two sets of pKa values from the trans- and cis-vacant models to construct the SCM on different edge surfaces.

On common edge surfaces of trans- and cis-vacant models (i.e. surface perpendicular to [010], [$0\bar{1}0$], [110] and [($\bar{1}\bar{1}0$] crystallographic directions), the surface charge decreased with increasing pH to a similar extent for the two models (Figure 6.10 top). Moreover, edge surface charge of both trans-

and cis-vacant models had little dependence on Mg^{2+} substitutions, but the dependence on the crystal plane orientation was strong.

The averaged charge of surfaces perpendicular to [010] and [$0\bar{1}0$] and [110] and [$\bar{1}\bar{1}0$] in the cis-vacant model was compared with to the charge of surfaces perpendicular to [010] and [110] in the trans-vacant model (Figure 6.10 bottom), respectively. At 0.1 $mol \cdot L^{-1}$ NaCl, the averaged charge of surfaces perpendicular to [010] and [$0\bar{1}0$] in the cis-vacant model was slightly higher than that of surface perpendicular to [010] in the trans-vacant model at pH<6.0, and identical to each other at higher pH values. The surface charge on cis-vacant surfaces perpendicular to [110] and [$\bar{1}\bar{1}0$] were higher than trans-vacant surface perpendicular to [110] at pH<8.8, but the surface charge of cis-vacant surfaces decreased with a larger slope than that of trans-vacant surface, leading to a more negative surface at pH above 8.8. Changes in ionic strength were predicted to have a significant effect on surface charge. Both cis- and trans-vacant models showed that a decrease in ionic strength results primarily in a reduction of the surface charge variation amplitude and in a shift of the point of zero charge towards higher pH values. The overall charge on all edge surfaces for cis- and trans-vacant structures was also calculated (Figure 6.11). The difference in overall charge between cis-vacant and trans-vacant structures was mainly controlled by the apparent discrepancy between trans-vacant surface perpendicular to [110] and cis-vacant surfaces perpendicular to [110] and [$\bar{1}\bar{1}0$] (Figure 6.10), and thus their profiles are similar to one another.

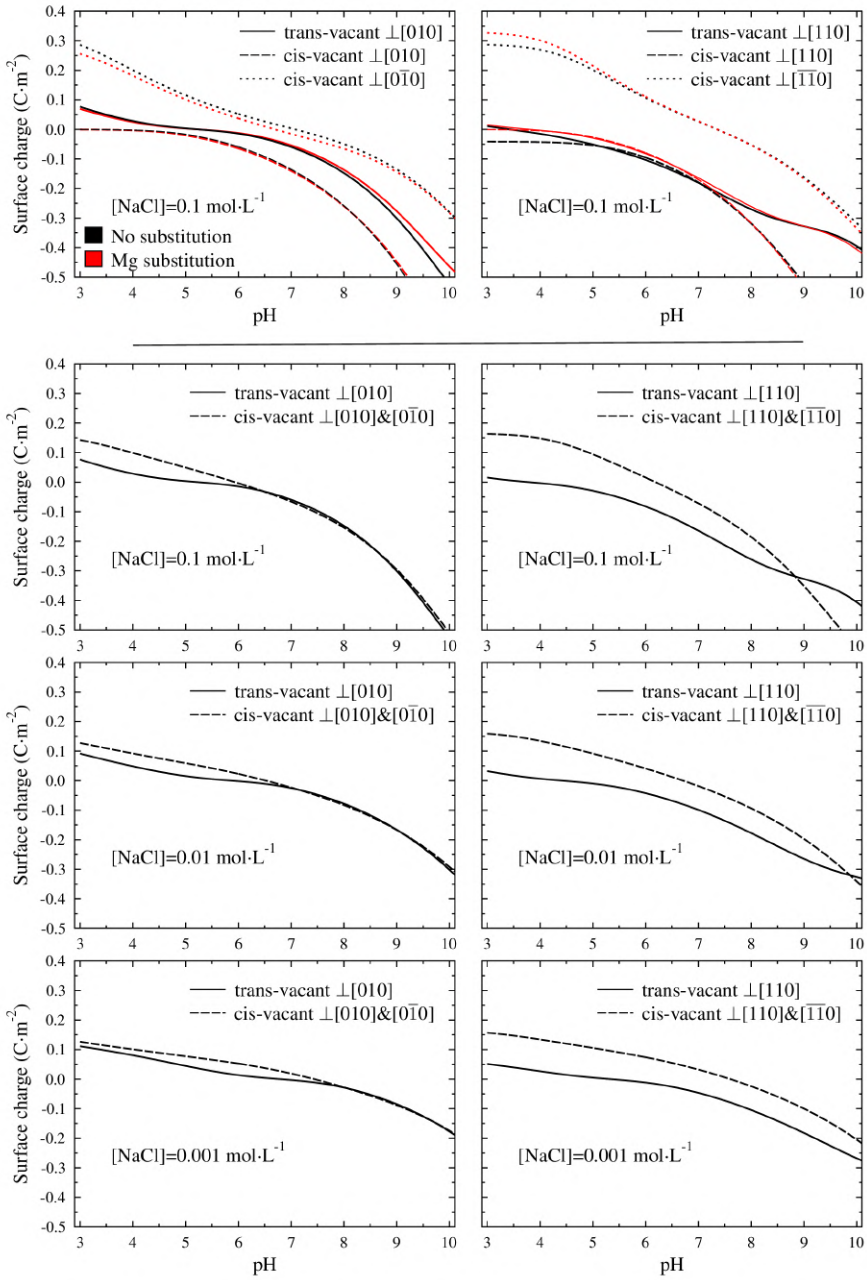

Figure 6.10 Comparison of the predicted titration model for No/Mg-sub cis- and trans-vacant structure on edges perpendicular to [010]/[0$\bar{1}$0] and [110]/[$\bar{1}\bar{1}$0]. The specific edge surface area was set to 14 $m^2 \cdot g^{-1}$ and both the relative abundance of edges perpendicular to [010] and [0$\bar{1}$0] and [110] and [$\bar{1}\bar{1}$0] were set to 1/1 respectively. The fractions of Mg substitution were set to 0.125.

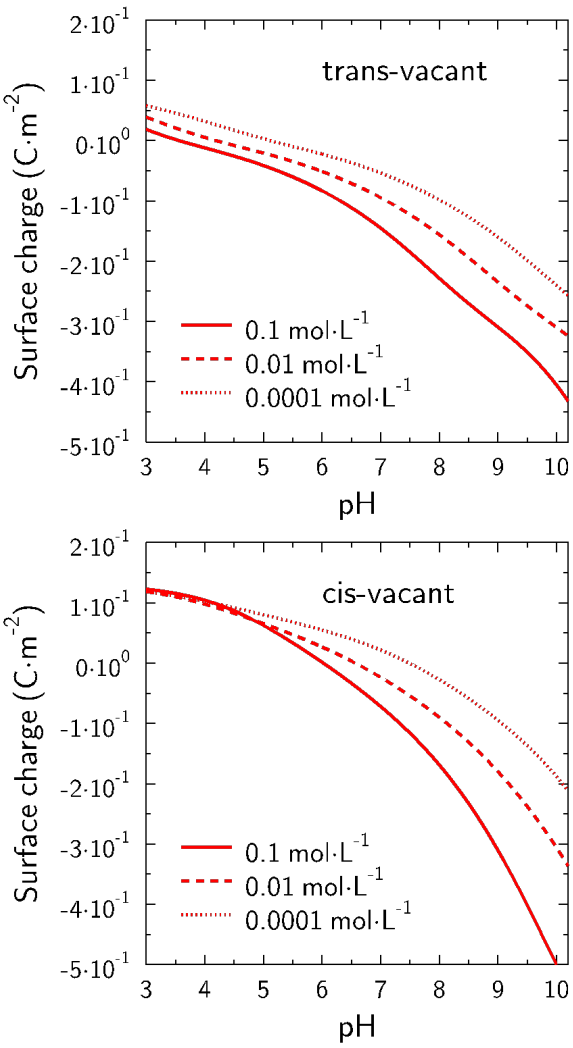

Figure 6.11 Overall charge on all edge surfaces for trans- and cis-vacant structures.

We noticed that the parameter of edge specific surface area in the SCMs was different from the experimental value. Among surface area measurement techniques, the derivative isotherms summation (DIS) method tends to overestimate the surface area (Reinholdt et al., 2013), whereas the atomic force microscopy (AFM) method could provide an accurate estimate of surface area. The AFM measured edge-specific surface area of 9 $m^2 \cdot g^{-1}$ for MX80 montmorillonite and no available AFM results for Swy-2 montmorillonite, but the modeled edge specific surface areas were 12 and 14 $m^2 \cdot g^{-1}$ for MX80 and Swy-2 montmorillonite, respectively, which were greatly different compared to the measurements.

The structural formulas of MX80 and SWy-2 montmorillonites were reported as

$(Si_4)(Al_{1.57}Mg_{0.25}Fe^{III}_{0.09}Fe^{II}_{0.09})Na_{0.34}O_{10}(OH)_2$ and $(Si_{3.87}Al_{0.13})(Al_{1.52}Mg_{0.25}Fe^{III}_{0.224}Fe^{II}_{0.006})Na_{0.39}O_{10}(OH)_2$, respectively. Hence, we pooled complete acidity constants of cis-vacant model to predict potentiometric titration data. An exercise on the edge-specific surface areas of the cis-vacant model was used to determine the corresponding specific surface area values (Figure 6.12). The agreement between experimental and predicted potentiometric titration curves was acceptable if the specific edge surface areas were set to 9 $m^2 \cdot g^{-1}$ and the relative abundance of cis-vacant edges perpendicular to [010], [$0\,\bar{1}\,0$], [110], and [$\bar{1}\bar{1}\,0$] was set at 0.15/0.15/0.35/0.35 for both MX80 and SWy-2 montmorillonites, which all in agreement with AFM results. Figure 6.13 included the comparison of predictions based on cis- and trans-vacant model. The relative abundance of trans-vacant edges perpendicular to [010] and [110] was set at 0.3/0.7 and the edge-specific surface areas were set to 14 $m^2 \cdot g^{-1}$ and 12 $m^2 \cdot g^{-1}$ for SWy-2 and MX80 montmorillonites, respectively. As we seen, a good agreement was found between experimental and predicted potentiometric titration data for cis- and trans-vacant model. Furthermore, for Swy-2 montmorillonite, a better agreement was found of cis-vacant model at pH above 6.0. For MX80 montmorillonite, the cis- and trans-vacant model predictions were overlapping. However, what made more sense was that the modeling parameters based on cis-vacant structure were totally derived from simulations and experiments without adjustable parameters. Hence, a completely constrained, parsimony-satisfying SCMs was successfully constructed to reproduce the titration data using acid-base database of cis-vacant model.

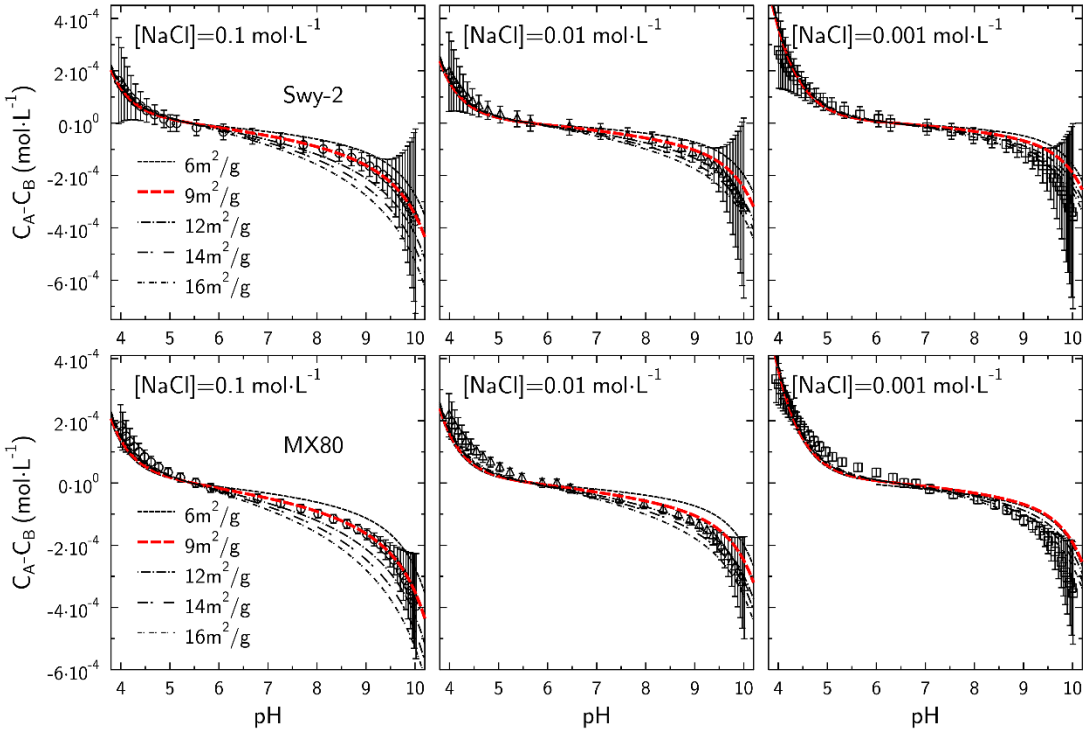

Figure 6.12 Comparison of model predictions based on cis-vacant structure at different edge specific surface areas (lines) and potentiometric titration data (symbols) for MX80 montmorillonite (bottom) and SWy-2 montmorillonite (top)

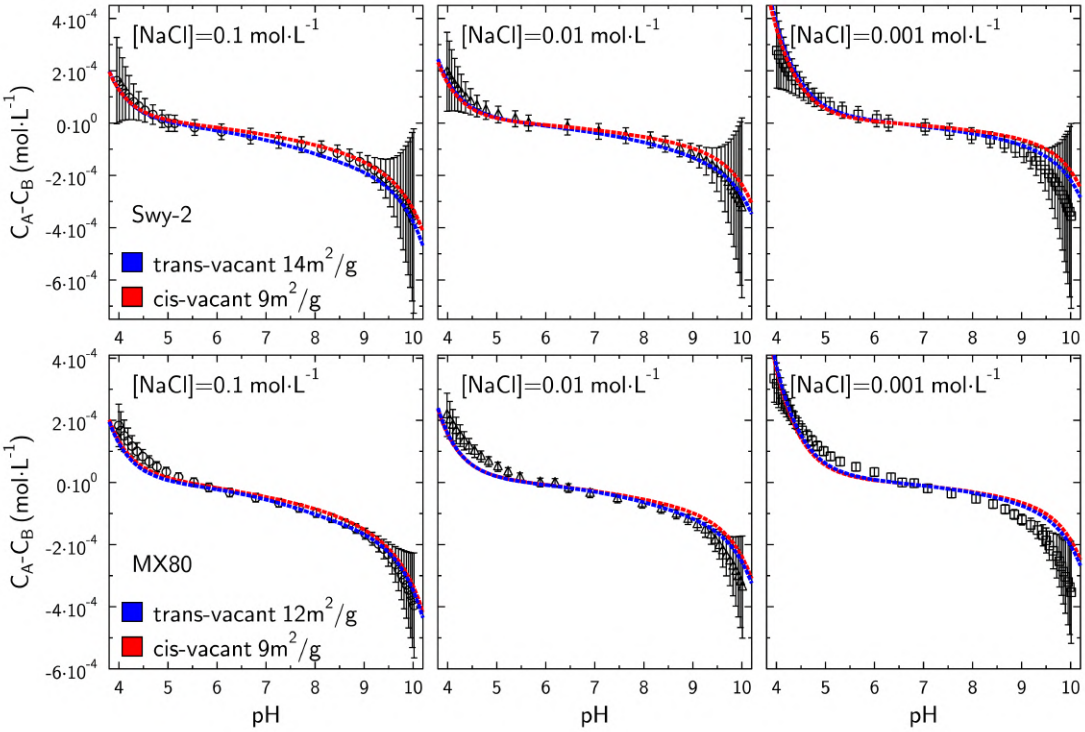

Figure 6.13 Comparison of model predictions (lines) and potentiometric titration data (symbols) for MX80 montmorillonite (bottom) and SWy-2 montmorillonite (top) as reported by Tournassat et al. (Tournassat et al. 2016)

The trans-vacant model predicts a negative surface potential at pH above 4 for the two types of surfaces present in the model, *i.e.* perpendicular to [010] and [110] (Figure 6.14). Contrastingly, the cis-vacant model predicts negative surface potential at pH above 4 for surfaces perpendicular to [010] and [110], but positive surface potential at pH below ~6-7 for surfaces perpendicular to $[0\bar{1}0]$ and $[\bar{1}\bar{1}0]$. Hence, for pH below 6-7 montmorillonite particles may exhibit edge surface with positive surface potential on one side and negative surface potential on the other side.

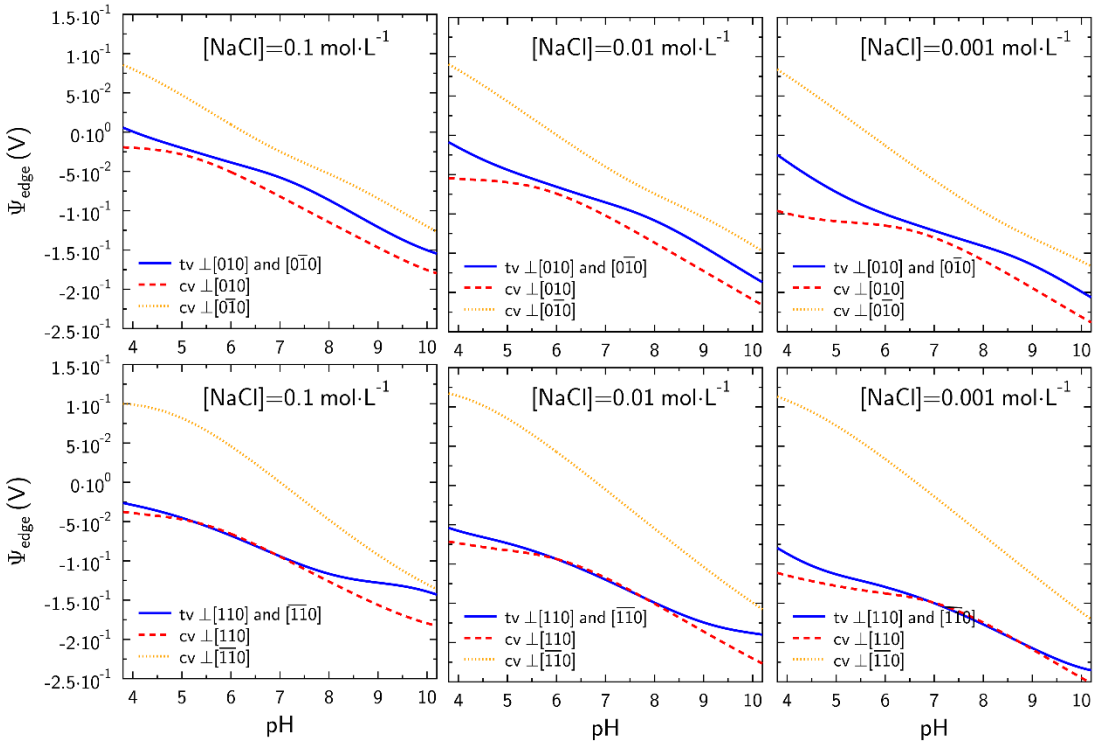

Figure 6.14 Swy-2 edge surface potentials as a function of surface directions, pH, and ionic strength. Comparison of our cis-vacant model and the trans-vacant model by Tournassat et al. (Tournassat et al. 2016)

Some anions, including metalloids, sorb weakly, but notably on montmorillonite surfaces. Arsenate - As(V) - adsorption is pH dependent and exhibits a bell-shaped with an adsorption maximum at pH 6-7. Our modeling findings makes it possible to give an explanation to this adsorption behavior. The maximum of adsorption corresponds to the presence of negatively charged aqueous $H_2AsO_4^-$ and $HAsO_4^{2-}$ species concomitantly with the presence of a positive surface potential on some of montmorillonite edge surfaces. At lower pH, As(V) species are dominated by the neutral species H_3AsO_4, which cannot interact electrostatically with the surface, while at higher pH, the electrostatic interaction between the negative surface potential and the negatively charged As(V) aqueous species is unfavorable. Similar adsorption behavior may also be explained for other oxyanions such as aqueous As(III), Se(IV) and Mo(VI).

The highly complex nature of clay mineral surface reactivity requires the application of multiple techniques to obtain insightful parameters for the building of predictive surface complexation models. Because of the complexity of the structure and chemistry on edge surfaces of montmorillonite, pKa values cannot be obtained unequivocally from the fitting of potentiometric titration experiments, and

information gained at atomistic scale is necessary to build constrained SCM. A key finding in the present study is related to the necessity to consider contrasted electrostatic properties at montmorillonite edge surfaces with various crystallographic directions in a single particle which arise from the non-centrosymmetric nature of montmorillonite cis-vacant layer structure.

Our complete set of acidity constants for 2:1 TOT layers enables predictive modeling of the interfacial properties for a wide range of clay minerals. Table 6.12 listed the structural formulas of some trans- or cis-vacant clay minerals, which include various substitutions. The predicted potentiometric titration and surface charge curves for these minerals are shown in Figure 6.15 The modeled edge-specific surface area was set as 9 $m^2 \cdot g^{-1}$ and minor Fe^{3+} tetrahedral substitutions were considered to have the same pKa parameters as the Al^{3+} substitutions. All other parameters were consistent with those used by Gao et al. (Gao et al. 2023) The modeling results indicated that the extent of the various isomorphic substitutions (tetrahedral vs. octahedral and Fe vs. Mg in octahedral position) had little influence on the predicted titration curves. Contrastingly, the consideration of cis-vacant vs. trans-vacant structures led to significant differences in surface charge at pH above pH 8.0.

Table 6.12 Structural formulas of some 2:1 type trans/cis-vacant (*tv*/*cv)* clay minerals.

2:1 Clay Samples	Structural Formulae	Model
Montmorillonite (Swy-1)	$(Si_{3.91}Al_{0.09})(Al_{1.64}Mg_{0.25}Fe^{3+}_{0.08}Fe^{2+}_{0.08})Na_{0.37}O_{10}(OH)_2$	*cv*
Montmorillonite (Kunipia)	$(Si_{3.825}Al_{0.175})(Al_{1.64}Mg_{0.215}Fe^{3+}_{0.155})Na_{0.265}Ca_{0.045}O_{10}(OH)_2$	*cv*
Beidellite (SBId-1)	$(Si_{3.574}Al_{0.426})(Al_{1.812}Mg_{0.09}Fe^{3+}_{0.112})K_{0.104}Ca_{0.185}O_{10}(OH)_2$	*tv*
Beidellite (SB1-350)	$(Si_{3.60}Al_{0.4})(Al_2)Na_{0.38}O_{10}(OH)_2$	*cv*
Nontronite (NG-1)	$(Si_{3.645}Fe^{3+}_{0.315}Al_{0.04})(Al_{0.44}Mg_{0.03}Fe^{3+}_{1.54}Fe^{2+}_{0.005})Na_{0.35}O_{10}(OH)_2$	*tv*
Nontronite (NAu-2)	$(Si_{3.775}Fe^{3+}_{0.145}Al_{0.08})(Al_{0.17}Mg_{0.025}Fe^{3+}_{1.77})Na_{0.36}O_{10}(OH)_2$	*tv*

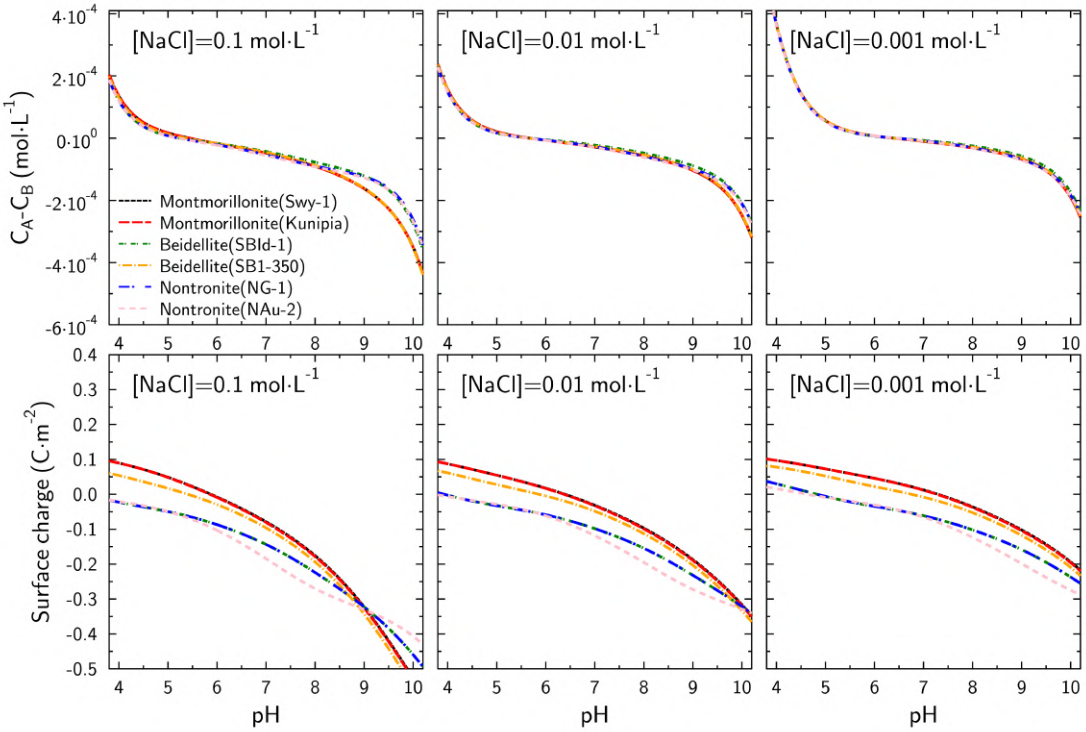

Figure 6.15 Model predictions of potentiometric titration and surface charge curves for different 2:1 clay minerals.

Obtaining insightful parameters for the building of predictive SCMs for clay minerals requires the application of multi-scale techniques. To obtain accurate pKa values, complete atomic-level information based on the real structure of natural montmorillonite is necessary. This study highlights the importance of considering the local structure of clay minerals to fully understand their reactivity. Overall, this work achieved a complete study of the acid-base properties of cis-vacant clay edge surfaces with regard to layer chemistry and structure, which provides fundamental information for the modeling of contaminant adsorption on natural clay minerals.

Chapter 7. Multi-Scale Insights into U(VI) Complexation on Cis-Vacant Montmorillonite Clay Edges: A Combined First-Principles Molecular Dynamics and Surface Complexation Modeling Approach

7.1 Introduction

Uranium is the most important radionuclide due to its relatively high natural abundance and its key role in nuclear waste (Burns and Finch, 1999). U(VI) migration raises many concerns in nuclear technology and environmental chemistry because of the threat to human health and the ecological environment (Clark et al., 1995; Choppin, 2006). One of the most relevant factors controlling U(VI) transport in nature is the adsorption to mineral surfaces (Greathouse and Cygan, 2006; Geckeis et al., 2013). Understanding the interaction between U(VI) and mineral surfaces is important for mastering its migration behavior.

In the natural or radioactive waste repository environments, 2:1-type clay minerals of a TOT (Tetrahedral-Octahedral-Tetrahedral) layered structure, play significant roles in the migration and retardation of U(VI) because of their high adsorption capacity and high abundance (Greathouse and Cygan, 2006; Tournassat et al., 2018; Liu et al., 2022). The TOT layer exhibits two kinds of surfaces, i.e., basal and edge surfaces. The interaction of U(VI) on basal surfaces is mainly the long-range, whereas on edge surfaces is strong chemical bonding with amphoteric groups. Therefore, edge surfaces are responsible for extensive U(VI) adsorption through surface complexation, which is determined by the interfacial properties of the edges and the binding affinity for U(VI). Moreover, the TOT clay layer models are described with either trans- or cis-vacant structures depending on the vacancy position in the octahedral sheet (Tsipursky and Drits, 1984; Brigatti et al., 2011). Cis-vacant structures are not centrosymmetric, which indicates that the edges perpendicular to the [010] and [$0\bar{1}0$], [110] and [$\bar{1}\bar{1}0$] are different, whereas the trans-vacant structures are the same. In natural samples, cis-vacant structure is probably the dominant, and thus the evaluation of U(VI) adsorption on montmorillonites should be rooted in the cis-vacant model. However, previous molecular-level studies were all based on a centrosymmetric trans-vacant configuration.

The adsorption of U(VI) on natural clay minerals has been investigated through batch experiments for decades, elucidating the basic laws governing the adsorption (Tsunashima, 1981;

Bradbury and Baeyens, 2005; Catalano and Brown, 2005). Moreover, the development of appropriate geochemical sorption models, i.e., surface complexation models (SCMs), to reliably describe and predict the environmental behavior of radionuclides is essential, which requires a deep understanding of adsorption mechanisms and actual surface species morphology. U(VI) surface complexation on clay minerals nowadays has been investigated in great detail with the increasing availability of spectroscopic techniques, especially EXAFS (extended X-ray absorption fine structure) and TRLFS (time-resolved laser-induced fluorescence spectroscopy) (Chisholm-Brause et al., 1990; Dent et al., 1992; Sylwester et al., 2000; Schlegel et al., 2002; Hennig et al., 2002; Tan et al., 2010; Marques Fernandes et al., 2012). For instance, Chisholm-Brause et al. used TRLFS to identify various types of uranyl surface species on montmorillonite edge sites, including outer-sphere complex on basal surfaces, inner-sphere mononuclear and multinuclear uranyl species on edge surfaces (Chisholm-Brause et al., 1990). Furthermore, EXAFS provides detailed structural information for the relevant U(VI) surface species. According to the neighbor atoms shell configurations of U, surface bidentate uranyl (UO_2^{2+}) complexes were observed to form at edge octahedral aluminol and tetrahedral silanol sites (Hennig et al., 2002; Schlegel and Descostes, 2009). Several mechanical SCMs were constructed based on the surface speciation spectroscopy results, which aimed to reproduce the U(VI)-montmorillonite system adsorption data. More comprehensive and accurate SCMs should be developed, which rely on specific model parameters such as surface site types, surface reactivity, *etc*. However, obtaining relevant knowledge is challenging due to the average nature of the experimental window.

Theoretical calculations are a powerful research tool based on structures, which provide information on the atomic scale for constructing constrained SCMs. Periodic density functional theory (DFT) calculations have been used to characterize uranyl surface species on clay edge surfaces by optimizing geometries. Mononuclear bidentate uranyl adsorption complexes were revealed on the trans-vacant model at ≡AlOHOH and≡AlOHSiO on (010) edges, as well as at ≡AlOHO$_a$ (O$_a$ represents apical bridge oxygen), ≡AlOHSiO, and ≡SiOO$_a$ on (110) edges.(Kremleva et al., 2011, 2015) These results provide an atomic level understanding of the surface site types, but cannot accurately evaluate the site affinity of uranyl due to the lack of solvation effects and the calculated binding energy as the potential energy at 0 K. Zhang et al. utilized the first-principles molecular

dynamics (FPMD) method to investigate the free energies of uranyl adsorbed on various trans-vacant edge surface sites, revealing that the binding free energies of uranyl are very close (Zhang et al., 2018). A state-of-the-art constrained SCM based on the simulation results was developed to reproduce the U(VI) adsorption data. However, all existing atomistic studies of metal ion adsorption on clays were based on the trans-vacant structure, which potentially leads to an incorrect prediction. Especially, previous studies pointed out that the different local structures (trans- and cis-vacant) lead to distinct surface sites and interfacial properties on the edges, which definitely affect the adsorptive properties (Gao et al., 2023). To the best of our knowledge, metal ion adsorption studies on the edge surfaces of the cis-vacant model at the atomic scale have not been reported.

In this study, we employed FPMD simulations to systematically investigate the complexation structures and free energies of uranyl adsorption on 2:1-type cis-vacant clay edge surfaces perpendicular to [010], [0$\bar{1}$0], [110] and [$\bar{1}\bar{1}$0]. By combining the surface acidity dataset for cis-vacant TOT layers, all of the atomic-level information was then implemented into a SCM for montmorillonite edge surface adsorption. Consequently, a thermodynamic U(VI) adsorption model with predictive capabilities, grounded in natural structures and possessing genuine physical significance was developed, which provides an improved tool for the evaluation of contaminants interaction with natural clay minerals.

7.2 Methodology

7.2.1 Models

The periodic slab models on surfaces perpendicular to [010], [0$\bar{1}$0], [110] and [$\bar{1}\bar{1}$0] of cis-vacant montmorillonite were constructed based on our previous work. The surface models include two unit cells. A solution region of 20 Å above the surface was filled with 130 water molecules, which approximates the density of bulk water at ambient conditions according to previous reports. Additionally, ten water molecules were inserted into the interlayer to create a monolayer hydrate. Finally, an orthorhombic box with dimensions of 12.45 Å × 10.44 Å × 33.56Å was utilized.

In the initial surface models, previous studies concluded that the functional groups ≡Si(OH), ≡Al$(OH_2)_2$/≡Al(OH)(OH_2), and ≡Si$(O_aH)_2$Al/≡Si$O_a$$(O_aH)$Al sites on surfaces perpendicular to [010] and [0$\bar{1}$0] and ≡Si(O_aH)Al, ≡Si(OH), ≡Al(OH_2), and ≡Al$(OH_2)_2$ on surfaces perpendicular to [110]

and [$\overline{1}10$] are reactive at the common pH value. Hence, the investigated surface sites included ≡SiO, ≡Si(O_a)$_2$Al, ≡Si(O_a)Al, ≡Al(OH)(OH_2)/≡Al(OH)$_2$, ≡Al(OH) on cis-vacant edge surfaces. UO_2^{2+} was placed at the complexing sites to form multidentate surface complexes, including surface complexes at ≡SiO(O_a)$_2$Al site on surface perpendicular to [010], at ≡Al(OH)$_2$ and ≡Al(OH)SiO sites on surface perpendicular to [0$\overline{1}$0], at ≡Al(OH)O_a and ≡Si$O O_a$ sites on surface perpendicular to [110], and at ≡Al(OH)SiO site on surface perpendicular to [$\overline{1}10$] (see snapshots in Figure 7.1).

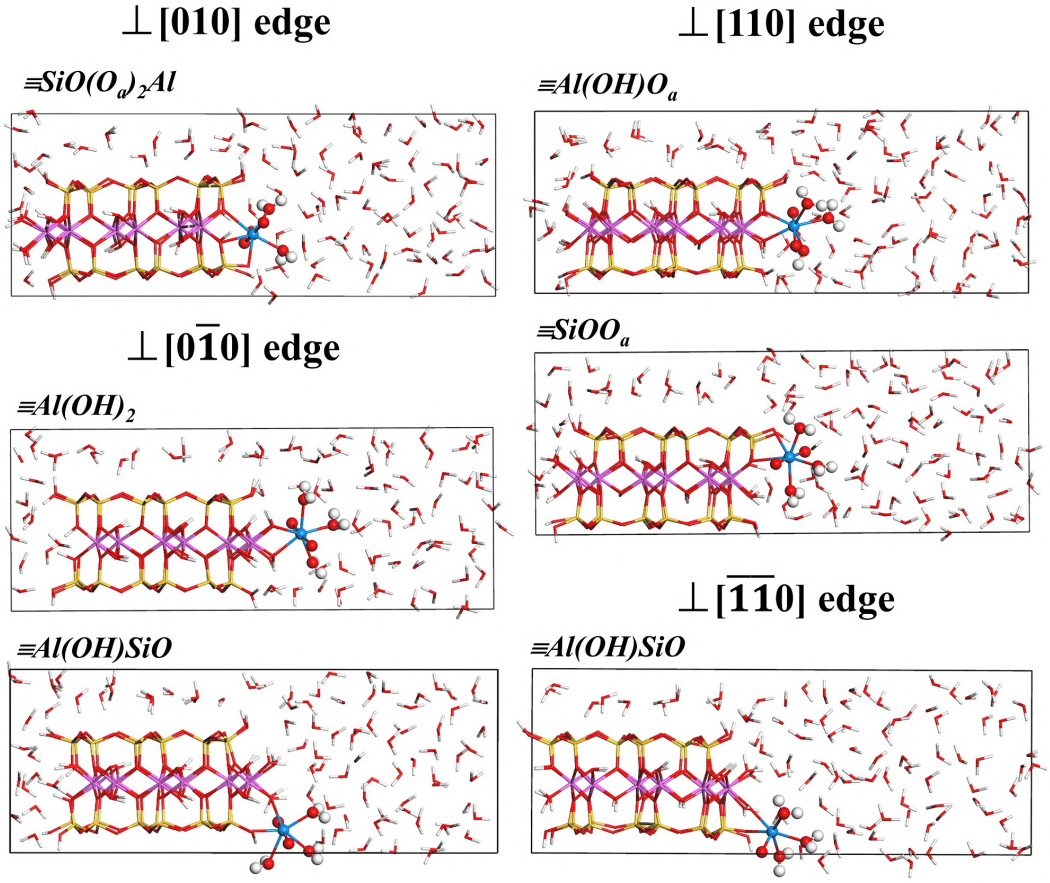

Figure 7.1 Initial models of uranyl complexation on edge surfaces of cis-vacant TOT clay layer. Color scheme: U(blue), Si (yellow), Al (pink), O (red), H (white).

7.2.2 First-Principles Molecular Dynamics

The FPMD simulations were performed using the CP2K/Quickstep package, based on Perdew−Burke−Ernzerh functional and a hybrid Gaussian Plane-Wave scheme (GPW). The Goedecker-Teter-Hutter (GTH) pseudopotentials were chosen to describe the core electrons. The

wave functions were expanded in optimized double-ζ Gaussian basis sets and the plane waves were expanded with a cutoff energy of 400 Rydberg. Dispersion correction was applied in all calculations with the Grimme-D3 method.

Born−Oppenheimer molecular dynamics simulations were performed in canonical (NVT) ensemble employing Nóse–Hoover thermostats with a time step of 0.5 fs at a finite temperature of 300 K. The wave function optimization tolerance was 10^{-6}. For each system, we performed an equilibration run of 3 ps and a production run of 10.0 ps.

7.2.3 Free Energy Calculations

Constrained FPMD simulations were conducted to quantitatively assess the stability of each surface complex and determine the respective desorption free energy. The free energy (ΔA) profile was obtained through the integration of average forces (*F*) along a specified reaction coordinate (*x*).

$$\Delta A(x) = -\int_{x_0}^{x} F(x')\mathrm{d}x'$$

For UO_2^{2+} surface complexes, the coordination number (CN) of U with O atoms at surface adsorption sites was chosen as reaction coordinate. At ≡$SiO(O_a)_2Al$ site on surface perpendicular to [010], UO_2^{2+} desorption process was from tridentate innersphere complex to outersphere complex. On surfaces perpendicular to $[0\bar{1}0]$, [110] and $[\bar{1}\bar{1}0]$, UO_2^{2+} desorption processes were all from bidentate inner-sphere complex to outer-sphere complex on ≡$Al(OH)_2$, ≡Al(OH)SiO, ≡$Al(OH)O_a$ and ≡$SiOO_a$ sites. The CN was defined as

$$\mathrm{CN} = \sum_i \frac{1-(r_i/r_c)^{12}}{1-(r_i/r_c)^{24}}$$

where r_i is the distance between U and O atoms of surface adsorption sites, and r_c is the cutoff value. Here, r_c was set to be 3.1 Å.

7.2.4 First-Principles Molecular Dynamics

An in-house version of PHREEQC, which takes into account the spillover of electrostatic potential from basal surfaces, was utilized to construct the U(VI) surface complexation models. THERMOCHIMIE v.11a thermodynamic database was used in the solute species, which is available at https://www.thermochimie-tdb.com/. PHREEQC scripts were also attached in the Supplementary Information.

7.3 Results and Discussion

7.3.1 Surface complexation structures

The evolutions of U-O, U-Al and U-Si distances over the duration of the simulation were shown in Figure 7.2, indicating that the uranyl surface complexes on cis-vacant clay edges were retained. The equilibrium surface complexation structures of uranyl on edge surface sites of cis-vacant model were illustrated in Figure 7.3. It can be seen that uranyl formed a stable tridentate complex on $\equiv SiO(O_a)_2Al$ site on surface perpendicular to [010]. This site can be considered as an analogous vacancy site to Ni^{2+} on the surface perpendicular to [010] of trans-vacant model. However, the vacancy site of the trans-vacant edge consists of two aluminum octahedral lattices, making it more suitable for metal ions with a small radius. In contrast, the vacancy $\equiv SiO(O_a)_2Al$ site of the cis-vacant edge has better equatorial coordination and adaptability for actinyl groups such as uranyl. Furthermore, uranyl formed bidentate complexes at $\equiv Al(OH)_2$, $\equiv Al(OH)SiO$, $\equiv Al(OH)O_a$ and $\equiv SiOO_a$ sites on surfaces perpendicular to [$0\bar{1}0$], [110] and [$\bar{1}\bar{1}0$], which were consistent with uranyl complexation on tran-vacant model edges.

For tridentate uranyl surface complex on $\equiv SiO(O_a)_2Al$ site on surface perpendicular to [010], two equivalent U-O_a bonds with an average bond length of 2.42 Å and one slightly longer U-O_{Si} bond of 2.53 Å. On surface perpendicular to [$0\bar{1}0$], uranyl formed bidentate surface complexes with two equivalent U-O_{Al} bonds of 2.37 Å on $\equiv Al(OH)_2$ site and U-O_{Si}/O_{Al} of 2.24/2.42 Å on $\equiv Al(OH)SiO$ site, respectively, which was identical to uranyl complexes of trans-vacant model on surface perpendicular to [010]. For the uranyl bidentate surface complexes on surface perpendicular to [110], the bond lengths of both U-O_a and U-O_{Al} distance on $\equiv Al(OH)O_a$ site were 2.42 Å. For the complex on $\equiv SiOO_a$ site, the bond lengths of U-O_a and U-O_{Si} were 2.58 and 2.27 Å, respectively. On surface perpendicular to [$\bar{1}\bar{1}0$], a uranyl bidentate complex similar to that on surface perpendicular to [$0\bar{1}0$] was also formed on $\equiv Al(OH)SiO$ site with U-O_{Si}/O_{Al} bonds of 2.27/2.49 Å. Additional U-Al/Si distances were also provided for comparison with the vast majority of EXAFS experiments and previous DFT calculations (Figure 7.3). However, EXAFS has considerable uncertainty in interpreting the second adjacent atom involved in the surface complex and previous atomic-level calculations were all based on the trans-vacant model, which led to a broad comparison. For instance,

U-Al/Si distances exhibited two distinct regions on trans-vacant edges, 3.17 Å and 3.47-3.62 Å, while three regions were observed on cis-vacant edges, 3.05-3.14 Å, 3.46-3.57 Å and 4.06-4.21 Å.

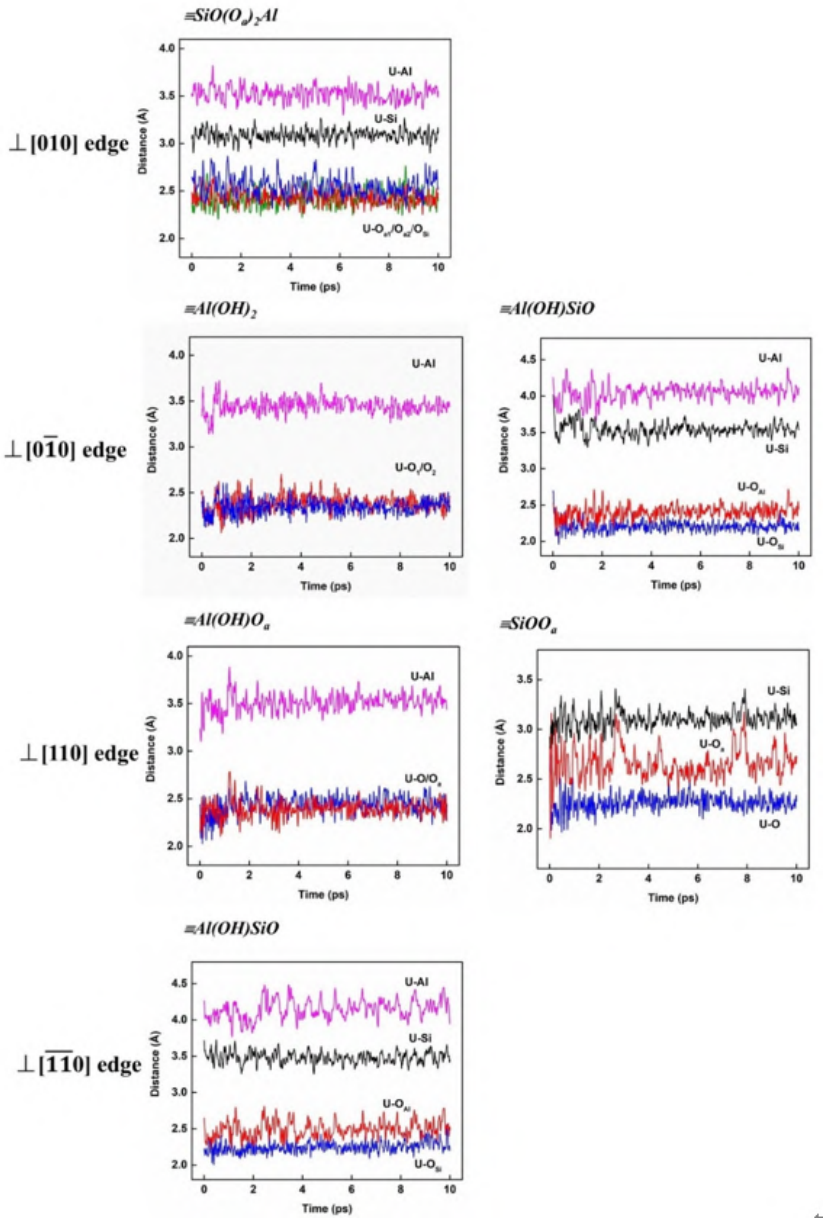

Figure 7.2 Time evolution for the various U-O distances of uranyl surface complexes on cis-vacant TOT layer edges

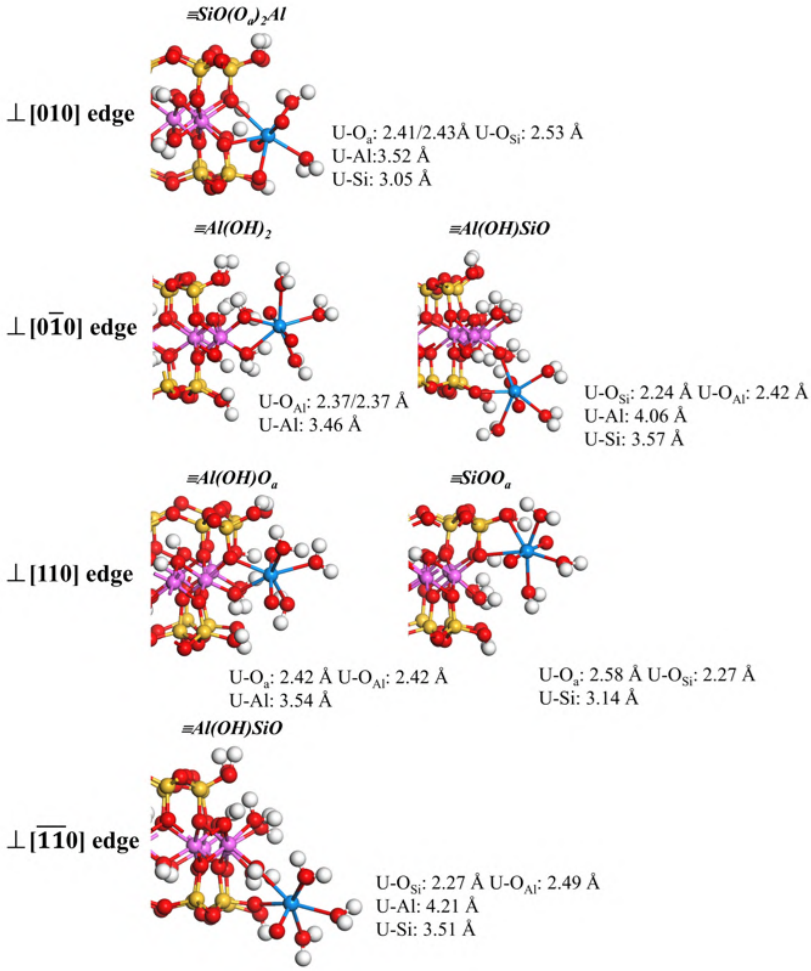

Figure 7.3 Equilibrium configurations of uranyl complexation on edge surfaces of cis-vacant TOT clay layer. Color scheme: U(blue), Si (yellow), Al (pink), O (red), H (white).

7.3.2 Free energies

The details of uranyl desorption processes on cis-vacant clay edges were described in Figure 7.4. All uranyl surface complexes on the adsorption sites were desorbed from inner-sphere bi/tri-dentate to outer-sphere complexes, and the derived free energy curves were shown in Figure 7.5.

The desorption free energy profile of tri-dentate uranyl surface complex on ≡SiO(O_a)$_2$Al site on surface perpendicular to [010] was illustrated in Figure 7.5a. The free energy value was 36.4 kcal/mol, indicating that the tri-dentate complex structure had higher stability than the bidentate uranyl complex on the trans-vacant edges (~20 kcal/mol). In addition, the changes in free energy gradually increased from CN=3 to CN=1, while it changes dramatically from the monodentate structure on ≡SiO site to the outer-sphere complex, indicating weaker binding of U atom with apical

bridge oxygen (O_a). Meanwhile, each apical O site exhibited a free energy of ~8 kcal/mol on $\equiv SiO(O_a)_2Al$ site which is higher than that of the apical O site on the $\equiv Al(OH)O_a$ and $\equiv SiOO_a$ sites on surface perpendicular to [110] of trans-vacant model (around 2 kcal/mol). The observation reflected the additional stability provided by the vacancy sites. On surface perpendicular to $[0\bar{1}0]$, the desorption processes of uranyl from $\equiv Al(OH)_2$ and $\equiv Al(OH)SiO$ sites were similar to that on the surface perpendicular to [010] of trans-vacant model (see Figures 7.5b-7.5c and 7.4). All of the monodentate complexes brought a local stable in the curve. Meanwhile, the free energies from $\equiv Al(OH)_2$ and $\equiv Al(OH)SiO$ sites were 25.0 and 25.9 kcal/mol respectively, which was slightly higher than the same types of sites on trans-vacant edges (21.5 and 21.1 kcal/mol respectively).

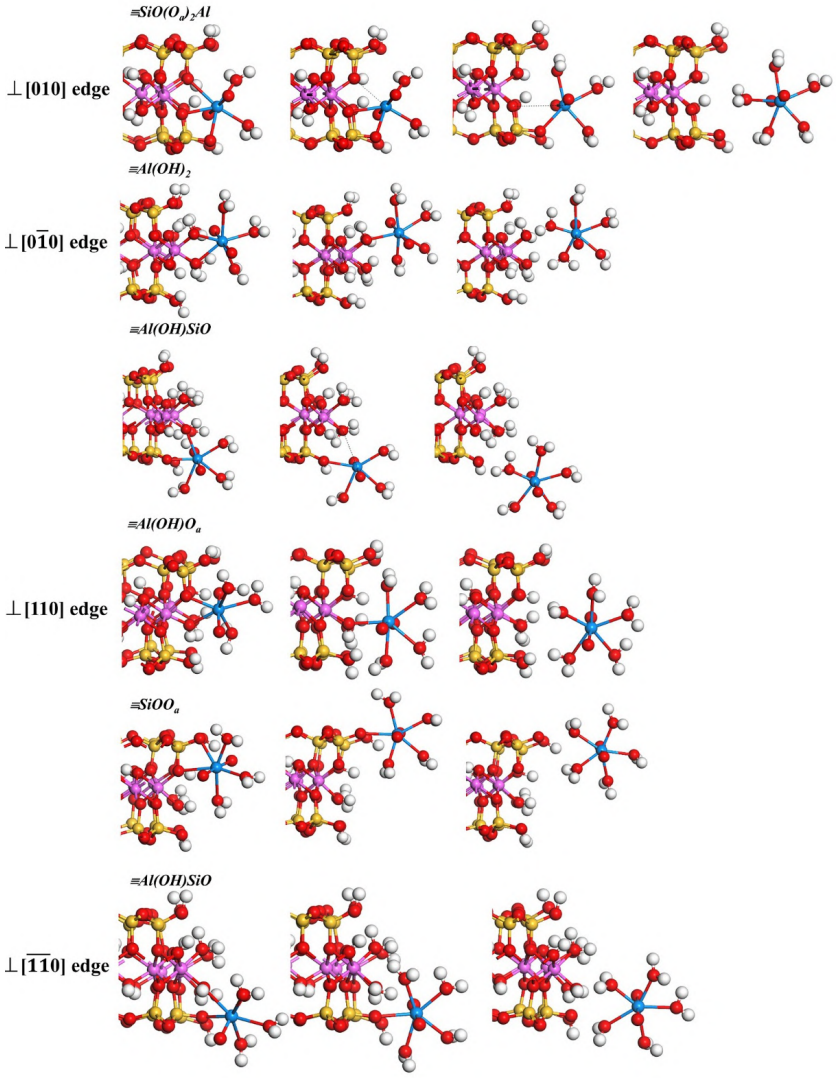

Figure 7.4 Structural transformation in the free energy calculations for the uranyl surface complexes on cis-vacant TOT layer edges.

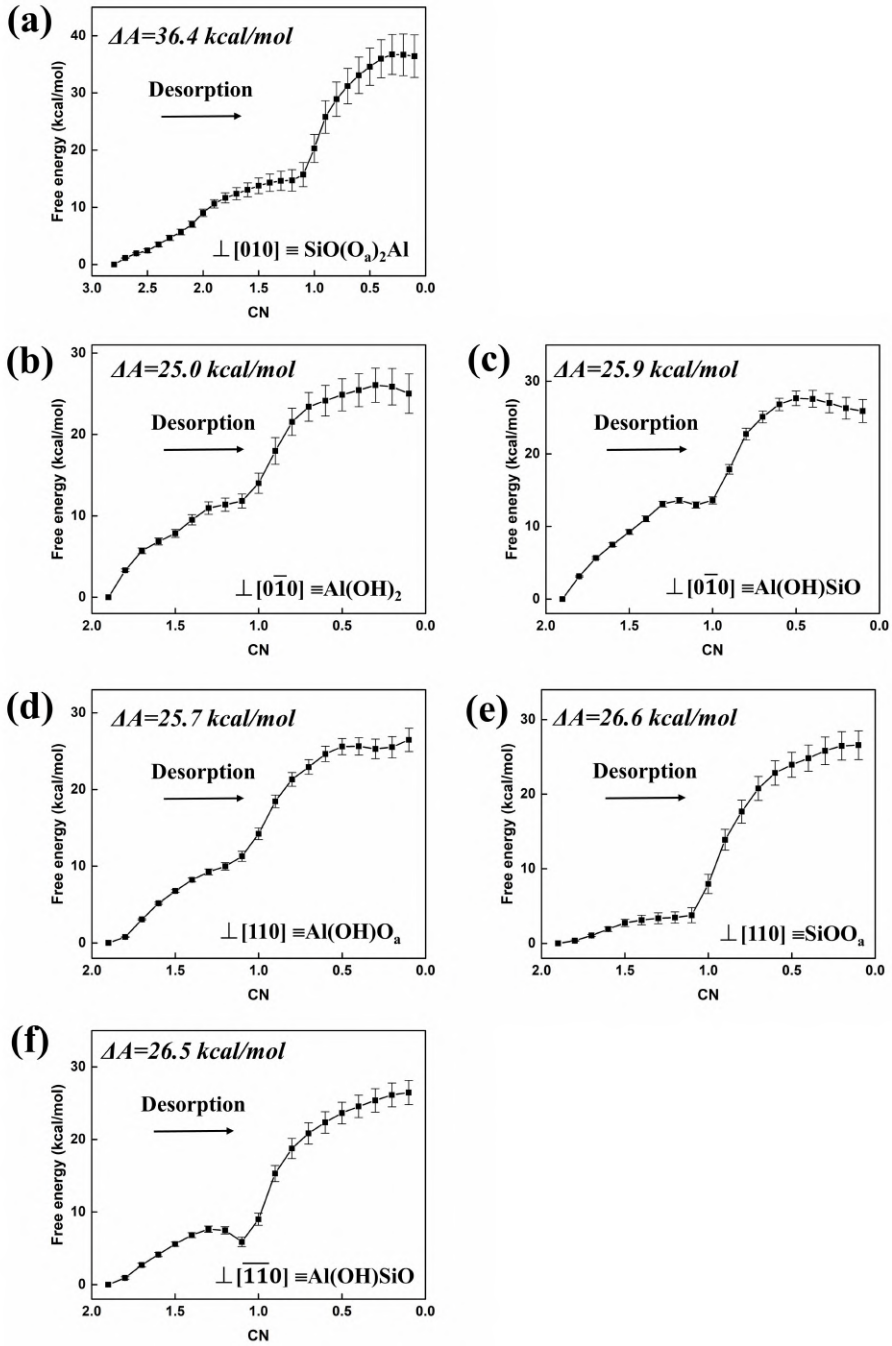

Figure 7.5 Desorption free-energy profile of UO_2^{2+} complexing on edge surface sites at (a) ≡$SiO(O_a)_2Al$ site on surface perpendicular to [010], (b) ≡$Al(OH)_2$ and (c)≡Al(OH)SiO sites on surface perpendicular to [0$\bar{1}$0], (d) ≡$Al(OH)O_a$ and (e) ≡$SiOO_a$ sites on surface perpendicular to [110], and (f) ≡Al(OH)SiO site on surface perpendicular to [$\bar{1}\bar{1}$0] of cis-vacant TOT clay layer. The statistical error in deisorption free energy was estimated by integrating the statistical errors in the mean forces, that were estimated as the semi-difference between the average forces using only the first half or the second half of the trajectory.

Similar to surface perpendicular to [110] of trans-vacant model, uranyl also formed bidentate

surface complexes at≡Al(OH)O_a and ≡SiOO_a sites on surface perpendicular to [110] of cis-vacant model, which had desorption free energies of 25.7 and 26.6 kcal/mol (Figures 7.5d and 7.5e). The free energies were higher than the trans-vacant model on surface perpendicular to [110] (20.0 kcal/mol for ≡Al(OH)O_a and 19.8 kcal/mol for ≡SiOO_a sites), whereas similar to those from ≡Al$(OH)_2$ and ≡Al(OH)SiO sites on the surface perpendicular to [$0\bar{1}0$] (25.0 and 25.9 kcal/mol). The desorption processes on apical bridge oxygen (O_a) still exhibited weak binding strength with slow energy increase from CN=2 to CN=1, which was consistent with surface perpendicular to [110] of trans-vacant model on ≡Al(OH)O_a and ≡SiOO_a sites, as well as surface perpendicular to [010] of cis-vacant model on ≡Si$O(O_a)_2$Al site. Figure 3f showed the desorption free energy curve for the uranyl at ≡Al(OH)SiO site on surface perpendicular to [$\bar{1}\bar{1}0$] of cis-vacant model. The free energy value of 26.5 kcal/mol was comparable to that of previous bidentate surface complexes on cis-vacant model edges.

All desorption free energy values of uranyl on cis- and trans-vacant edge surface sites were collected in Table 7.1. As we see, the free energies on all of the investigated sites in trans-vacant model were very close, which means the similar thermodynamic stability. For cis-vacant model, all bidentate surface complexes were also similar, but with higher values compared to the sites on tran-vacant model, which means that cis-vacant edge sites had higher thermodynamic stability for uranyl. The results indicated that the bidentate surface sites on specific clay models may be responsible to the single site as previous SCM studies proposed. In addition, tridentate uranyl surface complex on surface perpendicular to [010] of cis-vacant model had the highest value, which may correspond to a strong site with a low capacity and a high adsorption affinity in some SCMs.

Table 7.1 Desorption free energy values of uranyl from cis- and trans-vacant clay edge surface. sites

Surface	Cis-vacant		Trans-vacant	
	Sites	ΔA (kcal/mol)	Sites	ΔA (kcal/mol)
[010]	≡Si$O(O_a)_2$Al	36.4 ± 3.7	≡Al$(OH)_2$	21.5 ± 1.7
	—	—	≡AlOHSiO	21.1 ± 2.4
[$0\bar{1}0$]	≡Al$(OH)_2$	25.0 ± 2.4	—	—
	≡AlOHSiO	25.9 ± 1.6	—	—

[110]	≡Al(OH)O_a	25.7 ± 1.5	≡Al(OH)O_a	20.0 ± 1.5
	≡SiOO_a	26.6 ± 1.9	≡SiOO_a	19.8 ± 1.3
[$\overline{1}$10]	≡AlOHSiO	26.5 ± 1.7	—	—

[a]The uranyl desorption free energy values on trans-vacant model were taken from Zhang et al.

7.3.3 Constrained SCMs of U(VI) on cis-vacant montmorillonite

A state-of-the-art SCM was recently built for U(VI) adsorption on montmorillonite, which was constrained by FPMD simulations based on the trans-vacant model (Zhang et al., 2018). In that model, the shape of adsorption K_d-pH curves was determined by the acid-base properties of clay edge sites and uranyl complexes, while the uranyl adsorption affinity on edge sites dictated the amount of adsorbed U(VI). The acid-base properties were estimated by the FPMD simulations. The complete acidity constants database for cis-vacant TOT layers at atomic scale has recently been established. Hence, the shape of U(VI) adsorption curves on each edge site of cis-vacant model can be determined. As a first step to build the U(VI) adsorption SCMs, the uranyl affinity constants on the specific sites were liberally adjusted to fit the adsorption curves (empirical model from Tournassat et al.) (Figure 7.6) (Tournassat et al., 2018). As we see, all of the adsorption sites on surfaces perpendicular to [010], [0$\overline{1}$0] and [$\overline{1}$10] could be used to fit the adsorption curve above pH 5.0, while the adsorption sites on surface perpendicular to [110] were applicable below pH 5.0. In other words, the fitting of U(VI) adsorption curve had multiple ways without more constraints. Therefore, we needed to make further constraints of physicochemical significance. However, it should be noted that the binding free energy values obtained from FPMD calculations cannot be directly applied to determine surface complexation reaction constants, because the corresponding equilibrium constants were dependent on the electrostatic model, which was specific and parametric, but was not necessarily of strict thermodynamic significance. Nevertheless, the free energy values can also reveal fundamental patterns in U(VI) binding strength, which enabled the identification of surface complexation reactions that correspond to newly imposed constraints.

From free energy perspectives, for trans-vacant model, Zhang et al. proposed that all edge surface sites had similar affinities for uranyl, and thus an SCM was constructed with identical affinity constants log $K[UO_2^{2+}]$ at 7.3 for all edge sites, except for ≡Al(OH)O_a site on surfaces perpendicular

to [110] decreased by 2.2 log units.(Zhang et al. 2018) For cis-vacant model, all bidentate surface complexes at edge sites had similar free energies, which are slightly higher than those on tran-vacant model. In addition, a tridentate surface complex exhibited the highest free energy value. Accordingly, the adsorption extents of U(VI) on each of the six sites on cis-vacant edges were evaluated independently with a higher log $K[UO_2^{2+}]$ of 8.7 at ≡Al(OH)$_2$ and ≡Al(OH)SiO sites on surface perpendicular to [0$\bar{1}$0], ≡Al(OH)O$_a$ and ≡SiOO$_a$ on surface perpendicular to [110] and ≡Al(OH)SiO on surface perpendicular to [$\bar{1}\bar{1}$0], while the log $K[UO_2^{2+}]$ at ≡SiO(O$_a$)$_2$Al site on surface perpendicular to [010] was 9.2 (Figure 7.7a). Similar with ≡Al(OH)O$_a$ site on surface perpendicular to [110] of trans-vacant model, it was not possible to reproduce the U(VI) adsorption curve at ≡Al(OH)O$_a$ and ≡SiOO$_a$ sites on cis-vacant model. A 2.6 log unit decrease in log $K[UO_2^{2+}]$ at ≡Al(OH)O$_a$ and ≡SiOO$_a$ sites was conducted, which could be explained by the effect of pK_a errors.

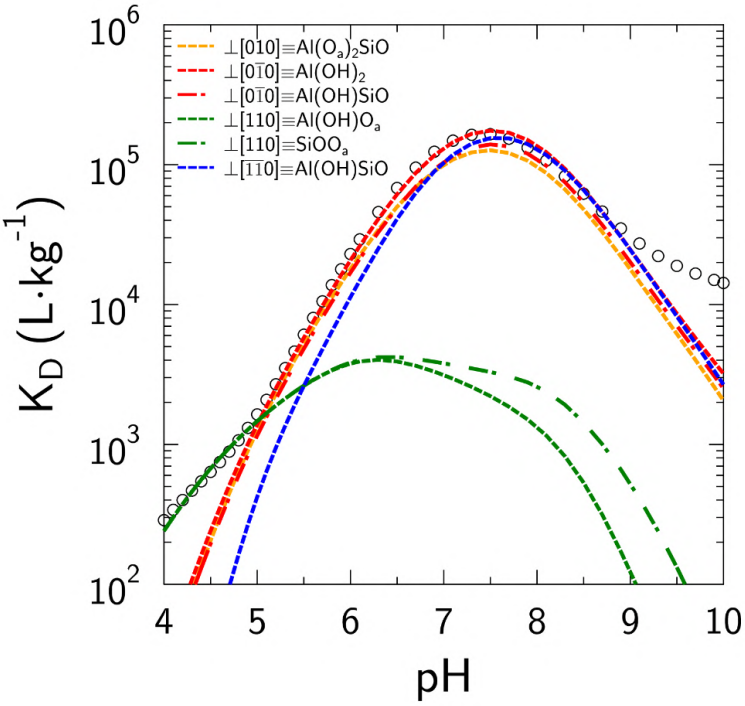

Figure 7.6 Comparison of U(VI) adsorption modeling results on independent edge sites without affinity constants constrained and the empirical model from Tournassat et al. (circles). All the surface model parameters were identical to Gao et al. (Gao et al. 2023) and calculation procedures were identical to Zhang et al. (Zhang et al. 2018)

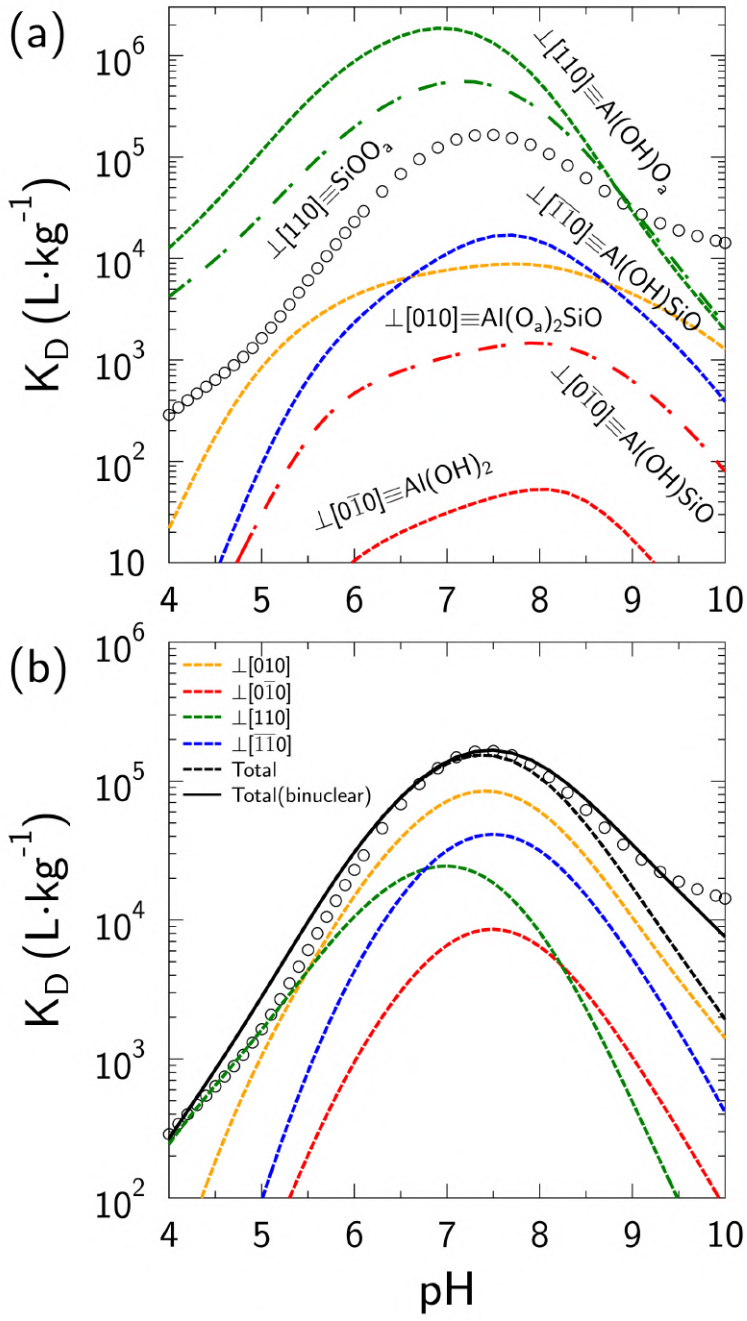

Figure 7.7 (a) Comparison of U(VI) adsorption modeling results on independent edge sites with affinity constants constrained and the empirical model from Tournassat et al. (circles). (b) U(VI) SCMs based on the cis-vacant edge acidity constants and binding free energy assessment at edge sites. All the surface model parameters were identical to Gao et al. and calculation procedures were identical to Zhang et al. (Zhang et al. 2018)

With these modeling conditions, a new SCM was developed to reproduce the U adsorption curve (Figure 7.7b, black dotted line). Similar to the SCMs in the trans-vacant model, the cis-vacant model data above pH 8.5 underestimated U adsorption, which could be ascribed to the formation of

multinuclear uranyl surface complexes as demonstrated in previous studies. Consequently, the U(VI) adsorption curve was adequately reproduced by further introducing surface binuclear uranyl reactions (Figure 7.7b, black line). Compared to the U(VI) SCMs on trans-vacant model (Figure 5 in Zhang et al. 2018), U(VI) SCMs on cis-vacant model achieved a better fit below pH 5.0. For a comprehensive understanding, the individual contributions of each edge were also shown in Figure 7.7b. As we observed, below pH 6.5, the U(VI) adsorption data was mainly contributed by surfaces perpendicular to [010] and [110], while above pH 6.5, all edges played a role and surfaces perpendicular to [010] and [$\overline{1}\overline{1}0$] were predominants. According to edge surface properties of cis-vacant model, at pH below 7, edge surfaces were positively charged on surfaces perpendicular to [$0\overline{1}0$] and [$\overline{1}\overline{1}0$] and negatively charged on surfaces perpendicular to [010] and [110], which provides an explanation for the U(VI) adsorption behavior.

Clay minerals are widely distributed and highly reactive in the critical zone. A comprehensive understanding of the structure-property relationships ofclay interfaces can help researchers and environmental engineers in developing effective strategies for managing environmental contamination behavior. The atomic-level acid-base reactivities of the two types of clay edges (i.e. trans- and cis-vacant) have been extensively investigated in previous studies, which is crucial for comprehending the complexation of pollutants. Additionally, the desorption free energies of U(VI) quantitatively assess the affinities on each edge site. Furthermore, the state-of-the-art SCMs, developed on the basis of all-encompassing atomic-level knowledge, provide a wealth of information on the interactions between uranyl and clay minerals, particularly regarding the physicochemical significance of the predictive model.

At the most fundamental level, our study contributed to the methodology and basis for investigating the fate of various pollutants in clay-rich environments. In particular, the connection between atomic-level and macroscopic information at the clay interface can help predict the environmental behavior of pollutants under different scenarios. For instance, compared to the U(VI) SCMs based on trans-vacant model, our U(VI) SCMs based on cis-vacant model further emphasized the necessity for predicting the environmental behavior of natural clays should be grounded in realistic models. The results also revealed specific crystallographic orientation properties governing the adsorption of U(VI) on cis-vacant clay, which offers valuable insights for future modeling studies

involving other contaminants such as anionic or metalloid substances.

Chapter 8. Conclusions and Perspectives

8.1 Conclusions

In the natural environment or deep geological repository of high-level radioactive waste, understanding the physical and chemical properties of key radionuclides and related minerals and their interactions, and thus quantification of the reaction processes of radionuclides ions at mineral-water interfaces can enable us to fundamentally predict the fate of radionuclides ions in the environment. In recent decades, a large number of experimental and simulation studies have been used to reveal the relevant reaction mechanism, but only the basic mode and characteristics of the adsorption reaction have been obtained, and there are still many problems to be solved. The main research issues focus on the lack of microscopic reaction mechanisms, that is, the structural information and physicochemical behavior at the molecular level of the adsorption, diffusion, migration and desorption processes at the solid/liquid interface. This information can be used to improve data modeling or to identify actinides in many different environments, yet not accessible through wet chemistry experiments and spectroscopic analysis.

This thesis systematically investigates the aqueous solution chemistry of the key radionuclide U(VI) using first-principles calculations, the interactions of key mineral surfaces with U(VI), revealing the reaction mechanisms of monodentate/bidentate inner-sphere complexation structures, outer-sphere complexation structures, mono/multinuclear complexation structures, surface polymerization and precipitation of U(VI) at atomic scale, and the effect of localized structure on the surface at the edges of clay minerals on acid-base and coordination reactivities. The results can be incorporated into predictive surface coordination models to constrain them, leading to advanced constrained SCMs. The main findings and conclusions of the thesis are summarized as follows:

1. Mechanism of uranyl adsorption on the orthoclase (001) surface

Uranyl can form outer surface complexes, monodentate and bidentate inner surface complexes on hydroxylated orthoclase (001) surface. The strong interaction between uranyl and the surface weakens as the adsorption site is protonated, indicating that the adsorption of uranyl increases with increasing pH until deprotonation is complete. At sites with the same degree of protonation, inner-sphere surface complexes were preferred to form. During the adsorption process, the hydrogen bond not only strengthens the adsorption strength but also affects the surface adsorption structure. Electronic structure analysis indicated that the electron density during the adsorption process was

mainly transferred from U to Os. Furthermore, the U f-O p and U d-O p hybridization is the main contribution of the strong covalent interaction of U(VI) with surface oxygen atoms. By comparing the adsorption properties of uranyl on the surface of silica and orthoclase, it is found that the adsorption of uranyl molecules by the two minerals has a high similarity. Therefore, when we model the adsorption of uranyl on the multi-component mineral granite with orthoclase and silica as the main components, we can use $\equiv SOH_2$ as a generalized site to homogenize the multi-component mineral surface adsorption sites. The results provide micro-level support for the feasibility of the generalized modeling method.

2. Structures of Multinuclear U(VI) Species on Hydroxylated α-SiO2 (001) Surface: Density Functional Theory Study

Three kinds of multinuclear U(VI) adsorbates, namely $(UO_2)_2(OH)^{3+}$, $(UO_2)_2(OH)_2^{2+}$ and $(UO_2)_3(O)(OH)_3^{+}$, formed multidentate inner-sphere surface complexes on α-SiO_2(001) surface. $(UO_2)_2(OH)^{3+}$ favored a side-on binding mode in which two uranyl of the dinuclear U(VI) species interact with two deprotonated surface sites, while $(UO_2)_2(OH)_2^{2+}$ and $(UO_2)_2(OH)_2^{2+}$ tend to end-on structures in which only one uranyl coordinates with the surface site via a bidentate mode. The bidentate surface structure on ≡SiO(H)O(H) or ≡SiO(H)SiO(H) sites has shorter U-Os bonds, higher binding energy and longer U-Si distance than the surface complexes of ≡SiO(H)SiO(H). Both electrostatic interactions and chemical bonds (partially covalent) are responsible for the complexation of multinuclear U(VI) species. Os-p orbitals are strongly hybridized with U-f and U-d orbitals, and a transfer of electron density from U to Os occurs simultaneously. The binding energy order of the same site is $(UO_2)_2(OH)^{3+}$ > $(UO_2)_2(OH)_2^{2+}$ > $(UO_2)_3(O)(OH)_3^{+}$, and The binding energy of the same multinuclear adsorbate at the same site of increases with the degree of deprotonation. The hydrogen bonds between the surface hydroxyl groups and the coordination water as well as the acyl oxygen of the uranyl molecule contribute slightly to the overall binding energy of the surface complexes. In addition, the end-on surface complexes of $(UO_2)_2(OH)_2^{2+}$ and $(UO_2)_2(OH)_2^{2+}$ also benefit from the U-f electron delocalization of the far side U atom. This study not only improves our understanding of U(VI) adsorption on silica, but also provides new insights into the structure of multinuclear U(VI) surface complexes.

3. Aggregation and Precipitation Mechanism of Multinuclear U(VI) Species in Aqueous Solution and Surface

The presence of multinuclear uranyl species has been found in both the aqueous solution and the surface. Through the free energy dissociation curve of the polymerization reaction of multinuclear uranyl on the surface and in aqueous, it is found that multinuclear uranyl is more likely to form in aqueous solution. Therefore, the multinuclear uranyl can be formed in aqueous solution and be considered as surface-adsorbed species, which provides a mechanistic confirmation at the microscopic level for widely using aqueous multinuclear species as surface coordination species in SCMs. Based on Hess law, the stability constants of $(UO_2)_2(OH)^{3+}$ and $(UO_2)_2(OH)_2^{2+}$ were calculated and obtained by constructing multinuclear uranyl polymer reaction, and the results were consistent with the experimental results. However, for a reaction involving a large number of elementary reaction steps, that is, $(UO_2)_3(O)(OH)_3^{+}$, a large error will occur. Uranyl oxyhydroxides can be constructed from mononuclear and multinuclear uranyl as elementary species, and we examined two possible reaction pathways. The first way is to build with $(UO_2)_2(OH)^{3+}$ and $(UO_2)_2(OH)_2^{2+}$; the second way is to build with UO_2^{2+} and $(UO_2)_2(OH)_2^{2+}$. The free energy calculation results show that the composition paths of trinuclear uranyl and mononuclear uranyl are thermodynamically more feasible. Therefore, we obtained the reaction mechanism of the early surface precipitation of uranyl from the microscopic level.

4. Acid-base reaction properties of cis-vacant montmorillonite edge surfaces

The high complexity of clay mineral surface reactivity requires the application of multiple techniques to obtain insightful parameters for predictive surface coordination models. We calculated the pKa values of each silanol and aluminol group site on the edge surface of the non-centrosymmetric cis-vacant model that most montmorillonites have in nature and pointed out that the surface structural hydroxyl groups have extremely high pKa values with nonreactivity. Clay minerals have an important intrinsic property of negative layer charge density, which is caused by the isomorphic substitution of metal ions in tetrahedrons or octahedrons. In dioctahedral clay minerals, the most common substitutions are Si(IV) in tetrahedral sheets replaced by Al(III), Al(III) in octahedral sheets replaced by Mg(II), Fe(II) or Fe(III) substitution. We investigated the intrinsic acidity constants of Mg(II), Fe(II)/Fe(III), Al(III) substitutions at cis-vacant montmorillonite edge surface sites. Fe(II) substitution resulted in a significant increase in the pKa value of the local site, whereas Fe(III) substitution resulted in a decrease. In addition, Fe(II) substitution simultaneously increases the pKa values of adjacent silanol sites, but the effect of Fe(III) is weak. Mg(II) substitutions lead to increased

pKa values at local or adjacent sites, while ≡Al(OH) sites in tetrahedrons have high pKa, and Al(III) substitutions in tetrahedral sheets lead to (010) and (110) significantly increased the pKa values of bridging oxygen sites on the surface. All available pKa values for cis-vacant smectites were generalized to state-of-the-art SCMs and successfully reproduced the best available experimental acid-base titration data without any other adjustable parameters. The cis-vacant montmorillonite edge surface charge has little dependence on lattice substitution but a strong dependence on crystallographic orientation. Especially at pH values below 7, the edge surfaces are positively or negatively charged depending on their orientation. These results provide a basis for simulating the adsorption properties of metal ions in natural clay minerals.

5. Mechanism of U(VI) adsorption on the edge surface of cis-vacant montmorillonite

Uranyl coordinated with a bidentate inner-sphere complexation structure on the edge surface of trans-vacant clay minerals. In contrast, the complexation structure of uranyl on cis-vacant (010), $(0\bar{1}0)$, (110) and $(\bar{1}\bar{1}0)$ edge surface were investigated. The adsorption sites include ≡$Al(O)_2SiO$, ≡$Al(OH)_2$, ≡Al(OH)SiO, ≡$Al(OH)O_a$ and ≡$SiOO_a$, etc. Uranyl forms a stable tridentate coordination structure at the ≡$Al(O)_2SiO$ site, and forms a bidentate coordination structure on other sites. The desorption free energies of all the bidentate coordination structures are very similar, which indicates that each site has similar thermodynamic stability and can exist stably, suggesting that a general site could be used to build the macroscopic SCMs. In addition, uranyl has a higher desorption free energy at the ≡$Al(O)_2SiO$ site, which just corresponds to a strong site in the SCM, that is, a site with high binding strength but low site capacity. According to the cis-vacant surface acidity constant and the constraints of the above-mentioned U(VI) adsorption sites, we constructed a U(VI) adsorption model based on the microstructure.

8.2 Perspectives

The research in this thesis reveals the physical and chemical properties of U(VI) and key minerals and the interaction between them. The results and findings help to understand the physical and chemical behavior of U(VI) and mineral interfaces at the atomic level, and provide a basis for future research. The research has laid the foundation, but also provides some enlightenment and new ideas.

(1) Anionic ligands play an important role in the interaction between radionuclide ions and mineral surfaces, such as inorganic acid ions, $OH^-/CO_3^{2-}/NO_3^-/PO_4^{3-}$, and other organic acids. At

present, the adsorption experiments and spectroscopy experiments of the mineral-radionuclide-anion ternary system have been studied, but the characterization of the interaction mechanism, geometric structure and anion's influence on the interaction strength is very lacking. The main reason is that the coordination mode and stability of anions bring great diversity to the system. Theoretical calculations can be used for anion systems to understand the impact of anions on the interfacial chemical behavior of radionuclide ions.

(2) Lanthanides and actinides are the main disposal objects in high-level radioactive waste repositories, most of which are highly toxic and radioactive, and are sensitive to redox reactions, involving oxidation states ranging from +3 to +6. At the same time, the adsorption process has an inductive effect on these redox-sensitive nuclides, and different redox environments affect the valence and speciation of nuclides, thereby affecting the adsorption process. Therefore, taking into account the limitations of the experimental conditions, the theoretical calculation can further introduce the electron transfer process to explore the influence of redox on the system, evaluate the interfacial chemical process of radionuclide ions on the mineral surface, and build a reasonable forecasting model for the geological repository of high-level radioactive waste.

(3) The decay heat of radioactive increases the temperature in deep geological repositories for high-level radioactive waste up to 150°C. A quantitative understanding of radionuclide adsorption at elevated temperatures is a prerequisite for predicting the fate of radionuclide ions in these environments. So far, atomic-level information on the aqueous chemistry of radionuclides at high temperatures and the coordination of mineral surfaces is still lacking. For example, complexation sites, complexation structures, and related thermodynamics information. Through the theoretical calculation, it is helpful to understand the migration and fixation of nuclides in the high-temperature geological environment of the high-level radioactive waste repository.

References

Alam F., Sarkar R. and Chowdhury H. (2019) Nuclear power plants in emerging economies and human resource development: A review. *Energy Procedia* 160, 3–10.

Bader R. F. W. and Matta C. F. (2013) Atoms in molecules as non-overlapping, bounded, space-filling open quantum systems. *Found. Chem.* 15, 253–276.

Baeyens B. and Bradbury M. H. (1997) A mechanistic description of Ni and Zn sorption on Na-montmorillonite part I: Titration and sorption measurements. *J. Contam. Hydrol.* 27, 199–222.

Bargar J. R., Reitmeyer R., Lenhart J. J. and Davis J. A. (2000) Characterization of U(VI)-carbonato ternary complexes on hematite: EXAFS and electrophoretic mobility measurements. *Geochim. Cosmochim. Acta* 64, 2737–2749.

Baumann N., Brendler V., Arnold T., Geipel G. and Bernhard G. (2005) Uranyl sorption onto gibbsite studied by time-resolved laser-induced fluorescence spectroscopy (TRLFS). *J. Colloid Interface Sci.*, 290, 318-324.

Becke A. D. and Edgecombe K. E. (1990) A simple measure of electron localization in atomic and molecular systems. *J. Chem. Phys.* 92, 5397–5403.

Bergaya F., Theng B.K.G. and Lagaly G. (2006) Chapter 12 Critical assessment of some analytical techniques. In *Developments in Clay Science*, Elsevier. pp. 753–754.

Blöchl P. E. (1994) Projector augmented-wave method. *Phys. Rev. B* 50, 17953–17979.

Bourg I. C., Sposito G. and Bourg A. C. M. (2007) Modeling the acid–base surface chemistry of montmorillonite. *J. Colloid Interface Sci.* 312, 297–310.

Bradbury M. H. and Baeyens B. (2005) Modelling the sorption of Mn(II), Co(II), Ni(II), Zn(II), Cd(II), Eu(III), Am(III), Sn(IV), Th(IV), Np(V) and U(VI) on montmorillonite: Linear free energy relationships and estimates of surface binding constants for some selected heavy metals and actinides. *Geochim. Cosmochim. Acta* 69, 875–892.

Bradbury M. H. and Baeyens B. (2011) Predictive sorption modelling of Ni(II), Co(II), Eu(IIII), Th(IV) and U(VI) on MX-80 bentonite and Opalinus Clay: A “bottom-up” approach. *Appl. Clay Sci.* 52, 27–33.

Bradbury M. H. and Baeyens B. (2009) Sorption modelling on illite. Part II: Actinide sorption and linear free energy relationships. *Geochim. Cosmochim. Acta* 73, 1004–1013.

Brigatti Maria Franca, Malferrari D., Laurora A. and Elmi C. (2011) Structure and mineralogy of layer silicates: recent perspectives and new trends. In *Layered Mineral Structures and their Application in Advanced Technologies*. Mineralogical Society of Great Britain and Ireland, London. pp. 1–71.

Burns P. C. and Finch R. J. eds. (1999) Uranium: Mineralogy, Geochemistry, and the Environment. In *Reviews in Mineralogy*, Mineralogical Society of America, Volume 38.

Camellone M. F. and Fabris S. (2009) Reaction Mechanisms for the CO Oxidation on Au/CeO_2 Catalysts: Activity of Substitutional Au^{3+}/Au^{+} Cations and Deactivation of Supported Au^{+} Adatoms. *J. Am. Chem. Soc.* 131, 10473–10483.

Campbell J. E. and Cranwell R. M. (1988) Performance Assessment of Radioactive Waste Repositories. *Science* 239, 1389–1392.

Catalano J. G. and Brown G. E. (2005) Uranyl adsorption onto montmorillonite: Evaluation of binding sites and carbonate complexation. *Geochim. Cosmochim. Acta* 69, 2995–3005.

Cheng J., Liu X., VandeVondele J., Sulpizi M. and Sprik M. (2014) Redox potentials and acidity constants from density functional theory based molecular dynamics. *Acc. Chem. Res.* 47, 3522–3529.

Cheng J., Sulpizi M. and Sprik M. (2009) Redox potentials and pKa for benzoquinone from density functional theory based molecular dynamics. *J. Chem. Phys.* 131, 154504.

Chisholm-Brause C. J., O’Day P. A., Brown G. E. and Parks G. A. (1990) Evidence for multinuclear metal-ion

complexes at solid/water interfaces from X-ray absorption spectroscopy. *Nature* 348, 528–531.

Choppin G. R. (2006) Actinide speciation in aquatic systems. *Mar. Chem.* 99, 83–92.

Clark D. L., Hobart D. E. and Neu M. P. (1995) Actinide Carbonte Complexes and Their Importance in Actinide Environmental Chemistry. *Chem. Rev.* 95, 25–48.

Costanzo F., Sulpizi M., Valle R. G. D. and Sprik M. (2011) The oxidation of tyrosine and tryptophan studied by a molecular dynamics normal hydrogen electrode. *J. Chem. Phys.* 134, 244508.

Cygan R. T., Greathouse J. A. and Kalinichev A. G. (2021) Advances in Clayff Molecular Simulation of Layered and Nanoporous Materials and Their Aqueous Interfaces. *J. Phys. Chem. C* 125, 17573–17589.

Davis J. A., Coston J. A., Kent D. B. and Fuller C. C. (1998) Application of the Surface Complexation Concept to Complex Mineral Assemblages. *Environ. Sci. Technol.* 32, 2820–2828.

Davis J. A., Meece D. E., Kohler M. and Curtis G. P. (2004) Approaches to surface complexation modeling of Uranium(VI) adsorption on aquifer sediments. *Geochim. Cosmochim. Acta* 68, 3621–3641.

Dent A. J., Ramsay J. D. F. and Swanton S. W. (1992) An EXAFS study of uranyl ion in solution and sorbed onto silica and montmorillonite clay colloids. *J. Colloid Interface Sci.* 150, 45–60.

Drits V. A., McCarty D. K. and Zviagina B. B. (2006) Crystal-chemical factors responsible for the distribution of octahedral cations over trans- and cis-sites in dioctahedral 2:1 layer silicates. *Clays Clay Miner.* 54, 131–152.

Duc M., Gaboriaud F. and Thomas F. (2005) Sensitivity of the acid–base properties of clays to the methods of preparation and measurement：1. Literature review. *J. Colloid Interface Sci.* 289, 139–147.

Fenter P., Cheng L., Park C., Zhang Z. and Sturchio N. C. (2003) Studying the Structure of the Orthoclase (001)-Water Interface and the (010)-Water Interfaceby High-resolution X-ray Reflectivity. *Geochim. Cosmochim. Acta* 67, 4267-4275.

Froideval A., Del Nero M., Gaillard C., Barillon R., Rossini I. and Hazemann J. L. (2006) Uranyl sorption species at low coverage on Al-hydroxide: TRLFS and XAFS studies. *Geochim. Cosmochim. Acta* 70, 5270–5284.

Gabriel U., Charlet L., Schläpfer C. W., Vial J. C., Brachmann A. and Geipel G. (2001) Uranyl Surface Speciation on Silica Particles Studied by Time-Resolved Laser-Induced Fluorescence Spectroscopy. *J. Colloid Interface Sci.* 239, 358–368.

Gao P., Zhang D., Jin Q., Chen Z., Wang D., Guo Z. and Wu W. (2021) Multi-scale study of Am(III) adsorption on Gaomiaozi bentonite: Combining experiments, modeling and DFT calculations. *Chem. Geol.* 581, 120414.

Gao P., Liu X., Guo Z., and Tournassat C. (2023) Acid–Base Properties of Cis-Vacant Montmorillonite Edge Surfaces: A Combined First-Principles Molecular Dynamics and Surface Complexation Modeling Approach. *Environ. Sci. Technol.* 2023, 57, 1341-1352.

Geckeis H., Lützenkirchen J., Polly R., Rabung T. and Schmidt M. (2013) Mineral–Water Interface Reactions of Actinides. *Chem. Rev.* 113, 1016–1062.

Giffaut E., Grivé M., Blanc Ph., Vieillard Ph., Colàs E., Gailhanou H., Gaboreau S., Marty N., Madé B. and Duro L. (2014) Andra thermodynamic database for performance assessment: ThermoChimie. *Appl. Geochem.* 49, 225–236.

Goedecker S., Teter M. and Hutter J. (1996) Separable dual-space gaussian pseudopotentials. *Phys. Rev. B* 54, 1703–1710.

Greathouse J. A. and Cygan R. T. (2006) Water Structure and Aqueous Uranyl(VI) Adsorption Equilibria onto External Surfaces of Beidellite, Montmorillonite, and Pyrophyllite: Results from Molecular Simulations. *Environ. Sci. Technol.* 40, 3865–3871.

Grenthe I., Fuger J., Konings R. J. M., Lemire R. J., Muller A. B., Nguyen-Trung C. and Wanner H. (1992) Chemical Thermodynamics of Uranium. In *Nuclear Energy Agency,* OECD.

Grimme S., Antony J., Ehrlich S. and Krieg H. (2010) A consistent and accurate *ab initio* parametrization of density

functional dispersion correction (DFT-D) for the 94 elements H-Pu. *J. Chem. Phys.* 132, 154104.

Grimme S., Ehrlich S. and Goerigk L. (2011) Effect of the damping function in dispersion corrected density functional theory. *J. Comput. Chem.* 32, 1456–1465.

Hattori T., Saito T., Ishida K., Scheinost A. C., Tsuneda T., Nagasaki S. and Tanaka S. (2009) The structure of monomeric and dimeric uranyl adsorption complexes on gibbsite: A combined DFT and EXAFS study. *Geochim. Cosmochim. Acta* 73, 5975–5988.

Hennig C., Reich T., Dähn R. and Scheidegger A. M. (2002) Structure of uranium sorption complexes at montmorillonite edge sites. *Radiochim. Acta* 90, 653–657.

IAEA, (2009) Classification of Radioactive Waste: General safety guide. In *IAEA Safety Standards Series*.

Jin Q., Su L., Montavon G., Sun Y., Chen Z., Guo Z. and Wu W. (2016) Surface complexation modeling of U(VI) adsorption on granite at ambient/elevated temperature: Experimental and XPS study. *Chem. Geol.* 433, 81–91.

Jin Q., Wang G., Ge M., Chen Z., Wu W. and Guo Z. (2014) The adsorption of Eu(III) and Am(III) on Beishan granite: XPS, EPMA, batch and modeling study. *Appl. Geochem.* 47, 17–24.

Kéri A., Dähn R., Krack M. and Churakov S. V. (2017) Combined XAFS spectroscopy and ab initio study on the characterization of iron incorporation by montmorillonite. *Environ. Sci. Technol.* 51, 10585–10594.

Kerisit S. and Liu C. (2012) Diffusion and Adsorption of Uranyl Carbonate Species in Nanosized Mineral Fractures. *Environ. Sci. Technol.* 46, 1632–1640.

Kerisit S., Liu C. and Ilton E. S. (2008) Molecular dynamics simulations of the orthoclase (001)- and (010)-water interfaces. *Geochim. Cosmochim. Acta* 72, 1481–1497.

Kirkwood J. G. (1935) Statistical Mechanics of Fluid Mixtures. *J. Chem. Phys.* 3, 300–313.

Kirkwood J. G. and Boggs E. M. (1942) The Radial Distribution Function in Liquids. *J. Chem. Phys.* 10, 394–402.

Kome G. K., Enang R. K., Tabi F. O. and Yerima B. P. K. (2019) Influence of clay minerals on some soil fertility attributes: A review. *OJSS* 09, 155–188.

Kowal-Fouchard A., Drot R., Simoni E. and Ehrhardt J. J. (2004) Use of Spectroscopic Techniques for Uranium(VI)/Montmorillonite Interaction Modeling. *Environ. Sci. Technol.* 38, 1399–1407.

Kremleva A. and Krüger S. (2016) Comparative Computational Study of Np(V) and U(VI) Adsorption On (110) Edge Surfaces of Montmorillonite. *clays clay miner* 64, 438–451.

Kremleva A., Krüger S. and Rösch N. (2013) Assigning EXAFS results for uranyl adsorption on minerals via formal charges of bonding oxygen centers. *Surf. Sci.* 615, 21–25.

Kremleva A., Krüger S. and Rösch N. (2010) Quantum chemical modeling of uranyl adsorption on mineral surfaces. *Radiochim. Acta* 98, 635–646.

Kremleva A., Krüger S. and Rösch N. (2011) Uranyl adsorption at (010) edge surfaces of kaolinite: A density functional study. *Geochim. Cosmochim. Acta* 75, 706–718.

Kremleva A., Kruger S. and Rosch N. (2015) Uranyl adsorption at solvated edge surfaces of 2 : 1 smectites. A density functional study. *Phys. Chem. Chem. Phys.* 17, 13757-13768.

Kresse G. and Furthmüller J. (1996a) Efficiency of ab-initio total energy calculations for metals and semiconductors using a plane-wave basis set. *Comput. Mater. Sci.* 6, 15–50.

Kresse G. and Furthmüller J. (1996b) Efficient iterative schemes for ab initio total-energy calculations using a plane-wave basis set. *Phys. Rev. B* 54, 11169–11186.

Kresse G. and Hafner J. (1993) Ab initio molecular dynamics for liquid metals. *Phys. Rev. B* 47, 558–561.

Kresse G. and Joubert D. (1999) From ultrasoft pseudopotentials to the projector augmented-wave method. *Phys. Rev. B* 59, 1758–1775.

Kühne T. D., Iannuzzi M., Del Ben M., Rybkin V. V., Seewald P., Stein F., Laino T., Khaliullin R. Z., Schütt O., Schiffmann F., Golze D., Wilhelm J., Chulkov S., Bani-Hashemian M. H., Weber V., Borštnik U.,

Taillefumier M., Jakobovits A. S., Lazzaro A., Pabst H., Müller T., Schade R., Guidon M., Andermatt S., Holmberg N., Schenter G. K., Hehn A., Bussy A., Belleflamme F., Tabacchi G., Glöß A., Lass M., Bethune I., Mundy C. J., Plessl C., Watkins M., VandeVondele J., Krack M. and Hutter J. (2020) CP2K: An electronic structure and molecular dynamics software package - Quickstep: Efficient and accurate electronic structure calculations. *J. Chem. Phys.* 152, 194103.

Kumar R., Schmidt J. R. and Skinner J. L. (2007) Hydrogen bonding definitions and dynamics in liquid water. *J. Chem. Phys.* 126, 204107.

Lippert G., Hutter J. and Parrinello M. (1997) A hybrid Gaussian and plane wave density functional scheme. *Mol. Phys.* 92, 477–488.

Liu J.-C., Luo L., Xiao H., Zhu J., He Y. and Li J. (2022) Metal Affinity of Support Dictates Sintering of Gold Catalysts. *J. Am. Chem. Soc.* 144, 20601–20609.

Liu X., Cheng J., He M., Lu X. and Wang R. (2016) Acidity constants and redox potentials of uranyl ions in hydrothermal solutions. *Phys. Chem. Chem. Phys.* 18, 26040–26048.

Liu X., Cheng J., Lu X. and Wang R. (2014) Surface acidity of quartz: understanding the crystallographic control. *Phys. Chem. Chem. Phys.* 16, 26909–26916.

Liu X., Lu X., Cheng J., Sprik M. and Wang R. (2015) Temperature dependence of interfacial structures and acidity of clay edge surfaces. *Geochim. Cosmochim. Acta* 160, 91–99.

Liu X., Lu X., Sprik M., Cheng J., Meijer E. J. and Wang R. (2013) Acidity of edge surface sites of montmorillonite and kaolinite. *Geochim. Cosmochim. Acta* 117, 180–190.

Lu J.-B., Ma X.-L., Wang J.-Q., Liu J.-C., Xiao H. and Li J. (2018) Efficient Nitrogen Fixation via a Redox-Flexible Single-Iron Site with Reverse-Dative Iron → Boron σ Bonding. *J. Phys. Chem. A* 122, 4530–4537.

Marques Fernandes M., Baeyens B., Dähn R., Scheinost A. C. and Bradbury M. H. (2012) U(VI) sorption on montmorillonite in the absence and presence of carbonate: A macroscopic and microscopic study. *Geochim. Cosmochim. Acta* 93, 262–277.

Martyna G. J., Klein M. L. and Tuckerman M. (1992) Nosé–Hoover chains: The canonical ensemble via continuous dynamics. *J. Chem. Phys.* 97, 2635–2643.

Momma K. and Izumi F. (2008) *VESTA* : a three-dimensional visualization system for electronic and structural analysis. *J Appl. Crystallogr* 41, 653–658.

Nebelung C. and Brendler V. (2010) U(VI) sorption on granite: prediction and experiments. *Radiochim. Acta* 98, 621–625.

Nguyen-Trung C., Palmer D. A., Begun G. M., Peiffert C. and Mesmer R. E. (2000) Aqueous Uranyl Complexes 1. Raman Spectroscopic Study of the Hydrolysis of Uranyl(VI) in Solutions of Trifluoromethanesulfonic Acid and/or Tetramethylammonium Hydroxide at 25°C and 0.1 MPa. *J. Solution Chem.* 29, 101-129

Orucoglu E., Grangeon S., Gloter A., Robinet J.-C., Madé B. and Tournassat C. (2022) Competitive adsorption processes at clay mineral surfaces: A coupled experimental and modeling approach. *ACS Earth Space Chem.* 6, 144–159.

Ozboyaci, M., Kokh, D., Corni, S., & Wade, R. (2016). Modeling and simulation of protein–surface interactions: Achievements and challenges. Quarterly Reviews of Biophysics, 49, E4.

Pan D., Zhao X., Wang P., Li P., Li Y., Wu W., Wang Z. and Fan Q. (2022) Insights into sorption speciation of uranium on phlogopite: Evidence from TRLFS and DFT calculation. *J. Hazard. Mater.* 427, 128164.

Pan Q.-J., Odoh S. O., Asaduzzaman A. and Schreckenbach G. (2012) Adsorption of Uranyl Species onto the Rutile (110) Surface: A Periodic DFT Study. *Chem. Eur. J.*, 18, 1458-1466.

Parkhurst D. L. and Appelo C. A. J. (2013) Description of input and examples for PHREEQC Version 3-A computer program for speciation, batch-reaction, one-dimensional transport, and inverse geochemical calculations. In *U.S. Geological Survey: Denver.*

Peng C., Min F., Liu L. and Chen J. (2016) A periodic DFT study of adsorption of water on sodium-montmorillonite (001) basal and (010) edge surface. *Appl. Surf. Sci.* 387, 308–316.

Perdew J. P., Burke K. and Ernzerhof M. (1997) Generalized gradient approximation made simple. *Phys. Rev. Lett.* 78, 1396–1396.

Reich T., Moll H., Arnold T., Denecke M. A., Hennig C., Geipel G., Bernhard G., Nitsche H., Allen P. G., Bucher J. J., Edelstein N. M. and Shuh D. K. (1998) An EXAFS study of uranium(VI) sorption onto silica gel and ferrihydrite. *J. Electron Spectrosc. Relat. Phenom.* 96, 237–243.

Reinholdt M. X., Hubert F., Faurel M., Tertre E., Razafitianamaharavo A., Francius G., Prêt D., Petit S., Béré E., Pelletier M. and Ferrage E. (2013) Morphological properties of vermiculite particles in size-selected fractions obtained by sonication. *Appl. Clay Sci.* 77–78, 18–32.

Richter C., Müller K., Drobot B., Steudtner R., Großmann K., Stockmann M. and Brendler V. (2016) Macroscopic and spectroscopic characterization of uranium(VI) sorption onto orthoclase and muscovite and the influence of competing Ca^{2+}. *Geochim. Cosmochim. Acta* 189, 143–157.

Schlegel M. L. and Descostes M. (2009) Uranium Uptake by Hectorite and Montmorillonite: A Solution Chemistry and Polarized EXAFS Study. *Environ. Sci. Technol.* 43, 8593–8598.

Schlegel M. L., Nagy K. L., Fenter P. and Sturchio N. C. (2002) Structures of quartz (100)- and (101)-water interfaces determined by x-ray reflectivity and atomic force microscopy of natural growth surfaces. *Geochim. Cosmochim. Acta* 66, 3037–3054.

Silvi B. and Savin A. (1994) Classification of chemical bonds based on topological analysis of electron localization functions. *Nature* 371, 683–686.

Sposito G. (2008) The chemistry of soils. *second edition.,* In *Oxford university press, New York.*

Sprik M. (1998) Coordination numbers as reaction coordinates in constrained molecular dynamics. *Faraday Disc.* 110, 437–445.

Sprik M. and Ciccotti G. (1998) Free energy from constrained molecular dynamics. *J. Chem. Phys.* 109, 7737–7744.

Stucki J. W. (2013) Chapter 11 - Properties and behaviour of iron in clay minerals. In *Developments in Clay Science* (eds. F. Bergaya and G. Lagaly). Elsevier. pp. 559–611.

Subramanian N., Whittaker M. L., Ophus C. and Lammers L. N. (2020) Structural implications of interfacial hydrogen bonding in hydrated Wyoming-montmorillonite clay. *J. Phys. Chem. C* 124, 8697–8705.

Sulpizi M. and Sprik M. (2008) Acidity constants from vertical energy gaps: density functional theory based molecular dynamics implementation. *Phys. Chem. Chem. Phys.* 10, 5238.

Sylwester E. R., Hudson E. A. and Allen P. G. (2000) The structure of uranium (VI) sorption complexes on silica, alumina, and montmorillonite. *Geochim. Cosmochim. Acta* 64, 2431–2438.

Tan X., Fang M. and Wang X. (2010) Sorption Speciation of Lanthanides/Actinides on Minerals by TRLFS, EXAFS and DFT Studies: A Review. *Molecules* 15, 8431–8468.

Tang W., Sanville E. and Henkelman G. (2009) A grid-based Bader analysis algorithm without lattice bias. *J. Phys.: Condens. Matter* 21, 084204.

Tang Y. and Reeder R. J. (2009) Uranyl and arsenate cosorption on aluminum oxide surface. *Geochim. Cosmochim. Acta* 73, 2727–2743.

Tazi S., Rotenberg B., Salanne M., Sprik M. and Sulpizi M. (2012) Absolute acidity of clay edge sites from ab-initio simulations. *Geochim. Cosmochim. Acta* 94, 1–11.

Tournassat C., Davis J. A., Chiaberge C., Grangeon S. and Bourg I. C. (2016) Modeling the Acid–Base Properties of Montmorillonite Edge Surfaces. *Environ. Sci. Technol.* 50, 13436–13445.

Tournassat C., Steefel C. I., Bourg I. C. and Bergaya F. eds. (2015) Natural and engineered clay barriers., *Elsevier, Amsterdam.*

Tournassat C., Tinnacher R. M., Grangeon S. and Davis J. A. (2018) Modeling uranium(VI) adsorption onto

montmorillonite under varying carbonate concentrations: A surface complexation model accounting for the spillover effect on surface potential. *Geochim. Cosmochim. Acta* 220, 291–308.

Tozini D., Forti M., Gargano P., Alonso P. R. and Rubiolo G. H. (2015) Charge Difference Calculation in Fe/Fe3O4 Interfaces from DFT Results. *Procedia Mater. Sci.* 9, 612–618.

Tsipursky S. I. and Drits V. A. (1984) The distribution of octahedral cations in the 2:1 layers of dioctahedral smectites studied by oblique-texture electron diffraction. *Clay miner.* 19, 177–193.

Tsuji Y. and Yoshizawa K. (2018) Adsorption and Activation of Methane on the (110) Surface of Rutile-type Metal Dioxides. *J. Phys. Chem. C* 122, 15359–15381.

Tsunashima A. (1981) Adsorption of Uranium from Solutions by Montmorillonite; Compositions and Properties of Uranyl Montmorillonites. *Clays Clay Miner.* 29, 10–16.

Tsushima S., Rossberg A., Ikeda A., Müller K. and Scheinost A. C. (2007) Stoichiometry and Structure of Uranyl(VI) Hydroxo Dimer and Trimer Complexes in Aqueous Solution. *Inorg. Chem.* 46, 10819–10826.

Tsushima S. and Suzuki A. (2000) Hydration numbers of pentavalent and hexavalent uranyl, neptunyl, and plutonyl. *J. Mol. Struct.: THEOCHEM* 529, 21–25.

Walter M., Arnold T., Geipel G., Scheinost A. and Bernhard G. (2005) An EXAFS and TRLFS investigation on uranium(VI) sorption to pristine and leached albite surfaces. *J. Colloid Interface Sci.* 282, 293–305.

Wang H., Chai Z. and Wang D. (2015) Adsorption of uranyl on hydroxylated α-SiO_2(001): a first-principle study. *Dalton Trans.* 44, 1646-1654.

Wang H., Chai Z. and Wang D. (2017) Influence of anions on the adsorption of uranyl on hydroxylated α-SiO_2(001): A first-principles study. *Green Energy Environ.* 2, 30–41.

Wang J. (2010) High-level radioactive waste disposal in China: update 2010. *JRMGE.* 2, 1-11.

Wang V., Xu N., Liu J. C., Tang G. and Geng W.-T. (2021) VASPKIT: A User-friendly Interface Facilitating High-throughput Computing and Analysis Using VASP Code. *Comput. Phys. Commun.* 267, 108033.

Wen X., Du Q. and Tang H. (1998) Surface Complexation Model for the Heavy Metal Adsorption on Natural Sediment. *Environ. Sci. Technol.* 32, 870–875.

Wheaton V., Majumdar D., Balasubramanian K., Chauffe L. and Allen P. G. (2003) A comparative theoretical study of uranyl silicate complexes. *Chem. Phys. Lett.* 371, 349–359.

Wolthers M., Charlet L. and Tournassat C. (2006) Chapter 20 - Reactivity of bentonite: an additive model applied to uranyl sorption. In *Interface Science and Technology* (ed. J. Lützenkirchen). Elsevier. pp. 539–552.

Yi W., Tang G., Chen X., Yang B. and Liu X. (2020) qvasp: A flexible toolkit for VASP users in materials simulations. *Comput. Phys. Commun.* 257, 107535.

Zhang C., Liu X., Lu X., Jan Meijer E., and Wang R. (2019) An atomic-scale understanding of the initial stage of nucleation of heavy metal cations on clay edges. *Geochim. Cosmochim. Acta*, 248, 161-171.

Zhang C. Liu X., Lu X., He M., Jan Meijer E., and Wang R. (2017) Surface complexation of heavy metal cations on clay edges: insights from first principles molecular dynamics simulation of Ni(II). *Geochim. Cosmochim. Acta*, 203, 54-68.

Zhang C., Liu X., Tinnacher R. M. and Tournassat C. (2018) Mechanistic Understanding of Uranyl Ion Complexation on Montmorillonite Edges: A Combined First-Principles Molecular Dynamics–Surface Complexation Modeling Approach. *Environ. Sci. Technol.*, 52, 8501-8509.

Zhang Y.-J., Lan J.-H., Wang L., Wu Q.-Y., Wang C.-Z., Bo T., Chai Z.-F. and Shi W.-Q. (2016) Adsorption of uranyl species on hydroxylated titanium carbide nanosheet: A first-principles study. *J. Hazard. Mater.* 308, 402–410.

Zhou Y. (2011) China's spent nuclear fuel management: Current practices and future strategies. *Energy Policy* 39, 4360–4369.

Zielinski R. A., Chafin D. T., Banta E. R. and Szabo B. J. (1997) Use of ^{234}U and ^{238}U isotopes to evaluate

contamination of near-surface groundwater with uranium-mill effluent: a case study in south-central Colorado, U.S.A. *Environ. Geol.* 32, 124–136.

Zwanzig R. W. (1954) High-Temperature Equation of State by a Perturbation Method. I. Nonpolar Gases. *J. Chem. Phys.* 22, 1420–1426.

Published Papers:

[1] **Pengyuan Gao**, Daming Zhang, Qiang Jin, Zongyuan Chen, Dongqi Wang, Zhijun Guo, Wamgsuo Wu. Multi-scale study of Am(III) adsorption on Gaomiaozi bentonite: Combining experiments, modeling and DFT calculations. *Chemical Geology*, 2021, 581, 120414.

[2] **Pengyuan Gao**, Xiandong Liu, Zhijun Guo, Christophe Tournassat. Acid–Base Properties of Cis-Vacant Montmorillonite Edge Surfaces: A Combined First-Principles Molecular Dynamics and Surface Complexation Modeling Approach. *Environmental Science and Technology*, 2023, 57, 1341-1352.

[3] **Pengyuan Gao**, Xiandong Liu, Zhijun Guo, Christophe Tournassat. Influence of Fe(II), Fe(III) and Al(III) Isomorphic Substitutions on Acid-Base Properties of Edge Surfaces of Cis-Vacant Montmorillonite: Insights from First-Principles Molecular Dynamics Simulations and Surface Complexation Modeling. *American Mineralogist*, 2023, xx-xx.

[4] **Pengyuan Gao**, Qiang Jin, Qiang Jin, Zongyuan Chen, Dongqi Wang, Christophe Tournassat , Zhijun Guo. Structures of Multinuclear U(VI) Species on Hydroxylated α-SiO_2 (001) Surface: Insights from DFT calculations. *xx,* (In submitted)

[5] Zhen Zhang, **Pengyuan Gao**, Gilles Montavon, Zongyuan Chen, Dongqi Wang, Zhaoyi Tan, Qiang Jin, Wangsuo Wu, Ju Wang, Zhijun Guo. Strengthened erosion resistance of compacted bentonite by layered double hydroxide: A new electrostatic interaction-based approach. *Chemosphere*, 2022, 292, 133402.

[6] Zongyuan Chen, Siyuan Wang, Huijuan Hou, Kang Chen, **Pengyuan Gao**, Zhen Zhang, Qiang Jin, Duoqiang Pan, Zhijun Guo, Wangsuo Wu. China's progress in radionuclide migration study over the past decade (2010–2021): Sorption, transport and radioactive colloid. *Chinese Chemical Letters*, 2022, 33, 3405-3412.

Conferences:

Goldschmidt 2023 Conference 2023.07 France·Lyon

Pengyuan GAO

Études théoriques de l'interaction entre l'U(VI) et les surfaces minérales

L'étude des processus d'adsorption des radionucléides sur les surfaces minérales est fondamentale pour la conception et l'évaluation de la sûreté des futurs systèmes de stockage des déchets radioactifs, ainsi que pour les diagnostics environnementaux des milieux pollués par des radionucléides. Parmi ces radionucléides, l'uranium a une abondance relativement élevée dans les systèmes naturels et a un rôle central dans le cycle du combustible nucléaire. L'uranium peut se trouver sous plusieurs états d'oxydation. L'U(VI) est l'état d'oxydation le plus pertinent dans la plupart des eaux de surface et des eaux souterraines oxygénées. L'adsorption de l'U(VI) sur les surfaces de divers minéraux a été largement étudiée par des expériences en batch complémenté par des techniques spectroscopiques. Des sites de complexation possibles et des espèces de surface ont été proposés, mais il est encore difficile d'obtenir des informations précises sur les mécanismes moléculaires responsables des processus d'adsorption. Ces informations sont essentielles pour comprendre les mécanismes physico-chimiques impliqués dans les expériences et pour développer des modèles prédictifs pour les environnements concernés. Les calculs théoriques à l'échelle moléculaire se sont avérés être un outil efficace pour étudier les processus d'adsorption des radionucléides à l'interface minéral-eau. Dans cette thèse, les caractéristiques structurales et les mécanismes d'adsorption des espèces d'U(VI) sur les surfaces des principaux minéraux constitutifs du granite (orthoclase et quartz) et des matériaux tampons/remblais (montmorillonite) des futurs systèmes de stockage en couche géologique profonde ont été obtenus à l'aide de calculs de dynamique moléculaire ab initio. Les mécanismes de polymérisation des espèces d'U(VI) en solution aqueuse et sur les surfaces minérales ont été étudiés. En outre, l'influence de la variabilité des sites d'adsorption des minéraux argileux de type montmorillonite sur les réaction d'adsorption a également été étudiée de manière systématique.

Mots-clés : U(VI) ; Orthoclase ; Silice ; Montmorillonite ; FPMD ; Structure des complexes de surface ; Structures électroniques ; Energie libre ; Constante d'acidité ; Modélisation de la complexation de surface.

Theoretical Studies of the Interaction between U(VI) and Mineral Surfaces

Studies of the adsorption characteristics of key radionuclides in the host rock and buffer/backfill materials of deep geological repositories for high-level waste (HLW) are fundamental to the design and safety assessment. Uranium is a radionuclide of widespread interest due to its relatively high abundance in nature and its central role in the nuclear fuel cycle, while U(VI) is the most relevant oxidation state in most surface waters and oxygenated groundwater. The adsorption of U(VI) on the surfaces of various minerals has been extensively investigated by conventional batch experiments and spectroscopic techniques. Possible complexation sites and surface species have been proposed, but it is still challenging to able to obtain mechanistically precise insights at the microscopic level. Information at the molecular level is essential to understand the physicochemical mechanisms involved in the experiments and to develop predictive models for the relevant environments. Theoretical computations have been proven to be an effective tool for studying the chemical processes of radionuclides at the mineral-water interface. In this thesis, the structural characteristics and adsorption mechanisms of U(VI) species on the surfaces of the main component minerals of granite (orthoclase and quartz) and buffer/backfill materials (montmorillonite) of the deep geological repository were calculated by first-principles calculations. The polymerization mechanisms of U(VI) species in aqueous solution and on mineral surfaces were investigated. In addition, the effect of local structural changes of montmorillonite on the nature of the adsorption reaction on the surface was also systematically investigated.

Keywords: U(VI); Orthoclase; Silica; Montmorillonite; First-principles simulation; Surface complexation structure; Electronic structures; Free energy; Acidity constant; Surface complexation modeling.

Institut des Sciences de la Terre d'Orléans
Université d'Orléans - CNRS-BRGM
45071Orléans - France